Final Report
A-4699-3

ULTRAFINE MICROSTRUCTURE COMPOSITES

PREPARED BY CHEMICAL VAPOR DEPOSITION

W. J. Lackey, Garth B. Freeman, John A. Hanigofsky,
John R. Thompson, and Géoving J. Gérard
Georgia Tech Research Institute

Woo Y. Lee and Pradeep K. Agrawal
School of Chemical Engineering

and

Douglas J. Twait, Thomas S. Moss III, and Andrew J. Green
School of Materials Engineering
Georgia Institute of Technology

Prepared for
Dr. Donald E. Polk
Code 1131
Office of Naval Research
800 North Quincy Street
Arlington, VA 22217-5000

Under Contract Number N00014-87-K-0036

Final Report for the period January 1987-December 1989

Approved for Public Release: Distribution is Unlimited

GEORGIA INSTITUTE OF TECHNOLOGY
A Unit of the University System of Georgia
Atlanta, Georgia 30332

GTRI
GEORGIA TECH RESEARCH INSTITUTE

Final Report
A-4699-3

ULTRAFINE MICROSTRUCTURE COMPOSITES

PREPARED BY CHEMICAL VAPOR DEPOSITION

W. J. Lackey, Garth B. Freeman, John A. Hanigofsky,
John R. Thompson, and Géoving J. Gérard
Georgia Tech Research Institute

Woo Y. Lee and Pradeep K. Agrawal
School of Chemical Engineering

and

Douglas J. Twait, Thomas S. Moss III, and Andrew J. Green
School of Materials Engineering
Georgia Institute of Technology

Prepared for
Dr. Donald E. Polk
Code 1131
Office of Naval Research
800 North Quincy Street
Arlington, VA 22217-5000

Under Contract Number N00014-87-K-0036

Final Report for the period January 1987-December 1989

Approved for Public Release: Distribution is Unlimited

TABLE OF CONTENTS

LIST OF TABLES

LIST OF ILLUSTRATIONS

SUMMARY

Two chemically different phases, hexagonal BN and wurtzite AlN, were simultaneously deposited by chemical vapor deposition (CVD). The BN+AlN films were grown on Al_2O_3 substrates using an impinging jet geometry from BCl_3-$AlCl_3$-NH_3-Ar reagent mixtures. Also, BN and AlN as single phase coatings (BN-CVD and AlN-CVD) were prepared for comparison purposes. The effects of processing parameters such as temperature, pressure, and reagent concentration on deposition rate and microstructure of the BN, AlN, and BN+AlN coatings were systematically investigated. The coatings were characterized using XRD, SEM, XPS, TEM, electron diffraction, and electron microprobe. In general, the BN+AlN coatings consisted of very small BN and AlN grains as two distinctly different crystalline phases. For example, a composite containing single crystal whiskers of AlN in a matrix of turbostratic BN of 2 nm grain size was prepared. The hardness of the BN+AlN coatings increased on increasing the AlN content.

A mass transfer model was developed to identify intrinsic deposition mechanisms for the BN and AlN systems. At typical operating conditions, the BN-CVD process was determined to be kinetically-controlled whereas the AlN-CVD process could be approximated by calculating mass transfer-thermodynamic limits when low $AlCl_3$ concentrations were used. At high $AlCl_3$ concentrations, a surface reaction involving $AlCl_3$ adsorbed on the deposition

surface appeared to be the rate-limiting step. The BN+AlN-CVD process could not be described in a quantitative manner by superimposing the deposition mechanisms obtained from the single phase CVD processes. However, the growth characteristics of BN and AlN in the codeposition system were similar to those expected from their single phase deposition processes except for several minor, but interesting differences. The growth of AlN whiskers was accentuated in BN+AlN-CVD comparing to that in AlN-CVD. In both BN+AlN-CVD and AlN-CVD, the growth of AlN whiskers became more apparent with increasing pressure or temperature. A physical competition between BN and AlN grains in the composites was suspected to cause the reduction in the ultimate grain size of BN and AlN.

As a result of this project, the following papers, reports, and presentations were completed or are planned.

Papers:

1. W. J. Lackey, Arlynn W. Smith, D. M. Dillard, and Douglas J. Twait, "Codeposition of Dispersed Phase Ceramic Composition," Invited paper in Proceedings of the 10th International Conference on Chemical Vapor Deposition, 1008-1027, ed. G. W. Cullen and J. M. Blocher, Jr., The Electrochemical Society, Inc., Pennington, New Jersey, 1987.

2. W. J. Lackey, Arlynn W. Smith, and Douglas J. Twait, "Chemical Vapor Deposition of Oxidation Resistant HfB_2+SiC Composite Coatings," Ceramic Engineering Science Proceedings, 9 (9-10) 1223-1232 (1988).

3. W. Y. Lee, P. K. Agrawal, and W. J. Lackey, "Chemical Vapor Deposition of Dispersed Phase Ceramic (BN+AlN) Composites," Proceedings of the 1988 AIChE Annual Meeting, Washington, D.C., (27 November - 2 December 1988).

4. D. J. Twait, W. J. Lackey, W. Y. Lee, and J. A. Hanigofsky, "Thermodynamic Analysis of the Chemical Vapor Deposition of BN+AlN Composite Coatings," Accepted for publication in J. Am. Ceram. Soc. (1990).

5. W. Y. Lee, W. J. Lackey, G. B. Freeman, P. K. Agrawal, and D. J. Twait, "Preparation of Dispersed Phase Ceramic BN+AlN Composite Coatings by Chemical Vapor Deposition," submitted for publication in Comm. Am. Ceram. Soc. (1990).

6. J. A. Hanigofsky, K. L. More, W. Y. Lee, and W. J. Lackey, "Microstructural Characterization of BN+AlN Codeposited Coatings," to be submitted to Comm. Am. Ceram. Soc. (1990).

7. W. Y. Lee, W. J. Lackey, and P. K. Agrawal, "Kinetic Analysis of Chemical Vapor Deposition of Boron Nitride," to be submitted to J. Am. Ceram. Soc. (1990).

8. W. Y. Lee, W. J. Lackey, and P. K. Agrawal, "Kinetic and Thermodynamic Analyses of Chemical Vapor Deposition of Aluminum Nitride," to be submitted to J. Am. Ceram. Soc. (1990).

9. W. Y. Lee, W. J. Lackey, and P. K. Agrawal, "Physicochemical Nature of Simultaneous Chemical Vapor Deposition of Boron Nitride and Aluminum Nitride," to be submitted to J. Am. Ceram. Soc. (1990).

10. W. Y. Lee, W. J. Lackey, and P. K. Agrawal, "Codeposition of BN+AlN Composite Coatings," submitted to Proceedings of the 11th International Conference on Chemical Vapor Deposition, Seattle, Washington (1990).

Reports:

1. W. J. Lackey et al., "Ultrafine Microstructure Composites Prepared by Chemical Vapor Deposition," Annual Report A-4699-1, Georgia Institute of Technology, Atlanta, Georgia, January-December 1987.

2. W. J. Lackey et al., "Ultrafine Microstructure Composites Prepared by Chemical Vapor Deposition," Annual Report A-4699-2, Georgia Institute of Technology, Atlanta, Georgia, January-December 1988.

Presentations:

1. W. J. Lackey et al., "Ceramic Multicomponent Coatings Prepared by Chemical Vapor Deposition," Symposium on Multicomponent Ultrafine Microstructures, Materials Research Society, Boston, Massachusetts, December 1986.

2. W. J. Lackey et al., "Codeposition of Dispersed Phase Ceramic Composites," Invited paper at 10th International Conference on Chemical Vapor Deposition, Honolulu, Hawaii, October, 1987.

3. W. J. Lackey et al., "Chemical Vapor Deposition of Oxidation Resistant Coatings," American Ceramic Society Conference on Composites, Cocoa Beach, Florida, January 1988.

4. W. Y. Lee et al., "Chemical Vapor Deposition of Dispersed Phase Ceramic (BN+AlN) Composites," AIChE Annual Meeting, Washington, D.C., November-December 1988.

5. D. J. Twait et al., "Chemical Vapor Deposition of BN+AlN Composite Coatings," Annual Meeting of the American Ceramic Society, Indianapolis, Indiana, April 1989.

6. W. Y. Lee et al., "Modeling of the CVD of BN+AlN Composites," AIChE Annual Meeting, San Francisco, California, November 1989.

7. W. J. Lackey et al., "Dispersed Phase BN+AlN Composites Via Chemical Vapor Deposition," submitted to Annual Meeting of the American Ceramic Society, Dallas, Texas, April 1990.

8. W. Y. Lee et al., "Kinetic and Thermodynamic Modeling of BN+AlN Codeposition," submitted to 11th International Conference on Chemical Vapor Deposition, Seattle, Washington, October 1990.

9. P. K. Agrawal et al., "Mass Transfer and Kinetic Phenomena during CVD of BN+AlN Composites," submitted to AIChE Annual Meeting, 1990.

Theses:

1. D. J. Twait, "Codeposition of Boron Nitride Plus Aluminum Nitride Composites by Chemical Vapor Deposition," M.S. Thesis, Georgia Institute of Technology, June 1989.

2. W. Y. Lee, "Chemical Vapor Deposition of Dispersed Phase Ceramic Composites," Ph.D. Thesis, Georgia Institute of Technology, January 1990.

CHAPTER I

INTRODUCTION

In recent years material requirements have become more strict and sophisticated for many novel applications such as space vehicles, ultrasonic jets, ceramic heat engines, high performance cutting tools, etc. It is of great interest to prepare advanced ceramics that possess high temperature stability and strength. A major difficulty exists, however, as the traditional brittleness of ceramics often causes catastrophic failures, thus, limiting their wide usage [1]. Dispersed phase ceramic composites appear to be one solution to this problem. The composites usually possess superior mechanical properties (e.g., fracture toughness, strength, resistance to wear and erosion, hardness, etc.) compared to those of single phase ceramics.

The performance of dispersed phase ceramic composites is strongly related to their microstructure. In general a microstructure consisting of a matrix of small equiaxed grains containing numerous uniformly dispersed small secondary particles is preferred. However, this type of structure is often difficult to obtain by using conventional techniques such as powder blending followed by sintering or hot pressing since the dispersed particles tend to be too large and they

segregate. A further problem in the case of powder mixtures is that it is difficult to achieve acceptably high densities by sintering for many ceramic systems.

Chemical vapor deposition (CVD) offers an alternate avenue of preparing ceramic composites in the form of coatings by either simultaneous deposition of multiple phases (i.e., codeposition) or by alternately depositing several phases. CVD is a sophisticated and complex material processing technique which requires a detailed understanding and application of the traditional chemical engineering fundamentals such as thermodynamics, kinetics, transport phenomena, and crystal nucleation and growth theory. In a conventional CVD system, precursors in the form of vapor are introduced to an open-flow reactor. The precursors react homogeneously and/or heterogeneously as activated by thermal means (e.g., 500 to 2000°C). Subsequent heterogeneous nucleation and growth result in film deposition on substrates placed inside the reactor. In the microelectronic industry the CVD technique has been widely used to deposit dielectric or metallic films (e.g., SiO_2, Si_3N_4, Si, Al and W) on integrated circuits. The technology is also used extensively to coat cutting tools with TiC, TiN and/or Al_2O_3 and therefore extend their life.

The major advantage of preparing dispersed phase ceramic composites by CVD is that mechanical as well as chemical, electrical, optical, and thermal properties of the composites

can be favorably tailored by controlling their composition and microstructure. The desired microstructure can be achieved by optimization of CVD process variables such as temperature, pressure, reagent concentration, substrate type, reactor geometry, etc. The potential for controlling deposit composition and microstructure, and therefore properties, offers a promising future for preparation of advanced ceramics by CVD. This, of course, overrides the relatively high cost of reagents used in many CVD systems.

Prior work in preparing dispersed phase ceramic composites by CVD has been recently reviewed by Lackey et al. [2] and Hirai and Goto [3-5]. Even though rapid progress has been made, the preparation of such composites has been severely limited by the facts that: (1) the governing principles of the CVD processes are not thoroughly understood and (2) accurate kinetic and mass transfer data are not generally available in the literature and are extremely difficult to obtain in a traditional CVD reactor configuration.

In order to describe a CVD process, a comprehensive model which integrates the underlying principles of thermodynamics, kinetics, transport phenomena, and nucleation and crystal growth theory is required. To date, sophisticated mathematical kinetic/mass transfer models have been developed to relate processing parameters to growth rate and coating uniformity for relatively simple and well-understood processes

used in the semiconductor industry (e.g., Si- and Si_3N_4-CVD). In the case of ceramic composites for structural applications, a realistic model which accounts for crystal nucleation and growth behavior as well as chemical and/or physical interaction between multi-chemical solid phases is needed in order to predict the composites' microstructure and ultimate properties. However, this type of modeling process becomes almost intractable in the absence of extensive and "meaningful" experimental work, which is virtually non-existent in the literature for most codeposition processes.

Therefore, the purpose of the present study has been to increase the understanding of codeposition of multiple ceramic phases by obtaining accurate experimental data and developing a model based on the data. Specifically, codeposition of boron nitride (BN) and aluminum nitride (AlN) from the BCl_3-$AlCl_3$-NH_3-Ar reactant mixture has been studied. The overall reactions are:

$$BCl_3 + NH_3 \Rightarrow BN(s) + 3HCl \qquad (1\text{-}1)$$

$$AlCl_3 + NH_3 \Rightarrow AlN(s) + 3HCl \qquad (1\text{-}2)$$

Soft hexagonal BN acts as a lubricating phase because of its laminar structure while AlN having a wurtzite structure provides the necessary hardness to the composites. The BN+AlN system offers the promise of tailoring properties such as thermal conductivity, friction coefficient, hardness, and

resistance to wear and erosion for possible radome, electronic, and tribological applications.

The present study has been conducted as follows. First, BN+AlN composite coatings as well as BN and AlN single phase coatings were prepared by CVD using an impinging jet geometry. The influences of temperature, pressure, and reagent concentration on deposition rate and microstructure of the BN+AlN-, BN-, and AlN-CVD systems were systematically investigated. Second, a mathematical model which describes the mass transport of gas species in the impinging jet geometry was developed. The model was used in identifying and quantifying intrinsic kinetic mechanisms of the BN- and AlN-CVD processes. Third, extensive characterization was performed to determine the microstructure of the coatings using X-ray diffraction (XRD), X-ray photoelectron spectroscopy (XPS), electron microprobe, scanning electron microscopy (SEM), and transmission electron microscopy (TEM). Finally, the physicochemical nature of the BN+AlN-CVD process was studied by: (1) comparing the BN-CVD and AlN-CVD to the BN+AlN-CVD from a kinetic standpoint and (2) analyzing the relationship between the microstructure and processing parameters.

CHAPTER II

REVIEW OF LITERATURE

The first two sections of this chapter review the CVD of BN and AlN as single phase materials (i.e., BN-CVD and AlN-CVD). Physical properties and microstructure of BN and AlN are discussed. Also, the relationship between deposition rate and processing conditions are reviewed from kinetic and thermodynamic standpoints. The next section surveys prior success in codepositing multiple ceramic phases by CVD. In the last section, a summary on the current theoretical understanding of CVD is introduced with emphasis on limitations and difficulties frequently encountered in analyzing complex CVD systems. As the current status and understanding of the CVD processes are being examined, experimental and theoretical methodologies used in the present research are developed and rationalized.

Boron Nitride

Properties and Microstructure

The hexagonal structure of BN is similar to that of graphite as shown in Figure 2-1. This laminar structure is responsible for the softness and lubricating behavior of BN. The bonding distance between B and N atoms is 1.45 Å and the

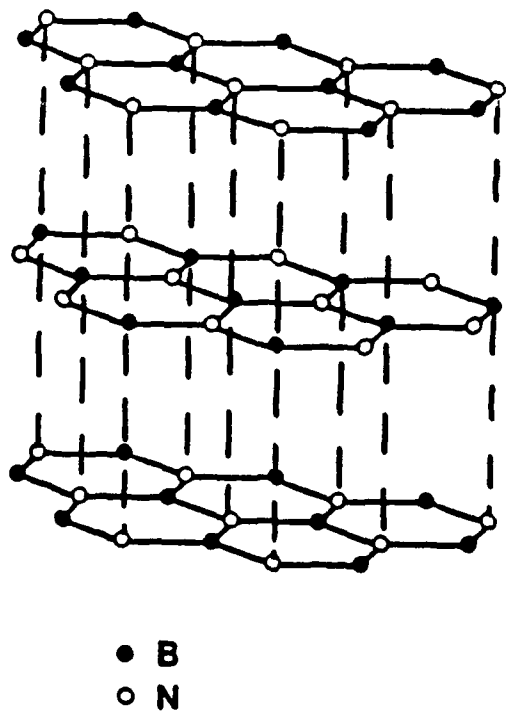

Figure 2-1. Crystal structure of hexagonal BN [6].

interlayer distance is 3.33 Å [6]. The theoretical density of BN is 2.27 g/cm^3.

BN is chemically inert and can only be dissolved by highly concentrated hydrofluoric or hydrosulfuric acid [6]. However, BN deposited below 1400°C may be susceptible to moisture by forming boric acid [7]. BN is a high temperature material. The resistance of BN to high temperature oxidation is superior to that of pyrolytic graphite. In an inert atmosphere, BN dissociates into B(s) and N_2(g) only at very high temperatures (e.g., above 2000°C). The equilibrium dissociation pressure of N_2 is: 760 torr at 2500°C, 11.5 torr at 2000°C, and 9.9×10^{-9} torr at 1100°C [8].

As shown in Table 2-1, the uniqueness of BN is that it is a good thermal conductor while it is also an electrical insulator. Also, in Table 2-1, other important properties of BN are compared with those of AlN and other materials relevant to the present investigation. The properties of BN and AlN prepared by hot pressing and CVD are separately listed for comparison purposes. As will be mentioned later, it is important to note that BN prepared by CVD can exhibit anisotropic behavior. Therefore, some properties listed in Table 2-1 should be used with care; contradictory results are sometimes reported in the literature. For example, the thermal expansion coefficient in the c-direction of BN prepared by CVD is reported to be anywhere from 7.3×10^{-6} to 36.0×10^{-6} $°C^{-1}$ (see Table 2-1).

Table 2-1. Properties OF BN, AlN, Al_2O_3, BN+AlN and C(graphite).

Properties	BN		AlN		Al_2O_3	BN+AlN* (Hot Pressed)	Pyrolytic Graphite
	HP	CVD	HP	CVD			
Micro-hardness (GPa)	0.1**	0.8**	10 to 12	-	~18	3.0**	5
Electrical Resistivity (Ωcm)	$>10^{13}$	$>10^{15}$	$>10^{13}$	$>10^{13}$	$>10^{14}$	-	-
Density theo:	2.27		3.26		3.97		2.21
obs: (g/cm³)	1.9 to 2.0	1.4 to 2.2	3.1 to 3.2	3.15 to 3.20		92%	
Young's Modulus (GPa)	82	-	340	-	378	-	-
Thermal Conductivity (W/m·°C)	⊥: 15 to 20 ∥: 40 to 58	a: 63 to 250 c: ~2	125 to 220	-	20 to 30	⊥: 44 ∥: 37	-
Thermal Expansion Coefficient (x10⁶/°C)	⊥: 0.8 to 3.2 ∥: 0.4 to 1.2	a: 2.5 to 6.4 c: 7.3 to 36	4.5 to 5.6	-	~7	⊥: 5.5 ∥: 6.3	a: ~2 c: ~25
Specific Heat (cal/g·°C)	0.441 at 700°C	0.24 at RT	0.25 at RT	-	0.26 at RT	-	0.25 at RT

HP: Hot Pressed
* Hot Pressed BN+AlN Composite (71wt% BN, 24wt% AlN, 5wt% B_2O_3), Courtesy of Union Carbide Corporation
** Obtained from the Present Investigation
theo: Theoretical Density
obs: Observed Density
⊥: Perpendicular to Pressing Direction
∥: Parallel to Pressing Direction
a: a-Crystallographic Direction
b: b-Crystallographic Direction
RT: Room Temperature

BN prepared by CVD exhibits increasing anisotropy as deposition temperature increases from 700 to 2100°C. The hexagonal phases of BN become preferentially oriented parallel to the deposition surface (i.e., preferred orientation of the (002) plane) with increasing deposition temperature. The highly anisotropic material is commonly called pyrolytic boron nitride (PBN) which is usually obtained at temperatures above 1900°C. PBN has been commercially manufactured for use as high quality crucibles in the semiconductor industry. The preparation and properties of PBN have been the subjects of numerous studies and are well documented [6,8-13]. BN can be deposited from many reagent systems such as BCl_3+NH_3, B_2H_6+NH_3, $B_3N_3H_6$, and $B_3N_3H_3Cl_3$. The BCl_3+NH_3 combination is most widely used.

Matsuda et al. [14] reported that BN deposited on graphite from the BCl_3-NH_3-H_2 reactant mixture below about 1400°C was usually isotropic. The transition from the anisotropic to isotropic crystalline state was also influenced by other variables such as pressure. For example, a mixture containing both anisotropic and isotropic BN phases could be deposited at 1200°C when the pressure was less than 10 torr. Takahashi et al. [15,16] observed that the transition occurred at about 1100°C. They examined the crystallinity of BN deposited on carbon steel from the BCl_3-NH_3-H_2-Ar mixture in the temperature range of 900 to 1200°C. BN became more crystalline with increasing deposition temperature. BN

coatings obtained below 1050°C were turbostratic as indicated by the appearance of a very broad (002) peak (Figure 2-2). Above 1050°C, the appearance of a sharp (002) peak at the expense of the broad peak was observed indicating the formation of pyrolytic BN. The authors cited that this transitional behavior of turbostratic BN was similar to that of turbostratic graphite. Motojima et al. [17] reported that transparent turbostratic BN was deposited on copper from the BCl_3-NH_3-H_2 mixture at temperatures in the range of 400 to 700°C. BN deposited below 450°C was found to be unstable upon exposure to air.

As shown in Figures 2-2a and 2-2b, the (002) XRD peak was the only major peak in the XRD spectrum of anisotropic BN. The sharp (002) peak resulted from the highly preferred crystalline orientation. However, for isotropic BN, as shown in Figures 2-2d and 2-2e, the (002) peak for isotropic BN was usually observed as a broad peak or hump, which was a representation of "turbostratic" structure. The turbostratic BN structure can be viewed as a semi-crystalline phase where "BN layers are stacked roughly parallel to each other but show random orientation and translation about the layer normal [18]" causing the broadening of the (002) peak.

Matsuda et al. [14] demonstrated that the grain size of BN decreased with decreasing deposition temperature. The average grain size of BN decreased continuously from 8 nm to about 1.5 nm when the deposition temperature was decreased

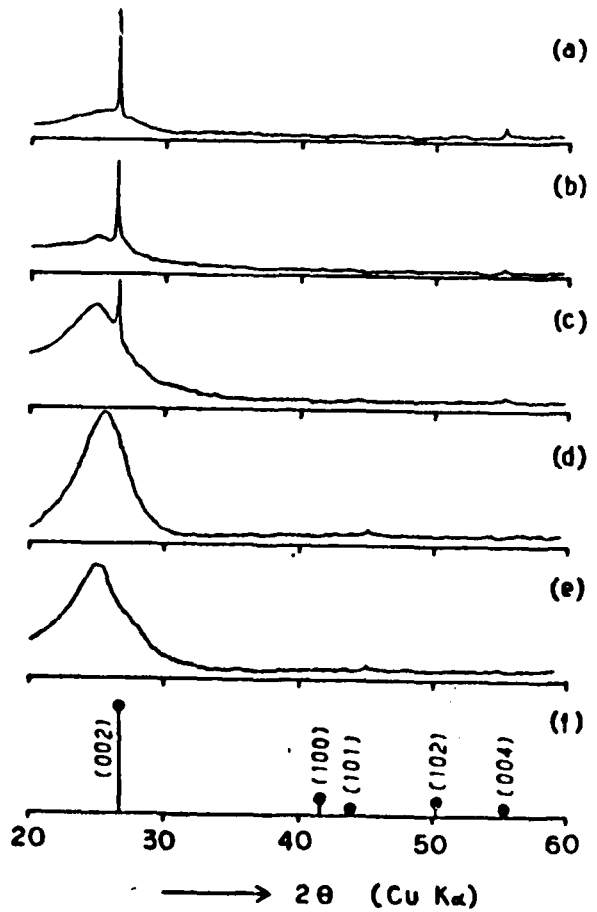

Figure 2-2. XRD patterns of BN deposited on carbon steel at various temperatures: (a) 1200°C, (b) 1150°C, (c) 1100°C, (d) 1050°C, (e) 1000°C, and (f) ASTM BN [16].

from 2000 to 1200°C. However, the grain size was not significantly influenced by pressure. The grain size was determined by measuring the FWHM (Full-Width at Half-Maximum) of the (002) peak.

The density of BN decreased linearly from about 2.15 g/cm^3 to about 1.45 g/cm^3 when deposition temperature was lowered from 2200 to 1450°C [6,19]. Also, Matsuda et al. [14] showed that the density of BN was strongly influenced by pressure. In general, deposition of the high density BN was favored at low pressures. For example, the density drastically increased from 1.6 to 2.1 g/cm^3 with decreasing pressure from 10 torr to 5 torr at 1400°C. It was explained that the decrease in the apparent density of BN with decreasing temperature was due to a steady increase in: (1) the interlayer spacing and (2) the number of internal micropores. They speculated that BN particles or clusters formed in the gas phase caused the formation of the micropores. The main idea behind their hypothesis was that recrystallization and/or sintering of the particles or clusters at low temperatures were limited and unlikely to yield high packing density.

Kinetics/Thermodynamics

Tanji et al. [12] studied LPCVD (low pressure chemical vapor deposition) of PBN (pyrolytic BN) on graphite from the BCl_3-NH_3-N_2 reactant system using a horizontal hot-wall tube furnace. The total operating pressure was typically 2 torr.

The influences of pressure, fluid velocity, and partial pressures of BCl_3 and NH_3 on deposition rate along the flow direction were investigated at a deposition temperature of 1900°C. Also, they performed a series of experiments in which the deposition temperature was varied.

For the temperature variation experiments, a graphite rod (3 cm in diameter and 7 cm in length) was used as a substrate. The graphite rod was placed coaxially in the tube furnace. The deposition rate was determined by measuring the weight gain on the substrate. The deposition rate exponentially increased from 5.60×10^{-9} to 5.60×10^{-8} moles/cm²/s with increasing temperature from 900 to 1250°C indicating the process was kinetically controlled in this temperature range. The apparent activation energy was calculated to be about 50 kcal/mole. The calculation was performed without accounting for any mass transfer contributions and reagent depletion along the axial direction. Above 1250°C, the process appeared to be diffusion-limited as the deposition rate eventually reached a constant level of about 1.2×10^{-9} moles/cm²/s at 1500°C. For the above experiments, a BCl_3 partial pressure of 0.3 torr and an NH_3/BCl_3 mole ratio of 4 were used.

The deposition rate increased with increasing gas velocity at 1900°C indicating that the growth of BN was diffusion-limited at this temperature. Also, the deposition rate on the graphite substrate decreased exponentially along the flow direction. The slope of the rate decrease along the

flow direction was steeper at lower gas velocities. It seemed that the steeper slope was due to the increase in residence time caused by decreasing the fluid velocity (i.e., more reagent depletion). They also reported that the deposition rate increased with increasing partial pressure of BCl_3 at 1900°C, but was independent of NH_3 partial pressure. Based on the observed results, they concluded that the diffusion of BCl_3 was the rate-limiting step for the BN growth at 1900°C. However, they did not provide much needed kinetic data in the temperature region of interest to the present investigation (e.g., 700 to 1300°C).

Malé and Salanboubat [13] reported results similar to those of Tanji et al. [12] supporting that mass transfer of BCl_3 was the rate limiting step at temperatures above about 1300°C. Their investigation was performed in a vertical cold wall reactor using the BCl_3-NH_3-He reagent system. Inside the reactor, the reagent gas stream impinged on the flat surface of a graphite disc, which was suspended in the reactor. The deposition rate increased linearly from 9.80×10^{-7} to 1.46×10^{-6} moles/cm^2/s with increasing temperature from 1450 to 1800°C. The temperature variation experiments were performed at 1 torr. With increasing pressure from 0.75 to 2 torr, the deposition rate first increased to a maximum value and then steadily decreased as pressure was further increased to 15 torr. The BCl_3 mole fraction of 0.061 and the NH_3/BCl_3 mole ratio of 3 were used for the pressure variation experiments

and also for the temperature variation experiments described earlier. The deposition rate increased linearly with increasing BCl_3 partial pressure. The deposition rate increased linearly on increasing the NH_3/BCl_3 mole ratio from 0 to 3 and then the rate reached a constant level when the ratio was higher than 3.

Matsuda et al. [20] observed formation of BN particles or clusters in the gas phase (i.e., homogenous nucleation) at high temperatures and high BCl_3 concentrations. They performed a series of kinetic experiments using a cold-wall reactor in the temperature range of 1200 to 2000°C and the pressure range of 5 to 60 torr using the BCl_3-NH_3-H_2 reagent system; the results are in Figure 2-3. The BCl_3 mole fraction of 0.156 and NH_3/BCl_3 mole ratio of 0.643 were used for the experiments.

As can be seen from Figure 2-3, the deposition rate steadily increased with increasing pressure from 5 to 60 torr at 1200 °C. However, at higher temperatures (i.e., 1400 to 2000 °C), the deposition rate started to decrease when a critical pressure level was reached. The critical pressure decreased as the deposition temperature increased. Matsuda and his coworkers explained that the decrease in the deposition rate was due to reagent depletion, which was caused by the formation of BN particles in the gas phase. Their explanation was supported by the fact that their data were qualitatively in agreement with the classical nucleation

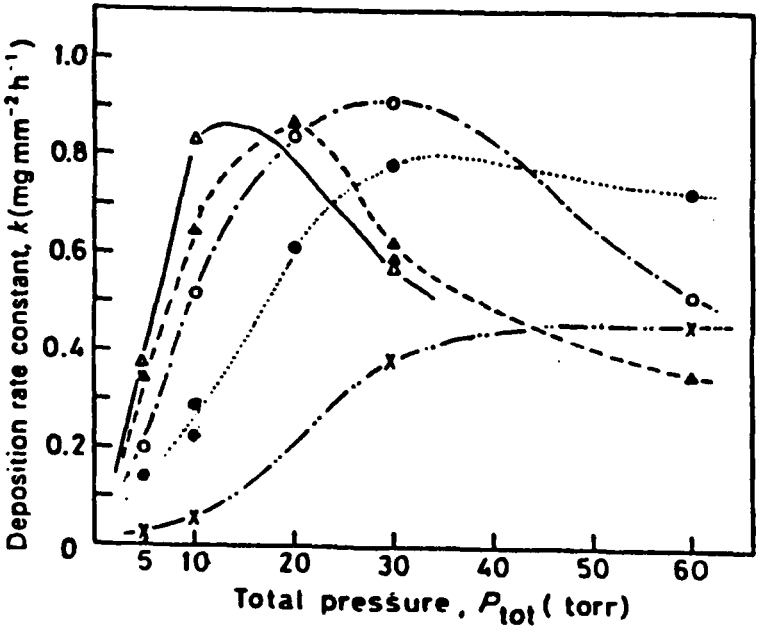

Figure 2-3. Effect of pressure and temperature on BN deposition rate; (x) 1200°C, (●) 1400°C, (o) 1600°C, (▲) 1800°C, and (△) 2000°C [20].

theory, which will be discussed in the last section of this chapter. Also, Tanji et al. [12] observed the formation of spherical BN particles in the gas phase at 1900°C when the BCl_3 partial pressure was higher than 0.226 torr. Matsuda et al. suspected that some of the BN particles became a part of the coating (i.e., imbedded) while heterogeneous deposition was taking place at the substrate level, thus, lowering the apparent density of the coatings.

Matsuda et al. calculated the apparent activation energy for the heterogeneous deposition process to be about 32 kcal/mole in the temperature range of 1200 to 1400°C and the pressure range of 5 to 10 torr. At the higher pressures, as expected, the Arrhenius relationship was not observed due to the occurrence of homogenous nucleation. The apparent activation energy of 32 kcal/mole is compared to that of 50 kcal/mole reported by Tanji et al. [12] whose work was mentioned earlier. Moore [7] observed the activation energy of 27.3 kcal/mole in the temperature range of 1000 to 1300°C. Moore's work was performed using a commercial reactor system in order to coat graphite substrates having a complex geometry from the BCl_3-NH_3-H_2 reagent system. The inconsistency in the reported apparent activation energy values was obviously due to the fact that mass transfer contributions and reagent depletion were not accounted for.

The effect of various substrates on the deposition behavior has been reported. Takahashi et al. [15] reported

that non-crystalline powdery BN or NH_4Cl was deposited on graphite at temperatures below 1600°C whereas a crystalline BN film was deposited on carbon steel, stainless steel, and nickel. However, other authors [7,12,14,20] reported that the deposition of turbostratic BN on graphite was possible in the temperature range of 900 to 1600°C. Sano and Aoki [21] reported that well-adherent and transparent BN was deposited on fused silica and sapphire in the temperature range of 1000 to 1100°C.

In most of the studies reviewed in this section, BCl_3 and NH_3 were separately introduced into reactors as they tended to form undesired NH_4Cl powder at temperatures below 450°C. The distance between the mixing position of BCl_3 and NH_3 and the substrate location (i.e., mixing length) influenced the growth rate as well as the quality of the deposit [11,15]. In the case of cold-wall reactors, it was found that there was an optimum length (usually less than 2 inches) as BCl_3 and NH_3 might react prematurely to form powdery NH_4Cl in the low temperature region before reaching the substrate.

Hannache et al. [22] studied the thermodynamics of the BCl_3-NH_3-H_2 reagent system by performing calculations, which were based on minimization of the Gibbs free energy of the system in the temperature range of 1027 to 1427°C and in the pressure range of 0.8 torr to 76.0 torr. The calculations predicted that complete conversion (100% yield) of BCl_3 to BN occurred as long as the NH_3/BCl_3 mole ratio was higher than 1.

When the ratio was less than 1, the formation of B as an additional solid phase was predicted at the expense of BN. When the NH_3/BCl_3 ratio was less than 0.25, the formation of B was favored over that of BN. The predicted deposition behavior was not strongly dependent on pressure or temperature.

In summary, the CVD of BN is a relatively well-understood process. However, intrinsic heterogeneous kinetic mechanisms have not been determined since most investigators' aim was to prepare pyrolytic BN and, therefore, their studies were usually performed under mass transfer controlled process conditions. The inconsistent results were attributed to the fact that the role of mass transfer on the observed deposition rate was not accounted for in interpreting the deposition data. Nevertheless, two important general kinetic characteristics were identified from these studies: (1) the CVD of BN appeared to be kinectically-controlled below about 1000 °C and (2) the formation of BN particles in the gas phase was observed at high temperatures and BCl_3 concentrations.

Aluminum Nitride

Properties and Microstructure

Aluminum nitride (AlN) is a hard material possessing the wurtzite crystal structure (i.e., distorted hexagonal). Recently AlN has received much attention in the microelectronic industry as a new substrate/packaging material

for electronic devices due to its high thermal conductivity, low electrical conductivity, and high flexural strength. AlN can be etched in a controllable fashion using diluted phosphoric acid. Thermal, electrical, physical, and optical properties of AlN prepared by hot pressing and CVD have been reported in the literature [23-29]. Some important properties of AlN are listed in Table 2-1 (p. 9) and compared with those of BN, Al_2O_3, and graphite. The thermal conductivity of hot-pressed AlN (usually 150 to 170 W/m°/K) is comparable to that of BeO or BeO-doped SiC, which has been extensively used for microelectronic applications [25]. BeO is a toxic material whereas AlN is known for its inertness.

AlN is usually prepared by hot-pressing with a sintering agent such as Y_2O_3, CaO, CaC_2, etc. A recent study by Iwase et al. [25] showed that the sintering agents actually increased the thermal conductivity of the hot-pressed AlN. However, when the oxygen content in the hot-pressed AlN was more than 3%, a decrease in the thermal conductivity by about 40% was observed. AlN grains with an average size of 1.5 μm were observed when sintering agents such as CaC_2 and Y_2O_3 were used. However, non-uniform AlN grains ranging from 1 to 5 μm were observed when the sintering agents were not used.

AlN thin films have been prepared by various techniques such as reactive evaporation, sputtering, MBE (molecular beam epitaxy), CVD, plasma-enhanced CVD (PECVD), etc. [29]. Among these techniques, CVD has been most widely used to prepare AlN

in the form of films. $AlCl_3$ and NH_3 have been mainly used as reagents although $AlCl_3*NH_3$ and organometallic precursors have been used in some studies [26,28,30].

Kelm [28] deposited AlN by CVD using $AlCl_3*NH_3$. The $AlCl_3*NH_3$ powder was placed in a boat and heated to 250°C. Hydrogen was used to carry the $AlCl_3*NH_3$ vapor into a hot-wall furnace. Transparent and well-adherent AlN was obtained on Si(111) substrates in the temperature range of 800 to 1200°C. Their TEM studies showed that the average grain size increased with increasing deposition temperature. The average grain size was: 10 nm at 800°C, 20 nm at 900°C, 60 nm at 1000°C, 110 nm at 1100°C, and 220 nm at 1200°C. Electron diffraction studies indicated that AlN deposited above 1000°C did not have any preferred orientation while AlN deposited between 800 and 1000°C was preferentially oriented to the (002) plane. The density of the AlN coating was measured to be about 3.15 to 3.2 g/cm^3.

Yim et al. [27] reported that single crystal AlN(002) could be deposited on sapphire from the $AlCl_3$-NH_3-H_2 reagent mixture in the temperature range of 1000 to 1100°C. The AlN coatings grew in a hexagonal-pyramidal fashion. Cracking of AlN on the sapphire substrate was observed because of the thermal expansion mismatch between the AlN coating and Al_2O_3 substrate.

Interrante et al. [30] deposited crystalline AlN on Si and SiO_2 substrates in the temperature range of 400 to 800°C

from an organometallic reagent, $[(CH_3)_3AlNH_2]_3$. The AlN coatings were generally transparent, smooth, and highly adherent. The Al/N atomic ratio was determined to be 1.0 by Auger spectroscopy. AlN grains were about 50 nm to 100 nm in size as determined by SEM and TEM. The TEM studies also showed that the AlN grains grew in a columnar fashion.

Chubachi et al. [31] demonstrated that AlN(002) could be grown on Si(111) and Si(001) surfaces from the $Al(CH_3)_3$-NH_3-H_2 reagent system as evidenced by XRD and RHEED (reflection high energy electron diffraction). Only the (002) peak was observed from the XRD spectra of the AlN coatings. They also performed X-ray rocking-curve analyses to determine the effect of the coating thickness on internal stress. The stress increased with an increase in coating thickness. Morita et al. [26] also used $Al(CH_3)_3$ and NH_3 to deposit AlN on Al_2O_3. They observed the growth of AlN fibers of 50 to 100 nm in diameter at about 1100°C. Only the (002) AlN peak was observed from XRD spectra of the AlN fibers.

Suzuki and Tanji [32] showed that the crystallinity of AlN was strongly affected by temperature and pressure. Polycrystalline AlN was deposited on graphite from the $AlCl_3$-NH_3-N_2 mixture using a vertical hot-wall reactor. Increasing temperature from 700 to 1400°C resulted in a more ordered polycrystalline AlN morphology as indicated by XRD and SEM. Powder was deposited below 600°C or when pressure was high (above 1 torr) at 600°C. Between 600 and 900°C, the AlN

coating contained cracked layers. Above 1000°C, a highly layered morphology was obtained. Decreasing pressure produced the same trend, but the effect of pressure was less significant than that of temperature.

Based on the findings from the above studies, it appeared that various AlN morphologies could be obtained depending on process conditions. Preferred orientation of the (002) plane was commonly observed at high deposition temperatures. Also, in many instances, AlN grains grew in a columnar or fibrous fashion. However, the relationship between the microstructure and processing parameters was not clearly identified in the above studies. Also, difficulties existed in comparing the AlN-CVD literature since different reagent systems were frequently used.

Kinetics/Thermodynamics

The AlN-CVD process is much less-understood in comparison to BN-CVD. As the present review will reveal, the major cause of the limited understanding on the AlN deposition is the inconsistency and complexity of reported experimental data. The inconsistent data can be attributed to several reasons. First, many investigators performed deposition experiments under conditions in which undesired homogeneous nucleation was observed. In the presence of homogeneous nucleation, an accurate surface kinetic analysis is practically impossible. Second, even for experiments in which homogenous nucleation was not observed, several studies

reported that the heterogeneous deposition rate decreased with increasing temperature or pressure, which could not be readily explained by simple kinetic or mass-transfer considerations.

The reason for the decrease in the deposition rate in the absence of homogeneous nucleation has not been addressed in the AlN-CVD literature. In Chapter V, an attempt will be made to explain this complex deposition behavior based on our experimental findings and thermodynamic calculations. It is briefly explained here that the deposition of AlN is not thermodynamically favored at high temperatures since $AlCl_x$ (x=1,2,3) becomes stable in the gas phase. Therefore, the stability of the $AlCl_x$ gas species with increasing temperature causes a decrease in the overall AlN deposition rate.

Another interesting feature of AlN deposition is that the Arrhenius relationship between deposition rate and temperature with a sufficient activation energy (about 30 to 50 kcal/mole) for a kinetically-controlled process has never been observed for AlN-CVD even at relatively low temperatures (about 300 to 600°C). This behavior indicates that the CVD of AlN is a mass-transfer limited process (i.e., surface kinetic steps are fast). Suzuki and Tanji [32] actually demonstrated that the AlN-CVD was indeed a diffusion-limited process at typical processing conditions.

Suzuki and Tanji deposited AlN on graphite from the $AlCl_3$-NH_3-N_2 reagent system in the temperature range of 600 to 1400°C at low pressures (2 to 50 torr) using a vertical hot-

wall reactor. The graphite substrate disc was placed at the center of the vertical reactor. However, it was not clear from their description as to whether or not the reagent gas stream impinged on the flat surfaces of the disc. They observed that deposition rate slowly reached a maximum level from 120 to 200 μm/hr with increasing temperature from 600 to 1000°C. The deposition rate gradually decreased to 100 μm/hr as temperature was further increased to 1400°C. It was also observed that the deposition rate reached a maximum at pressure of about 10 torr. The deposition rate increased linearly with increasing $AlCl_3$ partial pressure. However, the deposition rate remained constant with increasing $NH_3/AlCl_3$ mole ratio. Based on their findings, they concluded that the rate limiting step was the diffusion of $AlCl_3$ to the substrate surface.

Similar behavior has been observed by other investigators. Pauleau et al. [33-35] reported that the AlN deposition rate from $AlCl_3$-NH_3-H_2 mixtures reached a maximum at about 650°C. They proposed that the decrease in the deposition rate above 650°C was due to the formation of AlN particles in the gas phase. Arnold et al. [36] observed a decrease in the deposition rate above 1000°C. Kelm [28] reported that the AlN deposition rate from $AlCl_3$*NH_3 decreased with increasing temperature from 800 to 1000°C. However, Morita et al. [26] reported that the AlN deposition rate from the $Al(CH_3)_3$-NH_3 system remained at a constant value with

increasing temperature from about 1060 to 1200°C. However, the deposition rate increased linearly with increasing $Al(CH_3)_3$ concentration.

Pauleau et al. [33,34] performed thermodynamic analyses of the $AlCl_3$-NH_3-H_2 system. Their calculations predicted that 100% conversion from $AlCl_3$ to AlN was thermodynamically feasible as long as the $AlCl_3$ partial pressure was less than 0.76 torr at 927°C and 0.0076 torr at 1127°C. Above these partial pressures, the AlN yield decreased as $AlCl_3$ became thermodymically more stable. As the results indicated, the stability of $AlCl_3$ increased with increasing temperature. For the above calculations, an $NH_3/AlCl_3$ ratio of 1.0 was assumed.

Thermodynamic results similar to those of Pauleau et al. were later reported [37,38]. Hyun and Kim [37] predicted that the AlN yield would decrease at temperatures above 1000°C as the stability of $AlCl_2$ in the gas phase increased. Furthermore, Sarin [38] showed that AlN was the only solid phase predicted by the thermodynamic calculations when oxygen contents in the $AlCl_3$-NH_3-H_2-CO_2-H_2O reagent system were less than about 5%. If the oxygen content was higher than 5%, the formation of $Al_xO_yN_z$ (i.e., pseudo-binary solid solution of AlN and Al_2O_3) was predicted.

In order to obtain a dense and uniform coating, it is a common practice to avoid processing conditions which would lead to particle formation in the gas phase (i.e., homogeneous nucleation). However, in several studies [37,39,40], AlN

particles were deliberately synthesized in the gas phase in order to prepare high purity AlN powder for subsequent hot pressing applications. (Note: AlN powder is commercially produced by either direct nitridation of aluminum or carbon reduction of aluminum oxide.) Kimura et al. [39] reported that AlN in the form of powder could be prepared from the $AlCl_3$-NH_3-H_2 reactant mixture using a hot-wall horizontal tube furnace at 1 atm in the temperature range of 720 to 1190°C. They mentioned that most of the AlN powder with spherical shape was collected within about 17 cm from the $AlCl_3$ inlet position whereas the total length of the reaction zone was 30 cm. An $AlCl_3$ partial pressure of 58 torr was typically used for the AlN powder synthesis. The average particle size decreased from about 1.5 to 0.2 μm on increasing the temperature from 720 to 1190°C. The particle size ranged from 0.3 to 30 μm at 720°C and from 0.1 to 3 μm at 1190°C. However, at 1190°C, most of the AlN particles were in the narrow range of 0.1 to 0.3 μm. They explained that increasing temperature caused a "run-away" nucleation (i.e., generation of numerous stable nuclei) which resulted in a smaller particle size and an increase in the particle number concentration. Also, an increase in the total flow rate by a factor of 2.5 decreased the average particle size by 30%. The reduction in the particle size was attributed to a decrease in $AlCl_3$ partial pressure as the total flow rate increased.

Hyun and Kim [37] also observed the formation of AlN particles via homogenous nucleation from the $AlCl_3$-NH_3-H_2 reagent system at 1 atm in the temperature range of 650 to 880°C. Their XRD studies indicated that the powder contained both AlN and NH_4Cl. Also, it was determined that the AlN phase was preferentially oriented to the (002) plane. Below 650°C, the powder containing AlN was not generated. The $NH_3/AlCl_3$ ratio was about 1000. An $AlCl_3$ partial pressure of about 1 torr was typically used. The average particle size was about 0.09 to 0.12 μm depending on the $AlCl_3$ partial pressure. However, the particle size was not strongly influenced by temperature. The smaller particle size observed by Hyun and Kim in comparison to that by Kimura et al. [39] was probably due to the lower $AlCl_3$ concentration (1 torr versus 58 torr) used in the work of Hyun and Kim. Kim and Lee [40] reported that AlN whiskers were obtained at temperatures above 1000°C whereas spherical AlN particles were formed in the temperature range of 600 to 1000°C. They also observed the presence of NH_4Cl in the AlN powder from their XRD studies.

Komiyama et al. [41] utilized the formation of AlN particles in the gas phase to increase deposition rate by creating a thermophoretic motion of the particles from the gas phase to the substrate. Thermophoresis refers to a Brownian motion of fine particles from a hot region to a cold region. Their reactor was specially designed so that temperature at

the substrate surface could be lower than in the gas phase. (Note: For most CVD reactors, temperature at the substrate position is usually higher than that of the gas phase). Using the reactor, they could prepare thick AlN films which appeared to be fairly dense under SEM. They proposed that the densification was possible because a part of the AlN films was deposited heterogeneously at the substrate surface while the thermophoresis of the AlN particles was taking place. The AlN coatings were preferentially oriented to the (002) plane as determined by XRD.

Dispersed Phase Ceramic Composites

Several reasons exist for the current high interest in ceramic composites. First, the brittleness of traditional ceramics can be reduced (i.e., an increase in fracture toughness). The improved toughness and strength of zirconia-toughened alumina and transformation-toughened zirconia are outstanding examples of composites prepared by powder blending techniques such as sintering and hot pressing [2]. Second, tribological properties such as friction coefficient, hardness, resistance to wear and erosion, etc., can probably be enhanced by combining a soft lubricating phase with a hard phase. Also, other thermal, electrical, and optical properties can be favorably tailored by selection of the proper composite system.

Chemical vapor deposition is a unique way of preparing ceramic composites as discussed earlier in Chapter I. Coatings containing multiple chemical and/or crystalline phases can be prepared by codeposition or alternate-deposition. Prior success in preparing the composite coatings by codeposition has been recently reviewed in detail by Lackey et al. [2] and Hirai and Goto [3-5]. The present review will mainly focus on codeposition of the composite coatings containing either BN or AlN.

Hirai and coworkers [4,5] codeposited Si_3N_4 and BN from the $SiCl_4$-NH_3-H_2-B_2H_6 reagent mixture at temperatures of 1100 to 1300°C and pressures of 30 to 70 torr. A vertical cold-wall reactor was used. They observed that turbostratic BN was detected by XRD only when the boron content of the composites was greater than 33 weight percent as indicated by the appearance of broad (002) and (10x; x=0,1) peaks shown in Figure 2-4. The Si_3N_4 phase in the composite structure was amorphous. However, in the absence of B_2H_6 (i.e, single phase Si_3N_4-CVD), polycrystalline α-Si_3N_4 was deposited at the same temperature.

At 1100°C, the boron content of the composites increased with increasing B_2H_6 flow rate in an excess amount of NH_3 and $SiCl_4$ and with decreasing total pressure as determined by electron microprobe. However, above 1100°C, these trends were not consistently observed. At 1200 and 1300°C, the boron content increased with increasing B_2H_6 concentration only when

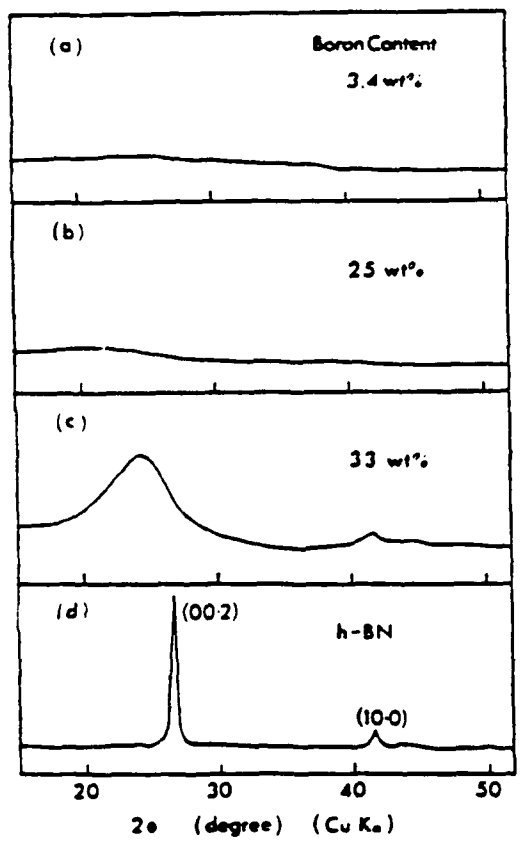

Figure 2-4. XRD patterns of $BN+Si_3N_4$ composites at various boron contents (T = 1200°C and P = 30 torr) [4].

the pressure was below 50 torr. The density of the composite linearly decreased with an increase in BN content. The color of the composites changed from white to yellow to brown to black with increasing B_2H_6 concentration. Thermodynamic analysis of the CVD of Si_3N_4+BN performed by Besmann [42] suggested that the codeposition of Si_3N_4+BN was favored over a wide range of reactant concentrations, pressures, and temperatures below 1100°C. However, a comparative analysis between the thermodynamic calculations performed by Besmann and the experimental data obtained by Hirai et al. has not been made.

Composite coatings containing AlN and Si_3N_4 were prepared from the SiH_4-$AlCl_3$-NH_3 mixture in the temperature range of 600 to 1100°C by Zirensky and Irene [43]. A long horizontal hot-wall reactor was used to prepare the composites. The AlN phase was usually polycrystalline and the Si_3N_4 phase was amorphous. The AlN grains became smaller in size with decreasing AlN content as detected by TEM. The AlN grain size increased from 25 to 50 nm when temperature was increased from 650 to 1075°C. It was observed that the AlN content of the composites increased with increasing $AlCl_3$ partial pressure in a somewhat linear fashion. They also performed codeposition of AlN and Al_2O_3 from the $AlCl_3$-NH_3-H_2-CO_2-H_2O reagent system [44,45]. Dispersed phase composites containing distinct AlN and Al_2O_3 phases were not deposited, instead the formation of $Al_xO_yN_z$ was observed.

Willkens [46] studied codeposition of Si_3N_4 and AlN from CH_3SiCl_3 (MTS) and $AlCl_3*NH_3$ (ACN) at 1000 °C. AlN and Si_3N_4 were deposited as separate polycrystalline phases as indicated by XRD when the MTS/ACN ratio was less than 1. The size of AlN grains increased with increasing AlN content. Between MTS/ACN ratios of 1 and 10, only amorphous Si_3N_4 was deposited. Above the ratio of 10, β-SiC and Si were codeposited.

Other composite systems containing Si_3N_4 such as Si_3N_4+C and Si_3N_4+TiN have also been prepared. The electrical conductivity of the Si_3N_4+C composites increased drastically by adding only 0.2 wt% carbon [5]. The Si_3N_4-TiN composites contained small TiN fibers of about 10 nm in length and 3 nm in diameter, which were dispersed in the polycrystalline α-Si_3N_4 matrix as determined by high resolution TEM [47]. The thermal conductivity of the Si_3N_4+TiN composites decreased with increasing TiN content.

Carbon+SiC composites prepared by codeposition have been commercially used for heart valves [2]. The C+SiC system has been extensively studied in comparison to other composite systems. Structurally, the composites contain SiC particles of 10 to 100 nm in size, which are dispersed in the carbon matrix consisting of numerous carbon grains of about 3 to 5 nm. Blocher [48] was the first investigator to show that the incorporation of SiC into a carbon matrix by CVD increased strength. Also, it was reported by others [49,50] that flexural strength, hardness, and Young's Modulus increased

with an increase in SiC content. The thermal expansion coefficient was found to depend on the carbon matrix density and the SiC content.

Alkins and Bokros [50] reported that the microstructure of the C+SiC composites was strongly affected by temperature and C_3H_8 concentration. For example, the grain size of carbon increased from 3 nm to 5 nm with increasing temperature from 1200 to 1350°C. The carbon grain size also increased with an increase in C_3H_8 concentration. The grain size of SiC increased with increasing SiC content [49]. The SiC content in the composites was primarily determined by the SiH_4 concentration, but was not strongly influenced by temperature. Increasing the SiC content from 0 to 48 wt% decreased the density of the carbon matrix from 2.0 to 1.65 g/cm^3 [49].

Stinton and Lackey [51,52] codeposited SiC and $TiSi_2$ from CH_3SiCl_3-$TiCl_4$-H_2 mixtures. Between 1400 and 1495°C, $TiSi_2$ grains were dispersed in the SiC matrix. However, only SiC was deposited in the temperature range of 1250 to 1325°C. Some coatings were deposited on graphite substrates which were suspended in a fluidized-bed containing carbon particles. Equiaxed $TiSi_2$ grains were observed when the fluidized-bed reactor arrangement was used. Otherwise, columnar and larger $TiSi_2$ grains were observed. The $TiSi_2$ grain size increased with increasing $TiCl_4$ flow rate. Increasing H_2 concentration produced more uniformly dispersed and denser coatings, which

resulted in higher fracture toughness. The toughness of the SiC+$TiSi_2$ composites was about twice that of SiC.

Nickl et al. [53,54] investigated the deposition behavior of the Ti-Si-C and Ti-Ge-C systems using $TiCl_4$, $SiCl_4$, CCl_4, and H_2 as reagents. More than a dozen possible two- and three-phase assemblages such as SiC+TiC, SiC+TiC+C, Ti_3SiC_2+$TiSi_2$, etc., could be deposited depending on processing conditions. The effects of temperature and reagent concentrations on the composites' microstructure were mainly studied. In general, the grain size increased with increasing temperature and hydrogen concentration.

Ceramic composites containing both BN and AlN phases (5 to 30% BN) were prepared by hot pressing of BN and AlN powders [55]. BN remained as a discrete phase and platy particles were oriented perpendicular to the pressing direction suggesting the preferred orientation of BN. This was supported by the appearance of a more intense (002) peak than expected from that of isotropic BN. The effects of sintering aids (e.g., CaC_2 and Y_2O_3) on various physical properties (e.g., flexural strength, thermal expansion coefficient, etc.) were the focus of this study.

As shown by the above review, most investigations so far have been phenomenological in relating processing conditions to CVD-composite's microstructure and properties. Detailed kinetic/mass transfer analyses have not been performed on any of the composite systems reported in the literature. As the

kinetic and mass transfer characteristics of the codeposition processes are not identified, it has been almost impossible to predict the exact composition of the composites and therefore the composites' microstructure and properties.

Theoretical Considerations

As schematically illustrated in Figure 2-5, a CVD process consists of various kinetic, mass transfer, and nucleation and growth steps, which may take place in series or parallel with respect to each other. For example, the heterogeneous deposition process occurs as a result of the following steps:

(1) introduction of reactants in the vicinity of the deposition surface from the reactor inlet by means of convective mass transfer;

(2) generation of intermediate species and/or products by homogeneous reactions during steps (1) and (3);

(3) diffusion of reactants and intermediate species, generated by homogenous reactions, to the deposition surface through a concentration boundary layer;

(4) adsorption of reactants and intermediate species on the deposition surface;

(5) surface reactions between adsorbed species and desorption of volatile products;

(6) nucleation and growth of non-volatile products which result in film deposition; and

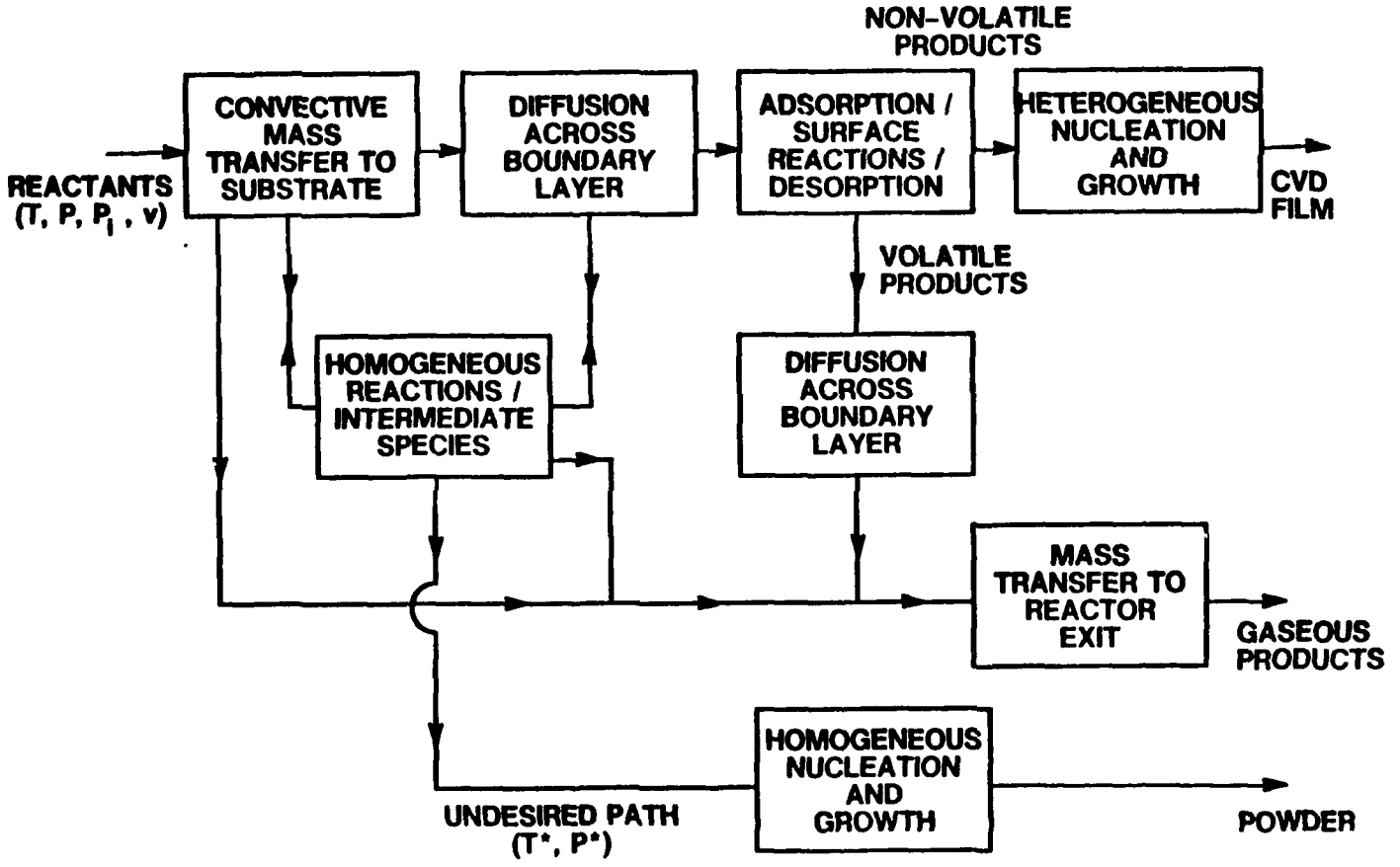

Figure 2-5. Comprehensive CVD modeling requires the integration of many mass tranfer, kinetic, and nucleation and growth steps.

(7) diffusion of volatile products from the deposition surface to the main gas stream and subsequent mass transfer to the reactor exit.

These steps need to be integrated to develop a comprehensive model of the heterogeneous process. The slowest step(s) of the above seven steps determines the overall deposition rate. Furthermore, undesired homogenous nucleation may occur in the gas phase in parallel to the heterogenous steps, which would make the modeling process almost intractable.

Conceptually, the role of each kinetic and mass transfer step on the overall deposition behavior can be simply illustrated by considering an equivalent electrical-resistance circuit. In this analogy, each CVD process step, shown in Figure 2-5, can be thought of as a resistor. If one of the steps is relatively fast in comparison to the others, the resistance of that particular step is small. (Note: The direct analogy between the CVD model and the electrical resistance circuit is not appropriate in a quantitative sense since the electrical circuit describes the motion of only single species, electrons, whereas the CVD model has to deal with the generation, consumption, and movement of many chemical species.) For example, powder formation will dominate over film deposition if the homogenous reactions and nucleation steps are faster than the diffusion and surface kinetic steps. This is equivalent to viewing the resistance of the homogeneous reaction and nucleation steps to be much

smaller than that of the diffusion and surface kinetic steps. In other words, the system moves toward a thermodynamic equilibrium via the homogeneous path. On the other hand, when homogeneous nucleation is not occurring or is very slow, the resistance of the nucleation step is said to be infinitely large so the nucleation step can be ignored during the CVD modeling process. Also, if all the kinetic steps are very fast (no kinetic resistances), the CVD process will take place near or at a thermodynamic equilibrium state. For this highly ideal case, a model which links thermodynamics and transport phenomena is sufficient to portray the CVD process.

Thermodynamics

Chemical equilibrium calculations are of great value since the thermodynamic feasibility of depositing desired solid phases can be determined prior to performing any costly experiments. Multi-phase chemical equilibria can be readily calculated by finding specific compositions of all possible chemical species in the gas, liquid, and solid phases, which would yield the lowest total Gibbs free energy of the system [56-59]. The calculations are equivalent to assuming a closed system with an infinite amount of reaction time. Furthermore, the thermodynamic results can be combined with diffusion characteristics of major gas species to determine "thermodynamic-mass transfer limits" [60]. The "thermodynamic-mass transfer limits" are the maximum heterogeneous deposition rates that can be obtained as long

as homogenous nucleation is not occurring. It should be cautioned that, while the calculations are helpful in avoiding unfavorable reaction conditions, they do not address the kinetic feasibility of depositing the desired phases.

Twait [61] recently reviewed previous thermodynamic investigations on various CVD systems. For some CVD systems such as V-Si-H-Cl [62], Si-C-Cl-H [63], Si-N-Cl-H [64], and B-Cl-H-N [65], good qualitative agreements between the thermodynamic predictions and experimental results (in terms of comparing the predicted and deposited solid phases) have been reported. However, the thermodynamic calculations and experimental results did not agree in other CVD systems (e.g., Si-C-H-Cl [66], Ta-C-Cl-H [67]). The survey by Twait indicated that the disagreement was probably caused by the following reasons: (1) kinetic limitations; (2) uncertainties in thermochemical data; and/or (3) omission of any possible stable intermediate or product species in the calculations, which will lead to erroneous predictions.

The thermodynamic feasibility of the BN+AlN-CVD system has been studied by Twait et al. [61,68]. Figure 2-6 shows a deposition diagram obtained from the thermodynamic calculations. The diagram shows solid phases which would be stable (i.e., deposited) at equilibrium as a function of reagent concentrations (i.e., $AlCl_3$, BCl_3, and NH_3) at 927°C and 20.2 kPa. The region of importance in the diagram is the two phase region identified as BN+AlN, located near the right

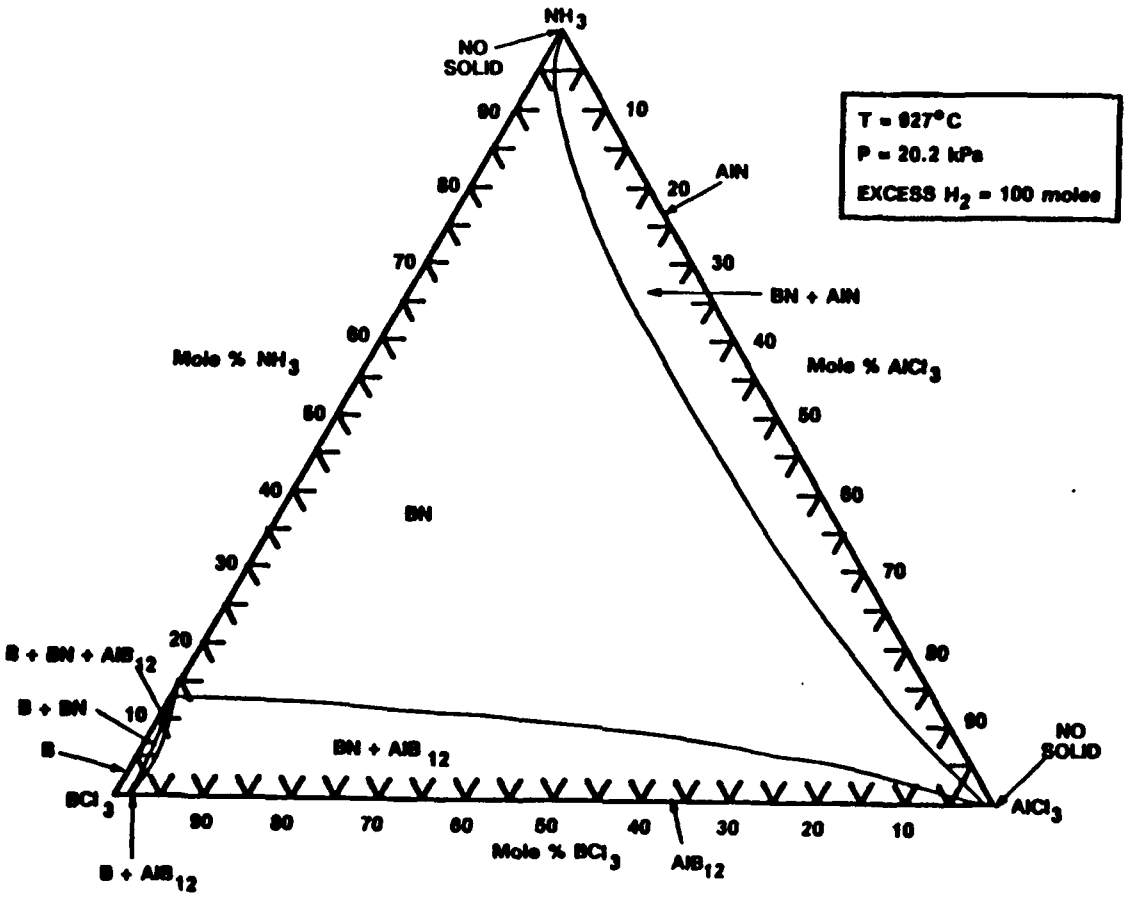

Figure 2-6. Deposition diagram of BN+AlN predicted by thermodynamic calculations [61].

side of the composition triangle. Codeposition of BN and AlN is predicted within this region. To the left of the two phase region is a large region where the only predicted solid is BN. Single phase AlN is predicted to deposit for reagent compositions falling along the $AlCl_3$-NH_3 line. At low NH_3 concentrations codeposition of BN and AlB_{12} is expected. At the two corners of the diagram representing 100 mole% $AlCl_3$ and 100 mole% NH_3, no solid phase is predicted to form. When the BCl_3 concentrations are high (e.g., above 85 mole%), various combinations of B, BN and/or AlB_{12} are predicted.

Furthermore, additional diagrams were constructed by Twait in order to evaluate the influence of temperature, pressure, and hydrogen concentrations on the codeposition process. In summary, it was found that: (1) increasing temperature from 923 to 1423°C significantly reduced the size of the BN+AlN phase region, (2) the addition of H_2 slightly increased the area of the BN+AlN region and caused the disappearance of the AlB_{12} phase, and (3) altering pressure did not have much effect on the deposition behavior at lower temperatures. Therefore, the thermodynamic studies suggested that the BN+AlN composite may be prepared over a fairly wide range of temperatures and reagent concentrations resulting in a BN content ranging from 0 to 100%. The thermodynamic predictions will be compared to experimental results obtained from the present investigation in Chapter V after kinetic characteristics of the BN+AlN-CVD system are identified.

Transport Phenomena and Kinetics

A CVD model, which predicts deposition rate from a given set of processing conditions, can be obtained by simultaneously solving momentum, energy, and mass (species) balances as well as kinetic rate expressions. Mathematically, this means that a set of coupled-partial (or ordinary) differential equations is required to describe a CVD process. Kinetics of the process is incorporated into the model as depletion terms in the specie balances for homogeneous reactions and as boundary conditions of the species balances for heterogeneous reactions. The general forms of these equations have been previously derived [69,70]. Therefore, the objective of this section is not to iterate these equations, but to introduce only those theoretical concepts which are pertinent to the experimental and modeling aspects of the present study.

Because the experimental capability of obtaining reliable kinetic data has been available during the course of the present investigation, one of the goals of our modeling approach has been to reduce the mathematical complexity to a level where the influence of processing conditions on deposition rate can be readily understood or quantified without having to perform a rigorous fitting of kinetic parameters. This philosophical approach can be best illustrated by considering the following example. To date, two "sophisticated" mathematical CVD models have been

developed. Rebenne and Pollard [60] have solved momentum, energy, and mass balances using a finite difference method to describe experimental results obtained by Vandenbulcke [71,72] on CVD of boron carbide in an impinging jet reactor. Roenigk and Jensen [73,74] have developed a two-dimensional model for low pressure chemical vapor deposition (LPCVD) of silicon and silicon nitride in a commercial scale "hot-wall multiple-wafers-in-tube" reactor using an orthogonal collocation method. The model by Roenigk and Jensen predicts the effects of operating conditions on deposition rate at various substrate and reactor positions. However, in both studies, the "true" physicochemical representation of the CVD processes by the models was questionable since Rebenne and Pollard had 24 adjustable kinetic parameters and Roenigk and Jensen used 12 adjustable kinetic parameters for the Si_3N_4-LPCVD system without having much of the necessary kinetic data. This type of kinetic investigation involving model discrimination and parameter estimation usually requires the accompaniment of extensive experimental work and statistical testing [75].

In the case of the silicon deposition, however, "educated guesses" in estimating kinetic parameters were possible because reaction mechanisms of the Si-CVD system were relatively well-understood through numerous experimental studies performed on this comparatively simple system. Therefore, it is obvious that the "sophisticated"

mathematical approach is suitable for simple and well-understood CVD processes. However, this approach loses its merit for complex systems as the true physicochemical nature of the processes may be lost during the empirical fitting process of numerous kinetic parameters unless a significant amount of kinetic data is available.

In comparison to the above mentioned CVD systems, codeposition processes (e.g., BN+AlN-CVD) are much more complex because more chemical species and phases are involved. However, the major difficulty in understanding or modeling the CVD of BN+AlN is due to the fact that the codeposition process has never been studied previously. In addition, as reviewed in the earlier sections, intrinsic kinetic mechanisms of the individual BN-CVD and AlN-CVD processes have not even been identified. Therefore, in order to accomplish the objectives of the present study, it should be the first priority to obtain intrinsic kinetic data of the BN-, AlN-, and BN+AlN-CVD systems. The kinetic analyses should be done in a simple and well-understood reactor geometry to minimize other complications such as non-uniform flow patterns and mass transfer. Then, the kinetic data can be interpreted by a realistic kinetic/diffusion model. The formulation of such a model is presented in Chapter IV.

An impinging jet geometry is chosen for the present investigation since its hydrodynamics is well-understood [76-78]. The geometry has been recognized as an ideal reactor

design for obtaining accurate kinetic data [69,79]. The reactant gas mixture (i.e., jet) flows perpendicular to the substrate and then flows away radially. The vicinity of the substrate surface where mass transfer is independent of the radial position is called the stagnation region. In this region, it is determined experimentally, as well as theoretically, that one-dimensional analysis (i.e., function of z only) is adequate to explain deposition data [60,71,72,79-82]. Inside the stagnation region, a thin momentum boundary layer with a constant thickness exists near the substrate surface along the radial direction. A more detailed description of the geometry is given in Chapter IV.

After the intrinsic kinetic data of the BN-, AlN-and BN+AlN-CVD processes are obtained, the processes can then be scaled-up. For example, as mentioned earlier, Roenigk and Jensen were able to model the Si-CVD process in the commercial reactor scale because the needed intrinsic kinetic data were available in the literature. Claassen et al. [83] developed a relatively simple kinetic expression for the rate of deposition of Si, J_{Si}, from SiH_4:

$$J_{Si} = \frac{kP_{SiH_4}}{1 + K_H P_{H_2} + K_e P_{SiH_4}} \qquad (2\text{-}1)$$

where P_{H_2} and P_{SiH_4} are the partial pressures of H_2 and SiH_4, respectively, at the substrate surface, k is the rate constant and K_H and K_e are the equilibrium constants. This

expression corresponds to a kinetic mechanism of: (1) adsorption/desorption equilibria of silane and hydrogen, (2) no homogeneous reaction, and (3) rate-controlling surface reaction (i.e., surface decomposition of silane). As mentioned previously, the CVD of Si is a much simpler and better-understood process than that of BN and AlN. However, even for this relatively simple process, a kinetic mechanism containing up to 20 intermediate reaction steps has been proposed [84].

It is again noted that the main purpose of the present study is to understand the influences of processing variables on the microstructure of the BN+AlN composites. Therefore, in the present investigation, the intrinsic kinetic data of the BN, AlN, and BN+AlN-CVD systems will be utilized in studying the nucleation and growth behavior of the BN+AlN composite coatings in comparison to that of BN and AlN as single phase coatings. Nevertheless, the kinetic data should provide a strong basis for any future scale-up work of the BN-, AlN-, and BN+AlN-CVD systems.

Nucleation and Crystal Growth

There are two different types of nucleation and growth phenomena commonly observed in CVD processes: heterogeneous and homogeneous. The heterogenous path is always desired for obtaining a good quality coating whereas even a very small amount of homogeneous nucleation is detrimental to the coating quality. In this section, homogeneous nucleation and

growth in CVD environments are first discussed. A brief introduction to the classical nucleation and growth theory, which is necessary in understanding both homogeneous and heterogeneous nucleation and growth mechanisms, is included. Second, the current understanding on heterogeneous nucleation and growth of CVD coatings is summarized.

Homogeneous Nucleation. As shown in Figure 2-5 (p. 38), homogenous nucleation and growth steps (i.e., particle formation in the gas phase) proceed in parallel with the heterogeneous deposition path. In every CVD operation, homogeneous nucleation is undesirable since some of the particles formed in the gas phase can become a part of the coating structure. The incorporation of the particles in the coating structure generally lowers film quality (e.g., poor adherence, low strength and hardness, powdery, low density, etc.). Therefore, processing conditions which will lead to homogeneous nucleation are to be avoided.

The suppression of undesired homogeneous nucleation can be rather easily achieved by keeping temperature and reagent concentrations low enough so that stable nuclei of non-volatile product molecules (i.e., condensible vapor) cannot be formed in the gas phase (i.e., classical nucleation theory). However, even at these conditions, the non-volatile product molecules formed on the surface via surface reaction(s) will still be able to nucleate and grow heterogeneously. Several reasons for the apparent difference

between the homogeneous and heterogenous nucleation mechanisms during the same CVD operation will be explained in the next few paragraphs in the context of classical nucleation and growth theory.

According to the classical nucleation theory, in order for a nuclei to grow, an increase in surface free energy should be overcome by a decrease in volume free energy, as non-volatile vapor will condense [85-87]. In the case of spherical nuclei, the governing equation is:

$$\Delta G = 4\pi r^2\varphi + \frac{3\pi r^3}{4V_m} RT \ln(C/C_{eq}) \qquad (2\text{-}2)$$

where ΔG is the total energy of a nucleating sphere (particle), r is the nuclei radius, φ is the specific surface free energy, and V_m is the molar volume of the condensed phase. For a particle nucleating in the gas phase of a CVD process, C is defined as the actual concentration of the non-volatile product(s) generated in the gas phase and C_{eq} is the equilibrium concentration of the product(s) in the gas phase. Obviously the C/C_{eq} ratio, which is commonly referred to as the supersaturation ratio, is fairly large in most CVD systems. The critical nuclei size, r^*, can be obtained by differentiating Eq. 2-2 and setting it equal to zero.

$$r^* = \frac{2\varphi V_m}{RT \ln(C/C_{eq})} \qquad (2\text{-}3)$$

If nuclei have a chance of becoming larger than r^*, then the nuclei will grow. Otherwise, the nuclei will decay.

It is more difficult to describe heterogeneous nucleation in a quantitative manner. In this review, only heterogeneous nucleation at a gas-solid interface will be discussed. In general, it is recognized that ΔG is lowered due to an additional interaction at the interface of a condensed phase (i.e., nuclei) and substrate surface [86]. In other words, the high-energy surface between the gas phase and the condensed nuclei is partially replaced by the low-energy surface between the condensed nuclei and the substrate surface. (Note: For nucleation of a liquid on a solid surface, the concept of "wetting angle" is used to account for the degree of the interface interaction.) Therefore, the critical size for heterogeneous nucleation is smaller than for homogenous nucleation. This allows for the possibility in which heterogeneous nucleation will take place, but homogeneous nucleation will not occur even at the same supersaturation conditions.

Also, there is another reason as to why heterogeneous nucleation occurs in typical CVD operating environments, under which homogeneous nucleation is not observed. As can be seen from Eq. 2-3, the critical size is influenced by the supersaturation term, C/C_{eq}. As defined earlier, C is the actual concentration of non-volatile CVD product(s). The

concentration of the product is directly related to the rate of reaction(s), which generate the product. In typical CVD conditions, the rate of surface reactions is faster than that of gas phase reactions resulting in a higher local supersaturation ratio at the surface than in the gas phase. An alternate view on the heterogenous nucleation and growth behavior of CVD coatings is that the non-volatile products generated on the substrate surface do not evaporate into the gas phase because of the high supersaturation ratio. Therefore, all of the non-volatile molecules produced at the surface will nucleate and grow. Due to this reasoning, the deposition of CVD films via heterogeneous nucleation and growth can occur without forming particles in the gas phase. The reason for the higher rate of the surface reactions in comparison to that of the gas phase reactions is simply because of the fact that the activation energy is usually lower for the surface reactions than for the gas phase reactions.

The above paragraphs described the qualitative features of homogeneous and heterogenous nucleation based on classical nucleation theory. The remainder of this section will summarize previous experimental investigations on homogeneous nucleation behavior under CVD or CVD-like environments. Since homogenous nucleation is not desired in most CVD processes, the general approach in the CVD research community has been to "run away" from conditions which would

result in homogenous nucleation. Therefore, the topic of homogeneous nucleation in CVD processes has not received much attention. The author's literature search indicates that the production of Si by the pyrolysis of SiH_4 is the only CVD process in which nucleation behavior in the gas phase has been systematically studied [88-90].

Flagan and his co-workers [88,89] have studied the homogeneous nucleation and growth characteristics of Si in an experimental aerosol system consisting of two or three reactors in series. First, one or two "seed" reactors were used to generate Si seed particles by the pyrolysis of SiH_4 diluted with N_2 (i.e, 1% SiH_4) at 823°C. The seed particles were introduced into a "primary reactor" with an additional gas stream containing SiH_4 and N_2. The growth behavior of the seed particles in the primary reactor was observed as a function of SiH_4 concentration at temperatures below about 723°C. Particle size and count were measured after each reactor stage.

When the SiH_4 concentration was below 3% in the primary reactor, the particles steadily grew in size without creating any particles (i.e, no homogeneous nucleation). In this case, it was explained that the growth of the seed particles resulted from diffusion of Si vapor produced by gas phase reactions to the particle surface and subsequent condensation of the vapor (i.e., "scavenging" of the vapor products by the seed particles). However, when the SiH_4 concentration reached

about 3%, the particle count increased by four orders of magnitude as can be seen in Figure 2-7, in which the number concentration of particles having a diameter of 0.7 μm is plotted. The sudden increase in the particle number (i.e., called "catastrophic" or "run away" nucleation) was due to homogeneous nucleation indicating that the critical supersaturation ratio for the Si vapor was reached in the gas phase at the SiH_4 concentration of 3%. A further increase in the SiH_4 concentration did not appreciably increase the particle count, as the coagulation of the fine particles produced by homogeneous nucleation was suspected for SiH_4 concentrations above 3.5%. The Si particles usually appeared as an assemblage of small fine spheres in SEM micrographs.

As described above, homogeneous nucleation in the CVD environment appears to follow the classical nucleation theory. Therefore, as long as processing conditions which yield the "catastrophic" or "run away" nucleation can be avoided, the homogeneous nucleation and growth steps shown in Figure 2-5 can be disregarded (i.e., "infinite resistance" in the equivalent circuit analogy). For a given process, the first step in obtaining intrinsic kinetic data or developing a quantitative model is to identify the processing conditions that do not result in homogeneous nucleation.

Heterogeneous Nucleation. The previous section on transport phenomena and kinetics was mainly concerned with predicting the rate of deposition from processing parameters.

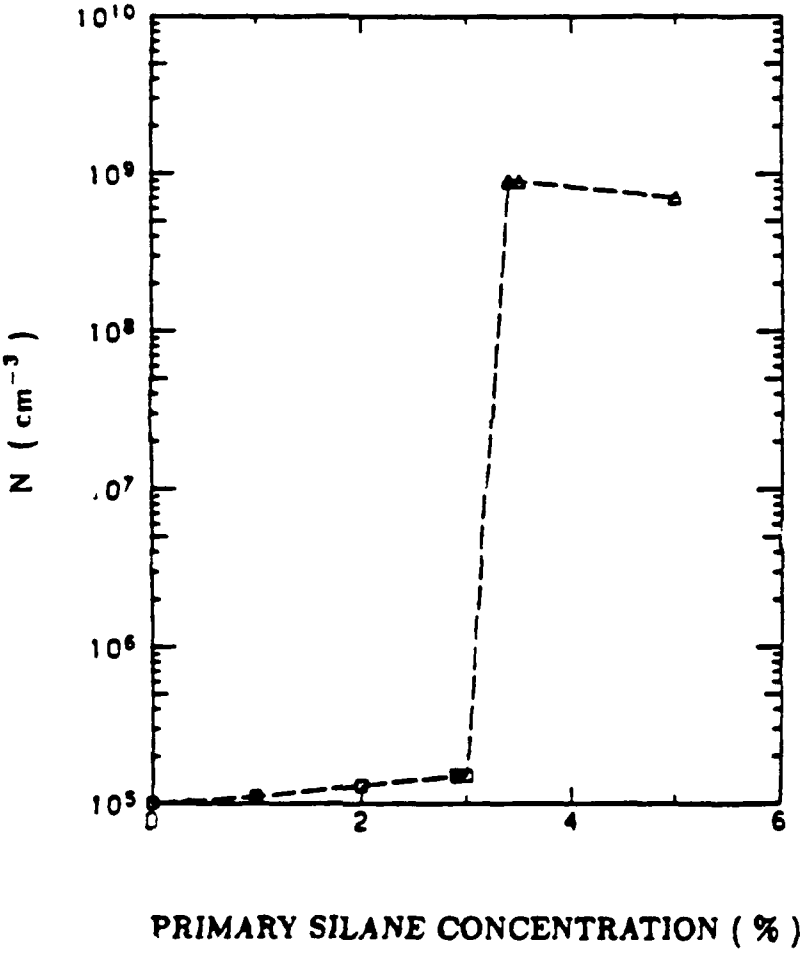

Figure 2-7. Effect of SiH_4 concentration on the final number concentration for fixed initial seed aerosol, i.e., 10^5 cm^{-3} (STP) seed particles of 0.7 μm diameter [88].

During the discussion, it was assumed that the heterogenous nucleation and growth steps were relatively fast. This is a valid assumption for most CVD processing conditions since the vapor pressure of solid product(s) formed heterogeneously on the deposition surface is usually very small (i.e., high supersaturation in the context of the classical nucleation theory). In other words, the products will not evaporate into the gas phase so the deposition rate is strictly determined by the mass transfer and/or surface kinetic steps. In terms of the equivalent electrical circuit analogy (see Figure 2-5), the resistance of the nucleation and growth steps is said to be small. However, at high temperatures near the deposit's melting (or sublimation) point, the nucleation and growth steps can be the rate-limiting steps as the vapor pressure of the product increases very rapidly with increasing temperature. In most CVD processes, this situation is not frequently encountered since the operating temperature is far below the deposit's melting (or sublimation) point.

The classical nucleation and growth concepts are usually good for explaining bulk phenomena (e.g., shape of nodules, surface morphology, etc.). However, in order to understand the crystallinity and microstructure of the deposit as a function of processing parameters, nucleation of molecules or atoms generated by surface reactions and their subsequent growth should be treated in a statistical-mechanical manner

[91-95]. The relationship between the classical and statistical-mechanical nucleation and growth theories is analogous to that between the classical Newton's laws and quantum mechanics. The statistical-mechanical approach is useful in portraying the nucleation and growth processes which occur at the atomic scale, just as quantum mechanics is most valuable in describing the motion of atomic or sub-atomic particles where Newton's laws fail. The nucleation behavior of simple deposition systems such as sputter deposition of Au and CVD of Si has been examined using this statistical-mechanical approach in a somewhat quantitative manner [92]. In general, however, such quantitative treatment is a formidable task for most CVD systems due to their complexity and the experimental difficulties in verifying proposed nucleation mechanisms.

In practice, three major types of heterogeneous nucleation can be qualitatively described using the statistical-mechanical approach [93-95]. First, amorphous growth is usually obtained when non-volatile adatoms are formed at a relatively high rate (i.e., high growth rate) and the surface diffusion of these adatoms is slow (i.e., low deposition temperature). This is because "a newly created adatom impinges on a specific site before the previously formed adatoms have made a sufficient number of diffusional jumps to reach energetically more favorable crystallographical sites [95]." When the mobility of the

adatoms becomes sufficiently high as temperature increases, formation of a polycrystalline structure results. Furthermore, when temperature is increased to a point where the process becomes diffusion-limited (i.e., surface kinetics is fast), epitaxial and/or single crystal growth takes place. This occurs because the mobility of the adatoms increases exponentially with temperature whereas the increase in the growth rate becomes a weak function of temperature in the diffusion-limited region.

Therefore, to a large extent, the same factors (e.g., temperature, pressure, reactant concentrations) which control the deposition rate also influence the nucleation and growth of the deposit and, therefore, its microstructure. The nucleation behavior is primarily influenced by temperature which affects the mobility of the adatoms as well as the deposition rate. However, other operating conditions such as pressure and reactant concentrations can also influence the final crystal structure by altering the deposition rate. For example, when pressure and reactant concentrations are changed to increase the deposition rate of silicon, the crystallinity of silicon is found to decrease [94]. Figure 2-8 shows the crystalline structure of Si as a function of the deposition rate and temperature. Polycrystalline Si was deposited when the Si deposition rate was high and the temperature was low. Otherwise, single crystal Si (i.e., epitaxial growth) was deposited. Based on the experimental

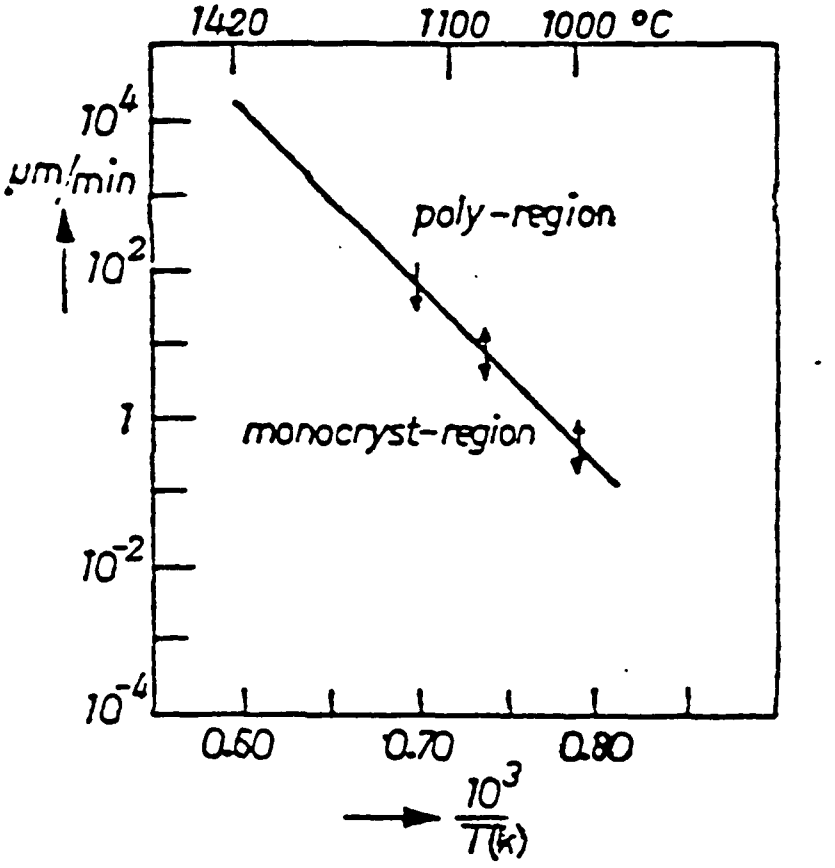

Figure 2-8. Crystalline structure of Si is strongly influenced by deposition rate and temperature [94].

observations, the general relationship between the final crystal structure, C, of CVD coatings with the growth rate, J, and the operating conditions can be qualitatively correlated as:

$$C = C \{ J(T,P,P_i,v), \ u_i(T) \} \qquad (2\text{-}4)$$

where P_i is the inlet partial pressure of reactant i, v is the linear fluid velocity to account for the mass transfer effect, and u_i is the surface mobility of adatoms i.

The correlation described in Eq. 2-4 is based on experimental observations from the CVD of single phase systems. However, to date, CVD of dispersed phase composites has not been studied enough to answer a basic, but important question: how should the simultaneous nucleation and growth of two chemically different phases (i.e., BN and AlN) be treated? In the present study, the question is answered using the following experimental approach. First, nucleation and growth characteristics of BN-CVD, AlN-CVD, and BN+AlN-CVD systems will be analyzed and tested to determine whether the three CVD systems follow the general nucleation behavior described by Eq. 2-4. Second, the nucleation and growth behavior of the BN+AlN-CVD process will be compared to that of the BN-CVD and AlN-CVD single phase deposition processes. The comparison will provide the first clue in understanding the nucleation and growth process for the BN+AlN composite system: Do BN and AlN grains in the composite environment

nucleate and grow independently? When the answer is "yes", the nucleation and growth process of the composite system will be nothing more than that in which the two independent BN-CVD and AlN-CVD processes occur simultaneously at the same space and time. Then the crystalline structure of the BN and AlN phases in the composite environment can be express as:

$$C_{BN} = C_{BN}\,(J_{BN},\ u_i) \tag{2-5}$$

$$C_{AlN} = C_{AlN}\,(J_{AlN},\ u_i) \tag{2-6}$$

On the other hand, when the answer to the above question is "no", any deviation from Eqs. 2-5 and 2-6 should be explained on the basis of possible chemical and/or physical interactions between the BN and AlN grains.

In summary, Eq. 2-4 describes the overall methodology of the present investigation. First, the kinetics and thermodynamics of the BN-, AlN-, and BN+AlN-CVD systems will be independently studied. The effects of process parameters on deposition rate and microstructure of the CVD coatings will be determined. Second, the microstructure of the BN+AlN composite will be compared to that observed from the BN-CVD and AlN-CVD.

CHAPTER III

EXPERIMENTAL EQUIPMENT AND PROCEDURE

The first section of this chapter describes the CVD equipment and materials used to prepare BN, AlN, and BN+AlN coatings. The section also includes detailed discussions on the vaporization of $AlCl_3$ powder and the configuration of the impinging jet reactor geometry arrangement inside the CVD furnace. The second section introduces various analytical techniques which were employed to characterize the coatings.

CVD Apparatus

Overall System Description

As schematically shown in Figure 3-1, the overall experimental arrangement consisted of: (1) a reagent supply system including stainless steel gas lines and control-valves, a stainless steel $AlCl_3$ vaporizer, and a stainless steel injector; (2) a resistively heated hot-wall vertical graphite furnace in a gas tight, water-cooled stainless steel shell (see Figure 3-2); and (3) a scrubber plus a corrosion resistant vacuum pump from Leybold, Inc. (Type D16BCS). A photograph of the apparatus is shown in Figure 3-3.

Pressure in the furnace was measured by an MKS Baratron pressure gauge (Type 122A) and was controlled by an MKS

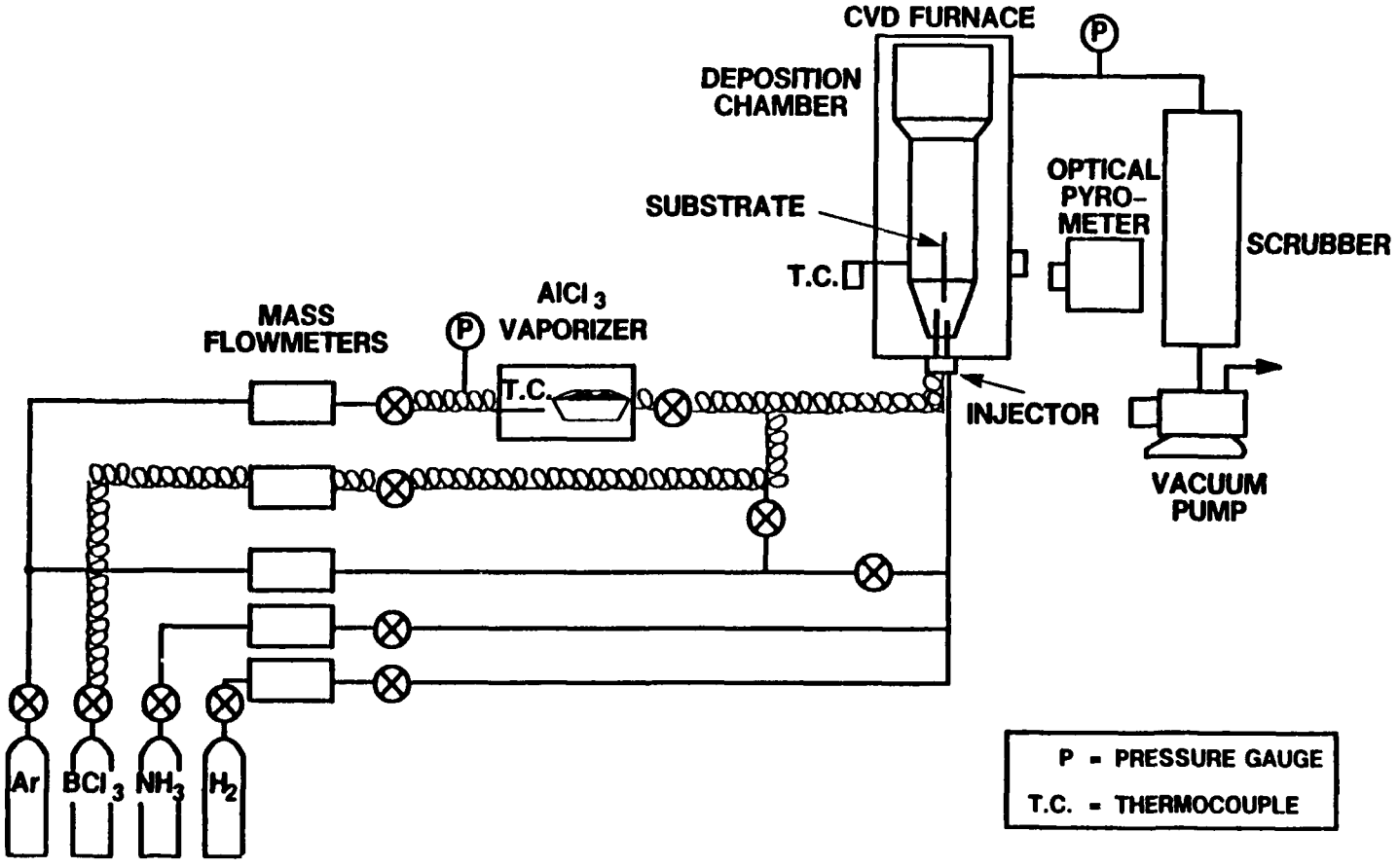

Figure 3-1. Schematic diagram of CVD system used to prepare BN, AlN, and BN+AlN coatings.

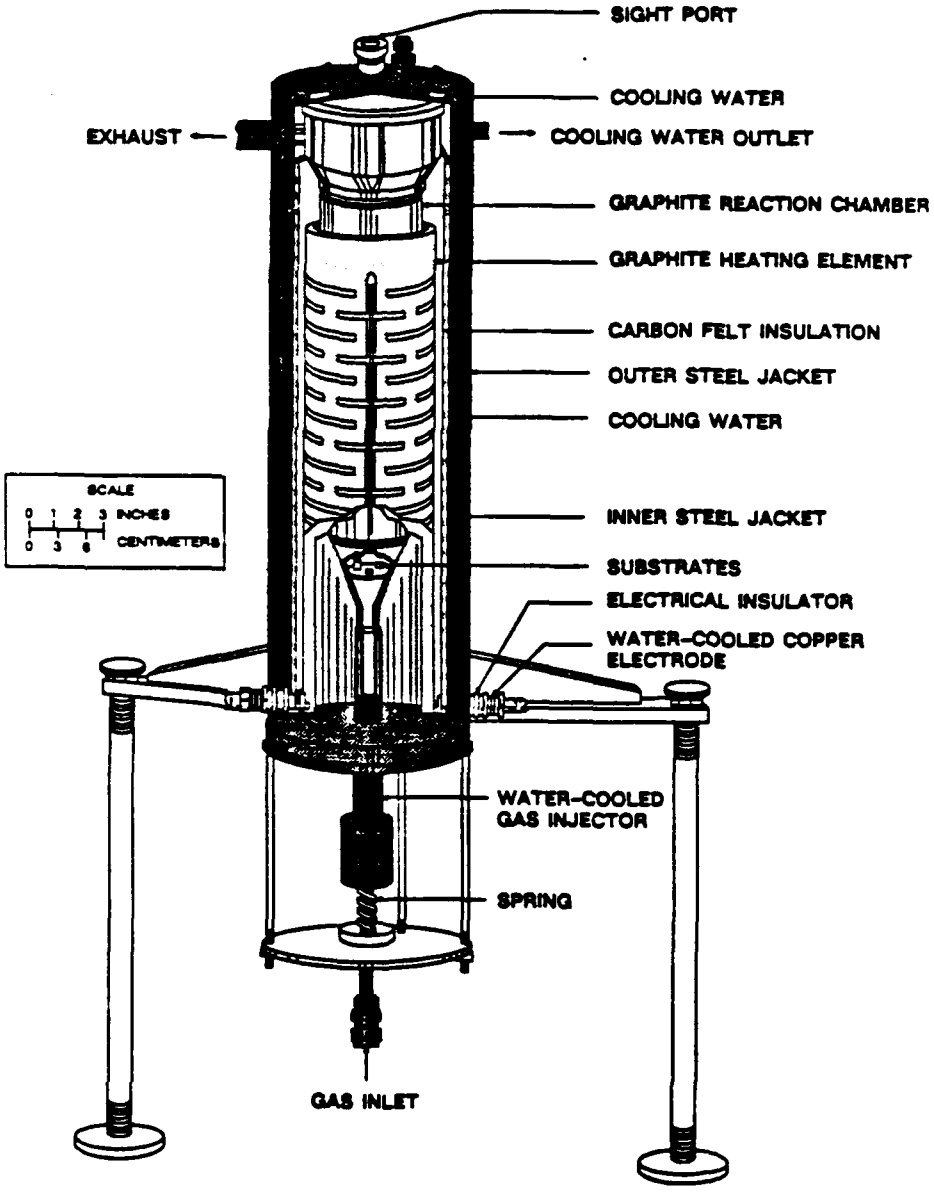

Figure 3-2. Detail features of the CVD furnace.

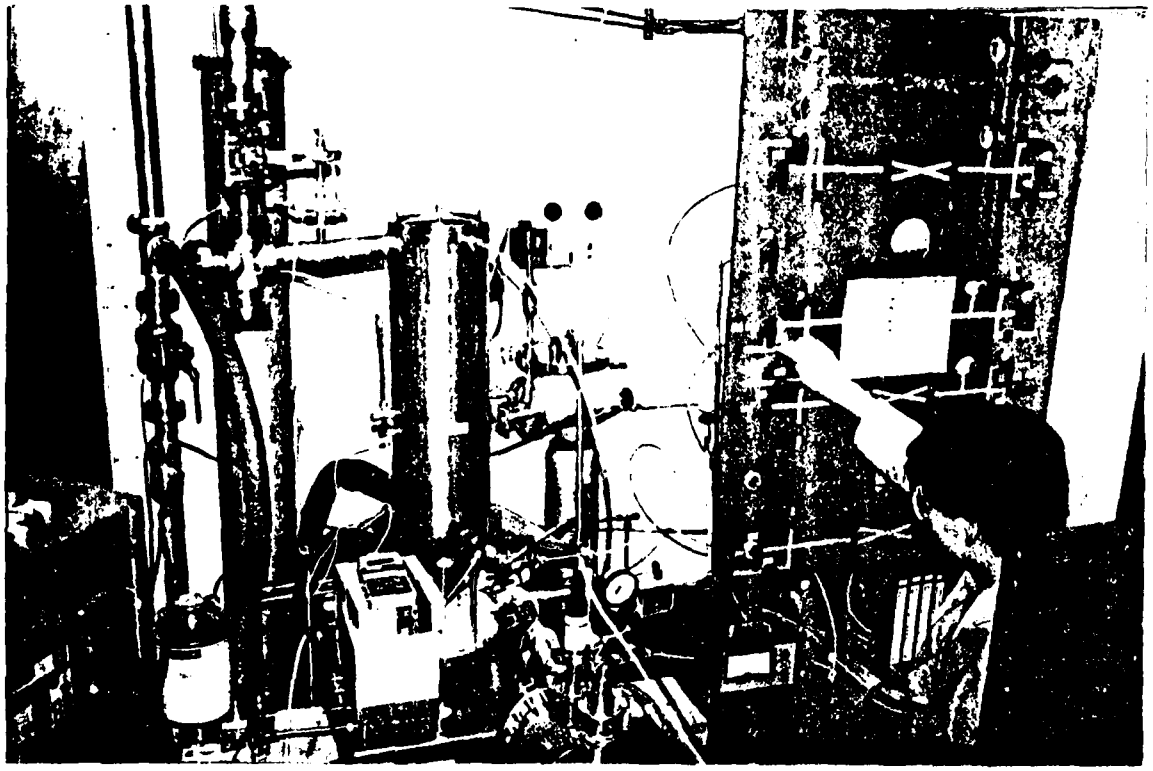

Figure 3-3. CVD experimental arrangement.

pressure controller (Type 250B). An optical pyrometer from Ircon Co. (Modline Plus, Type R) and a chromel-alumel thermocouple (Type K, Pyromation, Inc.) or a W-5%Re/W-0%Re thermocouple (Pyromation, Inc.) were used to measure deposition temperature at the exterior surface of the graphite reaction chamber) as shown in Figure 3-1. The deposition temperature was controlled using a temperature controller from Research, Inc. (Micristar, Model 828D), which was interfaced with the pyrometer and furnace power supply.

The thermocouples and pyrometer were periodically calibrated by: (1) placing a long W-5%Re/W-26%Re thermocouple (Pyromation, Inc.) inside the graphite chamber along the center line of the furnace, (2) placing an optical pyrometer from Pyrometer Instrument Co. on the top of the furnace and focusing it onto a graphite substrate inside the graphite chamber through a silica window, and/or (3) melting silver and checking its melting point (961°C). From these calibrations, it was determined that the temperature of the graphite chamber (or substrate) surface was usually about 30 to 50°C higher than that of the bulk gas phase. The higher temperature at the graphite surface was probably due to a small amount of radiational heat flux coming directly from the heating element to the graphite chamber. Therefore, it was suspected that the graphite chamber and substrate were mainly heated by convective heat transfer at typical operating temperatures (e.g., 800 to 1100°C). The idea was supported by the fact

that the gas phase temperature increased by about 30 to 40°C as the furnace pressure was decreased from 760 torr to 30 torr (i.e., an increase in the gas velocity increased the convective heat transfer rate).

The desired flow rates of BCl_3 (Matheson, 99.9%), NH_3 (Matheson, 99.99%), Ar (Matheson, 99.999%), and H_2 (Matheson, 99.999%) were controlled by mass flowmeters from MKS Instruments, Inc. (Type 1259B) with an MKS power source (Type 247C). The mass flowmeters were periodically calibrated with a bubble flowmeter using Ar. BCl_3 is liquid at room temperature, but its vapor pressure is high enough so that the mass flowmeter could be used. However, in order to minimize the condensation of BCl_3, the BCl_3 line and the mass flowmeter were heated with heater tapes in a manner such that the temperature downstream of the mass flowmeter was about 150°C while that upstream of the mass flowmeter was about 60°C. In most experiments, two types of thin α-Al_2O_3 strips were used as substrates: (1) 1.27 cm x 7.6 cm x 0.0794 cm, Coors Inc., Type-ADS-96, 99.6% and (2) 1.905 cm x 5.715 cm x 0.0635 cm, Materials Research Corp., Lot# 110236, 99.6%. Other substrate materials such as graphite (Grade 890S), hot pressed Si_3N_4 (NCX-34, Norton Co.), bearing steel (M50), tungsten (Victor Co.) and titanium (Grade 2, Tico, Inc.) were occasionally used.

The general deposition procedure is outlined as follows. After the substrate(s) were weighed and placed inside the

reactor, the reactor was heated to the desired temperature while flowing argon at the desired pressure. The deposition started when the reactants were simultaneously fed into the furnace. The deposition was terminated by stopping the reactant flows and subsequently cooling the furnace while flowing argon. For codeposition experiments (i.e., BN+AlN-CVD), both BCl_3 and $AlCl_3$ were simultaneously fed into the reactor. For single phase deposition experiments (i.e., BN-CVD and AlN-CVD), either BCl_3 or $AlCl_3$ was used. After each deposition experiment, the substrate was assigned to a "J-number" (e.g., J-833) for identification purposes.

The CVD apparatus was periodically checked for air leaks. During the leak checks, the furnace was evacuated to about 2 torr. The leak rate into the entire furnace chamber excluding the gas supply lines and vaporizer (about 13,000 cm^3 in volume) was typically about 6500 torr·cm^3/min. However, the actual reaction chamber volume (i.e., volume of the graphite chamber from the injector inlet to the substrate position where oxygen contamination with the reagent stream would be a significant problem) was much smaller (about 330 cm^3) than that of the entire furnace so the effective leak rate into the reaction zone was estimated to be only about 165 torr·cm^3/min. The leak rate into the vaporizer (145 cm^3 in volume) evacuated at 10 torr was about 30 torr·cm^3/min. The leak rate into the stainless steel gas supply lines before the CVD furnace was

about 350 torr·cm³/min. Therefore, the maximum total leak rate was 545 torr·cm³/min, which corresponded to a maximum air contamination of about 400 ppm at 2 torr.

Vaporization of $AlCl_3$

$AlCl_3$ was obtained from Aldrich Chemical Co., Inc. (99.99%) and Fisher Scientific (99.784%). Since the $AlCl_3$ powder is hydroscopic, it was always handled in an argon glove-box. Using the glove-box, the powder (about 10 g) was transferred into a stainless steel boat, which was then placed in the leak-tight stainless steel vaporizer (22.86 cm in length and 3.175 cm in diameter). The $AlCl_3$ vaporizer was heated with heater tapes to temperatures of 115 to 145°C depending on the operating pressure of the CVD reactor. The vapor pressure of $AlCl_3$, P_{vap}, can be easily determined from the following equation [96]:

$$\log P_{vap} = 15.45 - 5750/T \qquad (3\text{-}1)$$

where T is the temperature in K and P_{vap} is in torr. For example, the vapor pressure of $AlCl_3$ at 115 and 145°C are about 4 and 50 torr, respectively. A chromel-alumel thermocouple (Type K, Omega Engineering, Inc.) was used to measure temperature inside the vaporizer at its center position. The vaporizer temperature was controlled by a temperature controller from Omega Engineering, Inc. (Series CN 310). Pressure inside the vaporizer was measured by a

pressure gauge from Omega Engineering, Inc. (Type 232-10), which was located before the inlet control valve of the vaporizer.

The $AlCl_3$ powder in the vaporizer was cleaned by flowing Ar for at least 30 minutes, and the vaporizer was pressurized to about 150 torr with Ar. At the start of deposition, both exit and inlet valves of the vaporizer were simultaneously opened so an argon stream (usually 5 to 50 cm^3/min at STP) could pass through the vaporizer and carry $AlCl_3$ vapor into the reactor. After the deposition was completed, the average flow rate of the $AlCl_3$ vapor was calculated from the overall weight loss of the vaporizer. Figure 3-4 shows the $AlCl_3$ weight loss as a function of time at two different vaporization conditions. The fairly linear relationship between the weight loss and time (extrapolated to the origin) indicated that the flow rate, or flux, of the $AlCl_3$ vapor into the furnace was constant throughout the deposition process. Figures 3-5 and 3-6 show the effects of the vaporizer temperature and the carrier Ar flow rate, respectively, on the vaporization rate of $AlCl_3$. The vaporization rate of $AlCl_3$ increased rapidly with increasing temperature and, therefore, was very sensitive to even a slight temperature variation during the whole vaporization process. The error bars in Figures 3-4, -5, and -6 were drawn to indicate the uncertainty in measuring weight of the vaporizer (± 0.04 g).

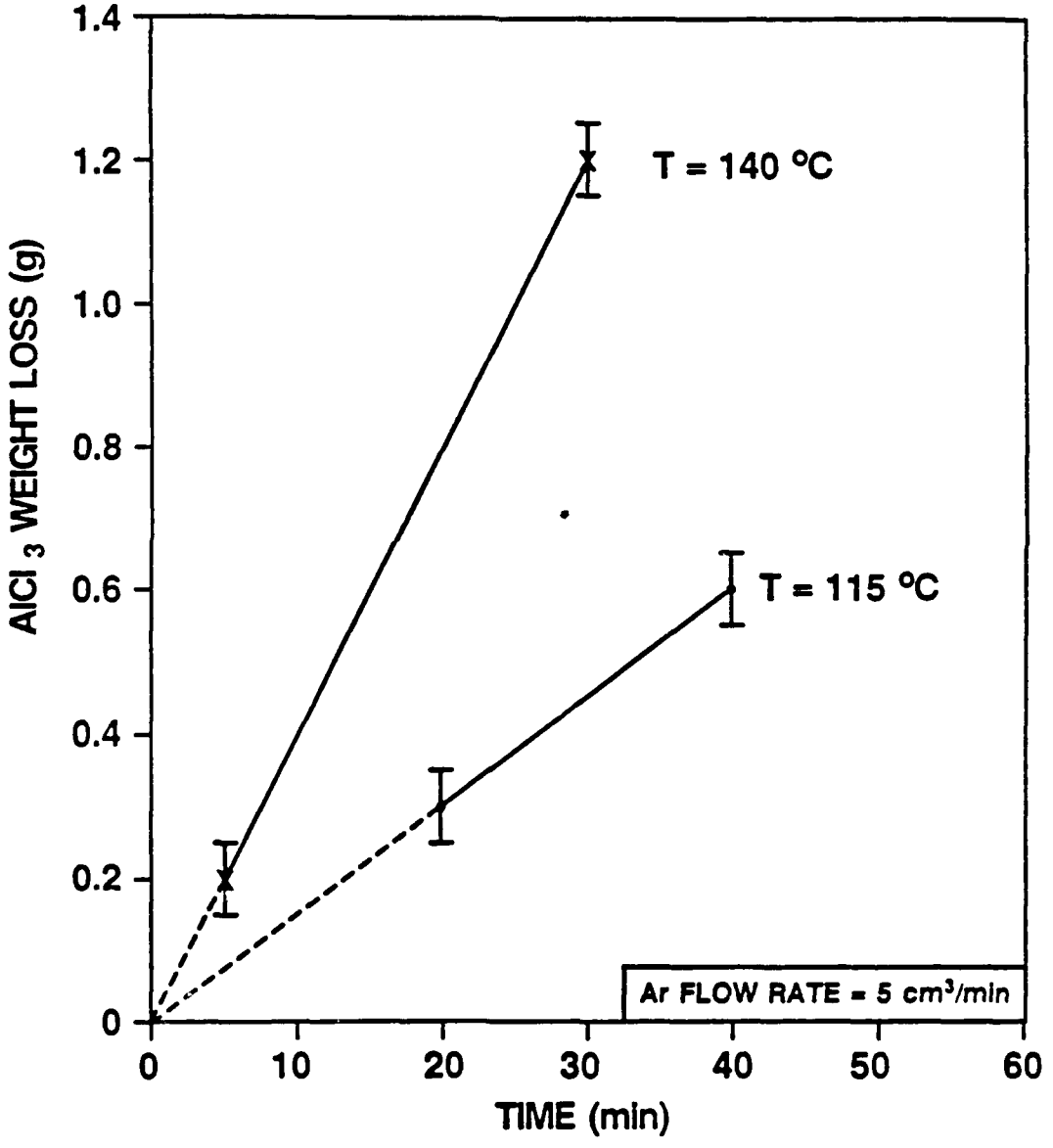

Figure 3-4. Weight loss of AlCl, versus time.

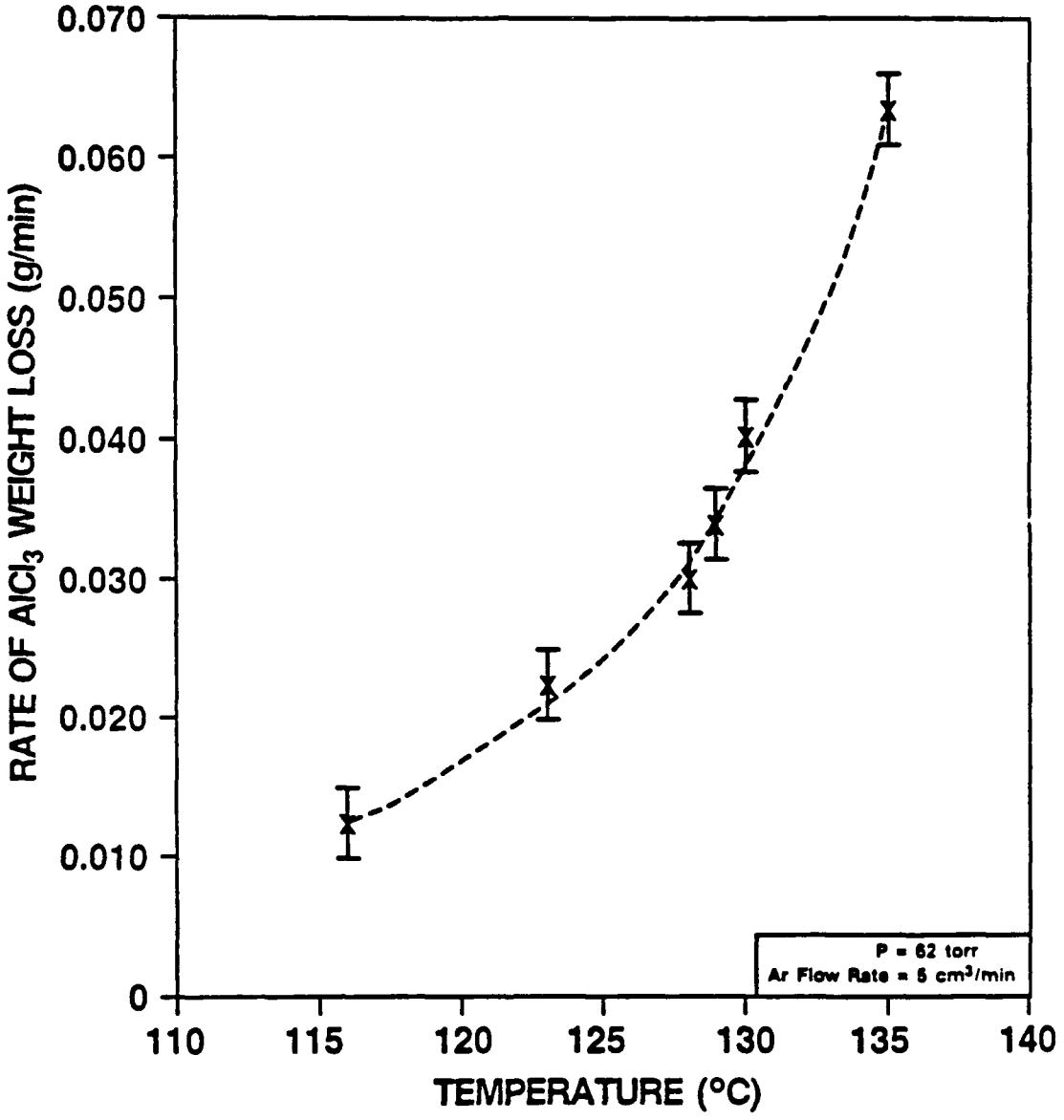

Figure 3-5. Rate of AlCl, weight loss versus temperature.

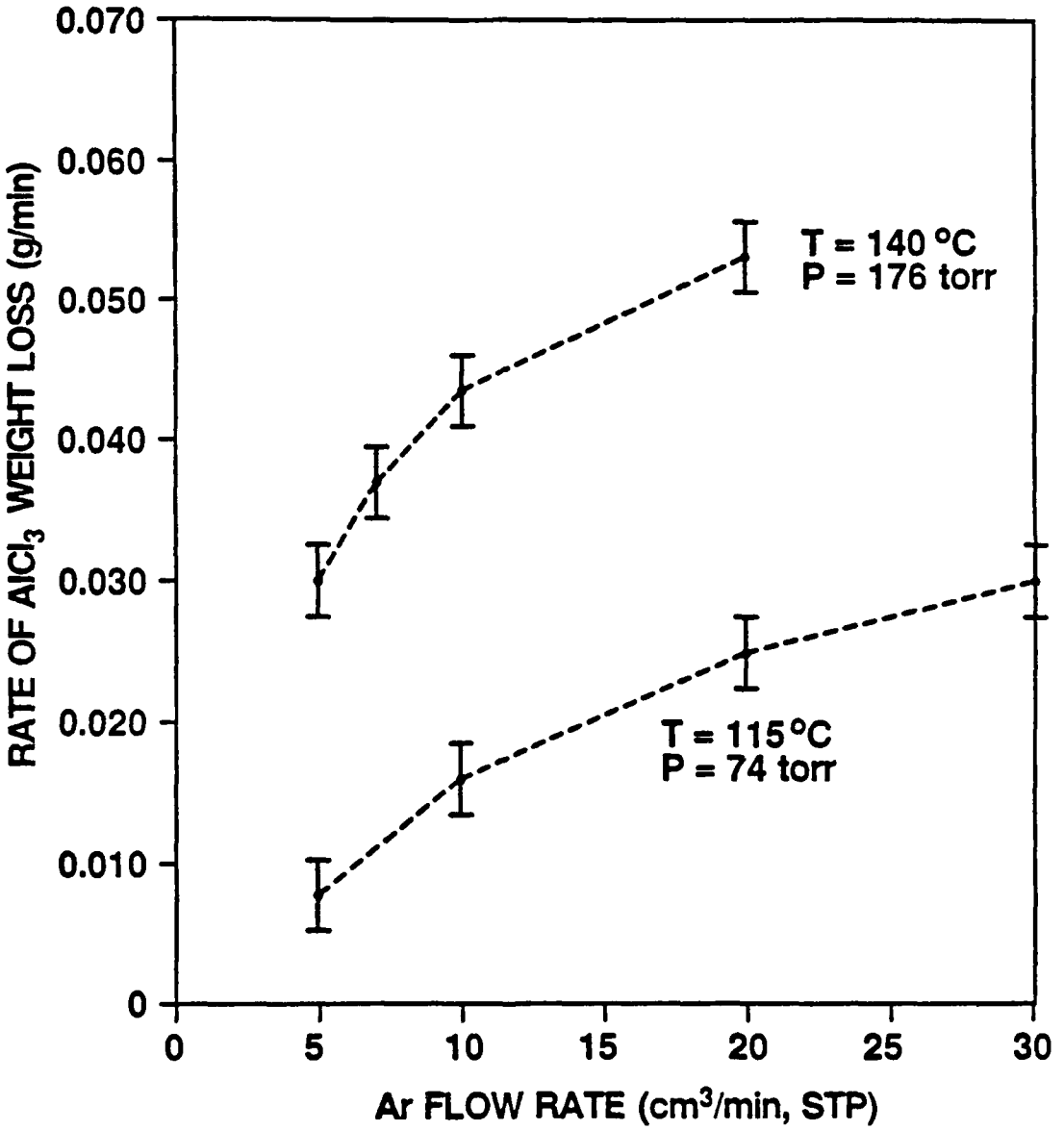

Figure 3-6. Rate of $AlCl_3$ weight loss versus Ar carrier flow rate.

The vaporizer data shown in Figures 3-4,-5, and -6 were qualitatively in agreement with predictions from simple calculations performed on the assumption that the carrier Ar stream is fully saturated with the $AlCl_3$ vapor. However, a precise match between the data and predictions from the calculations was not obtained due to: (1) uncertainties and errors associated with measuring temperature and pressure, as the vaporization behavior was very sensitive to these parameters and (2) temperature variations in the radial and axial directions, which were not accounted for during the calculations, and (3) "local" cooling at the solid surface due to the vaporization. In addition, the Ar carrier stream might not be fully saturated when the carrier flow rate was high, as evidenced by the fact that the slope of the $AlCl_3$ vaporization rate slowly decreased with increasing the Ar flow rate (see Figure 3-6). Nevertheless, any desired flow rate of $AlCl_3$ vapor within an accuracy of $\pm$ 0.2 cm^3/min at STP could be supplied to the CVD chamber by mainly controlling the vaporizer temperature and Ar carrier flow rate. Once the vaporizer was loaded with $AlCl_3$ in the glove-box, the $AlCl_3$ powder could typically be used for more than ten deposition experiments as long as the powder was not contaminated by air. The air contamination could be minimized by pressurizing the vaporizer with Ar between the deposition runs.

The stainless steel injector, shown in Figure 3-2, contained two co-axial gas paths so NH_3/H_2 and $AlCl_3/BCl_3$

mixtures could be separately fed into the furnace without the metal-chlorides reacting prematurely with NH_3. Both paths were diluted with argon. The injector had a cooling shell and was cooled with compressed air for experiments performed in the early stage of the present study (up to J-748). However, it was found that about 50% of the $AlCl_3$ vapor tended to condense inside the injector due to the low temperature of the air stream even though the injector was heated with heater tapes from the outside. The condensation often caused clogging of the inside path. Also, the $AlCl_3$ flow rate could not be accurately determined. In order to avoid the condensation of $AlCl_3$ vapor, an oil bath (Type 001-4200, Haake Co.) was used to keep the temperature inside the injector at 170°C. The circulation of oil through the injector cooling shell allowed the injector temperature to be higher than that of the vaporizer. The use of the oil bath effectively eliminated the condensation problem.

Reactor Configuration and Geometry

As shown in Figure 3-7, a graphite extension tube (ID = 0.635 cm and OD = 0.953 cm), which was threaded into the inner reagent path of the injector, was used to control the mixing position of the two gas streams in the vertical suspension geometry. The outer diameter of the outer path (i.e., inside diameter of the bottom end of the graphite cone) was 1.588 cm. Without the extension tube, NH_4Cl powder was deposited on the top of the injector due to premature reaction

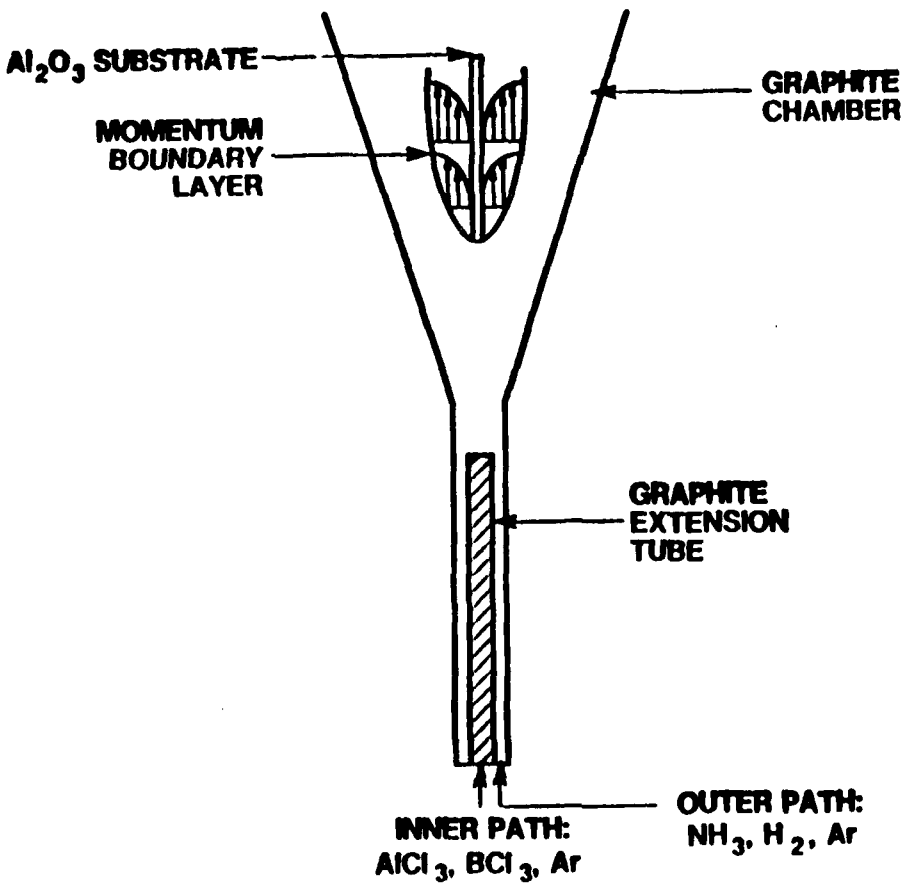

Figure 3-7. Vertical suspension geometry.

between $BCl_3/AlCl_3$ and NH_3 [11,15]. The premature reaction was caused by low temperature areas probably located around the top region of the injector as the injector was cooled at by circulating oil (or compressed air) during the deposition process.

In the beginning of the present investigation (J-549 to J-655), the alumina substrate was vertically suspended in the graphite chamber using molybdenum wire ("vertical suspension geometry") as shown in Figure 3-7. The vertical suspension geometry was used in hopes of understanding how the deposition behavior would be influenced by: (1) the development of a concentration boundary layer along the substrate surface and (2) the depletion of reagents along the flow direction. However, extensive kinetic/mass transfer treatment of the deposition data obtained from this geometry was extremely difficult for several reasons. First, the flow pattern inside the graphite chamber sometimes deviated significantly from the expected fully developed and mixed flow due to channeling, improper reagent mixing, etc., which were evidenced by some unexplainable experimental observations such as non-uniform bands and sections of coatings on the same substrate. Second, the characterization of the coatings became fairly difficult as the coating characteristics changed continuously from the bottom to the top end of the substrate. Third, and most importantly, two dimensional analyses of the complex BN-, AlN- and BN+AlN-CVD processes were not possible with the limited

amount of kinetic data available in the literature. In order to avoid these problems, an impinging jet geometry was employed. As discussed earlier in Chapter II, the major advantages of using the impinging jet geometry are that: (1) uniform convective mass transfer can be obtained and (2) one dimensional analysis in the axial direction is sufficient to describe the deposition data obtained inside the stagnation region. It has been determined that mass transfer is independent of the radial direction inside the stagnation region [76,77]. A more detailed description of the impinging geometry is given in Chapter VI. Nevertheless, the experimental data obtained using the vertical suspension geometry provided a significant contribution to the understanding of the BN-, AlN-, and BN+AlN-CVD processes as will be described in Chapter V.

The presence of a circular graphite disc with a center hole, as shown in Figure 3-8, forced the gas mixture to become a jet stream. Typically, the Reynolds number (Re) of the jet stream was in the range of 50 to 250. The Re number is defined as:

$$Re = \frac{vD}{\nu} \qquad (3\text{-}2)$$

where v is the linear gas velocity, D is the diameter of the center hole of the graphite disc, and ν is the kinematic

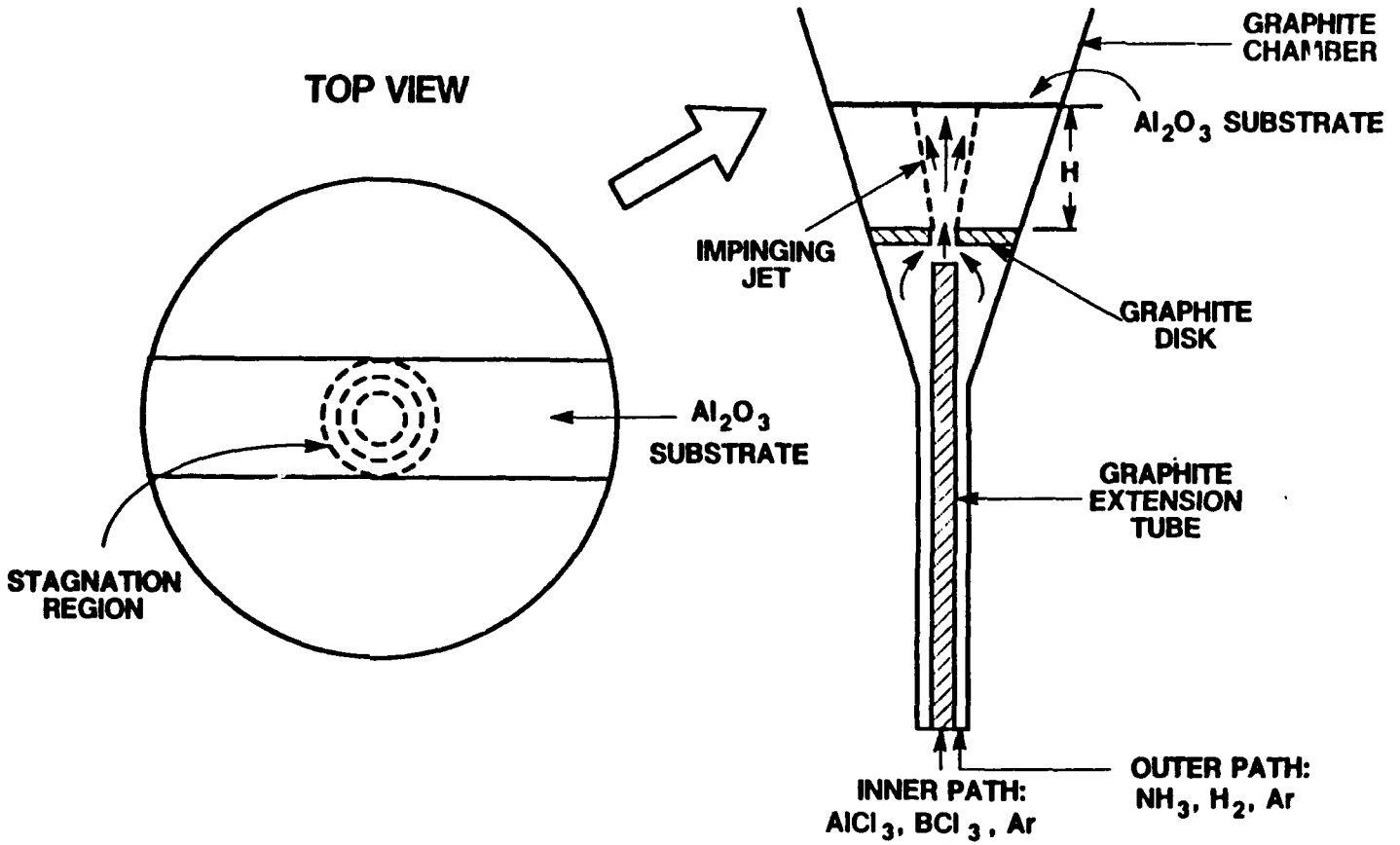

Figure 3-8. Impinging jet geometry I.

viscosity. Daily and Harleman [78] calculated that a round jet stream was laminar up to Re numbers of about 80. Shapiro [97] experimentally showed that the jet stream became fully turbulent when Re was about 5,000. Therefore, these studies suggested that our jet stream was basically laminar. When the Al_2O_3 substrate was placed perpendicular to the flow as shown in Figure 3-8, the impinging jet geometry could be assumed. Four different diameters of the center hole were used: (1) 0.635 cm, (2) 1.270 cm, (3) 1.5875 cm, and (4) 2.540 cm. The diameter of 1.5875 cm was extensively used due to various reasons as will be discussed momentarily. The distance from the disc to the substrate position, H, was fixed at 1.905 cm (see Figure 3-8). By employing this configuration which will be called "impinging jet geometry I", circular-shaped coatings were deposited inside the stagnation region (J-661 to J-747 and J-770 to J-781).

However, even with this geometry, accurate kinetic information could not be gathered because the reagent streams of BCl_3-$AlCl_3$-Ar and NH_3-Ar coming out of the inner- and outer-path tubes, respectively, could not be adequately mixed before reaching the substrate surface. The inadequate mixing resulted in undesired non-uniform coating patterns at the center region of the substrate (Note: Because of the mixing problem, the definition of the stagnation region becomes ambiguous.) For example, a multiple-ring-pattern consisting of variable coating color and thickness was usually observed

in the center region of the substrate suggesting that the coating characteristics changed significantly in the radial direction. Therefore, the one-dimensional analysis of the deposition data could not be used.

The mixing problem can be clearly illustrated by considering the Peclet number, Pe. Pe is defined here as:

$$Pe = \frac{vH}{D_i} \qquad (3\text{-}3)$$

where H is the distance from the mixing position to the substrate surface and D_i is the diffusion coefficient of gas species, i. When the Pe number is high and the jet stream is laminar, the gas species would not be fully mixed as the convective mass transfer in the vertical flow direction is much faster than the lateral diffusion of the gas species. In other words, the gas molecules will not have enough time to be fully mixed by molecular diffusion during their travel to the vicinity of the substrate by convection. For typical operating conditions used in the present investigation (e.g., about 30 to 150 torr, 700 to 1100°C, and 2400 cm^3/min at STP), the Pe number was higher than 5 as the Pe number could not be lowered any further because of various system limitations such as minimum operating pressure, geometrical dimensions, etc.

Two approaches were used to solve the reagent mixing problem. First, the diameter of the mixing disc hole, D, was decreased to 0.635 cm (J-751 to J-769) so that the hole

diameter was smaller than the outside diameter of the graphite extension tube (0.953 cm). For this configuration, it was hoped that the gas species would be mixed by the turbulence created by deflecting the NH_3 flow from the outer path toward the inner path as the NH_3 stream passed through the hole. However, the reduction in the hole diameter caused several undesired effects: (1) it appeared that the extent of homogeneous nucleation became more severe and (2) the deposition rate was too high to yield a uniform surface coating morphology. Therefore, the first approach was not fruitful.

In the second approach, the inner path stream was released through multiple small holes (10 in number and 0.238 cm in diameter) located on the side wall of the top section of the graphite extension tube as shown in Figure 3-9. The top end of the extension tube was sealed using graphite cement. This configuration, which will be called "impinging jet geometry II", yielded very uniform and circular-shaped coatings on the center part of the Al_2O_3 substrate (i.e., uniform stagnation region).

However, some undesired side-effects were observed. As the $AlCl_3$-BCl_3-Ar stream was released toward the graphite chamber wall (horizontally), a significant amount of coating could be deposited on the chamber wall. However, by flowing more Ar through the outer path than through the inner path (e.g., 2200 cm^3/min versus 150 cm^3/min), most of the

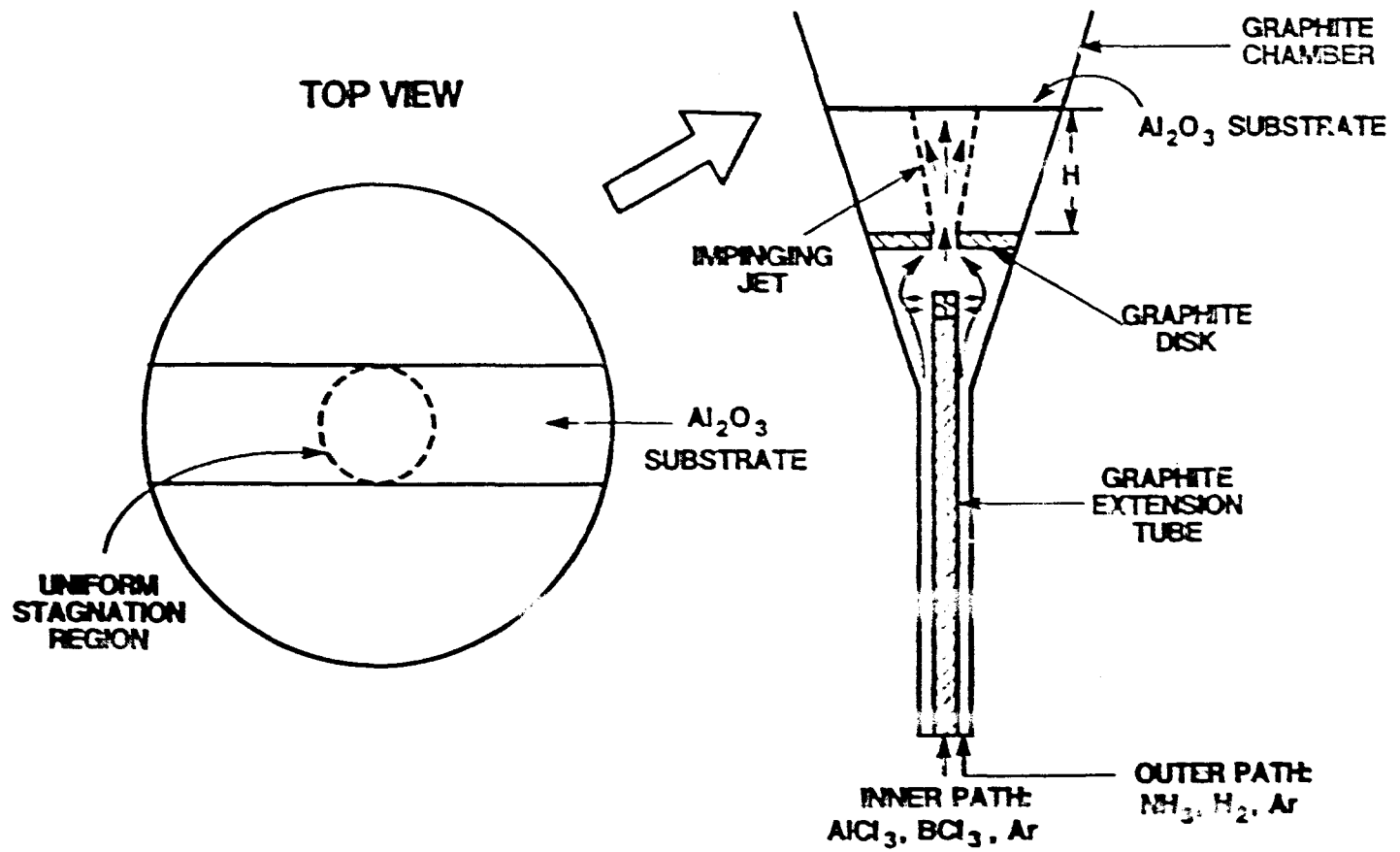

Figure 3-9. Impinging jet geometry II.

$AlCl_3/BCl_3/NH_3$ stream could be carried upward by the outer path stream without being deposited on the chamber wall. Also, it is important to note that some regions of the graphite mixing disc (mostly the area near the mixing hole) were coated in both impinging jet geometries I and II. However, the amount of coating on the graphite parts was not usually significant in comparison to that deposited on the Al_2O_3 substrate (less than 5%). Nevertheless, the coating on the graphite parts should be considered as one of the major uncertainties in obtaining accurate kinetic data. Most deposition data on the BN-, AlN-, and BN+AlN-CVD processes (J-799 to J-862), which have been extensively analyzed in Chapter V were obtained using this impinging jet geometry with a mixing hole diameter of 1.588 cm. The diameter of the stagnation region averaged about 1.5 cm.

Characterization Equipment and Procedure

X-ray Diffraction (XRD)

Coated substrates were X-rayed using a Philips 1800 automated diffractometer with monochromatic $Cu_{K\alpha}$ radiation operated at 40 KV and 30 mA. The Phillips diffractometer was equipped with a sample spinner which rotated the specimen during the diffraction measurement. The samples were scanned at steps of 0.015° for a period of 1.0 second at each step. Also, uncoated substrates were X-rayed for comparison purposes.

Scanning Electron Microscopy (SEM)

A Cambridge 150 Stereoscan scanning electron microscope was used to determine the coating thickness and analyze the surface morphology. The CVD coated substrates were coated with very thin films (e.g., less than about 20 nm) of carbon and Au/Pd by sputter deposition to minimize the charging of the highly insulating BN and AlN by the electron beam. The cross-section images of the CVD coatings were obtained by scribing and fracturing the coated substrate along its center line.

X-ray Photoelectron Spectroscopy (XPS)

The elemental surface composition (i.e., detection depth of less than 1 nm) and the chemical bonding information were obtained using an X-ray photoelectron spectrometer (Surface Science Laboratories, Model SSX-100).

Electron Microprobe

An electron microprobe analyzer (Acton MS-64 Microscope) was used to determine the elemental bulk composition (i.e., detection depth of about 1 μm). The CVD coatings were cross-sectioned and polished before the electron microprobe analyses were performed.

Transmission Electron Microscopy (TEM)

The TEM specimens were prepared by mechanical thinning to about 75 μm, dimpling, and ion beam milling with low energy (6 KeV) Ar^+ ions from the substrate side. The coatings were

examined using both JEOL 2000 FX and JEOL 4000 EX transmission electron microscopes.

Hardness Measurement

Coating hardness was measured using a Tukon Hardness Tester from Wilson Mechanical Instrument Division. The CVD coatings were cross-sectioned and polished before the hardness was measured at various spots along the coating direction.

CHAPTER IV

MODEL DEVELOPMENT

This chapter focuses on the development of a mathematical mass transfer model. The model describes transport of gas species in the impinging jet reactor geometry used in the present research. The mass transfer model is coupled with several possible surface kinetic mechanisms in order to illustrate how the model can effectively be used to interpret experimental data. In Chapter V, the model will used as a valuable tool to identify kinetic contributions in the BN-CVD, AlN-CVD processes. During development of the model many assumptions were made; these are explained in this chapter. Also, limitations of the model resulting from the assumptions are considered.

Major Assumptions

As illustrated in Figure 2-5 (p. 38), a comprehensive CVD model requires the integration of various mass transfer, kinetic, and nucleation and growth steps. As previously discussed in Chapter II, this type of modeling is not suitable for the CVD systems considered in the present investigation mainly because of the lack of accurate experimental data. However, some justifiable simplifications and assumptions can be introduced to formulate a much simpler, but realistic mass

transfer/kinetic model which will describe the CVD experimental arrangement used in the present investigation. The following paragraphs explain the major assumptions.

(1) An energy balance on the CVD reactor was not considered since it was assumed that temperature in the vicinity of the substrate was constant (i.e., uniform temperature profile). This is a fairly reasonable assumption since a hot-wall reactor is used. The temperature calibration studies discussed in Chapter III indicated that temperature at the deposition surface and in the gas phase differs by less than 50°C. The temperature gradient of less than 50°C is too small to induce any fluid motion or to significantly change physical properties of gas species. Also, it was calculated that the heat generated at the substrate surface as BN forms (i.e., exothermic reaction) would cause an adiabatic temperature rise of less than 30°C (assuming 100% conversion of BCl_3 to BN). Furthermore, in codeposition runs, this temperature increase is expected to be compensated by the slightly endothermic AlN reaction.

(2) Because of assumption (1), constant physical properties are assumed.

(3) Gas species are transferred from the nozzle (mixing hole shown in Figure 3-9) to their concentration boundary layer by convection only. This assumption is valid since the Peclet number, Pe, is much higher than one at typical

operating conditions (usually 5 to 50). The Peclet number is defined here as:

$$Pe = \frac{v\ H}{D_i} \qquad (4\text{-}1)$$

where v is the linear velocity of the fluid mixture, H is the distance from the nozzle to the deposition surface, and D_i is the diffusion coefficient of gas species i in the fluid stream. The Peclet number can be thought of as the ratio of rate of convective mass transfer rate over that of molecular diffusion in the flow direction.

(4) The rate of homogeneous reactions is negligible in comparison to that of heterogenous kinetic steps. This assumption is most critical in assuring the validity of the model. Several reasons are presented to justify the assumption. First, as mentioned in Chapter II, the nature or extent of homogeneous reactions occurring in the BN, AlN, and BN+AlN-CVD processes has not been reported in the literature. Therefore, gas phase chemistry involved in these processes is currently not known. Second, an in-situ study of high temperature CVD environments can not be readily performed due to many technical difficulties and material limitations. At temperatures above 450°C, mass spectroscopy with a delicate sampling technique (e.g., Knudsen cell chamber

with an orifice probe, which is differentially-pumped) and laser Raman spectroscopy are the only two known methods which would allow the identification of gaseous species in the CVD environments. In facing this dilemma, some investigators took an approach in which they first guessed plausible homogeneous kinetic mechanisms and fitted kinetic parameters empirically to match experimental data. However, as discussed in detail in Chapter II, it seems that this "empirical fitting" approach introduces uncertainties as well as difficulties in representing the true physicochemical nature of the CVD processes. During the present investigation, the effects of homogeneous reactions on deposition behavior are assumed to be negligible. Physically, the assumption is not that unrealistic. The rate of homogeneous reactions is usually much lower than that of heterogenous reactions at typical CVD conditions as already discussed in Chapter II. Also, even if intermediate species (e.g., BHCl, AlCl, etc.) are generated by homogenous reactions, they would not have drastically different physical properties or mass transfer characteristics in comparison to the original reagents ($AlCl_3$ and BCl_3). Therefore, the intermediates and reagents are assumed to behave similarly as they diffuse through the boundary layer.

(5) Because of assumption (4), homogenous nucleation of non-volatile products is not expected to occur in the gas

phase. Also, in order to ensure the validity of the assumption, processing conditions under which homogeneous nucleation was observed are experimentally determined as will be described in Chapter V.

(6) The diffusion of BCl_3 through the concentration boundary layer and the surface kinetic steps involving BCl_3 are two processes in series, which determine the overall BN deposition rate. The same assumption applies to $AlCl_3$ for the AlN deposition rate. As reviewed in Chapter II, the BN and AlN deposition processes are not strongly influenced by NH_3 as long as an excess amount of NH_3 is present. For all experiments performed in the present research, a ratio of $NH_3/AlCl_3$ or NH_3/BCl_3 higher than 2.5 was always used.

(7) The Stefan-Maxwell equations required for a multi-component diffusion process are not used since the reactant mixture typically contains more than 98% Ar (i.e., pseudo-binary mixture). Thus, the binary diffusion coefficients can be used to describe the molecular diffusion of BCl_3 and $AlCl_3$ in the fluid mixture. From this point, D_i denotes the binary diffusion coefficient of gas species i in Ar.

(8) Heterogeneous nucleation and growth steps are fast. This assumption was already explained in Chapter II.

The physical significance of assumptions (1) to (8) is schematically illustrated in Figure 4-1. It is assumed that

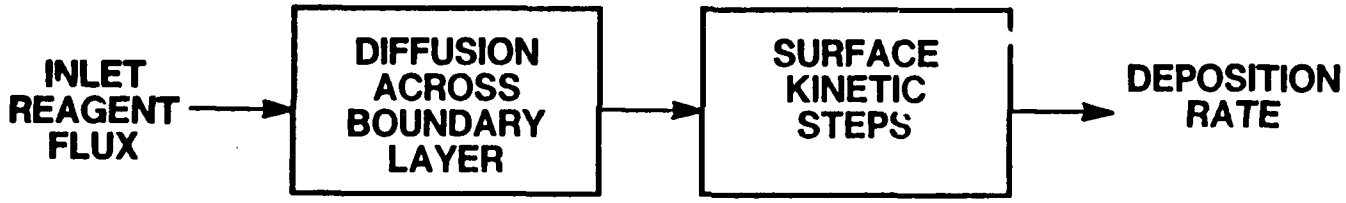

Figure 4-1. Simplified CVD model.

the BN-CVD and AlN-CVD processes can be described by considering: (1) mass transfer of the reagent gas species $AlCl_3$ and BCl_3 to the deposition surface from the reactor inlet and (2) subsequent heterogeneous kinetic steps involving the reagent species at the surface.

Hydrodynamics and Mass Transfer

As described in Chapter II, when a jet stream impinges upon a flat substrate, a stagnation region forms along the substrate surface (Figure 4-2). Inside the stagnation region, mass transfer is independent of the radial direction. Therefore, a one-dimensional analysis along the flow direction (i.e, z-axis) is adequate to describe mass transfer characteristics inside the stagnation region. Chin and Tsang [76] determined that the diameter of the stagnation region was about 1/2 the nozzle diameter, d, for laminar jets and less than 1 the nozzle diameter for turbulent jets. Within the stagnation region, a momentum boundary layer with a constant thickness, δ_m, exists along the radial direction. The governing Navier-Stokes equations were previously derived and solved with the assumption of axisymmetric stagnation flow [77]. The resulting boundary layer solutions are well documented by Schlichting [77] and therefore are not iterated here.

When gas species are depleted or consumed at the substrate surface due to chemical reactions, adsorption,

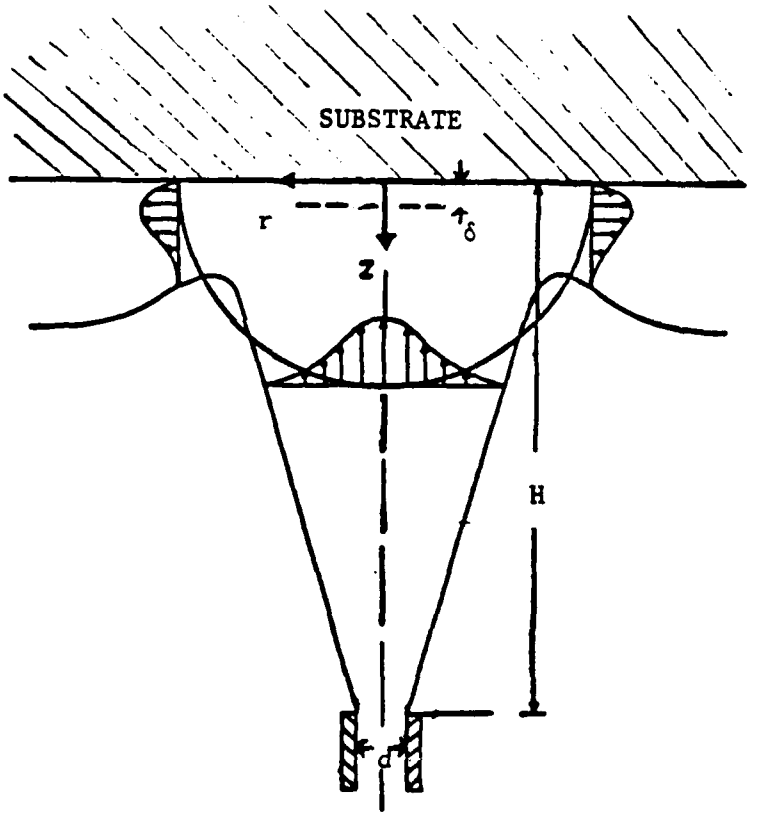

Figure 4-2. A stagnation region, in which mass transfer is independent of radial direction, develops when a jet stream is impinged upon a flat substrate surface for r/d < 1 [76].

nucleation, etc., a concentration boundary layer develops for each gas species along the substrate surface. The concentration boundary layer for species i with a thickness of δ_i is portrayed in Figure 4-3. At a steady state, the rate of mass transfer for species i, J_i, across the concentration gradient can be determined using Fick's law:

$$J_i = - \frac{D_i}{RT} \left(\frac{dP_i}{dz} \right) \quad \text{at } z=0 \tag{4-2}$$

or empirically

$$J_i = \frac{K_i}{RT} (P_i^\circ - P_i^*) \tag{4-3}$$

where K_i is the overall mass transfer coefficient in the stagnation region, D_i is the diffusion coefficient of gas species i in the fluid stream, and P_i° and P_i^* are the partial pressures at $z= \delta_i$ and $z=0$, respectively. Chin and Tsang [76] solved momentum and mass balance equations numerically and determined the mass transfer coefficient, K_i, to be:

$$K_i = 0.85002 \, D_i \sqrt{a/\nu} \, Sc_i^{1/3} \, g(Sc_i) \tag{4-4}$$

$$\text{for } Sc_i > 0.7$$

where a is a hydrodynamic constant which has a unit of sec^{-1}, ν is the kinematic viscosity of the fluid, Sc_i is the Schmidt number which is defined as ν/D_i, and $g(Sc_i)$ is an asymptotic

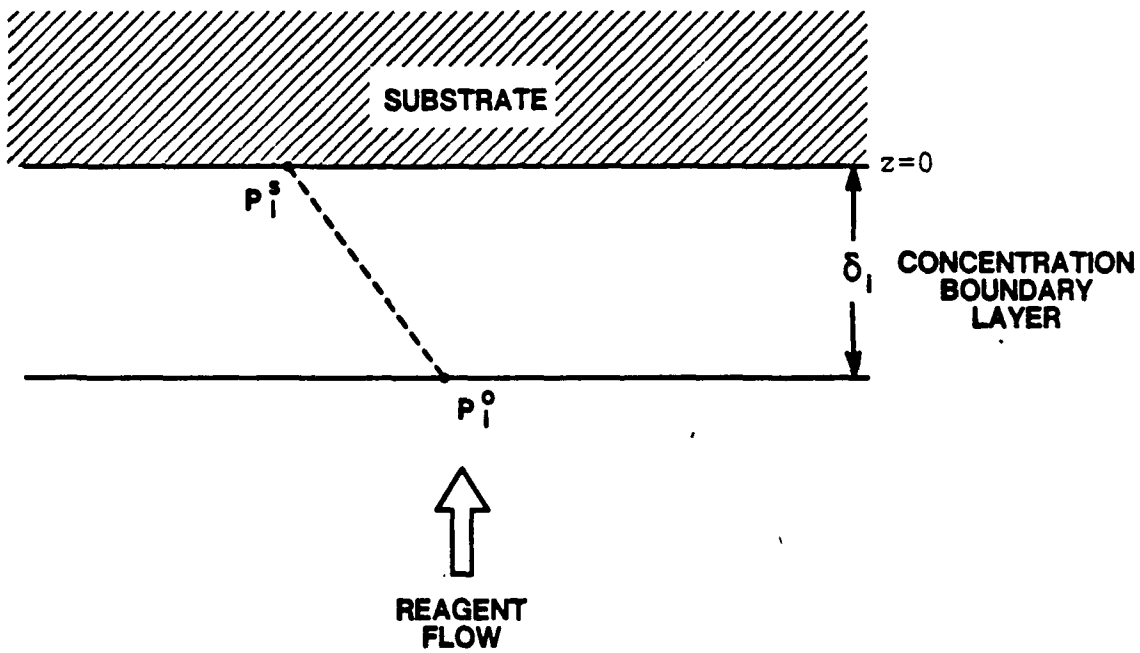

Figure 4-3. Illustration of mass transfer inside stagnation region.

series of Sc_i such that:

$$g(Sc_i) = \left(1 - \frac{0.084593}{Sc_i^{1/3}} - \frac{0.016368}{Sc_i^{2/3}} \right. \qquad (4\text{-}5)$$

$$\left. - \frac{0.0057398}{Sc_i} + \frac{0.0014288}{Sc_i^{4/3}} + \ldots \right)$$

In order to illustrate the physical meaning of the mass transfer coefficient, K_i, Eq. 4-4 can be rewritten:

$$K_i = \frac{D_i}{\delta_i} \qquad (4\text{-}6)$$

where

$$\delta_i = \frac{1.176 \sqrt{\nu/a}}{Sc_i^{1/3}\, g(Sc_i)} \qquad (4\text{-}7)$$

Thus, Eq. 4-3 can also be expressed as:

$$J_i = \frac{D_i}{\delta_i RT} (P_i^\circ - P_i^s) \qquad (4\text{-}8)$$

The physical interpretation of Eq. 4-8 is that the main mechanism for the mass transfer flux across δ_i is molecular diffusion. But, it is important to note that the overall flux, J_i, still depends on the δ_i value, which can be thought of as the convective contribution to the overall flux. The δ_i value increases with decreasing the volumetric flow rate or linear gas velocity.

Using Eq 4-8, the steady state mass transfer flux from the bulk gas phase to the deposition surface can be estimated if P_i^s is known. There are two possible extreme situations in which P_i^s will be determined: (1) surface kinetics, if the surface kinetic steps are slow or (2) thermodynamics, if the kinetic steps are very fast (i.e., $P_i^s = P_i^{eq}$). The first scenario will be called "mass transfer-kinetic model" whereas the mass transfer rate calculated from the second case will be called "mass transfer-thermodynamic limits." First, in order to understand the mass transfer-kinetic model, a simple surface kinetic mechanism is considered. In this mechanism, it is assumed that the rate of consumption of species i at the surface has the first-order relationship with respect to the gas species i. The rate of consumption of gas species i is:

$$J_i = \frac{k_i}{RT} P_i^s \qquad (4\text{-}9)$$

and

$$k_i = k_o \exp(-\Delta E/RT) \qquad (4\text{-}10)$$

where k_i is the first-order kinetic rate constant in cm/s, k_o is the frequency factor, and ΔE is the intrinsic activation energy. The substitution of Eq. 4-9 into Eq. 4-8 gives:

$$J_i = \frac{P_i^\circ/RT}{\delta_i/D_i + 1/k_i} \qquad (4\text{-}11)$$

All the variables on the right hand side of Eq. 4-11 except k_i can be determined from either processing conditions or equations derived earlier. The magnitude of k_i should be determined experimentally.

Although the above derivation is based on a simplified process description, it provides a fundamental basis for understanding the CVD process. The terms δ_i/D_i and $1/k_i$ can be thought of as "diffusion resistance" and "kinetic resistance" to the process, respectively. In other words, the process is limited by diffusion if δ_i/D_i is larger than $1/k_i$ and is kinetically controlled if the reverse case is true. As can be seen from Eq 4-10, k_i has an exponential dependence on temperature whereas D_i/δ_i is a weak function of temperature ($D_i/\delta_i \propto T^{1.656}$). Therefore, in most CVD processes, deposition rate increases exponentially with temperature in a low temperature region. The process is then said to be "kinetically-controlled." At higher temperatures the process becomes limited by a slow increase in the diffusional flux resulting in near saturation of the deposition rate (i.e, diffusion-limited).

For the situation in which the surface kinetic steps are very fast, the steady state mass flux (or "mass transfer-thermodynamic limits") becomes simply:

$$J_i = \frac{D_i}{\delta_i RT} (P_i^\circ - P_i^{eq}) \qquad (4\text{-}12)$$

P_i^{eq} can be rather easily calculated using the computer code SOLGASMIX [59] with the assumption of "local equilibrium" being established at the substrate surface. The SOLGASMIX program was briefly described in Chapter II. Physically, the mass transfer-thermodynamic limits can be thought of as the maximum deposition rate which can be obtained from a CVD process via the heterogenous mechanism as long as the extent of homogeneous reactions is not too great. The computational procedure for determining P_i^{eq} is illustrated in detail in the next section.

Computation

This section introduces correlations used to estimate various physical properties of the reagent species and fluid mixture. Also, the computational procedures used to calculate the steady state mass flux, J_i, for both the kinetically- and thermodynamically-limited situations are described.

The theory of Chapman and Enskog works well in low pressure and high temperature conditions [98] and therefore is ideal for CVD environments. The Chapman and Enskog viscosity equation was used to determine the viscosity of gas species i.

$$\eta_i = 26.69 \times 10^{-6} \frac{\sqrt{M_i T}}{\sigma_i^2 \Omega_v} \qquad (4\text{-}13)$$

where η_i is the viscosity in poise (P or g/sec/cm), M_i is the

molecular weight, T is temperature in K, σ_i is the molecular diameter in Å, and Ω_v is the collision integral. M_i and σ_i values for the reagents used in the present study are listed in Table 4-1. The collision integral, Ω_v, accounts for the intermolecular forces and is given by [98]:

$$\Omega_v = \frac{A}{T^{*B}} + \frac{C}{\exp DT^*} + \frac{D}{\exp FT^*} \qquad (4\text{-}14)$$

and

$$T^* = \frac{kT}{\epsilon_i} \qquad (4\text{-}15)$$

$$A = 1.16145,\ B = 0.14874,\ C = 0.52487,$$

$$D = 0.77320,\ E = 2.16178,\ F = 2.43787$$

where k is Boltzman's constant and ϵ_i is the characteristic energy. The ϵ_i/k ratio is tabulated in Table 4-1. Also, the theory of Chapman and Enskog can be extended to estimate the viscosity of a low-pressure multicomponent gas mixture [98]:

$$\eta_m = \sum_{i=1}^{n} \frac{x_i \eta_i}{\sum_{j=1}^{n} x_i \varphi_{ij}} \qquad (4\text{-}16)$$

where x_i is the mole fraction of gas species i in the fluid mixture and φ_{ij} is determined by using the Wilke's approximation [98]:

$$\varphi_{ij} = \frac{[1+(\eta_i/\eta_j)^{1/2}(M_j/M_i)^{1/4}]^2}{[8(1+M_i/M_j)]^{1/2}} \qquad (4\text{-}17)$$

Table 4-1. Physical and thermochemical properties of reagents [98].

Reagents	ϵ/k(K)	d(Å)	M(g/mole)
BCl_3	337.7	5.127	117.17
$AlCl_3$	524.0	5.5	133.34
NH_3	558.3	2.900	17.03
Ar	93.3	3.542	39.95
H_2	59.7	2.827	2.01

where η_m is the viscosity of the gas mixture. The average density of the reagent gas mixture is calculated using the ideal gas law:

$$\rho = \frac{PM_{av}}{RT} \tag{4-18}$$

and

$$M_{av} = \sum_{i=1}^{n} x_i M_i \tag{4-19}$$

The kinematic viscosity of the mixture is simply:

$$\nu = \eta_m/\rho \tag{4-20}$$

The linear velocity of the fluid mixture is:

$$v = \frac{Q}{(\pi/4)d^2} \tag{4-21}$$

where Q is the volumetric flow rate and d is the diameter of the nozzle (mixing hole in Figure 3-9). The Reynolds number is defined as:

$$Re = \frac{vd}{\nu} \tag{4-22}$$

Also, the characteristic length, H^*, is defined as:

$$H^* = H/d \tag{4-23}$$

where H is the distance from the nozzle to the substrate surface. The hydrodynamic constant, a, introduced in Eqs. 4-4 and 4-7 can now be determined using a correlation given in Chin and Tsang [76]:

$$a = \frac{a^* v}{d} \tag{4-24}$$

and

$$a^* = 1.5129 H^{*-0.204} \tag{4-25}$$

The Chapman and Enskog theory, which was used to estimate viscosity, can be used to describe molecular diffusion of gas species in the fluid mixtures [98]. In the first section of this chapter, it was assumed that the reagent stream could be thought of as binary mixtures of species i in Ar. With this assumption, the Chapman and Enskog equation becomes [98]:

$$D_i = 1.858 \times 10^{-3} \, T^{3/2} \frac{[(M_i + M_{Ar})/M_i M_{Ar}]^{1/2}}{P \, \sigma_{i\text{-}Ar}^2 \, \Omega_D} \tag{4-26}$$

and

$$\Omega_D = \frac{A}{T^{*B}} + \frac{C}{\exp DT^*} + \frac{D}{\exp FT^*} + \frac{G}{\exp HT^*} \tag{4-27}$$

$$A = 1.06036, \; B = 0.15610, \; C = 0.19300$$

$$D = 0.47635, \; E = 1.03587, \; F = 1.52996$$

$$G = 1.76474, \; H = 3.89411$$

and

$$T^* = kT/\epsilon_{i\text{-}Ar} \qquad (4\text{-}28)$$

where D_i is the diffusion coefficient of gas species i in Ar in cm^2/sec, T is temperature in K, P is pressure in atm, $\sigma_{i\text{-}Ar}$ is the characteristic diameter of the binary mixture in Å, Ω_D is the diffusion collision integral, k is Boltzman's constant, and $\epsilon_{i\text{-}Ar}$ is the characteristic energy of the binary mixture. The following rules were used to determine $\sigma_{i\text{-}Ar}$ and $\epsilon_{i\text{-}Ar}$:

$$\epsilon_{i\text{-}Ar} = (\epsilon_i \ \epsilon_{Ar})^{1/2} \qquad (4\text{-}29)$$

$$\sigma_{i\text{-}Ar} = (\sigma_i + \sigma_{Ar})/2 \qquad (4\text{-}30)$$

A computer code, *CVDWYL*, was written to calculate J_i (when $P_i^* = 0$) as a function of T, P, x_i and Q using Eqs. 4-3 to 4-30. The program is printed in APPENDIX. By choosing the concentration boundary layer as a system boundary and performing a mass balance around the system, the flux when $P_i^* = 0$ can be thought of as the rate of mass transfer into the system, $J_{i,in}$. The overall mass balance at a steady state is:

$$J_{i,in} - J_{i,out} = J_{i,consumed} \text{ or } J_{i,net} \qquad (4\text{-}31)$$

For the kinectically-controlled process, $J_{i,net}$ equals J_i as given by Eq. 4-11. As explained earlier, k_i should be determined experimentally. For the thermodynamically/ diffusion-limited process, $J_{i,out}$ becomes $J_{i,eq}$ which is the mass flux at equilibrium. $J_{i,in}$ is calculated using CVDWYL and

therefore the mole fraction of species i into the system, $x_{i,in}$, can be determined. Furthermore, $x_{i,in}$ is input to the SOLGASMIX program to determine $x_{i,eq}$. Therefore, for the thermodynamically/diffusion-limited process, the net rate of mass transfer at the steady state becomes:

$$J_{i,net} = J_{i,in} - J_{i,eq} \tag{4-32}$$

or

$$= \frac{D_i P}{\delta_i RT} (x_i^\circ - x_i^{eq}) \tag{4-33}$$

or

$$= \frac{D_i}{\delta_i RT} (P_i^\circ - P_i^{eq}) \tag{4-12}$$

The models derived in this chapter will be compared to experimental data in Chapter V. Also, the merits of the models will be discussed.

CHAPTER V

RESULTS AND DISCUSSION

In this chapter, the morphology and microstructure of BN, AlN, and BN+AlN coatings will be reported and their dependence on processing conditions will be addressed. For the BN-CVD and AlN-CVD processes, their deposition mechanisms are identified and discussed. The insights provided by the kinetic and characterization studies on the BN-CVD and AlN-CVD systems are utilized to interpret the experimental data obtained from the BN+AlN-CVD process and subsequently its physicochemical nature.

BN-CVD

Nineteen BN deposition experiments using Al_2O_3 substrates were performed as described in Table 5-1. The crystalline structure of the BN coatings as determined by XRD is also listed in Table 5-1. The first nine experiments (J-164 through J-619) were performed using the vertical suspension geometry (Figure 3-7). These preliminary experiments were performed to determine "suitable" processing conditions for depositing high quality BN films. The last ten experiments (J-8xx series) were performed using the impinging jet geometry (Figure 3-9) in order to study the kinetics of the BN-CVD system. First, the morphology and crystalline structure of

Table 5-1. Experimental conditions for BN-CVD experiments and crystalline structure of BN coatings determined by XRD.

Sample #	T (°C)	P (torr)	Flow Rates (cm^3/min)				Run Time (min)	Mixing Length* (cm)	Geometry**	Coating Thickness (μm)***	Crystallinity****
			BCl_3	NH_3	H_2	Ar					
J-164	1200	760	25	100	15	500	60	15	V	-	TBN
J-170	1200	760	25	425	25	200	60	15	V	-	TBN
J-175	1200	75	25	100	25	500	60	15	V	-	TBN
J-618	700	150	10	50	-	400	60	5	V	-	TBN
J-615	900	150	10	50	-	400	60	5	V	-	TBN
J-556	1100	150	10	50	-	400	60	15	V	-	TBN
J-606	1100	150	10	50	-	400	60	5	V	-	TBN
J-609	1100	150	10	50	50	400	60	5	V	-	TBN
J-619	1300	150	10	50	50	400	60	5	V	-	-
J-802	800	40	6	30	-	2364	40	3	I	1.1	TBN
J-808	900	40	6	30	-	2364	40	3	I	2.5	TBN
J-803	1000	40	6	30	-	2364	40	3	I	14.0	TBN
J-804	1100	40	6	30	-	2364	40	3	I	HN *****	TBN
J-805	1100	40	3	30	-	2367	40	3	I	HN *****	TBN
J-810	900	40	12	30	-	2358	40	3	I	6.0	TBN
J-812	900	40	18	30	-	2352	40	3	I	10.0	TBN
J-800	900	30	6	30	-	2364	20	3	I	1.2	TBN
J-816	900	80	6	30	-	2364	40	3	I	5.4	TBN
J-818	900	150	6	30	-	2364	40	3	I	10.5	TBN

* Distance from the mixing position of BCl_3 and NH_3 to the substrate.

** V = vertical suspension geometry shown in Figure 3-7; I = impinging jet geometry shown in Figure 3-9.

*** Coating thickness was measured from fracture surface SEM micrographs.

**** TBN = Turbostratic BN.

***** Homogenous Nucleation.

the BN coatings will be reported in this section. Second, heterogeneous deposition mechanism(s) of the BN-CVD process will be evaluated and discussed.

Deposition Behavior

Impinging Jet Geometry. SEM micrographs in Figures 5-1 through 5-8 show the fracture surface and surface morphology of BN coatings deposited on Al_2O_3 using the impinging jet geometry. In general the coatings appeared to be dense and very adherent to the Al_2O_3 substrates. For each sample, the average coating thickness was measured from the fracture surface micrographs, and was later used to calculate deposition rate. All the micrographs were taken within the stagnation coating region (see Figure 3-9). The coating thickness was relatively uniform in the stagnation region (i.e., less than 5% variation from the average thickness as determined by SEM).

As shown in Figures 5-1 through 5-8, the coatings' surface morphology appeared to be fairly smooth except for the appearance of "nodules". The nodules referred to here are hemispherical or dome-shaped growth features observed in the micrographs. The average nodule size steadily increased with an increase in the coating thickness (or deposition rate). For example, when the coating thickness was about 1 μm (Figure 5-1; J-802), the average nodule size was about 1.5 μm. However, the average nodule size increased to about 4 μm as the coating thickness increased to near 14 μm (Figure 5-3, J-

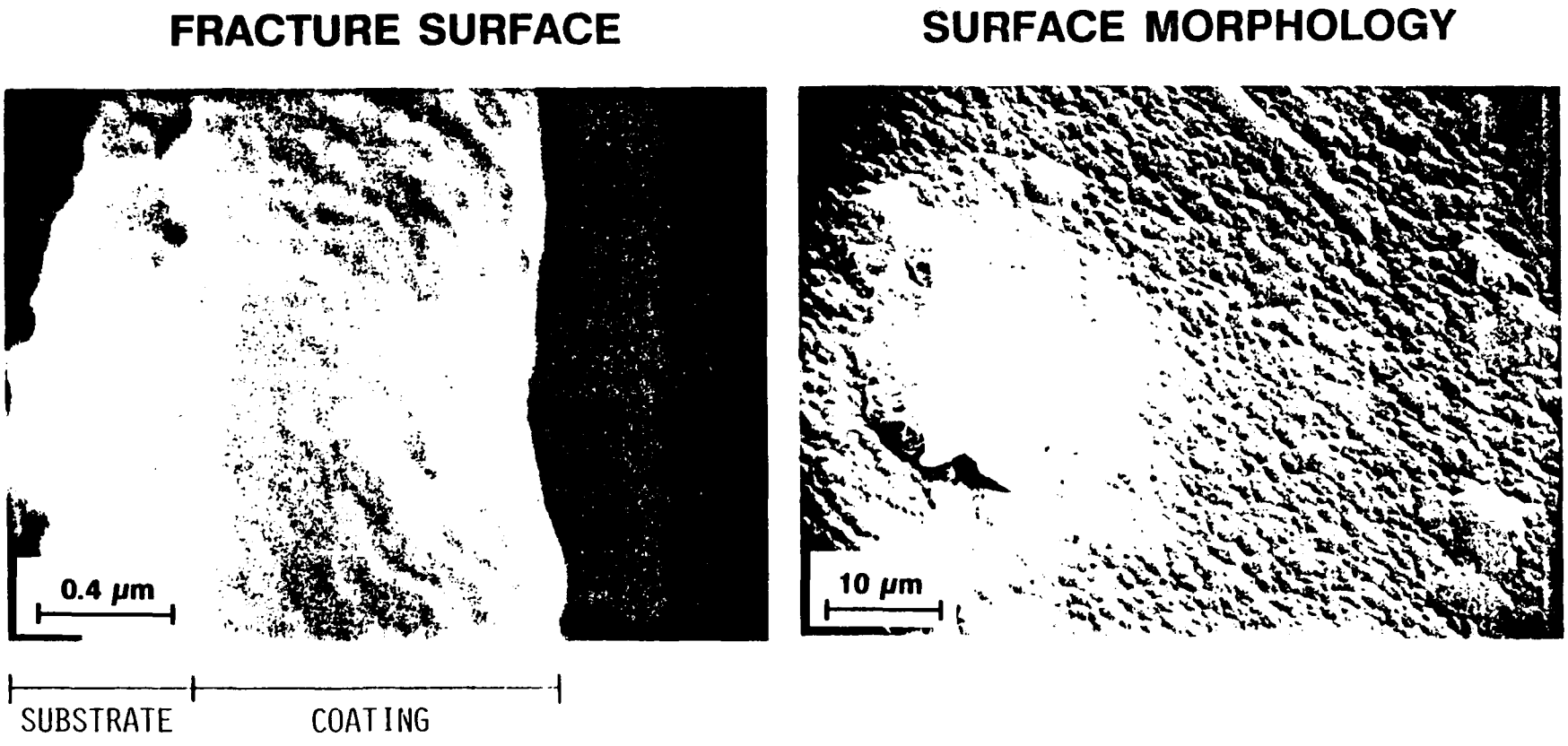

Figure 5-1. SEM micrographs of BN (J-802).

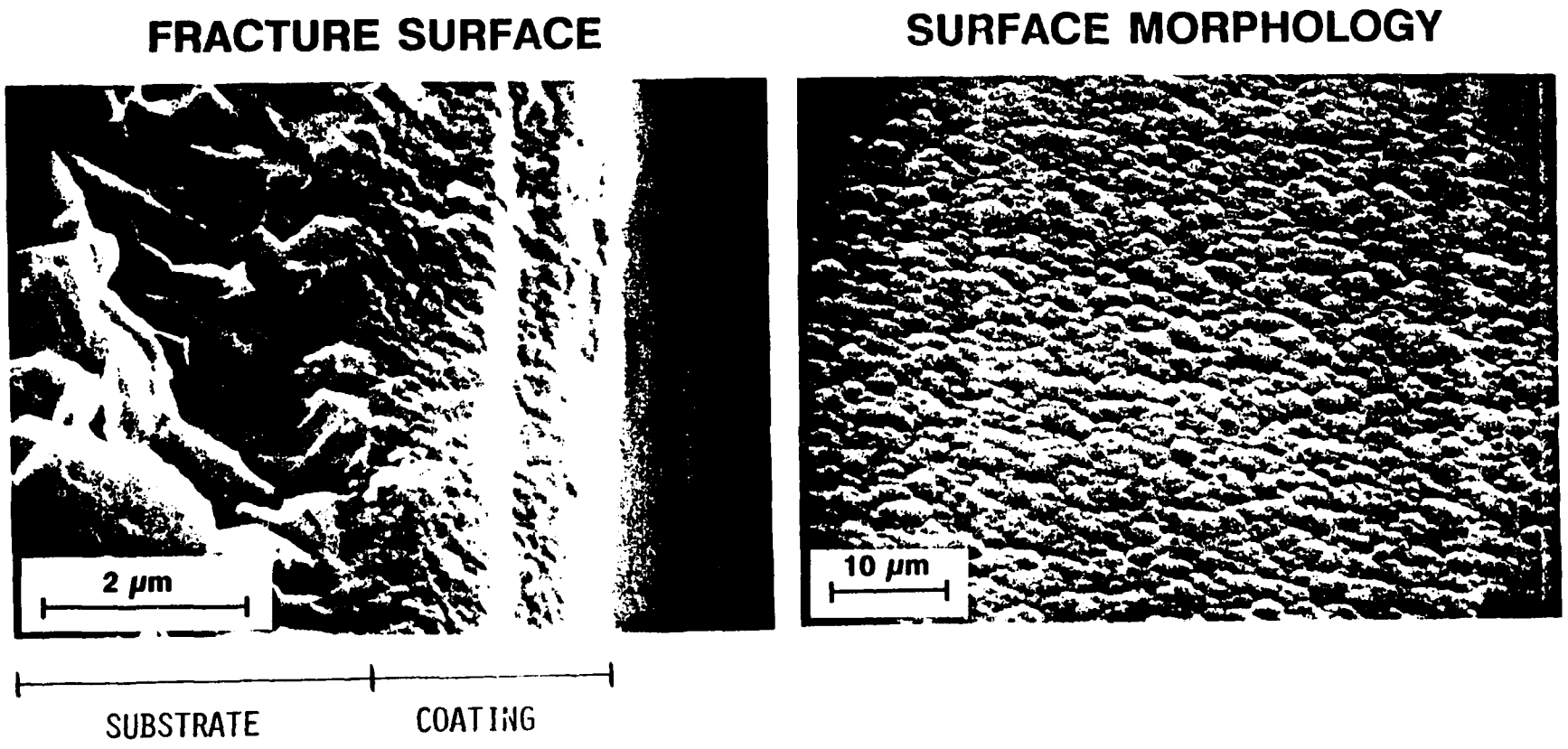

Figure 5-2. SEM micrographs of BN (J-808).

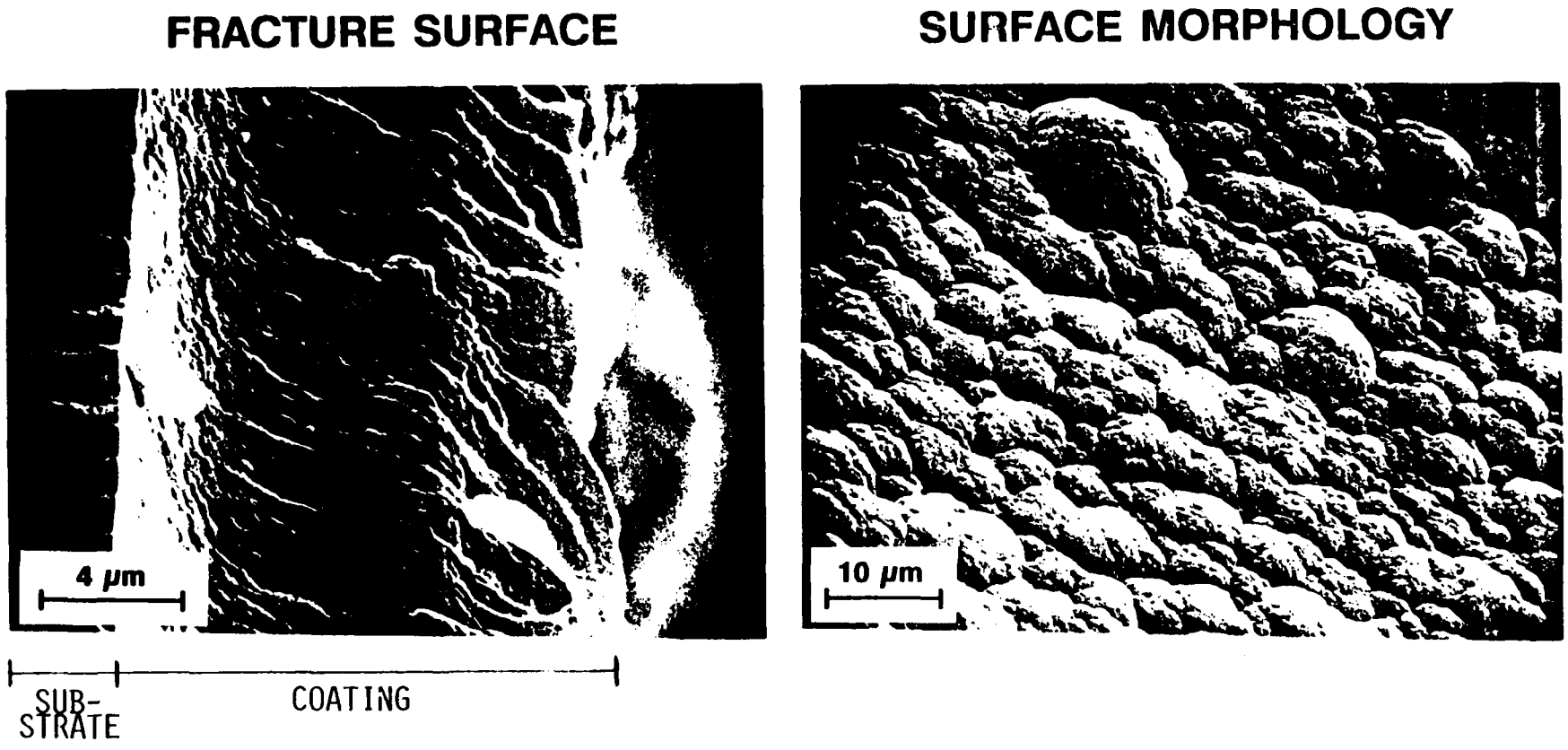

Figure 5-3. SEM micrographs of BN (J-803).

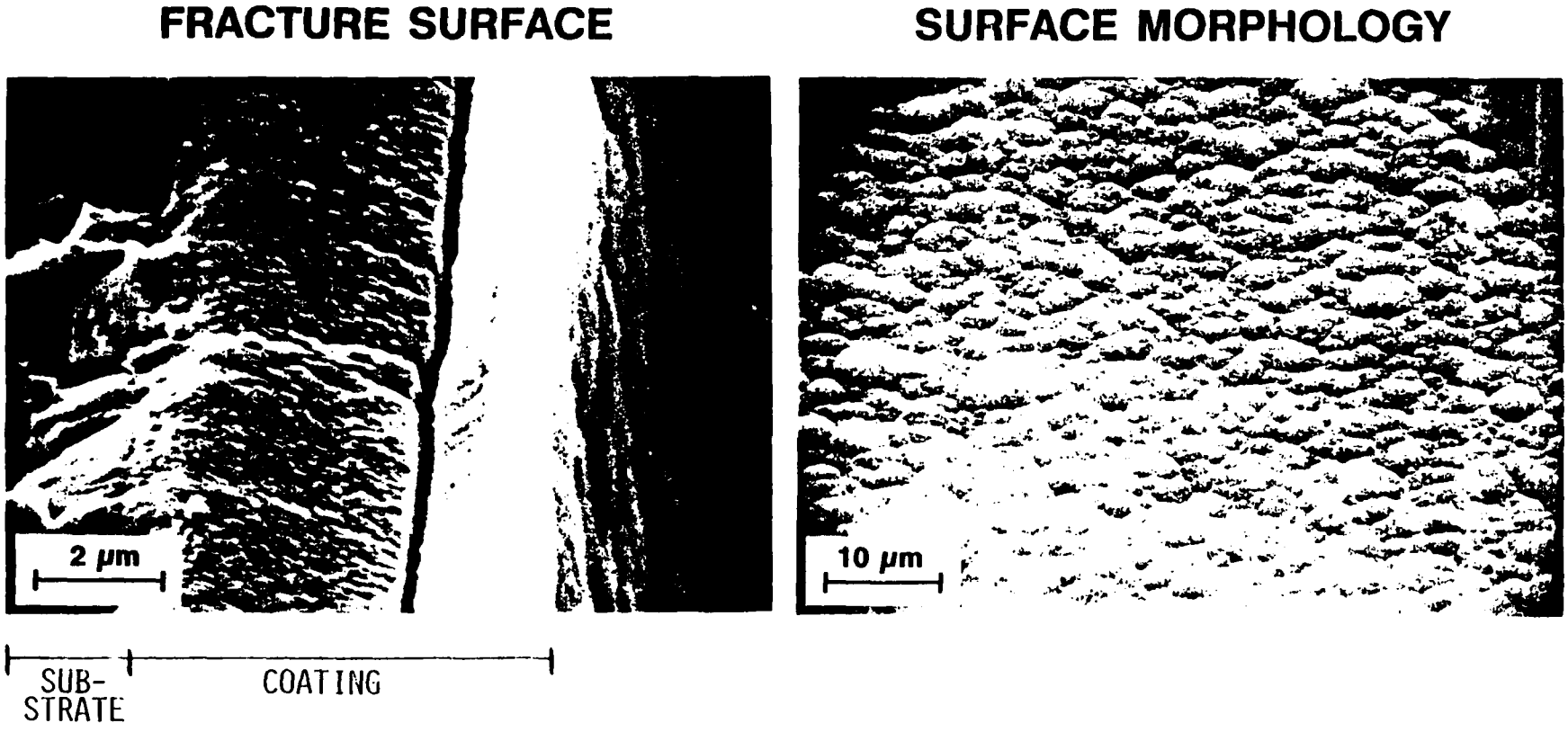

Figure 5-4. SEM micrographs of BN (J-810).

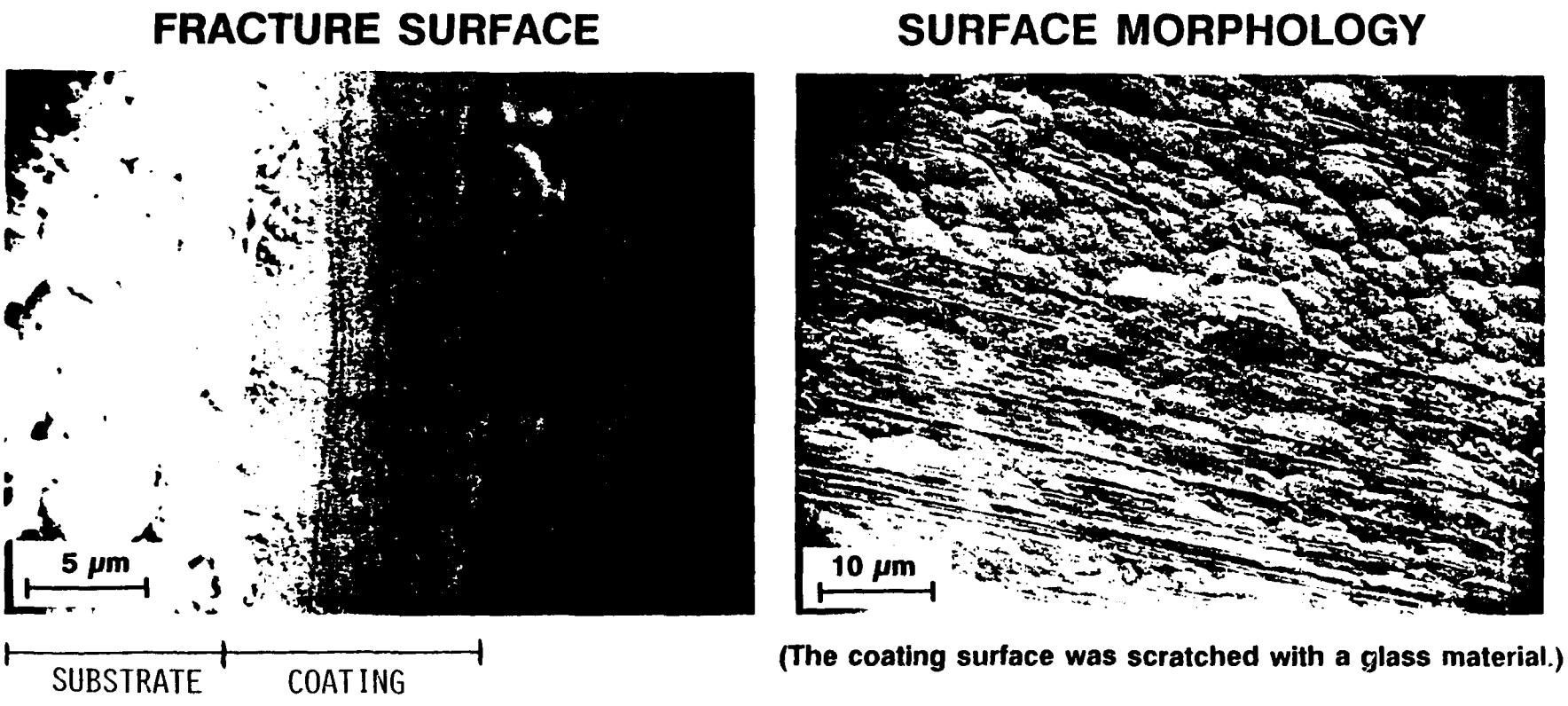

Figure 5-5. SEM micrographs of BN (J-812); the coating surface was scratched with a glass material.

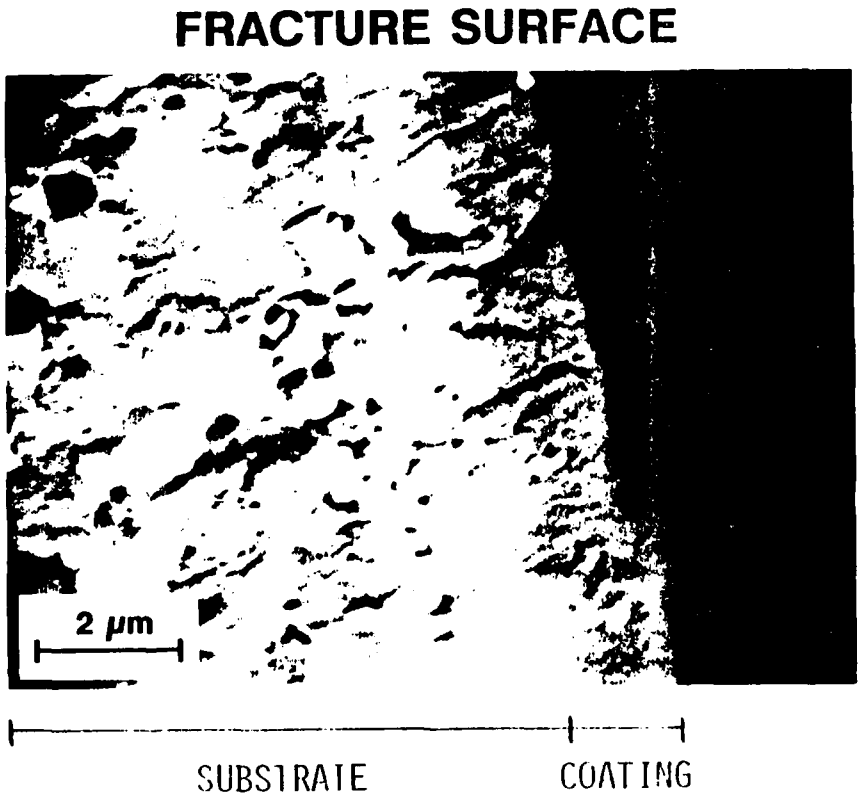

Figure 5-6. SEM micrograph (backscattered) of BN (J-800).

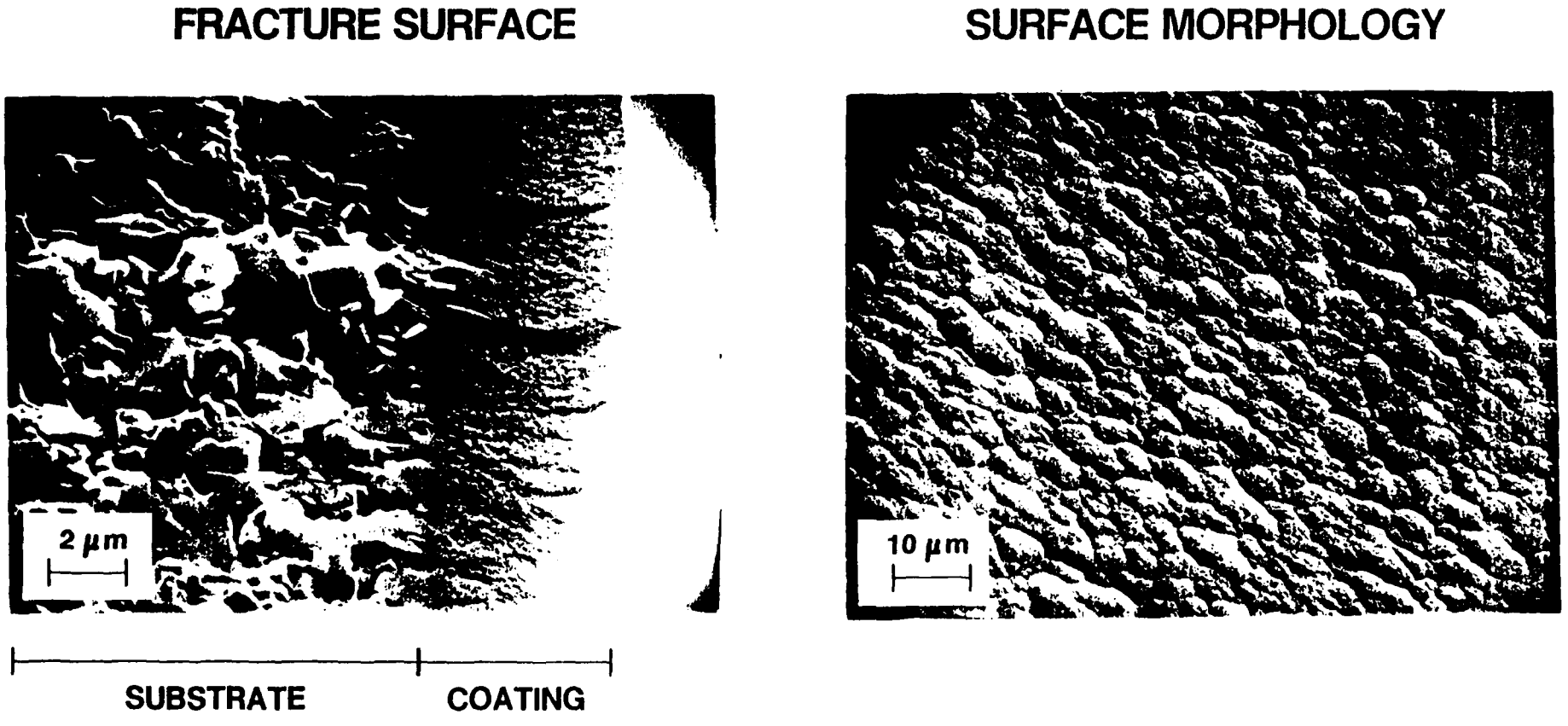

Figure 5-7. SEM micrographs of BN (J-816).

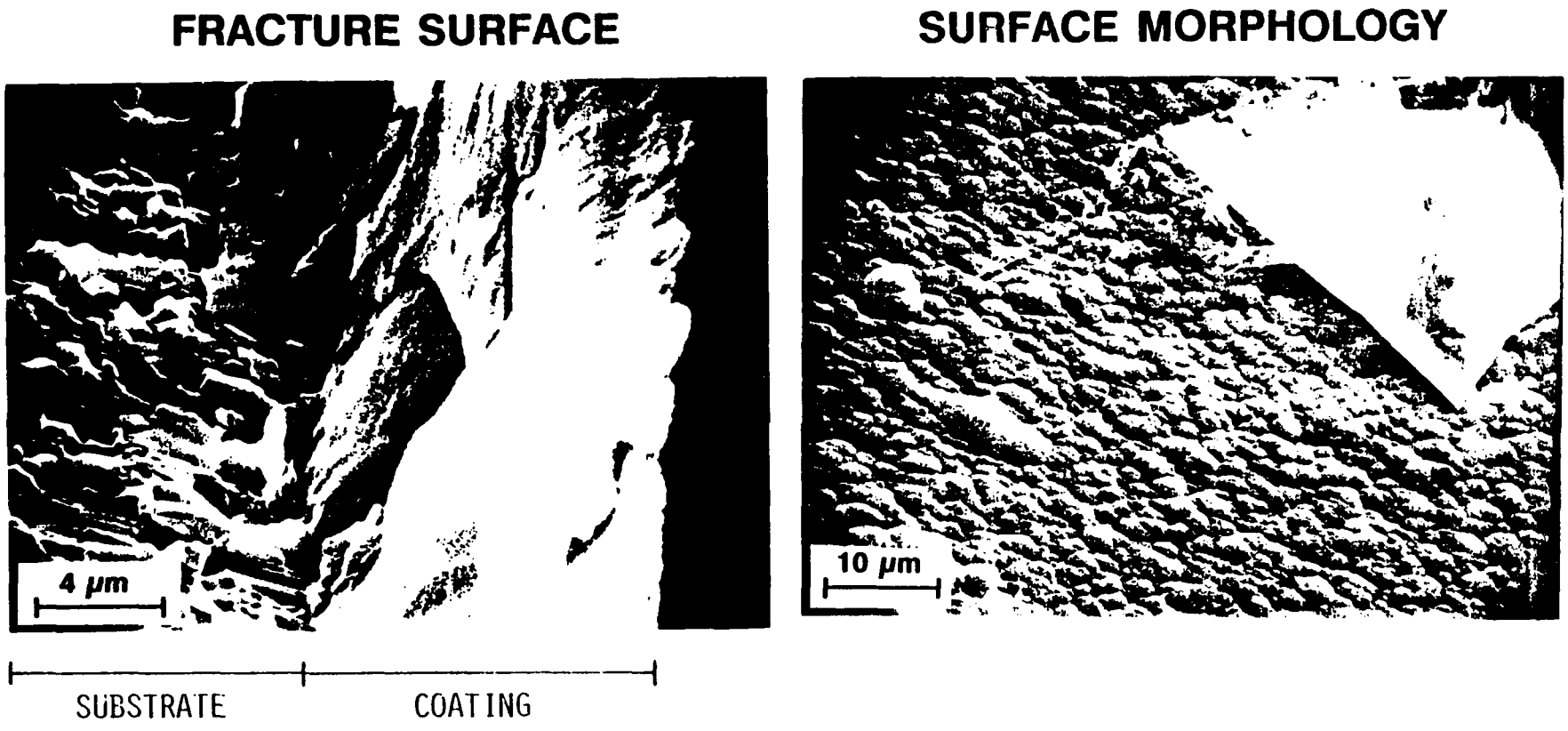

Figure 5-8. SEM micrographs of BN (J-818).

803). The increase in the nodule size with the coating thickness suggested that BN grew in a conical fashion. The BN surface was fairly soft and therefore could easily be scratched by glass as shown in Figure 5-5. Sometimes cracked regions in the coatings were observed (Figure 5-4). The cracks were probably caused by the thermal expansion coefficient mismatch between the BN coating and Al_2O_3 substrate.

In most instances, morphological features of BN looked very similar to that of the Al_2O_3 substrate, especially for BN deposited near the initial substrate surface. The backscattered electron micrograph shown in Figure 5-6 was a clear example of this behavior. Without using the backscattered mode, the thin BN coating of 1.2 μm and the Al_2O_3 substrate could not be easily distinguished. Also, other micrographs (see Figures 5-2, 5-4, and 5-7) supported the observation that BN tended to "copy" the Al_2O_3 substrate morphology during the initial stages of the deposition process.

XRD spectra of the BN coatings are shown in Figures 5-9 through 5-11. Also, the XRD patterns of pyrolytic BN (PBN, Union Carbide Corporation) and uncoated Al_2O_3 substrate (MRC) are included in Figure 5-9 for comparison purposes. A very broad (002) peak (or hump) corresponding to the turbostratic BN structure [14,18] was observed from the XRD spectra. Also, minor BN peaks (10x; x=0,1) appeared as another broad hump

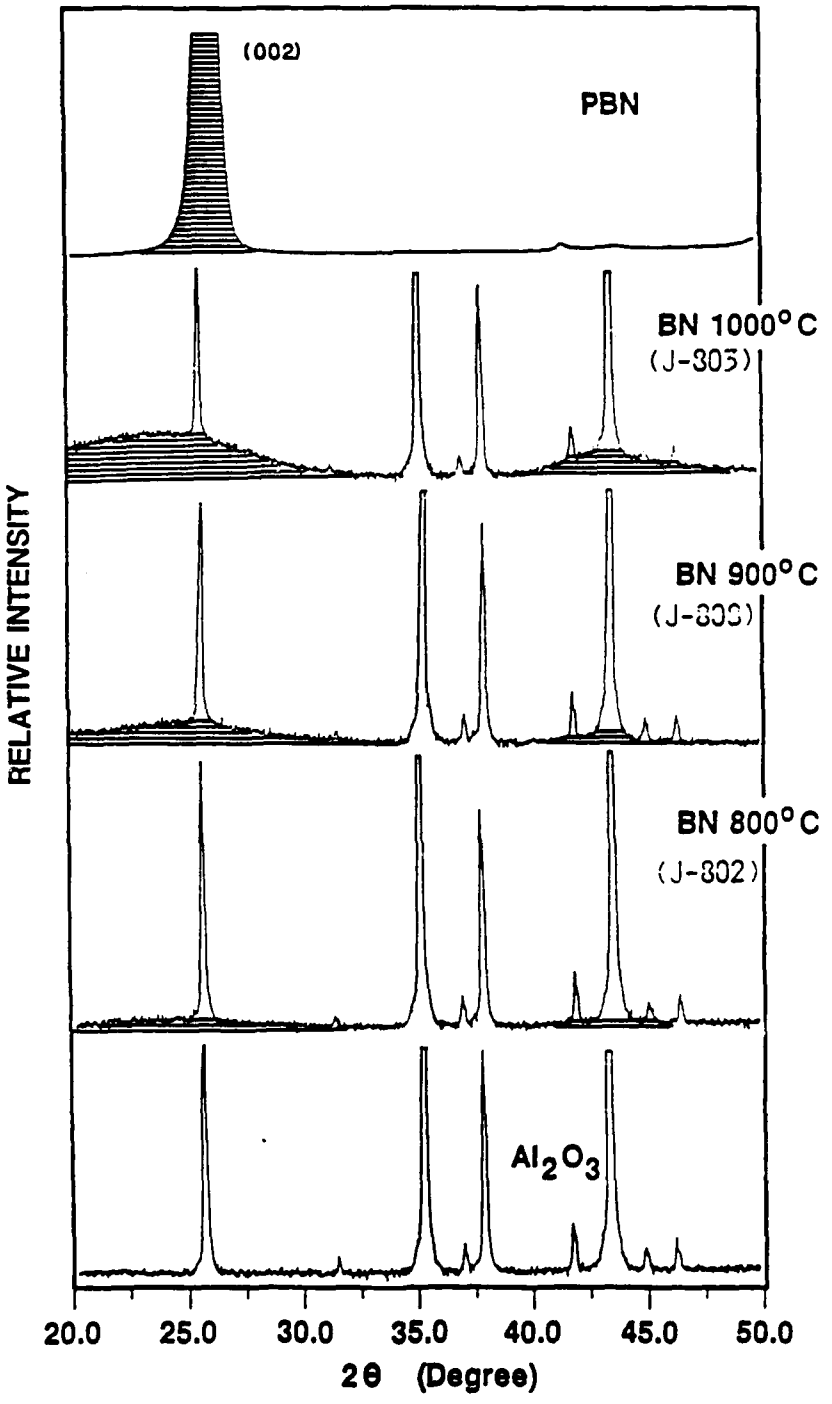

Figure 5-9. XRD patterns of BN deposited on Al_2O_3 at various temperatures (pressure = 40 torr and mole fraction of BCl_3 = 0.0025).

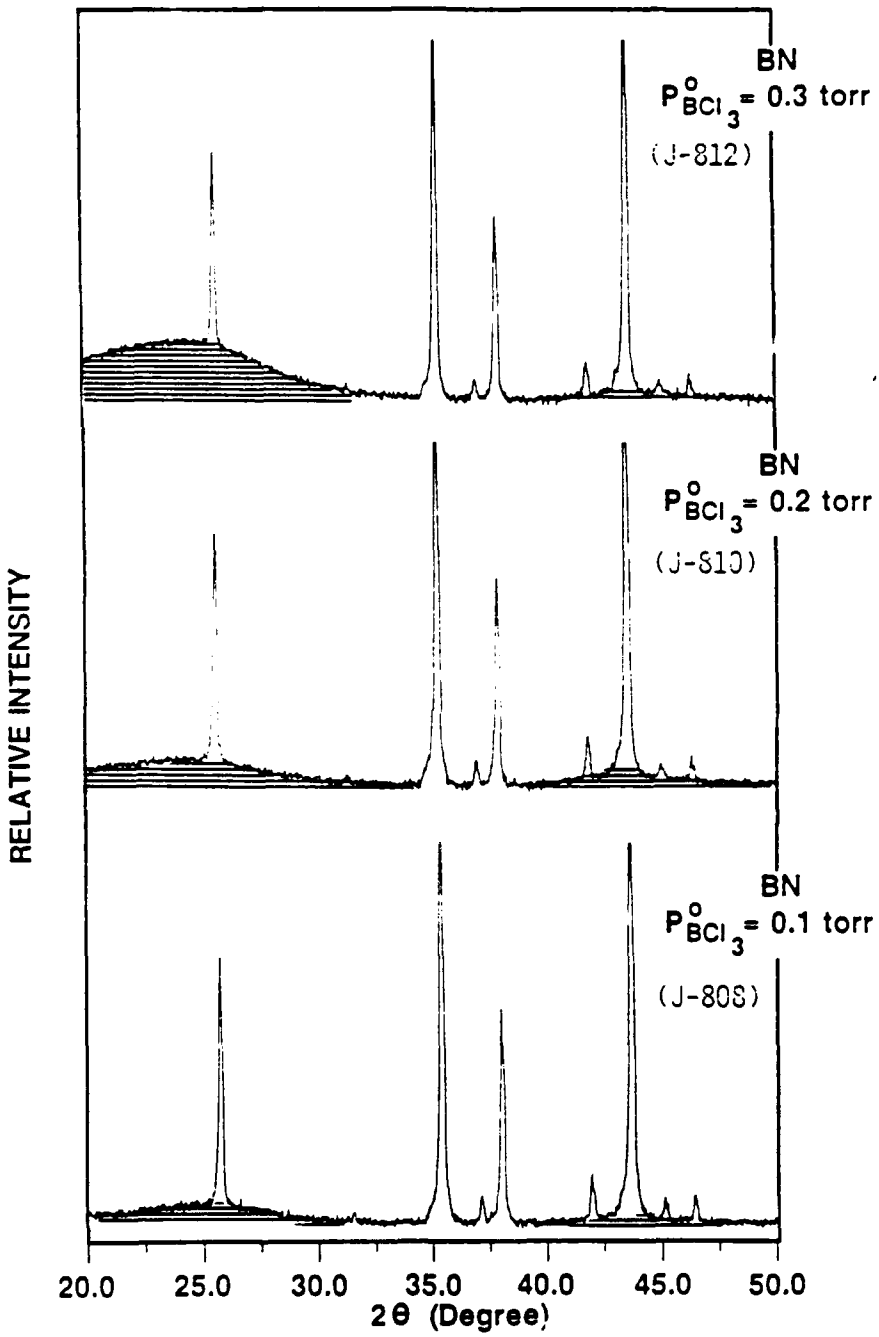

Figure 5-10. XRD patterns of BN deposited on Al_2O_3 at various BCl_3 partial pressures (temperature = 900°C and pressure = 40 torr).

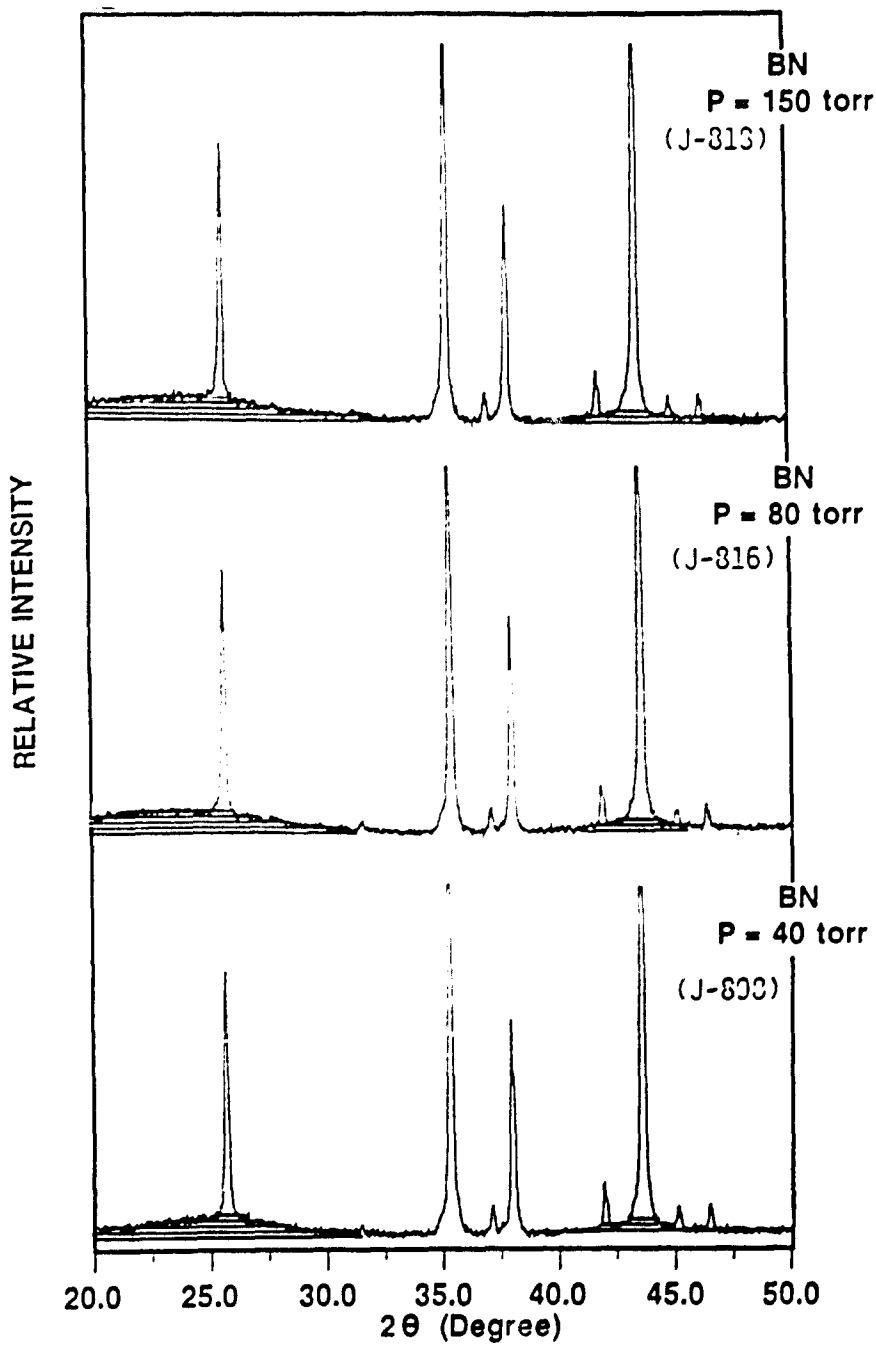

Figure 5-11. XRD patterns of BN deposited on Al_2O_3 at various pressures (temperature = 900°C and mole fraction of BCl_3 = 0.0025).

near 2θ = 42 to 44° with much less intensity in comparison to that of the (002) peak. The appearance of the (10x) peaks indicated that the BN coatings were isotropic. Due to the highly transparent behavior of BN to the incoming X-ray beam, Al_2O_3 substrate peaks were always observed in the XRD spectra even when a fairly thick BN coating (up to 100 μm) was deposited.

The broad (002) peak was usually shifted to the lower 2θ direction by about 2° in reference to the center position of the PBN (002) peak. It seemed that the shift was caused by an expansion of the interlayer spacing (c_o) from about 3.4 Å to about 3.6 Å as BN became more turbostratic (i.e., less crystalline). Matsuda et al. [20] also reported the expansion of the interlayer spacing by as much as 0.15 Å with decreasing deposition temperature from 2000 to 1200°C. The interlayer spacing of their BN deposits was in the range of 3.45 to 3.6Å.

The average grain size of the BN coatings was approximated to be in the range of 13 to 18 Å by measuring the full-width at half-maximum (FWHM) of the (002) BN peak shown in Figures 5-9 and 5-11. The estimated size was in agreement with the findings of other investigators. Matsuda et al. [14] reported that the average grain size of BN deposited at 1200°C was about 15 Å. The grain size increased to about 80 Å with increasing deposition temperature up to 2000°C.

The XRD features of the BN coatings were not significantly affected by processing conditions. However, a

small increase in the (002) peak area was usually noticed with an increase in coating thickness (or deposition rate). As will be discussed later, the deposition rate increased with increasing temperature, pressure, or partial pressure of BCl_3. For example, the intensity of the (002) peak steadily increased with increasing temperature from 800 to 1000°C (see Figure 5-9). Also, an increase in the BCl_3 partial pressure increased the peak intensity as shown in Figure 5-10. The small increases in the (002) peak area were probably due to an increase in the amount of BN being X-rayed as the coating became thicker. Nevertheless, the changes observed in the XRD spectra were minor suggesting that the crystalline structure of the BN coatings remained essentially unchanged for the experimental ranges tested in this study.

The chemical composition of the BN coating (J-816) was determined using electron microprobe. Three different positions along the cross section of the coating were analyzed. In average, the coating was composed of 53.1% (atomic) B, 45.9% N, and 1.0% O indicating the coating contained a slightly excess amount of boron. The composition did not vary much (e.g., less than 1%) along the coating direction. A small amount of Al (about 1 wt%) was detected near the Al_2O_3 substrate.

Homogeneous nucleation was observed at high temperature or high concentration conditions. The occurrence of homogenous nucleation and its effect on the coating morphology

were clearly noticed from SEM micrographs of J-804 and J-805 shown in Figures 5-12 and 5-13, respectively. The XRD pattern of J-804 is shown in Figure 5-14. As discussed earlier, the deposition rate steadily increased when the deposition temperature was increased from 800 to 1000°C (J-802 to J-808 to J-803), but the BN coatings were still dense and smooth in appearance. However, for a deposition temperature of 1100°C, BN having a rough, porous, and powdery surface was deposited on Al_2O_3. Figure 5-12 shows the rough features of the BN coating deposited at 1100°C. Figure 5-12 also shows assemblages of fine BN particles of about 0.2 μm in average size, which were occasionally found on the top of the BN coating surface. These assemblages had the same appearance as silicon particles nucleated in the gas phase from the pyrolysis of SiH_4 in an aerosol reactor system [88]. The very rough and porous morphological features shown in Figure 5-12 were probably caused by the presence of the assemblages of the fine BN particles on the deposition surface. It was speculated that the assemblages of the BN particles underwent the following steps: (1) moved toward and adhered onto the Al_2O_3 substrate; (2) became a part of the coating surface; and (3) were covered and partially-infiltrated by subsequent heterogeneous deposition.

Homogeneous nucleation was suddenly observed as the deposition temperature increased from 1000 to 1100°C. In the context of the classical nucleation and growth theory

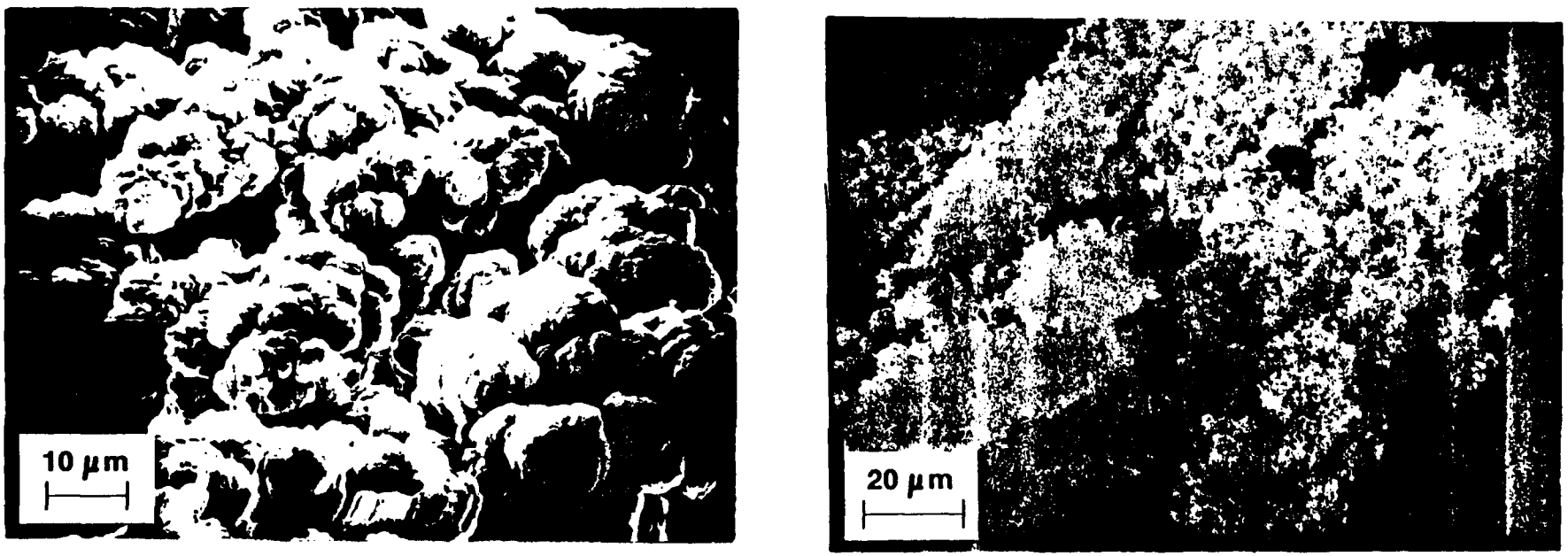

Figure 5-12. SEM micrographs of BN (J-804) showing homogeneous nucleation at 1100°C and 40 torr.

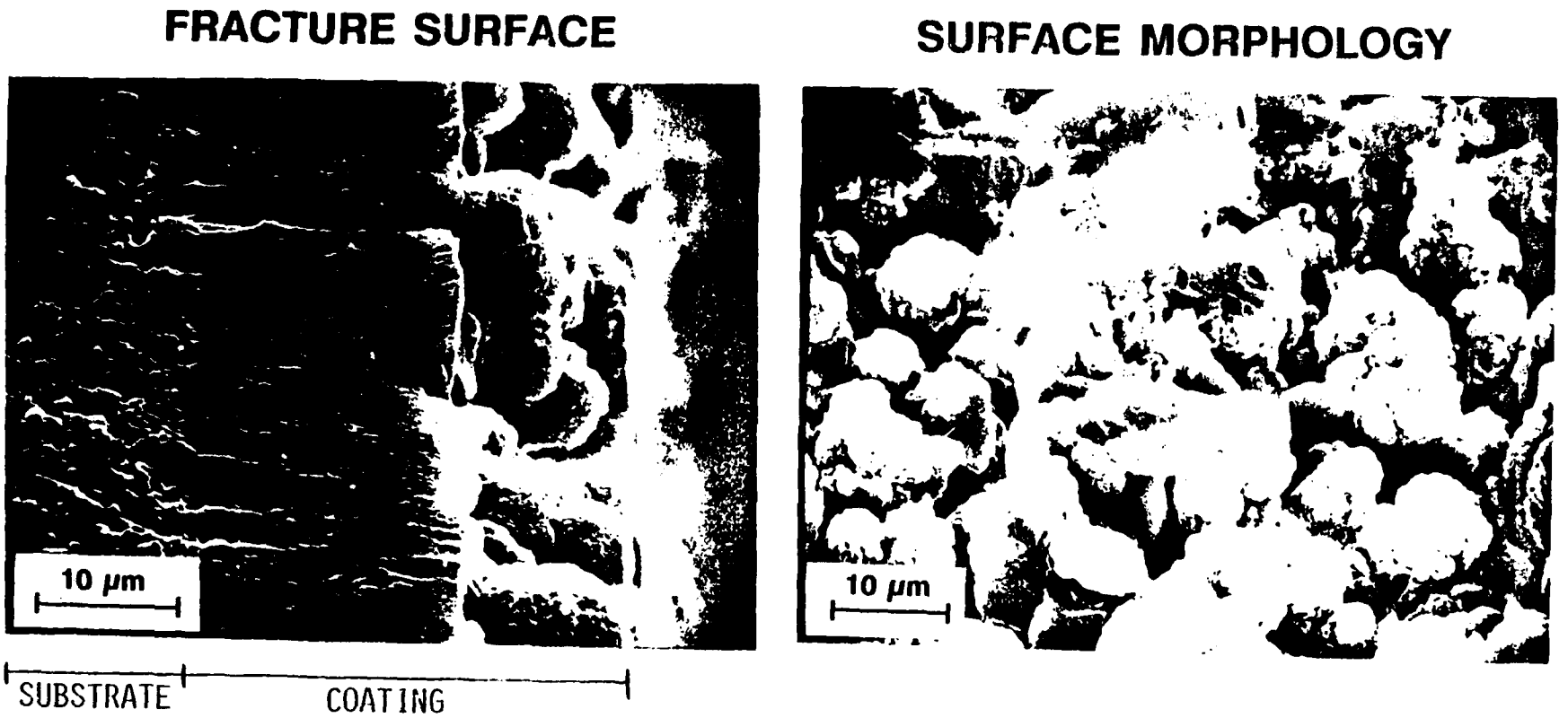

Figure 5-13. SEM micrographs of BN (J-805).

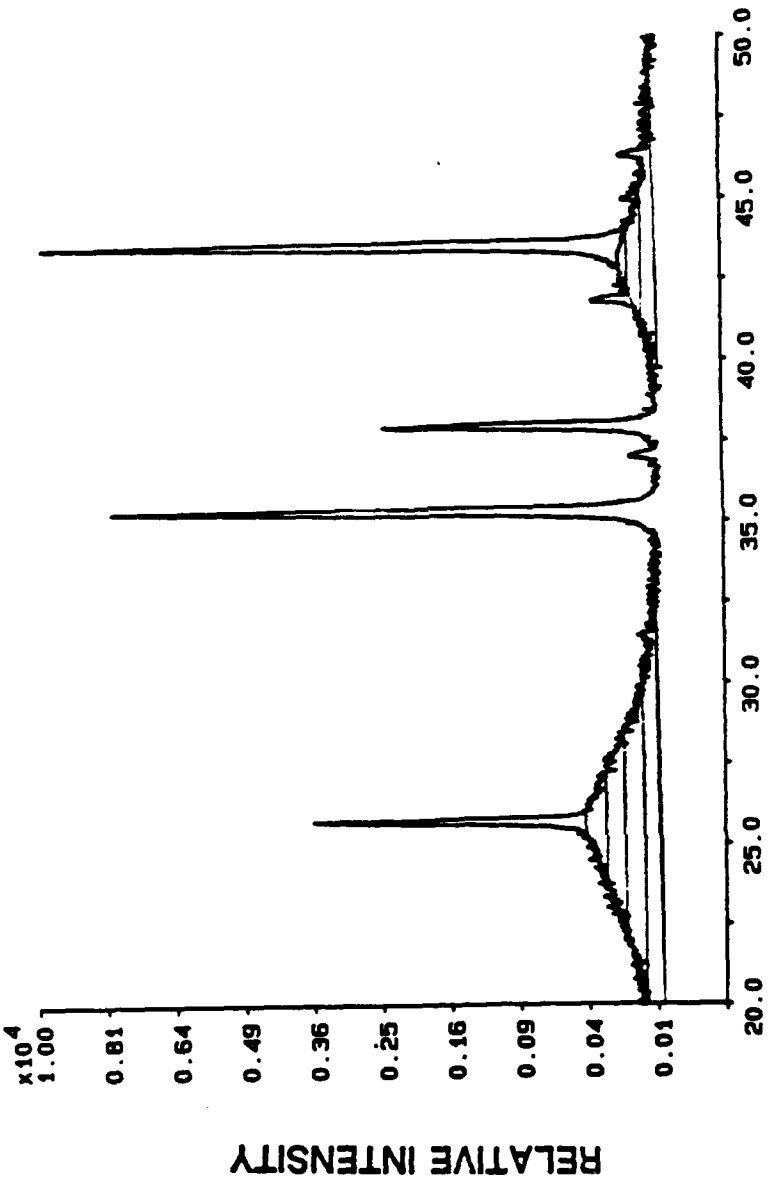

Figure 5-14. XRD pattern of BN (J-804) deposited at 1100°C.

described in Chapter II, this drastic behavior suggested that the gas phase concentration of BN produced by homogenous reactions reached the critical supersaturation level for stable nuclei to form in the gas phase. On increasing the deposition temperature from 1000 to 1100°C, the BN concentration in the gas phase also increased as the rate of the homogeneous reactions was expected to increase exponentially (assuming an Arrhenius relationship between the rate and temperature). Therefore, the sudden occurrence of homogenous nucleation was not surprising, but was expected from the classical nucleation and growth theory. Similar behavior was also observed by Wu et al. [88]. As reviewed in Chapter II, their work indicated that homogeneous nucleation started sharply as soon as a critical SiH_4 reagent concentration was reached. Below the critical level, the generation of new silicon particles in the gas phase was not detected.

The reduction in the BCl_3 partial pressure from 0.1 torr (J-804) to 0.05 torr (J-805) decreased the extent of homogenous nucleation. As shown in Figure 5-13, the BN coating deposited at a BCl_3 partial pressure of 0.05 torr contained two distinct regions: (1) dense coating near the initial Al_2O_3 substrate (i.e., first 20 μm of the coating) and (2) rough and porous outer coating (about 12.5 μm in thickness). It appeared that the dense region was a result of the infiltration of BCl_3 and subsequent heterogeneous BN

deposition inside of the initially porous structure created by the adhesion of homogeneously nucleated BN particles. Nevertheless, the BN coating obtained at the lower BCl_3 concentration was less porous, indicating that the extent of homogeneous nucleation was apparently reduced. Most importantly, this trend was expected from the classical nucleation and growth theory. Furthermore, the processing conditions which would lead to homogenous nucleation were determined from the above experiments. It is important to note that the mass-transfer/kinetic models developed in Chapter IV would not be valid under the conditions which would yield homogeneous nucleation.

Vertical Suspension Geometry. BN coatings obtained using the vertical suspension geometry were typically powdery, soft, waxy, non-adherent and white/opaque when the mixing length (i.e., distance from the mixing position of BCl_3 and NH_3 to the substrate) was 15 cm (e.g., J-164, J-170, J-175, and J-556). As can be seen from Figure 3-7, the mixing length of 15 cm corresponded to the distance from the injector tip to the substrate position (i.e., no graphite extension tube was used). The mixing length could be reduced and controlled by threading the graphite extension tube into the inner path of the injector. The reduction of the mixing length to 5 cm produced BN coatings which were harder and more translucent and adherent (J-618, J-615, J-606, and J-609). The SEM studies showed that the hard and translucent coatings were

denser in appearance than the powdery coatings. Other investigators [11,16] reported similar behavior. They explained that the formation of the powdery deposits was probably due to the premature reaction between BCl_3 and NH_3 to form NH_4Cl powder at low temperature regions. They further postulated that the premature reaction depleted NH_3, resulting in the higher boron content compared to nitrogen in the coating.

In our experiments where the graphite extension tube was not used (i.e., mixing length of 15 cm), the NH_4Cl powder was usually deposited (or fell down) on the injector tip since the injector was usually kept below 170°C by circulating compressed air or oil. However, our evidence was not extensive enough to confirm or dispute the other investigator's explanations. There might be two other possible reasons for the observed behavior: (1) incorporation of the NH_4Cl particles formed in the gas phase into the coating structure, provided that the decomposition of the NH_4Cl particles in the high temperature region was not fast enough during their travel (at the fluid velocity of 1650 cm/s) to the substrate position and/or (2) homogeneous nucleation occurred when the mixing distance of 15 cm was used. In the second case, it might be possible that the extent of homogenous reactions to produce BN in the gas phase increased enough to cause homogeneous nucleation when the longer mixing distance (or longer reaction zone) was used.

In other words, the concentration of BN produced by the homogeneous reactions in the gas phase increased along the flow direction, and eventually reached a threshold level for homogeneous nucleation to start.

When the mixing length of less than 5 cm was used, the BN coatings were generally translucent and became more glassy with decreasing deposition temperature. When the vertical suspension geometry was used, the deposition rate decreased drastically along the flow direction. However, the deposition rate profile along the flow direction could not be accurately measured since non-uniform flow patterns and/or channeling were suspected during the deposition process. Figure 5-15 shows SEM micrographs obtained from sample J-615 at various spots along the flow direction. The micrographs clearly suggested that the surface morphology gradually changed along the flow direction. It is noted that "flower-shaped" features on the coating surface were identified to be B_2O_3 by XPS. The surface morphology varied from a fairly continuous surface containing 10 μm size nodules from the bottom position to a surface consisting of discrete granules of about 1 μm in size at the top. The BN coatings having the granular morphology tended to be opaque-white in color, soft and somewhat powdery. The exact cause(s) for the observed granular morphology has not been determined.

Figure 5-16 shows a typical XPS spectrum of the BN coatings and the corresponding surface elemental composition.

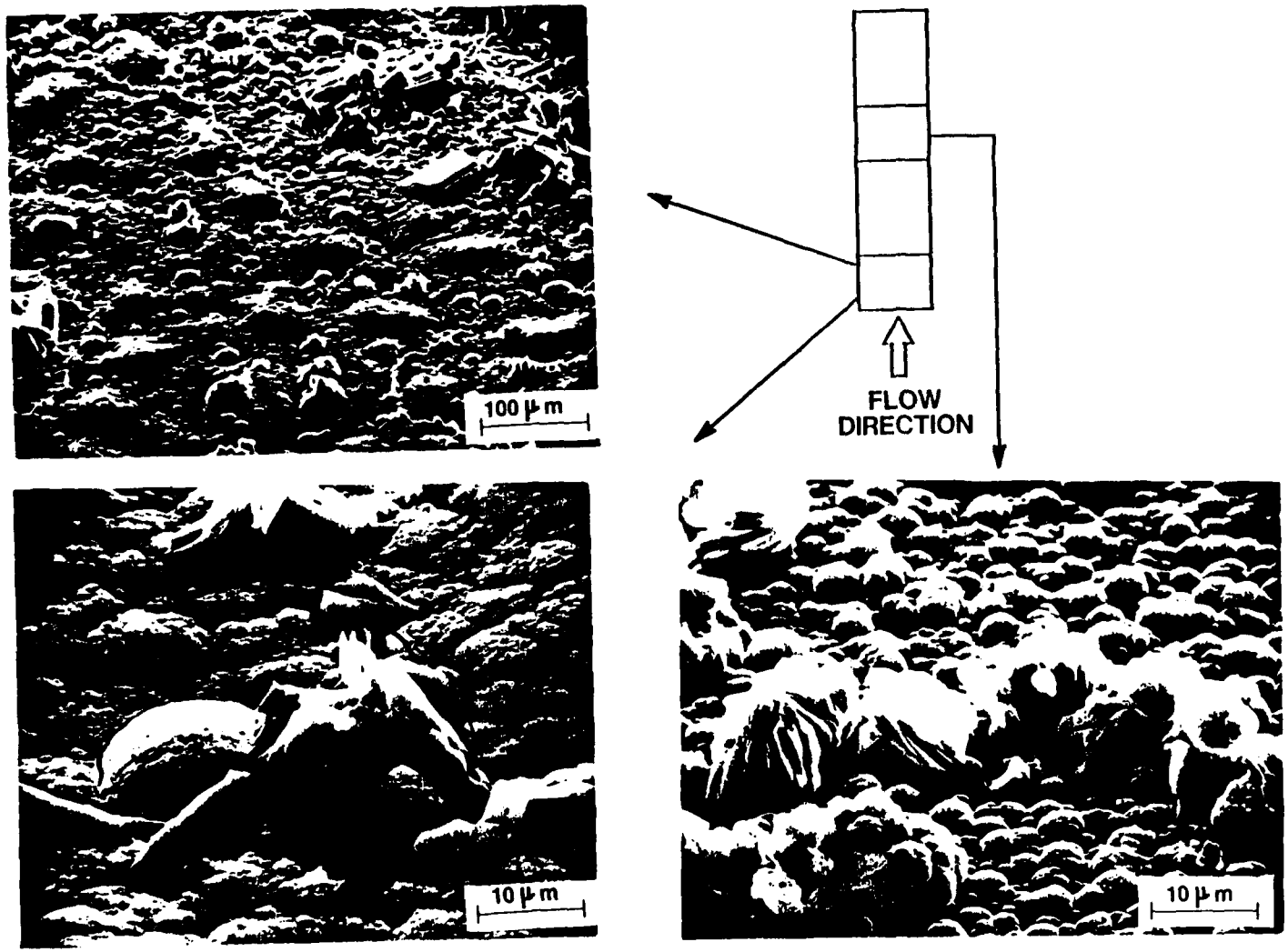

Figure 5-15. SEM micrographs of BN at different positions along flow direction (J-615).

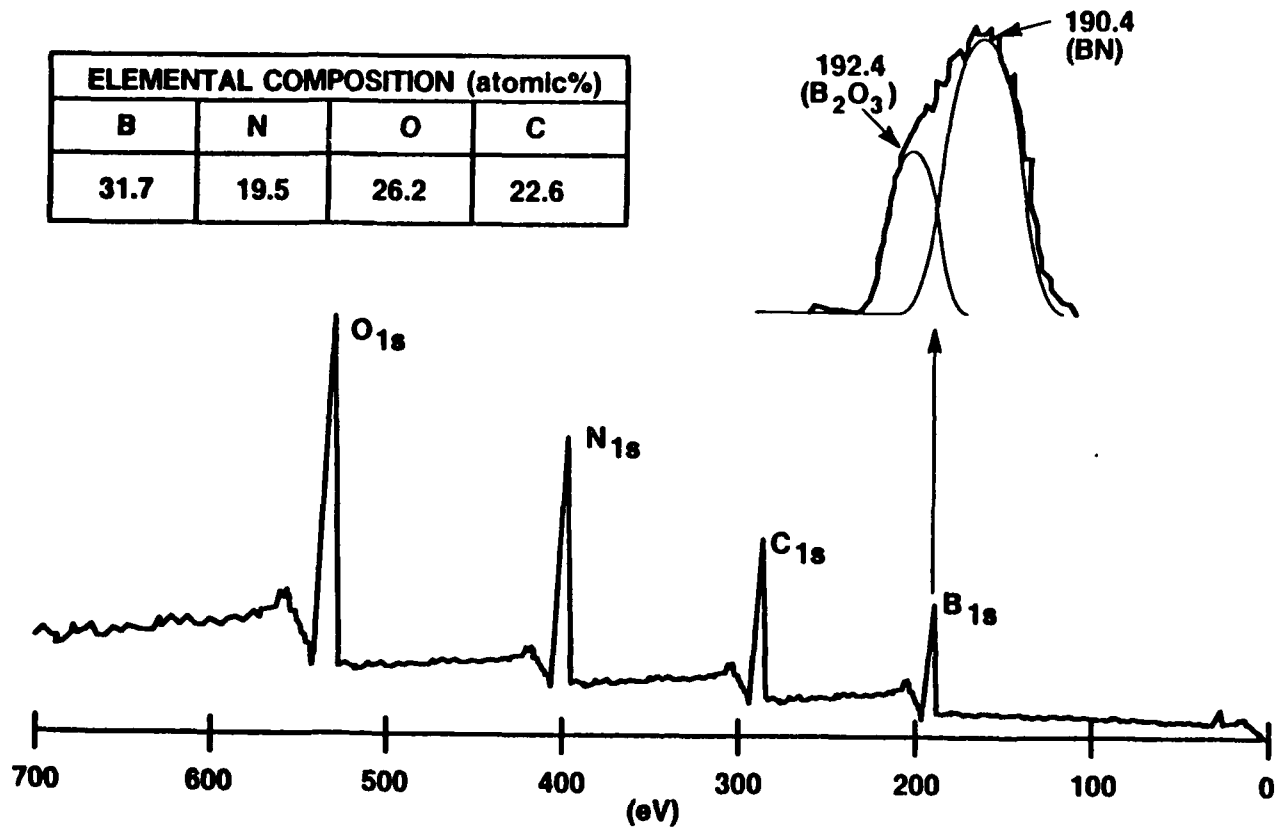

Figure 5-16. XPS spectrum of BN.

The presence of BN was identified by the peak at 190.4 eV. The top surface layers of the coating were not removed by sputtering before the XPS scan was taken. The presence of B_2O_3 as a minor phase on the coating surface was indicated by the appearance of the boron peak at 192.4 eV and the relatively high surface oxygen content (26.2 atomic%). It was suspected that most of the B_2O_3 formation was due to the surface reaction of BN upon exposure to moist air after the deposition process. BN deposited at relatively moderate temperatures (e.g., below 1200°C) is known to be susceptible to moisture although the kinetics of the oxidation process have not been thoroughly understood [7]. The surface boron content was usually higher than that of nitrogen for most BN coatings. The surface boron and nitrogen contents were not influenced in any regular fashion by the changes in operating conditions.

BN could not be deposited on Al_2O_3 at 1300°C (J-619) as evidenced by: (1) negligible weight gain after the deposition and (2) the absence of XRD features attributable to BN in the XRD spectrum as shown in Figure 5-17. As reviewed in Chapter II, BN can be easily deposited onto graphite at temperatures up to 2100°C. Furthermore, several earlier studies showed that the crystallinity of BN deposited on graphite increased strongly with temperature [14-16]. It was speculated that BCl_3 reacted with and/or etched the Al_2O_3 surface at 1300°C in the presence of NH_3 to form AlN as evidenced by the appearance of a small (100) AlN peak in Figure 5-17. This explanation

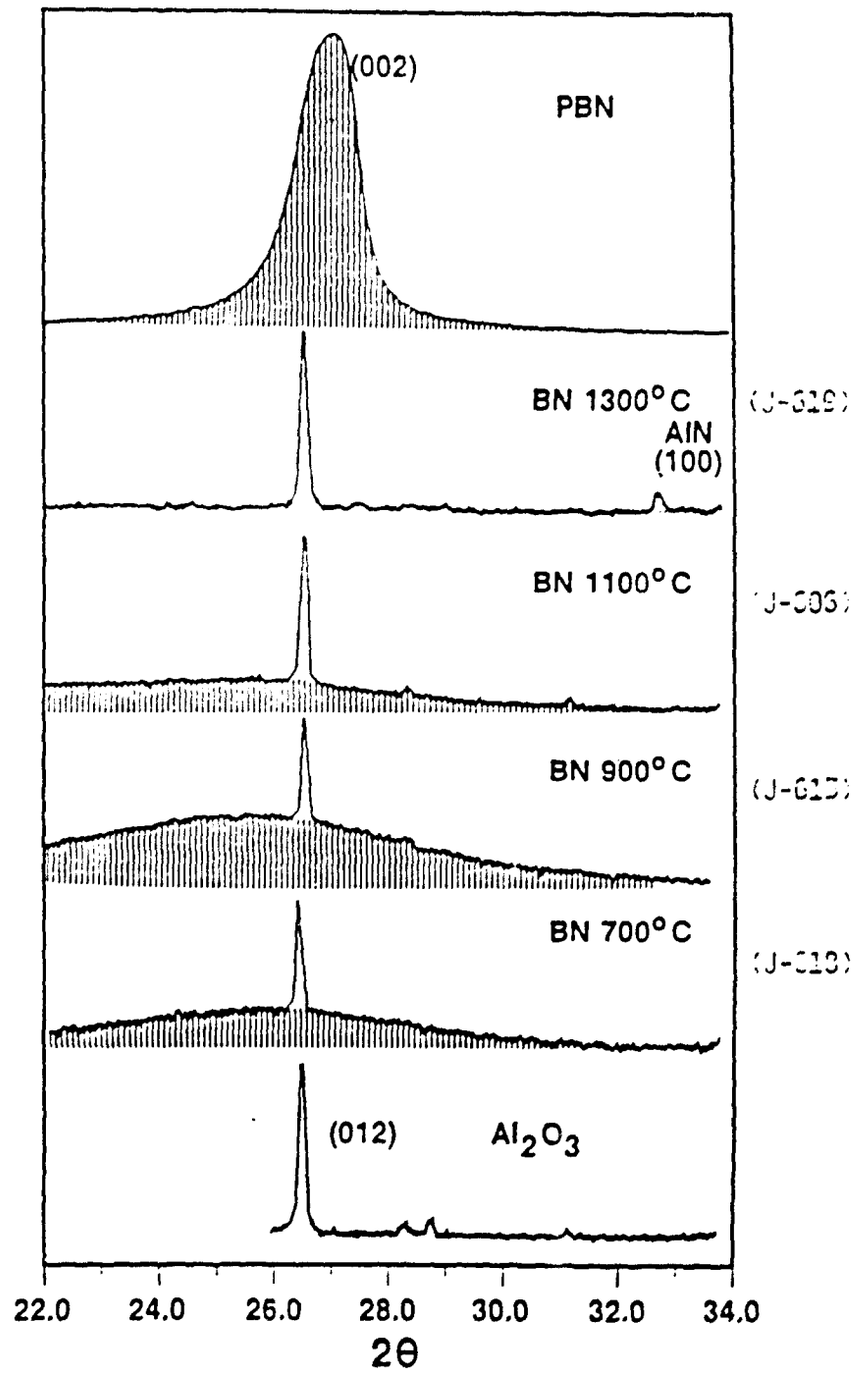

Figure 5-17. XRD patterns of BN deposited at various temperatures using vertical suspension geometry.

was also supported by the fact that a whisker surface morphology was observed by SEM. As will be discussed in the next two sections, it was found that AlN had a tendency to grow as whiskers in many instances. Therefore, it appeared that BN deposition on Al_2O_3 from BCl_3 and NH_3 was not favorable at temperatures above about 1300°C.

When the suspension geometry was used, homogenous nucleation was observed at high temperatures and pressures as in the case of the impinging jet geometry. BN deposited on Al_2O_3 at 760 torr and 1200 °C (J-164 and J-170) had a very non-uniform and porous surface containing small spherical-shaped particles of 0.1 μm diameter as shown in Figure 5-18. The appearance of these particles indicated that homogeneous nucleation was favored under these conditions.

Kinetic Analysis and Interpretation

BN deposited on Al_2O_3 using the impinging jet geometry (J-8xx samples) had uniform thickness inside of the stagnation region. The diameter of the stagnation region was usually measured to be about 1.5 cm or less when a nozzle diameter of 1.59 cm was used. The average coating thickness, L, of each J-8xx sample was measured from the SEM micrographs of the fracture surfaces already shown in Figures 5-1 through 5-8. The measured thicknesses for the J-8xx samples are tabulated in Table 5-1. Deposition rate, J_{BN}, was determined from the coating thickness using the following equation:

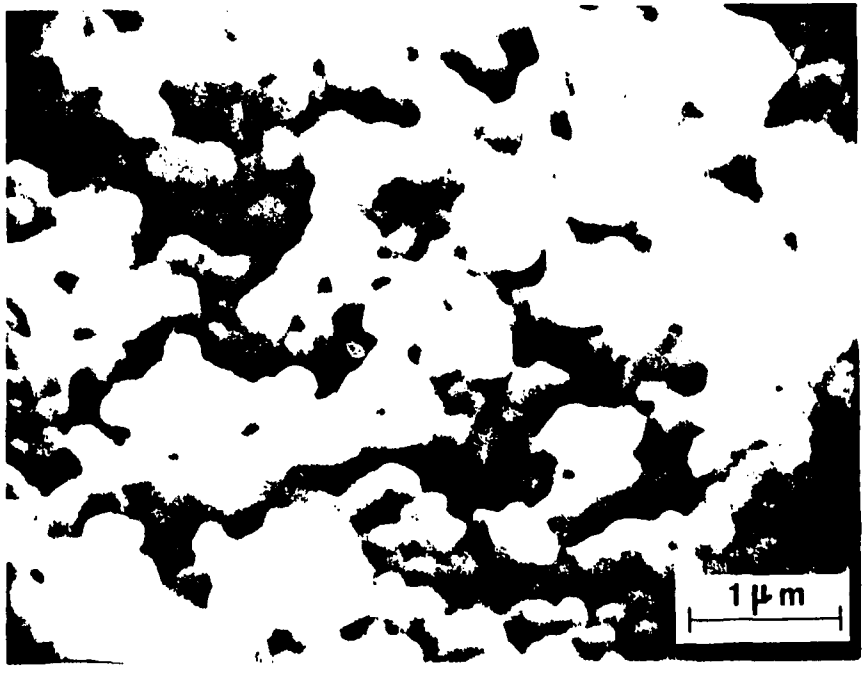

Figure 5-18. SEM micrograph showing homogeneous nucleation of BN at 760 torr.

$$J_{BN} = \frac{L\ \rho_{BN}}{t\ M_{BN}} \qquad (5\text{-}1)$$

where J_{BN} is in moles/cm^2/sec, ρ_{BN} is the density of BN, t is the deposition time, and M_{BN} is the molecular weight of BN. The BN density was assumed to be 1.6 g/cm^3 even though the theoretical density of BN is 2.27 g/cm^3. As discussed in Chapter II, the density of BN prepared by CVD was found to be strongly influenced by deposition temperature and pressure [7,20]. The density could range anywhere from 1.35 to 2.20 g/cm^3. The BN density usually increased when high temperature and/or low pressure were used. A density of 1.6 g/cm^3 was assumed because the number corresponded to an average value reported by other investigators [7,20] at processing conditions similar to those in the present study (i.e., 900 °C and 40 torr). The uncertainties in the density of the BN coatings should be considered as one of the major sources of error in the kinetic analysis.

As tabulated in Table 5-1, three types of experiments were performed in order to determine the intrinsic kinetic mechanism(s) of the BN-CVD system. First, deposition temperature was varied from 800 to 1100°C at increments of 100°C (J-802, J-808, J-803, and J-804). Second, inlet BCl_3 partial pressure was varied from 0.1 to 0.3 torr at 900°C and 40 torr by increasing BCl_3 flow rate while keeping the total flow rate constant at 2400 cm^3/min (J-808, J-810, and J-812).

Third, total system pressure was varied from 30 to 150 torr at 900 °C while the mole fraction of BCl_3 in the reagent mixture was fixed at 0.0025 (J-800, J-808, J-816, and J-818). After performing the kinetic experiments, a surface kinetic rate equation which would fit the deposition data was sought. The following simple first-order expression was determined to be adequate in describing the deposition data:

$$J_{BN} = k_{BN} \frac{P^s_{BCl_3}}{RT} \qquad (5\text{-}2)$$

where k_{BN} is the first-order kinetic rate constant and $P^s_{BCl_3}$ is the partial pressure of BCl_3 at the deposition surface. At steady state, the production rate of BN should be the same as the net rate of mass transfer of BCl_3 through the concentration boundary layer. The net mass transfer rate of BCl_3 was previously derived in Chapter IV:

$$J_{BCl_3} = \left(\frac{D_{BCl_3}}{\delta_{BCl_3} RT}\right)\left(P^\circ_{BCl_3} - P^s_{BCl_3}\right) \qquad (5\text{-}3)$$

where $P^\circ_{BCl_3}$ is the partial pressure of BCl_3 in the bulk gas phase, D_{BCl_3} is the binary diffusion coefficient of BCl_3 in Ar, and δ_{BCl_3} is the thickness of the concentration boundary layer for BCl_3. Substitution of Eq. 5-2 into Eq. 5-3 gives the following overall rate expression, which accounts for both the mass transfer and kinetic contributions to the deposition process.

$$J_{BN} = \frac{P^{\circ}_{BCl_3}/RT}{(\delta/D)_{BCl_3} + 1/k_{BN}} \qquad (5\text{-}4)$$

From the first set of experiments in which the deposition temperature was varied, an Arrhenius relationship between the deposition rate and temperature was observed as plotted in Figure 5-19. In the Arrhenius plot, the deposition rate, J_{BN}, was normalized for various BCl_3 partial pressures used in the experiments by plotting $J_{BN}/P^{\circ}_{BCl_3}/RT$ on the y-axis. The data from J-804 and J-805 were not used in Figure 5-19 since homogeneous nucleation was observed for these experiments. The observed Arrhenius relationship indicated that the BN-CVD process was kinetically-controlled in the temperature range of 800 to 1000°C. If the process was diffusion-limited, the deposition rate should be a weak function of temperature ($\alpha T^{1.656}$). Also, the experimental results were in agreement with the findings of Tanji et al. [12]. They reported that the BN deposition rate exponentially increased with increasing temperature from 900 to 1250°C supporting that the BN-CVD was kinetically-controlled below 1250°C.

The magnitude of (D/δ) for BCl_3 was computed using the computation procedures described in Chapter IV. Also, the magnitude of $J_{BN}/P^{\circ}_{BCl_3}/RT$ was determined from the experimental data and conditions. Therefore, the intrinsic rate constant, k_{BN}, for each data point in the Arrhenius plot could easily be

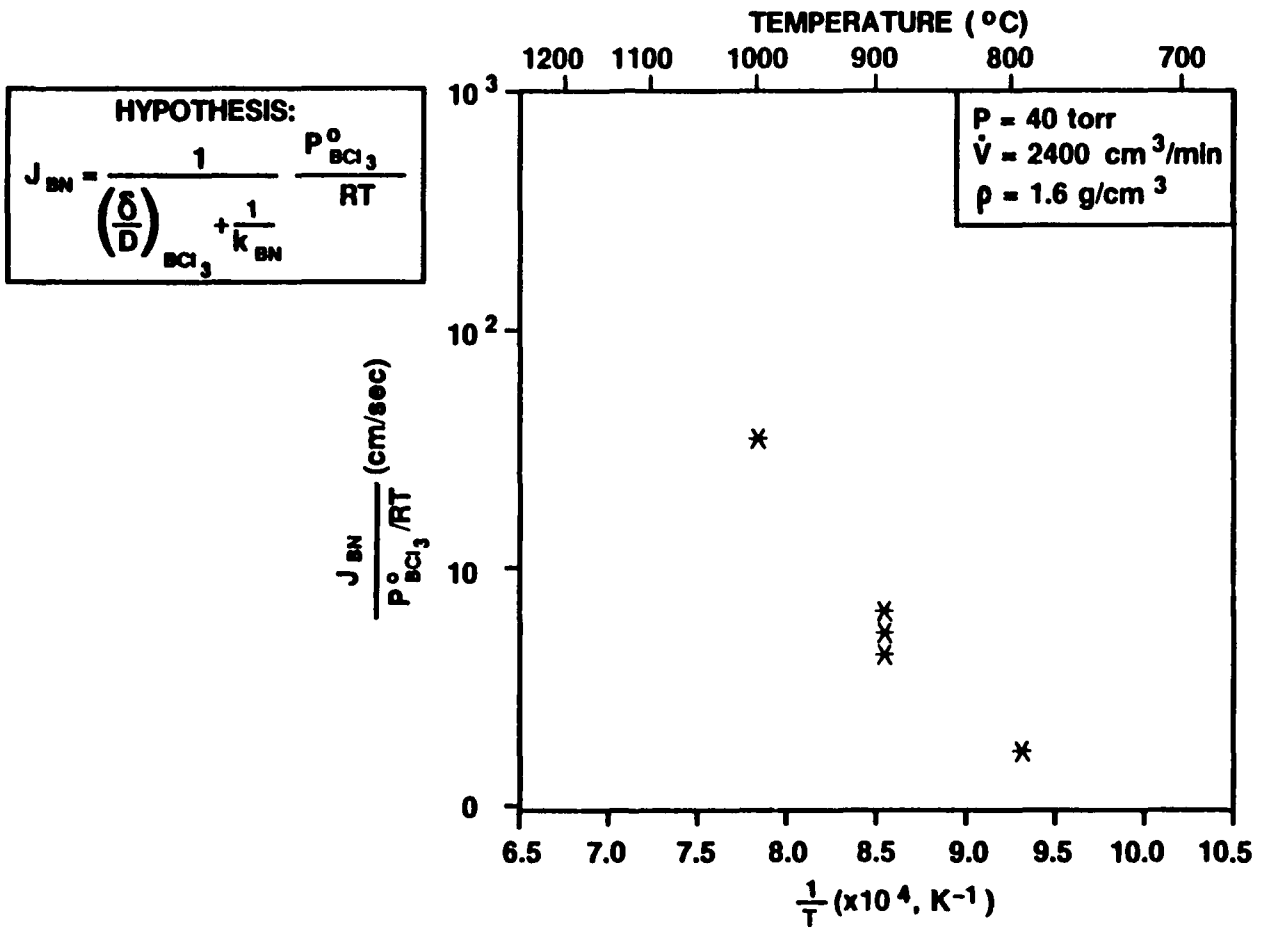

Figure 5-19. Arrhenius relationship between deposition rate and temperature.

calculated using Eq. 5-4. Furthermore, the calculated k_{BN} values were fitted using the least square method resulting in the following expression:

$$k_{BN} = k_{oBN} \exp(-\Delta E/RT) \qquad (5\text{-}5)$$

where the frequency factor, k_{oBN}, was determined to be 1.88×10^8 cm/sec and the intrinsic activation energy, ΔE, was 39.4 Kcal/mole. The fitted expression for k_{BN} and $(D/\delta)_{BCl_3}$ values are plotted in Figure 5-20. These results can be best interpreted by considering the "resistance" analogy introduced in Chapter II. In order to clearly illustrate this concept, Eq. 5-4 can be rewritten:

$$\frac{1}{J_{BN}} = \left(\frac{1}{k_{BN}} + \frac{1}{(D/\delta)_{BCl_3}}\right) \frac{1}{P^{\circ}_{BCl_3}/RT} \qquad (5\text{-}6)$$

where $1/k_{BN}$ and $1/(D/\delta)_{BCl_3}$ can be thought of as "kinetic resistance" and "diffusion resistance", respectively. When $1/k_{BN}$ is much greater than $1/(D/\delta)_{BCl_3}$, the process is said to be "kinectically-controlled" as the rate equation becomes essentially that of the kinetic rate expression. At the other extreme case (i.e., $1/k_{BN} << 1/(D/\delta)_{BCl_3}$), the diffusion of BCl_3 becomes the rate limiting step (i.e., "diffusion-limited"). At 900°C, k_{BN} and $(D/\delta)_{BCl_3}$ were about 9.5 cm/sec and 131.5 cm/sec, respectively. Therefore, $1/k_{BN}$ was greater than $1/(D/\delta)_{BCl_3}$ so the deposition process was mostly limited by the

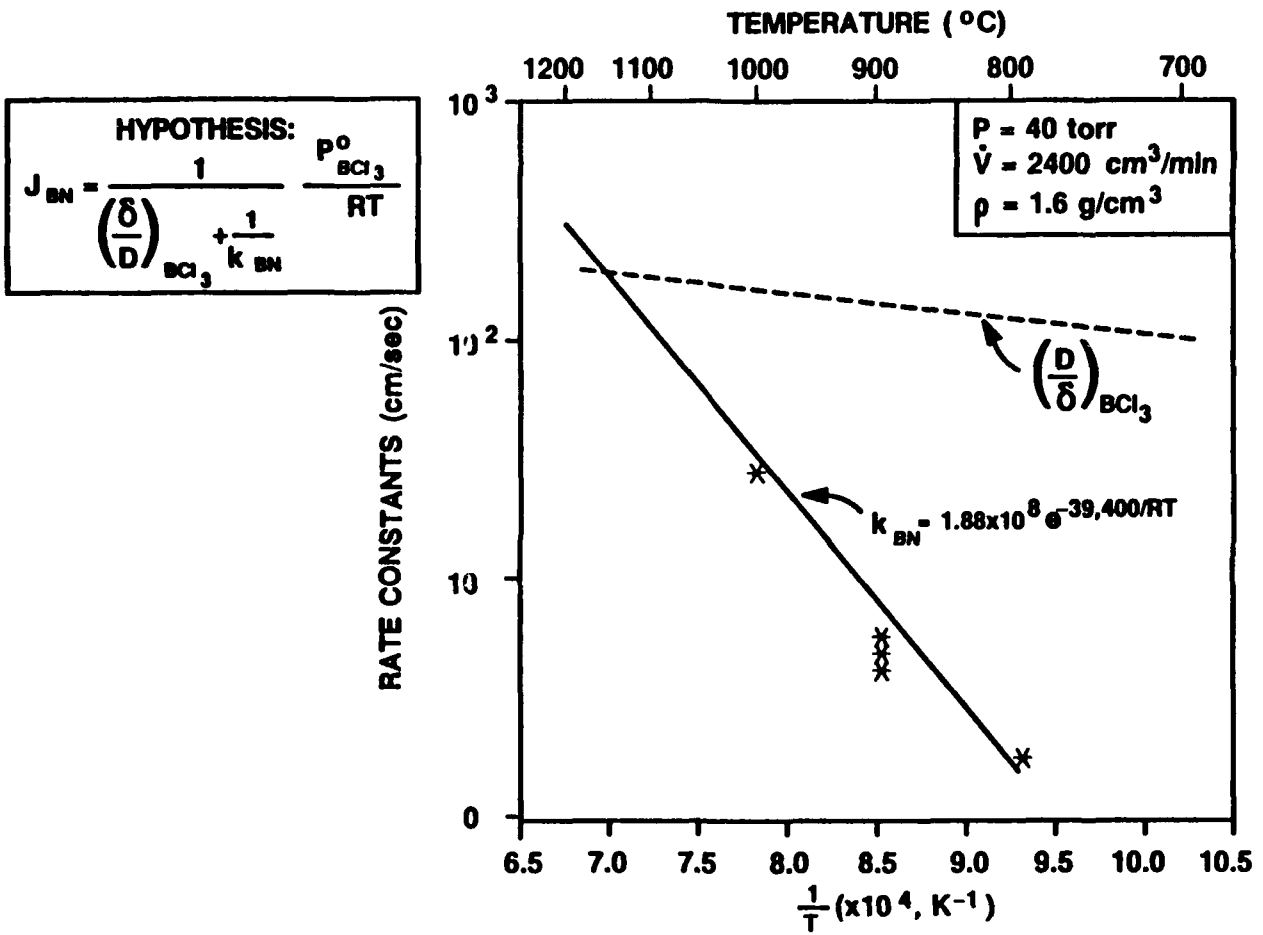

Figure 5-20. First-order intrinsic rate constant, k_{BN}.

slow kinetics (i.e., "kinetic resistance" of 93% at 900°C and 83% at 1000°C).

The overall rate expression, Eq. 5-4, was also adequate to describe the experimental results obtained from the second set of kinetic experiments. As shown in Figure 5-21, the deposition rate increased linearly with increasing inlet BCl_3 partial pressure. The linear relationship between J_{BN} and $P^{\circ}_{BCl_3}$ was expected from Eq. 5-4 since first order kinetics was assumed. Even if the process was diffusion-limited, the deposition rate would also have the first order relationship with respect to $P^{\circ}_{BCl_3}$. Therefore, the mass transfer and kinetic contributions to the deposition rate could not be resolved from this experimental set alone. However, the experiments were performed in the kinetically-controlled region (i.e., at 900°C). Thus, the linear relationship observed between J_{BN} and $P^{\circ}_{BCl_3}$ supports the assumption that the surface reaction step had a first order dependency on the BCl_3 surface partial pressure.

The deposition rate data obtained from the third set of kinetic experiments could also be described by Eq. 5-4. In Figure 5-22, the BN deposition rate was plotted as a function of total pressure. For these experiments, the deposition temperature, BCl_3 mole fraction, and volumetric flow rate were the same as indicated in Figure 5-21. In order to clearly illustrate the effect of pressure on the deposition rate, Eq. 5-4 can be reexpressed without changing any meaning:

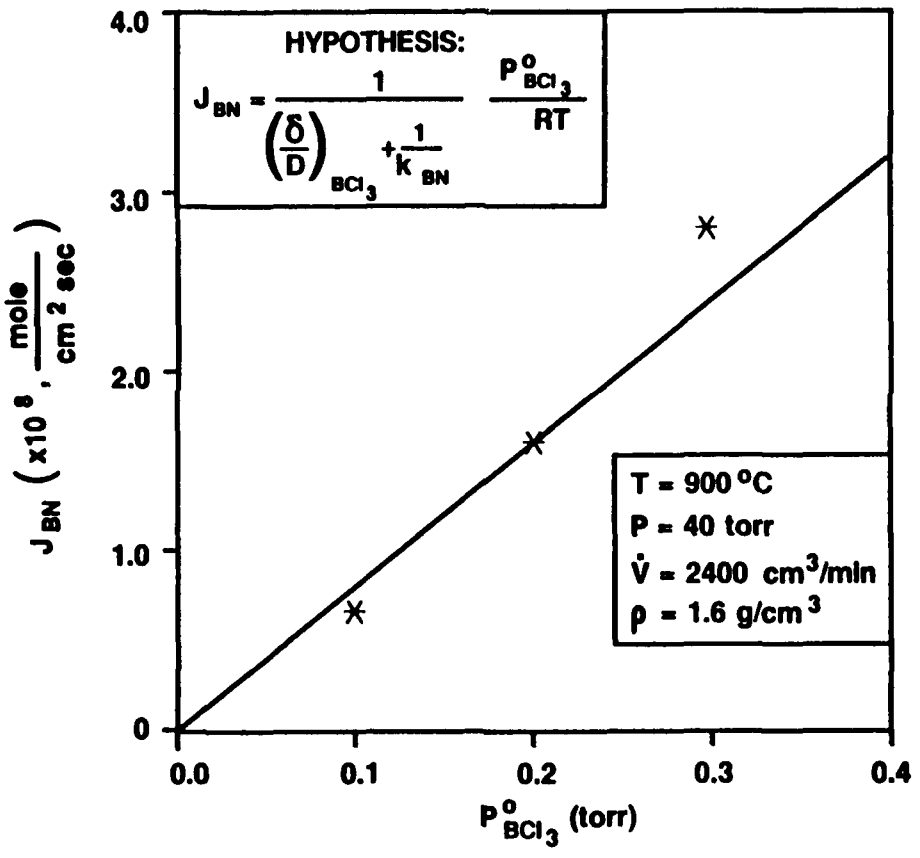

Figure 5-21. Deposition rate of BN versus BCl_3 partial pressure.

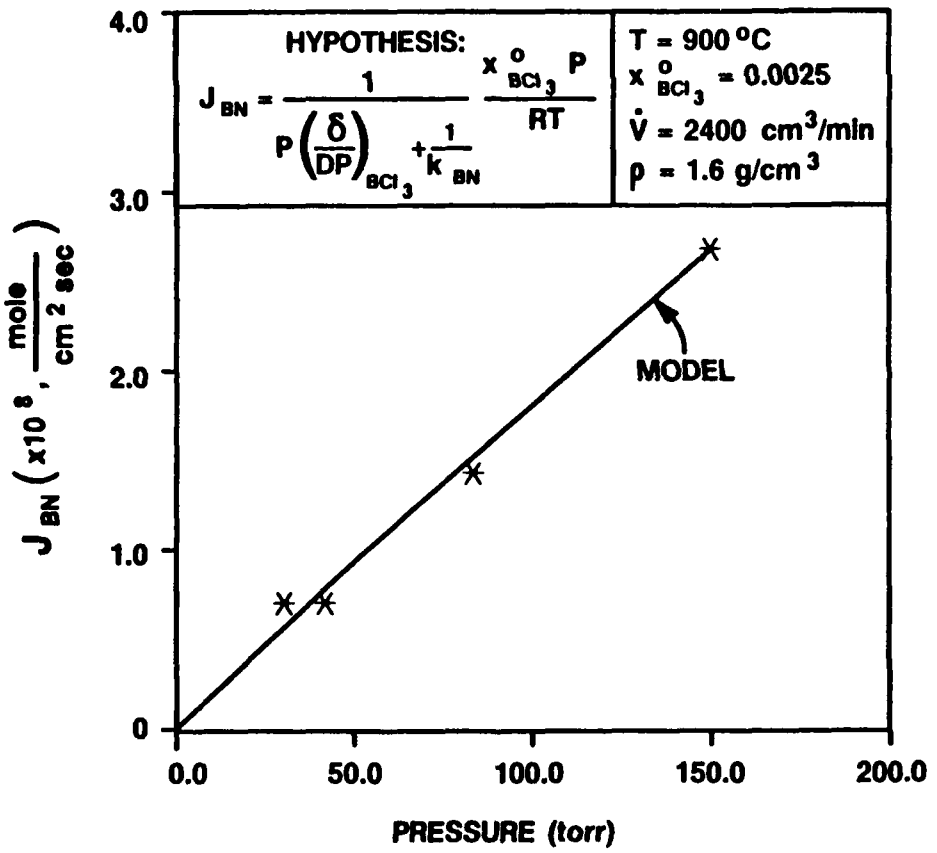

Figure 5-22. Deposition rate of BN versus pressure.

$$J_{BN} = \frac{1}{P\left(\frac{\delta}{DP}\right)_{BCl_3} + \left(\frac{1}{k_{BN}}\right)} \frac{x^{\circ}_{BCl_3} P}{RT} \qquad (5\text{-}7)$$

In Eq. 5-7, $P^{\circ}_{BCl_3}$ is expressed as a product of $x^{\circ}_{BCl_3}$ and total pressure, which is the definition of partial pressure. Also, pressure was multiplied to both numerator and denominator of the $(\delta/D)_{BCl_3}$ term (i.e., ratio of 1). When $(\delta/D)_{BCl_3}$ is much larger than $(1/k_{BN})$, the overall rate expression reduces to:

$$J_{BN} = \left(\frac{DP}{\delta}\right)_{BCl_3} \frac{x^{\circ}_{BCl_3}}{RT} \qquad (5\text{-}8)$$

But, the (DP) term is constant with respect to changes in pressure because the diffusion coefficient is inversely proportional to pressure according to Eq. 4-26. In addition, the δ value is independent of total pressure. (Note: The δ value can be decreased by increasing the volumetric flow rate.) Therefore, the deposition rate remains constant with respect to changes in total pressure for the diffusion-limited process. However, for the kinetically-controlled process (i.e., $1/k_{BN} >> (\delta/D)_{BCl_3}$) the deposition rate linearly increases with pressure. As shown in Figure 5-22, the deposition data could be well predicted by Eq. 5-4. The deposition rate increased with increasing pressure confirming that the BN-CVD process was indeed kinetically-controlled at 900°C.

In the above kinetic analysis, it was shown that the relatively simple rate expression of Eq. 5-4 was adequate to portray the kinetics and mass transfer characteristics of the BN-CVD process with the impinging jet geometry. For the remainder of this section, the experimental results will be interpreted in a more mechanistic manner. Also, our observations are discussed in view of some of the assumptions made during development of the model, and compared with other investigator's findings.

The surface kinetic rate expression of Eq. 5-2 can be elaborated to permit speculation of possible surface kinetic mechanism(s) for the BN-CVD process. The first-order relationship between the deposition rate and the surface BCl_3 partial pressure suggests that the rate-limiting step of the BN deposition process may be either: (1) adsorption of BCl_3 onto an empty surface site or (2) surface reaction involving adsorbed BCl_3. The adsorption process can be expressed as follows:

$$J_{BN} = k' P^s_{BCl3} \theta_v \qquad (5\text{-}9)$$

where θ_v is the fraction of surface sites which are not covered by adsorbed species and k' is the adsorption rate constant. But, since the θ_v value will be close to unity when the rate-limiting step is the adsorption [99], the resulting equation is simply: $J_{BN} = k'P^s_{BCl3}$. On the other hand, the first order reaction of the adsorbed BCl_3 molecules can be

written as:

$$J_{BN} = k'' \theta_{BCl_3} \qquad (5\text{-}10)$$

where θ_{BCl_3} is the fraction of surface sites occupied by BCl_3 and K'' is the surface reaction rate constant. During the above derivation, the presence of NH_3 and its role in the deposition mechanism were ignored. Other investigations [12,13] showed that the BN-CVD process was usually independent of the NH_3 concentration as long as an excess amount of NH_3 was present. In our experiments, the ratio of NH_3 to BCl_3 was always larger than one in order to ensure that excess NH_3 was present. Therefore, it is assumed that every surface kinetic step involving NH_3 is fast in comparison to those involving BCl_3, and the kinetic role of NH_3 during the deposition process is negligible.

The term θ_{BCl_3} in Eq. 5-10 can be replaced by functions of surface concentrations of gas species and equilibrium adsorption constants by applying the Langmuir isotherm equation [99]. After this treatment, Eq. 5-10 can be expressed:

$$J_{BN} = \frac{k\ P^{s}_{BCl_3}}{1 + \Sigma\ K_i P^{s}_{i}} \qquad (5\text{-}11)$$

where k is a rate constant, i represents each adsorbed gas species (i.e., BCl_3, NH_3, HCl etc.), K_i is the adsorption

equilibrium constant for gas species i, and P^s_i is the partial pressure of gas species i at the deposition surface. When the magnitude of the $\Sigma K_i P^s_i$ series is smaller than 1, Eq. 5-11 essentially reduces to Eq. 5-2:

$$J_{BN} = k_{BN} \frac{P^s_{BCl3}}{RT} \qquad (5\text{-}2)$$

where k_{BN}=kRT. The small magnitude of $\Sigma K_i P^s_i$ corresponds to a situation in which all gas species are weakly adsorbed on the surface sites. Therefore, in both adsorption- and surface reaction-controlled cases (see Eqs. 5-9 and 5-2), the deposition rate has the first order dependency on BCl_3 partial pressure at the surface. Thus, based on our experimental data, the question as to whether the adsorption or the surface reaction is the rate-limiting step can not be resolved.

However, our careful observation suggests that the adsorption of BCl_3 plays an important role in the BN-CVD process. One of the most intriguing findings from our investigation was that BN could not be deposited on graphite substrates under the same processing conditions (i.e., 900°C and 40 torr) which yielded BN on Al_2O_3 substrates. However, many earlier studies [7,11-13,20] have shown that BN could be deposited on graphite at temperatures as low as 900°C. Takahashi et al. [15] reported that the non-crystalline BN or NH_4Cl was deposited on graphite below 1600°C whereas

crystalline BN was deposited on metallic substrates below 1600°C. However, to date, a systematic investigation has not been performed to assess the role of initial substrate surface on the BN-CVD process. The contradiction between our work and the other studies can be attributed to the following possibility.

It is speculated that the BN deposition can not start heterogeneously on a graphite surface because the surface does not contain active sites for the adsorption of BCl_3. Thus, the deposition process has to be initiated by other means such as: (1) the presence of impurities on the surface serving as the initial nucleation and growth sites and/or (2) physical deposition of BN molecules produced by homogenous reactions or particles nucleated in the gas phase. For the second scenario, the heterogenous deposition process is expected to be dominating over (or faster than) the homogenous nucleation process as soon as the initial BN layer is formed in order to yield smooth and dense coatings.

This speculation is supported by several experimental observations. First, when BN was deposited on graphite, the BN coating could be easily peeled off the graphite substrate. But, BN on the Al_2O_3 substrate was strongly bonded suggesting the interaction between BN and Al_2O_3 is chemical in nature rather than Van der Wall. Obviously, the Al_2O_3 surface was expected to be chemically more active than the graphite surface. In other words, the BN-CVD on graphite could not be

started heterogeneously because the adsorption (or chemisorption) of BCl_3 on the non-active graphite surface could not take place. Second, more importantly, our results have already shown that BN could not be deposited on graphite under conditions where homogeneous nucleation was negligible. Third, BN could be codeposited with AlN on graphite indicating that the presence of the foreign AlN surface apparently started the BN deposition. Therefore, our observations lead to the conclusion that the adsorption (chemisorption) of BCl_3 appeared to be the rate-limiting step for the deposition of the initial layers of BN on graphite.

By extending the above argument, the most critical and uncertain assumption which was made for the mass transfer model can be tested. In Chapter IV, it was assumed that there were no homogeneous reactions occurring in the gas phase during the BN-CVD process. Experimentally, homogeneous nucleation of BN started above 1100°C in the impinging jet geometry indicating that the homogenous reactions were fast enough to produce BN in the gas phase. At the lower temperatures (i.e., below 1100°C), BN could still be formed in the gas phase, but not to the extent necessary to cause homogenous nucleation. If the BN molecules were formed in the gas phase, they could be physically deposited on the graphite substrate, thus initiating the heterogenous deposition process. Since BN was not deposited on the graphite substrate, the amount of BN formed in the gas phase was

expected to be negligible or zero. Therefore, our assumption of "no homogenous reactions" could be indirectly validated at temperatures below 1000°C. However, it should be cautioned that the above assumption should be experimentally tested for each reactor geometry since gas phase kinetics depends strongly on the reactor configuration, reaction volume, and residence time.

The intrinsic activation energy of 39 Kcal/mole obtained in the present investigation was compared to "apparent" activation energy values reported by other investigators. The "apparent" activation energy is referred to here as the activation energy calculated without considering mass transfer contributions to the observed deposition rate. Tanji et al. calculated the apparent activation energy of the BN-CVD process to be 50 kcal/mole in the temperature range of 900 to 1250°C. Matsuda et al. [20] reported an activation energy of 32 Kcal/mole in the temperature range of 1200 to 1400°C. Also, the activation energy of 27 Kcal/mole in the temperature range of 1000 to 1300°C was calculated from data provided by Moore [7]. Several reasons were suspected for the inconsistency in the reported activation energy values. First, the BN-CVD experiments by Tanji et al. and Moore were performed in complex reactor geometries in comparison to the impinging jet geometry used in the present investigation. Tanji et al. deposited BN on a graphite rod placed coaxially along a hot-wall tube reactor. Moore used a box-shaped

graphite substrate in a commercial-scale furnace. Both Tanji et al. and Moore determined the deposition rate from the overall weight gained by the substrates. Without the aid of a two dimensional model, the mass transfer and reagent depletion contributions to the observed deposition rate could not be resolved during the activation energy calculations. Since the resolution of the kinetic and mass transfer influences on the observed deposition rate was difficult, a direct comparison of our activation energy value and theirs was inappropriate. Nevertheless, Moore's activation energy of 27 Kcal/mole was not surprising since the deposition rate was expected to be impeded due to the mass transfer contributions as well as the reagent depletions along the flow direction, thus, lowering the absolute magnitude of the activation energy. However, the discrepancy between 50 Kcal/mole reported by Tanji et al. and 39 Kcal/mole obtained from the present study could not be easily explained. However, if the deposition process of Tanji et al. involved the contribution of both heterogeneous and homogeneous deposition, the apparent activation energy may indeed be higher since the homogeneous deposition is expected to have a higher activation energy than the heterogeneous deposition. They actually reported the occurrence of homogeneous nucleation in their deposition system. But, the above argument could not be speculated further since processing

conditions resulted in homogeneous nucleation were not addressed in detail in their work.

Matsuda et al., on the other hand, used a reactor geometry which resembled an impinging jet arrangement. But, at their deposition temperature range of 1200 to 1400°C, the mass transfer contribution to the deposition rate was expected to be significant since Tanji et al. reported that the BN-CVD process appeared to be diffusion-limited above 1250°C. Malé and Salanboubat [13] also observed that the BN-CVD became diffusion-limited at about 1300 °C. Therefore, the difference of 5 Kcal between the activation energy values reported by Matsuda et al. and that obtained from the present study could probably be attributed to the fact that the mass transfer contribution to the overall deposition rate observed by Matsuda et al. was not taken into account. In principle, the CVD reactor system used by Matsuda et al. could be simulated using the CVDWYL program to verify the above speculation. But, the simulation was not possible, because the exact dimensions of their reactor system were not reported.

AlN-CVD

Eighteen AlN deposition experiments using Al_2O_3 substrates were performed as presented in Table 5-2. The crystalline structure of the AlN coatings as determined by XRD is also listed in Table 5-2. The first seven experiments (J-184 through J-589) were performed using the vertical suspension

Table 5-2. Experimental conditions for AlN-CVD experiments and crystalline structure of AlN coatings determined by XRD.

Sample #	T (°C)	P (torr)	Flow Rates (cm³/min)			Run Time (min)	Mixing Length* (cm)	Geometry**	Coating Thickness (μm)***	Crystallinity****
			$AlCl_3$	NH_3	Ar					
J-184	1200	760	3	100	1750	60	15	V	-	-
J-197	1200	760	3	100	1900	60	15	V	-	-
J-193	1200	760	5	100	1900	60	15	V	-	-
J-574	700	150	4	50	1500	60	15	V	-	PAlN
J-564	900	150	4	50	1500	60	15	V	-	CAlN
J-561	900	760	6	50	1500	60	15	V	-	CAlN
J-589	1100	150	7	50	1500	60	15	V	-	-
J-817	700	40	2.1	30	2368	40	3	I	6.0	CAlN
J-809	800	40	2.5	30	2368	40	3	I	5.8	CAlN
J-815	900	40	2.1	30	2368	40	3	I	12.5	BAlN
J-811	1000	40	2.5	30	2368	40	3	I	4.3	BAlN
J-813	1100	40	2.5	30	2368	40	3	I	1.8	-
J-807	900	40	0.9	30	2369	20	3	I	3.0	-
J-806	900	40	1.3	30	2369	40	3	I	11.1	-
J-821	900	40	4.2	30	2366	40	3	I	11.4	CAlN
J-801	900	30	2.1	30	2368	20	3	I	3.4	BAlN
J-819	900	80	3.4	30	2367	40	3	I	4.6	CAlN
J-820	900	150	3.8	30	2366	40	3	I	1.1	CAlN

* Distance from the mixing position of $AlCl_3$ and NH_3 to the substrate.

** V = vertical suspension geometry shown in Figure 3-7; I = impinging jet geometry shown in Figure 3-9.

*** Coating thickness was measured from fracture surface SEM micrographs.

**** CAlN = Anisotropic AlN; PAlN = Polycrystalline AlN; BAlN = Broad AlN peaks.

geometry (Figure 3-7) in order to determine "suitable" processing conditions for depositing high quality AlN films. The next eleven experiments (J-8xx) were performed using the impinging jet geometry (Figure 3-9) in order to study the kinetics of the AlN-CVD process. In this section, morphology and crystalline structure of the AlN coatings will be reported. Also, the kinetics and thermodynamics of the AlN-CVD process will be analyzed and discussed.

Deposition Behavior

Impinging Jet Geometry. SEM micrographs in Figures 5-23 through 5-33 show the fracture surface and surface morphology of the AlN coatings deposited using the impinging jet geometry. The micrographs were taken from the stagnation region. The coating thickness was relatively uniform in the radial direction inside of the stagnation region. The average coating thickness for each sample was measured from the micrographs, and was later used to compute deposition rate.

In general, the surface morphology of the AlN coatings was rough in comparison to that observed from the BN-CVD experiments. Also, nodules observed for the AlN coatings were larger and less-uniform in size than those of the BN coatings. For example, some of the AlN and BN coatings having similar thickness were compared. The AlN coating obtained from J-821 (Figure 5-30) had a thickness of 11.4 μm. The thickness of the BN coating obtained from J-816 (Figure 5-7) was 10.0 μm. The nodules observed for J-821 had various sizes ranging

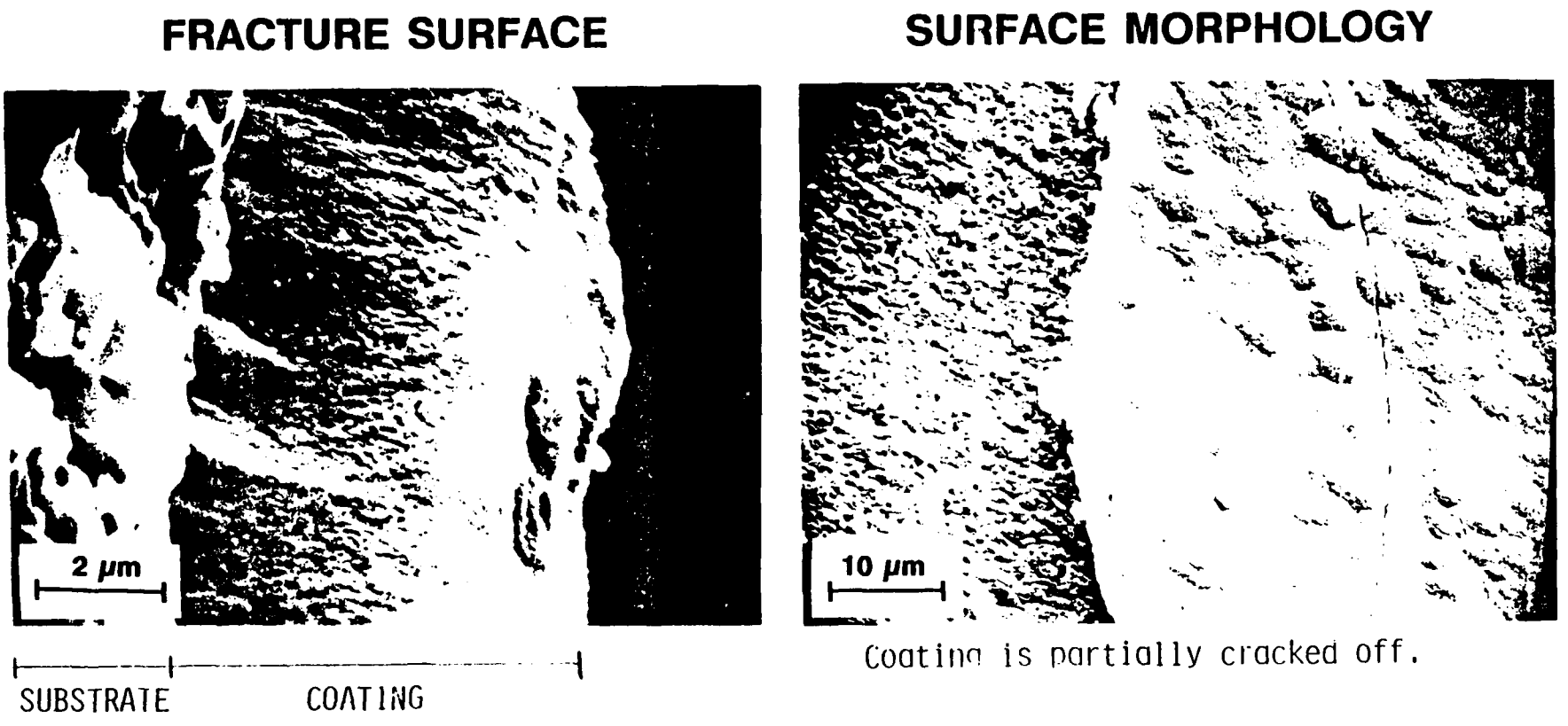

Figure 5-23. SEM micrographs of AlN (J-817).

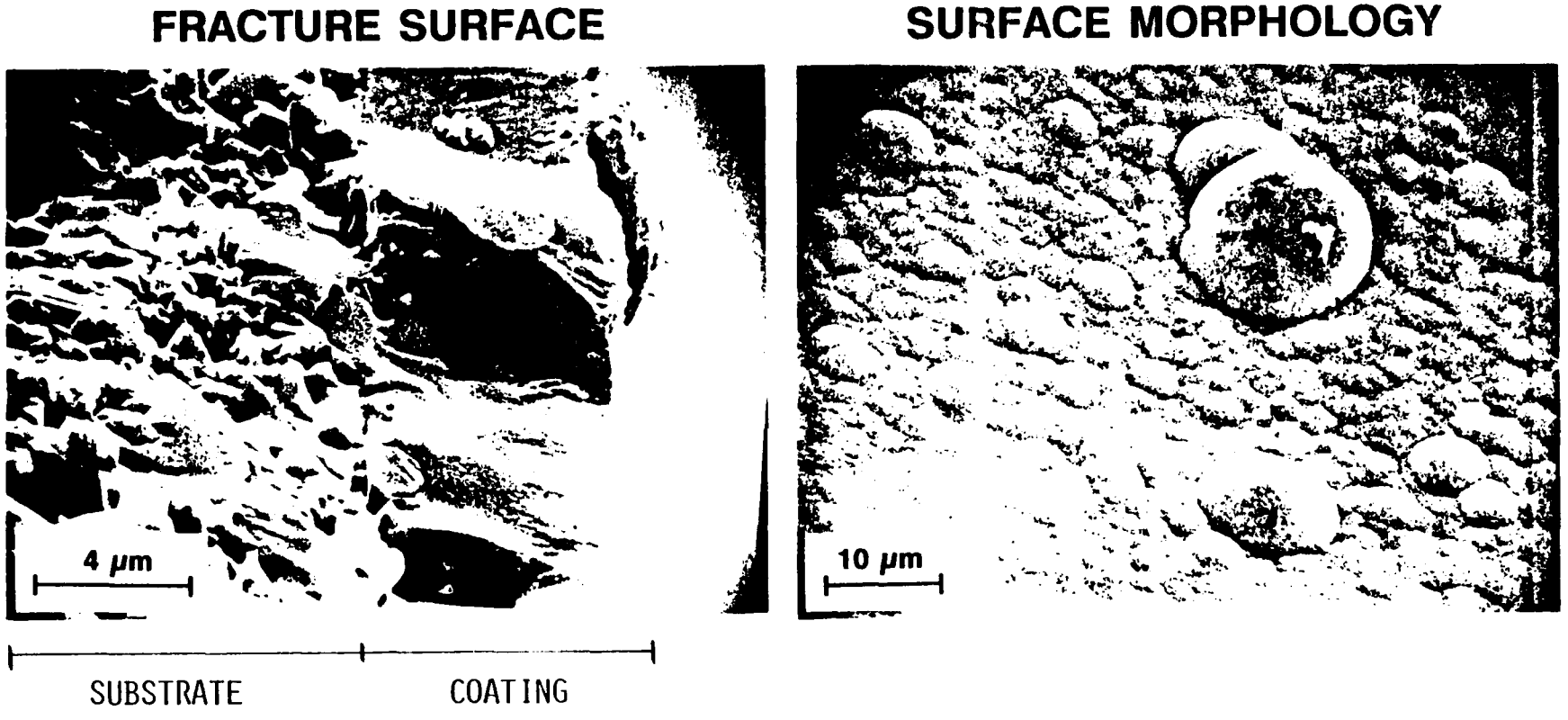

Figure 5-24. SEM micrographs of AlN (J-809).

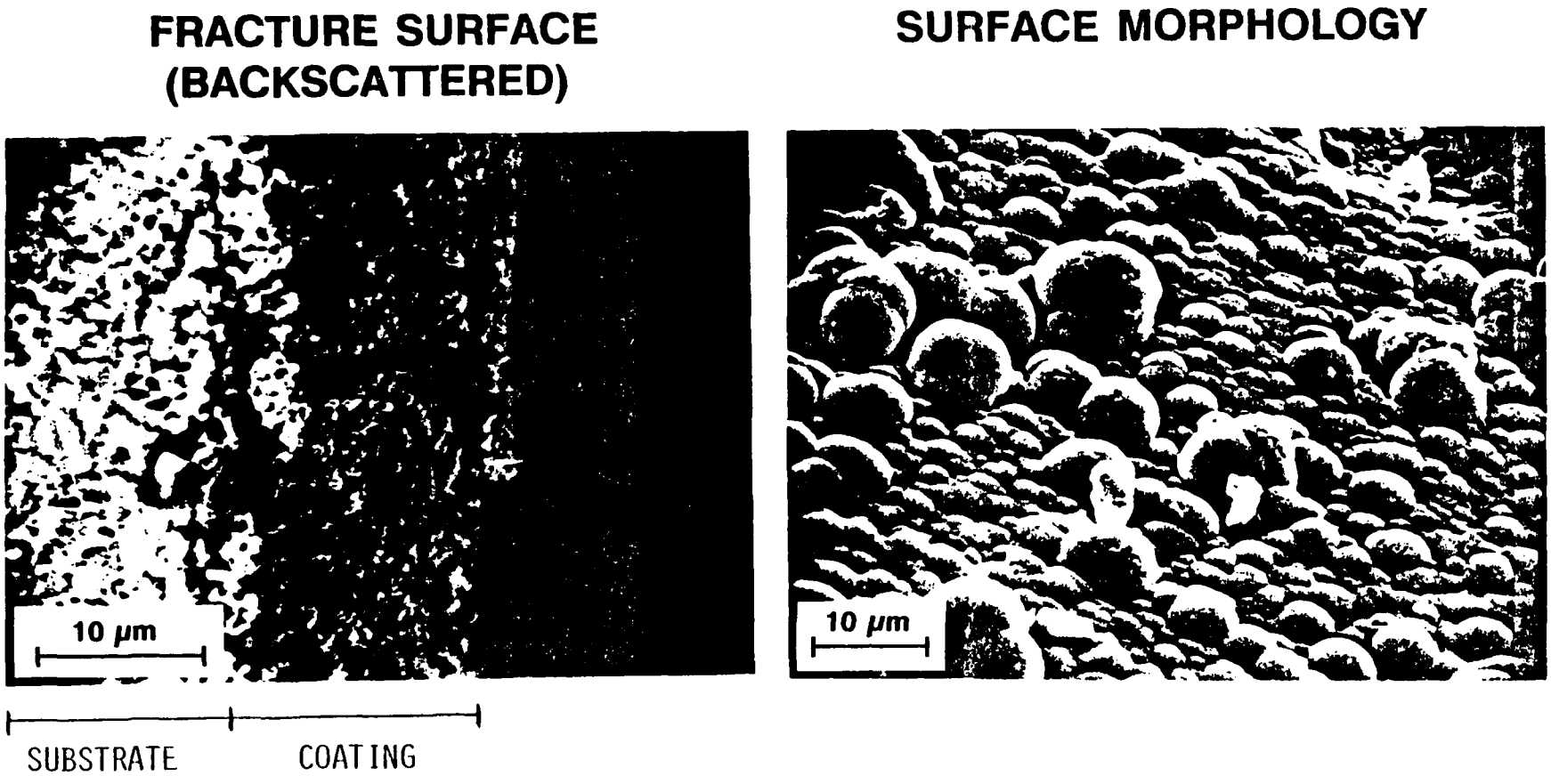

Figure 5-25. SEM micrographs of AlN (J-815).

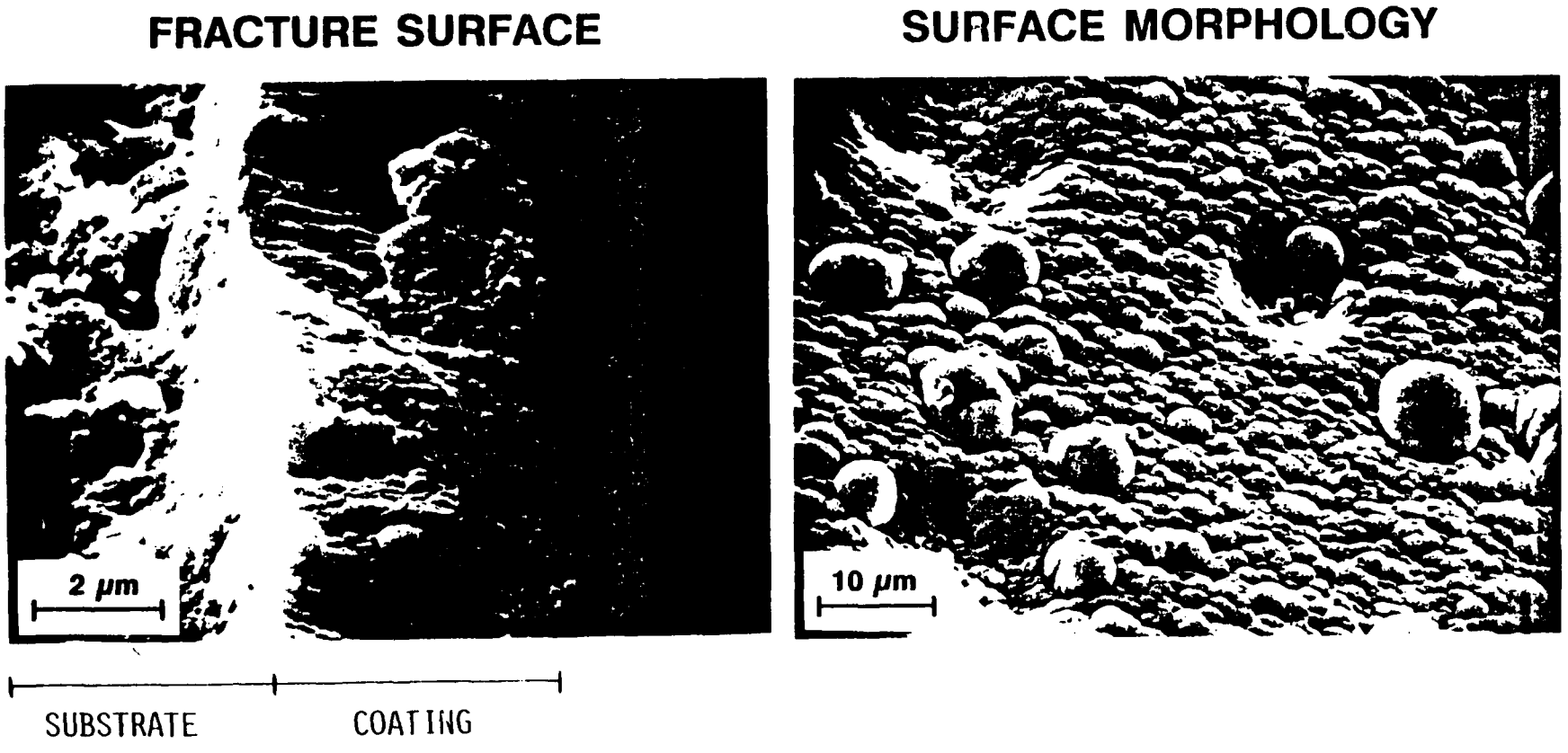

Figure 5-26. SEM micrographs of AlN (J-811).

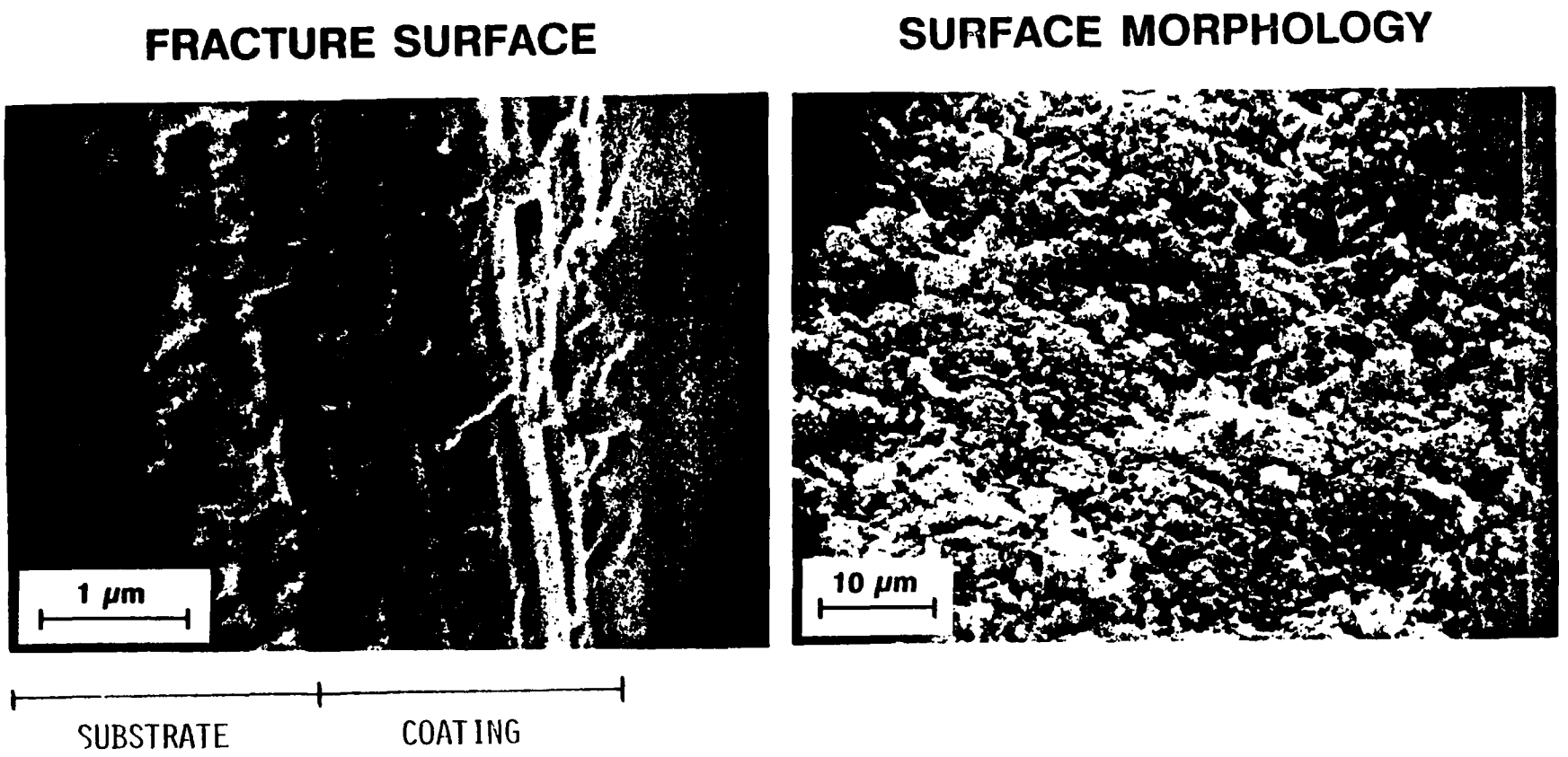

Figure 5-27. SEM micrographs of AlN (J-813).

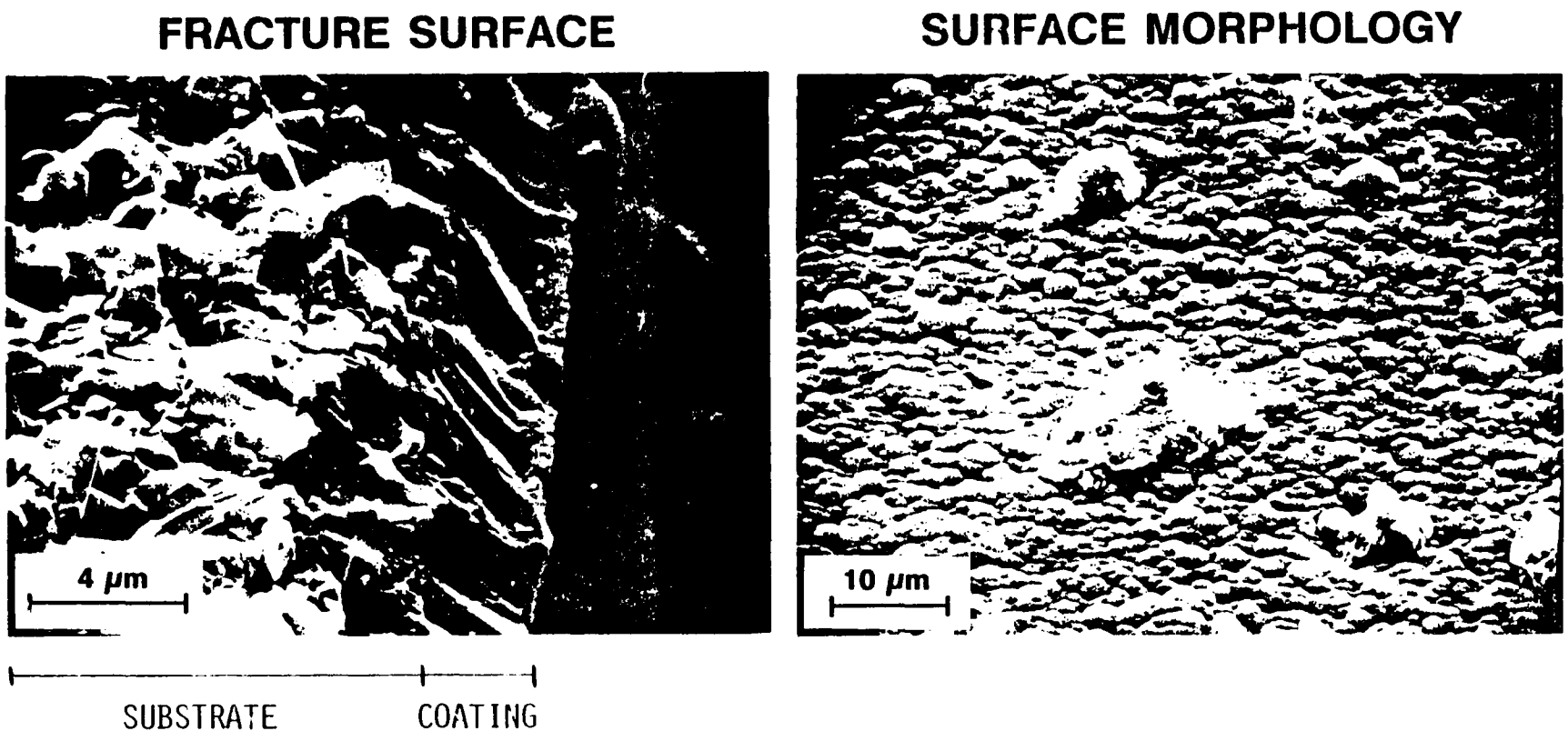

Figure 5-28. SEM micrographs of AlN (J-807).

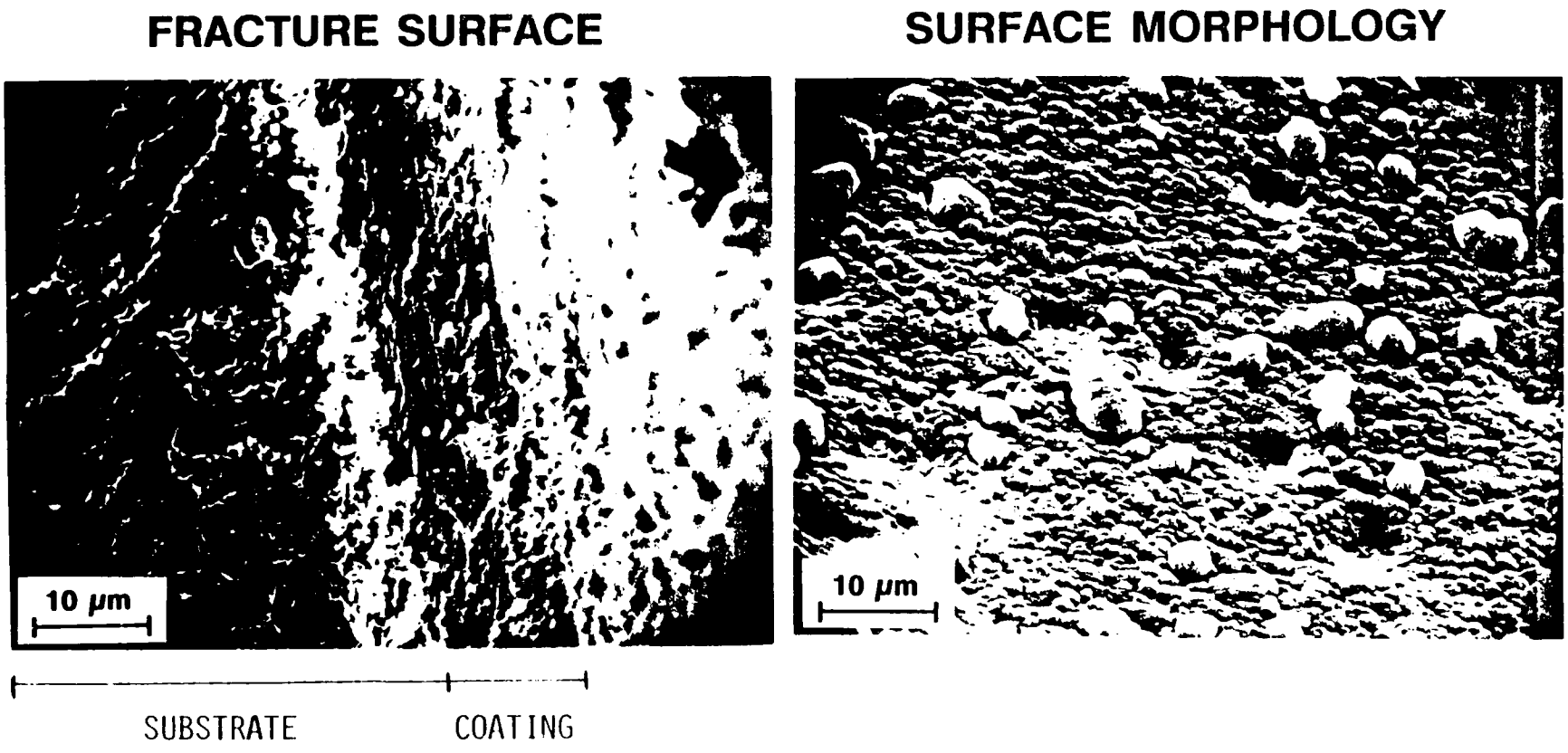

Figure 5-29. SEM micrographs of AlN (J-806).

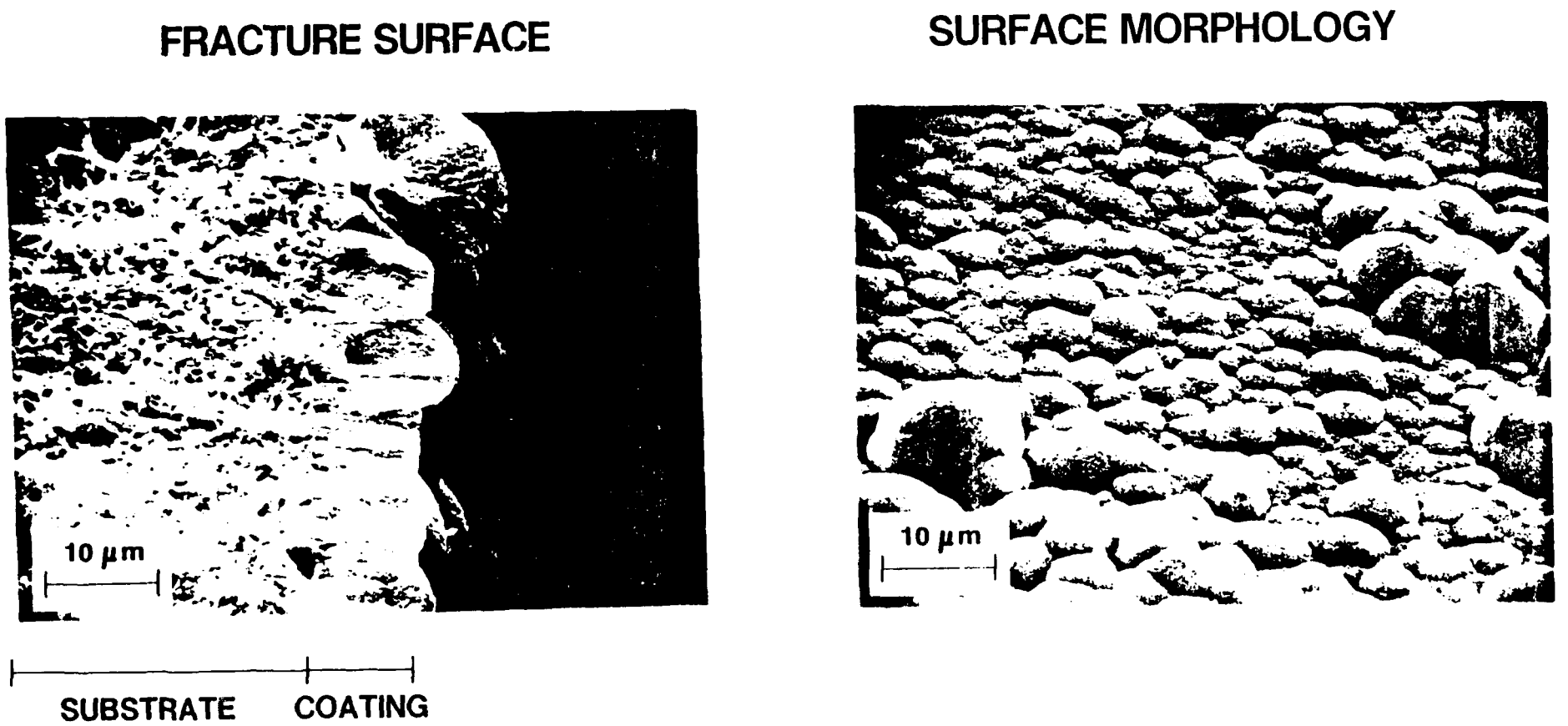

Figure 5-30. SEM micrographs of AlN (J-821).

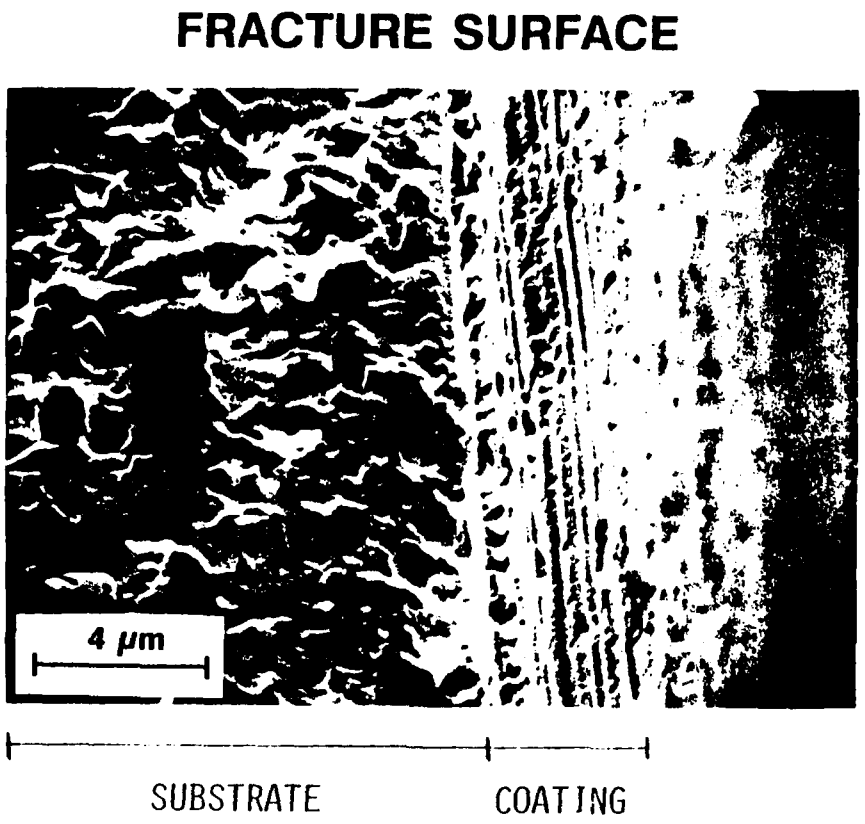

Figure 5-31. SEM micrograph of AlN (J-801).

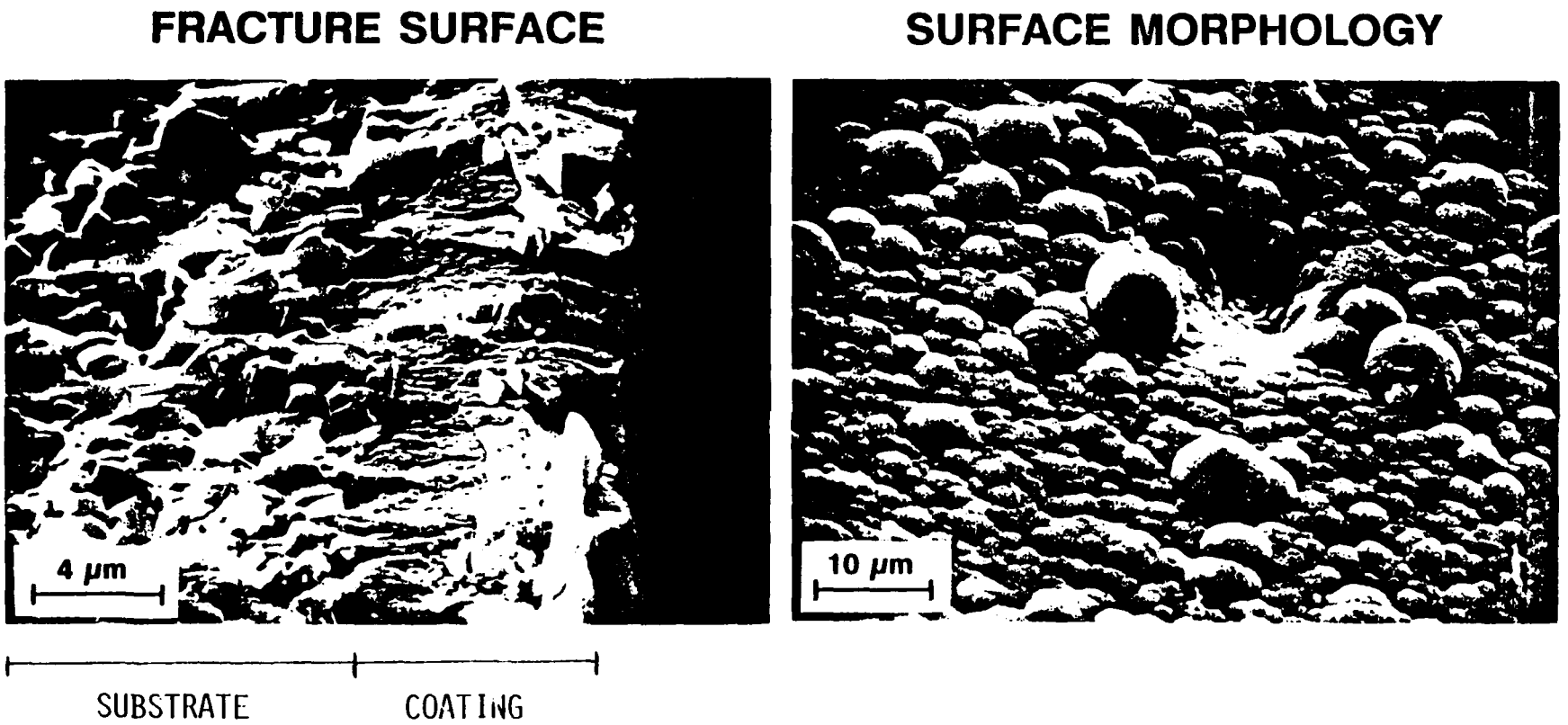

Figure 5-32. SEM micrographs of AlN (J-819).

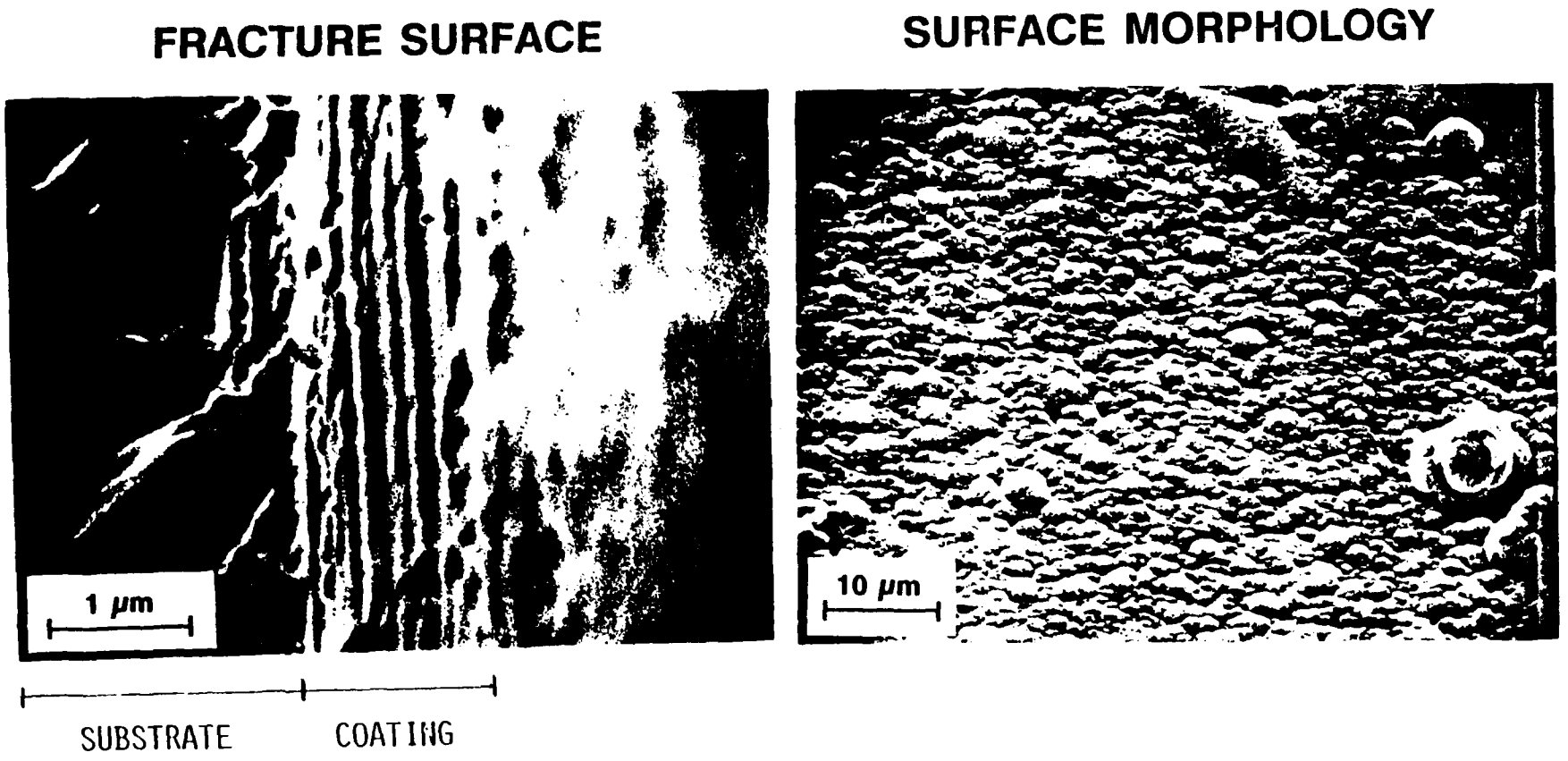

Figure 5-33. SEM micrographs of AlN (J-820).

anywhere from 2 to 12 μm. However, the nodules observed from J-816 were fairly uniform and about 3 μm in average size. Also, the nodules of the AlN coatings appeared to be more spherical than the BN nodules (see J-821 in Figure 5-30).

The average nodule size of the AlN coatings increased with the coating thickness. When the coating thickness was about 3 to 6 μm (e.g., J-817, J-809, J-811, etc.), the nodule size was in the range of about 1 to 7 μm. When the coating thickness was greater than 10 μm (e.g., J-815, J-806, J-821), the range of the nodule size was extended to about 12 μm. The apparent increase in the nodule size with the coating thickness suggested that AlN also grew in a conical fashion similar to BN. The spherical and columnar growth features observed from the fracture surface of J-821 (Figure 5-30) were indicative of the conical-type growth process. When the coating thickness was about several microns or less (e.g., J-813, J-806, J-820), a layered-morphology was observed (see Figures 5-27, 5-29, and 5-33). When the coating thickness was more than several microns, the coatings usually looked columnar (e.g., J-809, J-811, J-807, J-819, etc.).

The AlN surface was hard and could not be scratched by glass. The AlN coating deposited at 700°C (J-817) cracked and portions "popped off" the substrate as soon as it was taken out of the CVD furnace. A partially cracked region of J-817 is shown in Figure 5-23. The other J-8xx AlN coatings were, however, very adherent to the Al_2O_3 substrates.

XRD spectra of the AlN coatings (J-8xx samples) are shown in Figures 5-34 through 5-36. Also, the XRD spectra of uncoated Al_2O_3 and hot-pressed AlN (Denka, Inc.) are included in Figure 5-34 for comparison. As shown in these figures, the XRD features of the AlN coatings and therefore their crystalline structure were strongly influenced by pressure, temperature, and $AlCl_3$ concentration. This observation was in contrast with the results reported in the previous section that the crystalline structure of BN remained almost the same (i.e., turbostratic) when these variables were changed. As shown in Figure 5-34, the crystallinity of AlN increased with increasing pressure. At 40 torr (J-815), three of the major AlN peaks [(100), (002), and (101)] appeared as a single broad hump; the peaks could not be resolved. At 80 torr (J-819), the three peaks could be distinguished. The (002) peak was more intense than the other two peaks indicating preferred orientation of the AlN grains; the c-axis was perpendicular to the substrate (i.e., anisotropic AlN). For isotropic AlN, the relative intensity levels of the (100), (002), and (101) peaks are 100:60:80, respectively. On increasing the pressure to 150 torr (J-820), the (002) peak became even more intense and dominating. Therefore, the AlN became more crystalline and preferentially oriented with increasing pressure.

The effect of pressure on the AlN crystalline structure can be readily understood from a kinetic standpoint. As will be elaborated later in more detail, the deposition rate (or

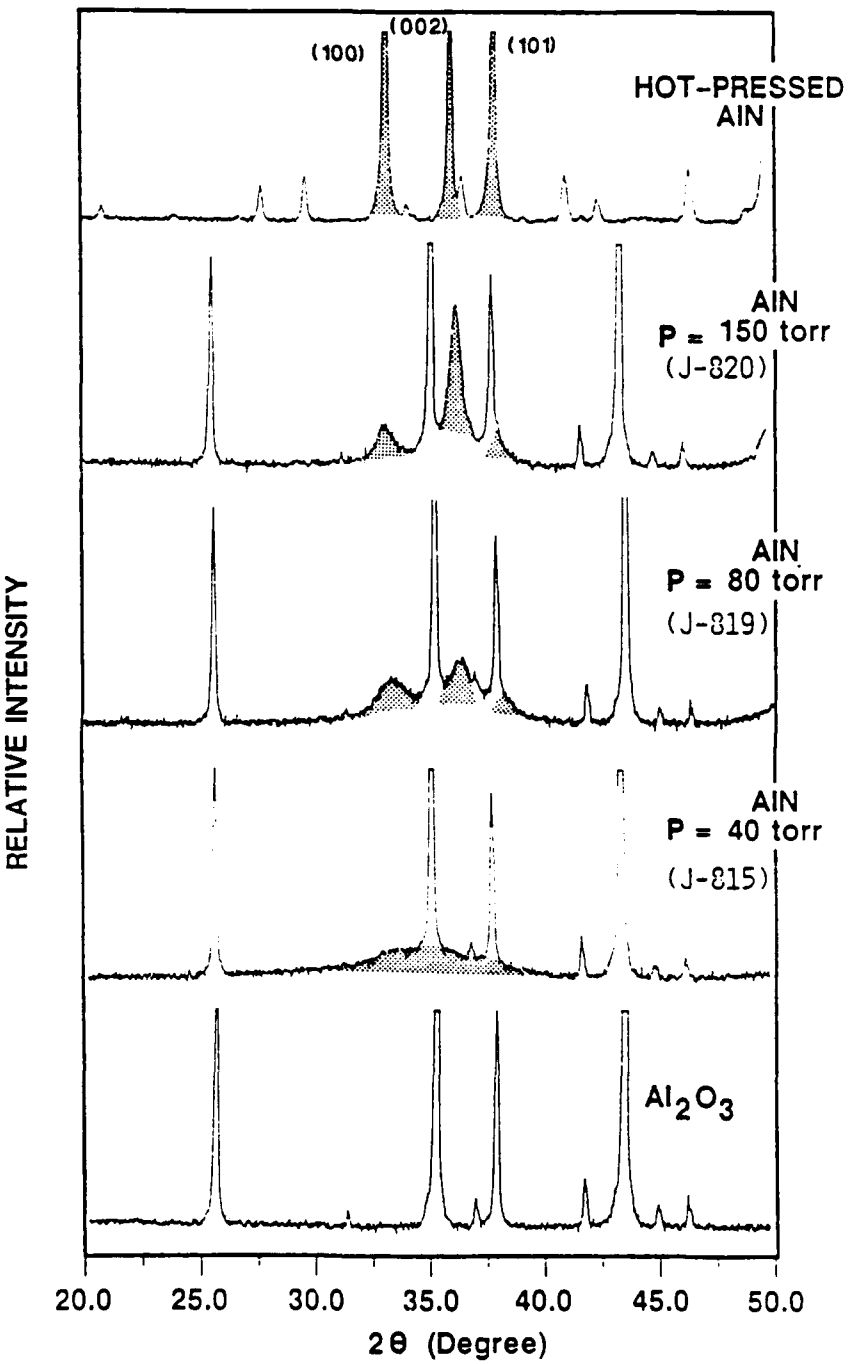

Figure 5-34. XRD patterns of AlN deposited on Al_2O_3 at various pressures (temperature = 900°C and mole fraction of AlCl, ≈ 0.001).

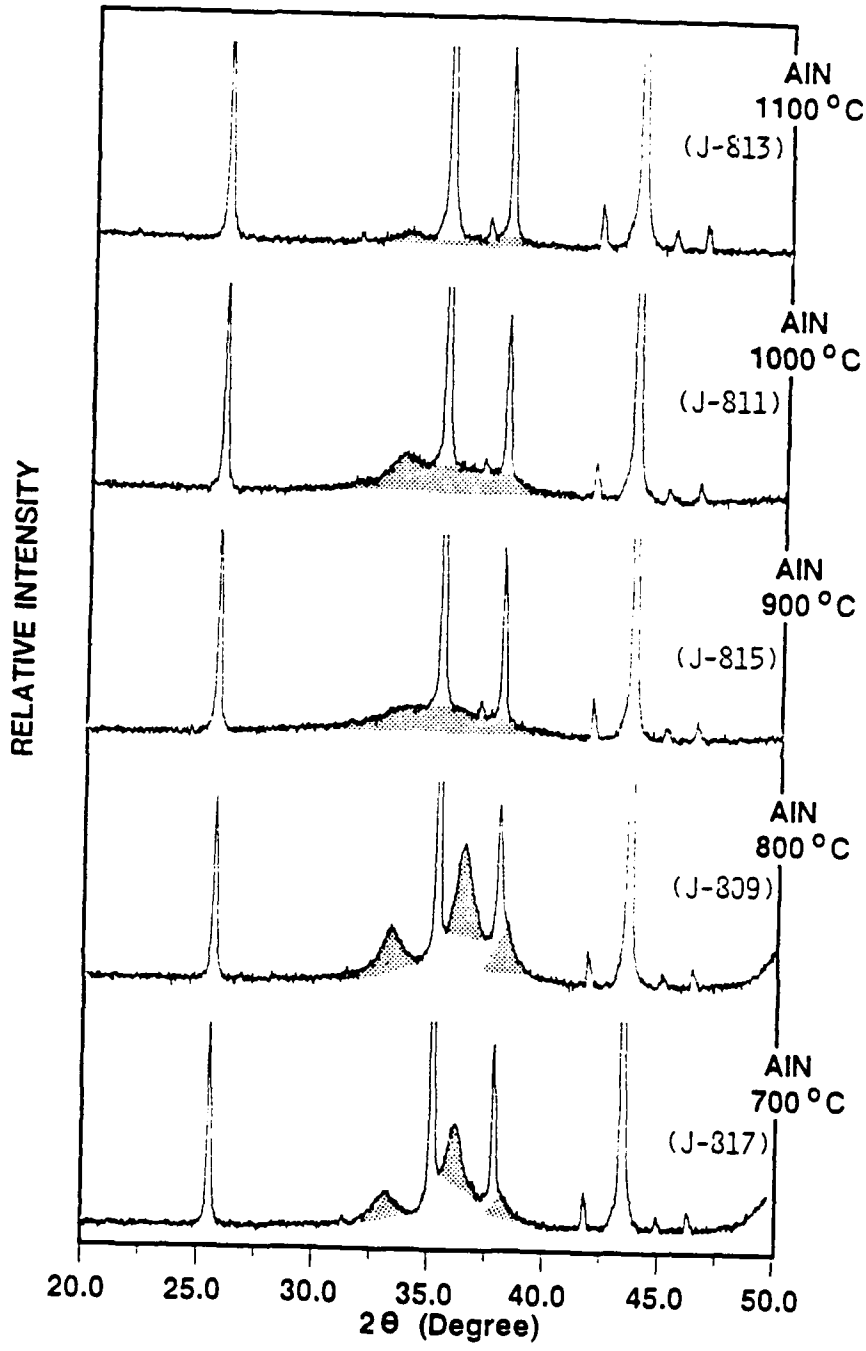

Figure 5-35. XRD patterns of AlN deposited on Al_2O_3 at various temperatures (pressure = 40 torr and mole fraction of $AlCl_3 \approx 0.001$).

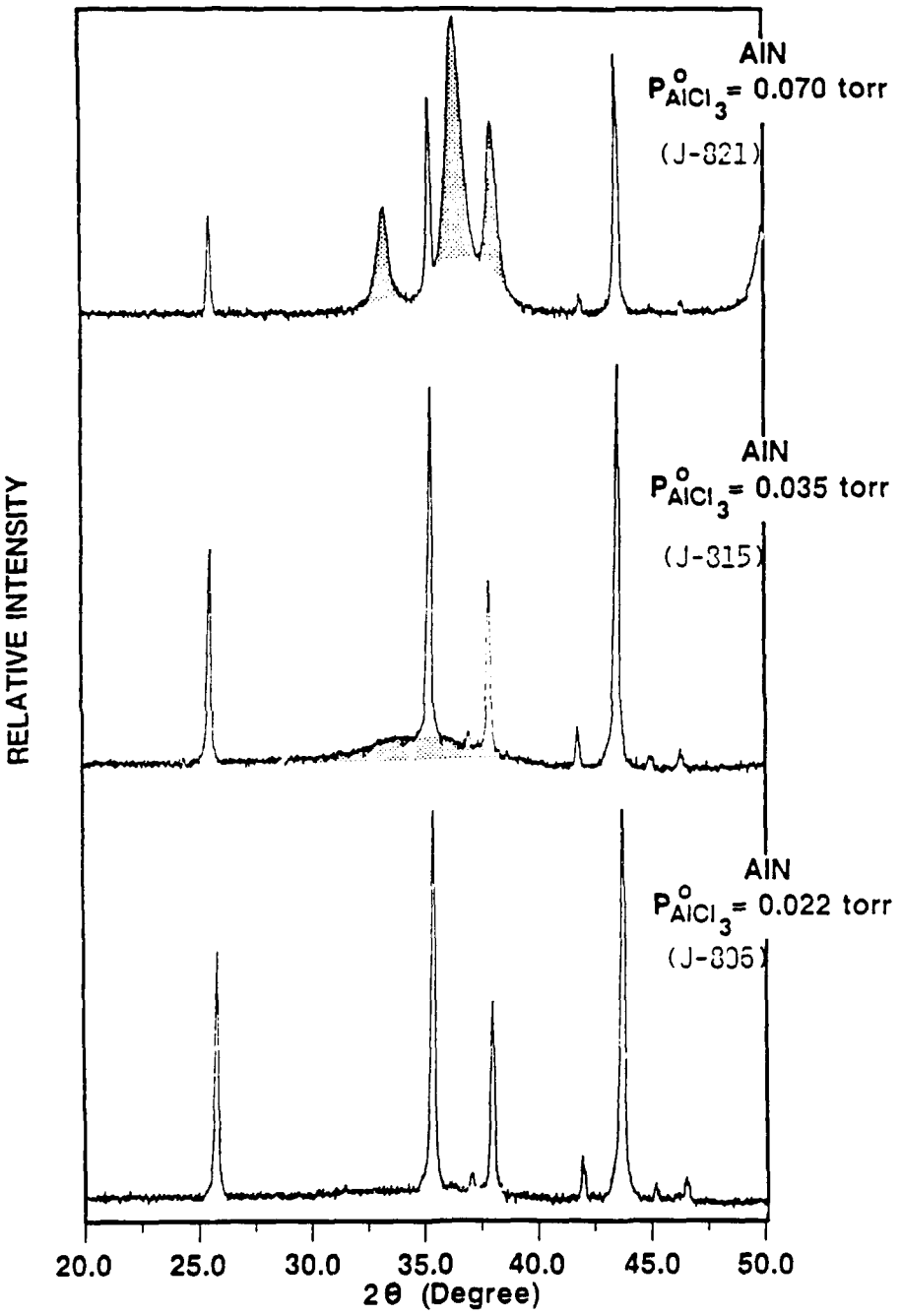

Figure 5-36. XRD patterns of AlN deposited on Al_2O_3 at various $AlCl_3$ partial pressures (temperature = 900°C and pressure = 40 torr).

coating thickness) of AlN decreased with increasing pressure. Also, as reviewed in Chapter II, the crystallinity of CVD films increases with increasing temperature or decreasing deposition rate. When the AlN deposition rate decreased with increasing pressure at 900°C, the rate of AlN production at the surface also decreased. As a result, newly formed Al, N, or AlN adatoms (or molecules) at the surface level had to go through less competition to find energetically stable crystallographic sites to form more crystalline AlN coatings.

The effect of temperature on the AlN crystalline structure was as drastic as that of pressure. As shown in Figure 5-35, the three major peaks of AlN were clearly identified and resolved for the coatings deposited at 700 (J-817) and 800°C (J-809). At these temperatures, the dominance of the (002) peak over the other two peaks indicated the AlN grains were preferentially oriented. When the deposition temperature was increased to 900°C (J-815), the sharp AlN peaks observed at the lower temperatures were replaced by a broad hump. The appearance of the broad hump was not surprising since the deposition rate of AlN was doubled with increasing temperature from 800 to 900°C (see Table 5-2).

At 1000°C (J-811), the XRD pattern did not change much from that at 900°C, but a slight increase in intensity for the (100) peak was observed. At 1100°C (J-813), the XRD features attributable to AlN were hardly noticeable. The coating thickness for the AlN coating deposited at 1100°C was 1.8 μm,

which was thick enough for the X-ray signals to be detected if the coating was crystalline. For example, AlN deposited at 900°C and 150 torr (J-820) had a thickness of only 1.1 μm, but its XRD features were highly intense as shown in Figure 5-34. Therefore, it was suspected that the AlN coating deposited at 1100°C was not highly crystalline. The lower degree of AlN crystallinity might be caused by homogenous nucleation of AlN; there were several indirect indications of homogeneous nucleation. First, some "snow-like" particles on the coating surface were observed in the SEM micrographs shown in Figure 5-27. Second, the intensity of the (100) peak appeared to be stronger than that of the (002) and (101) peaks at 1100 and 1000°C suggesting that a part of the AlN coatings might be isotropic. AlN could be isotropic only if the particles were formed in the gas phase since AlN deposited heterogeneously should become more preferentially oriented with increasing temperature.

Figure 5-36 shows the XRD patterns of AlN deposited at various inlet $AlCl_3$ partial pressures (J-806, J-815, and J-821). Although the AlN deposition rate decreased by a very small amount with increasing $AlCl_3$ partial pressure (see Table 5-2), the crystallinity of the AlN coatings increased tremendously with the $AlCl_3$ partial pressure. At an $AlCl_3$ partial pressure of 0.022, the XRD features attributable to AlN were not visible. However, at an $AlCl_3$ partial pressure

of 0.070 torr, the highly crystalline and oriented AlN phase was detected.

For the AlN coatings having the discernable and sharp (002) peak (e.g., J-820, J-819, J-817, etc.), the coatings' average grain size was estimated to be in the range of about 80 to 164 Å from the full-width at half-maximum of the peak. However, the number of the highly-crystalline AlN samples was not sufficient to observe any trends between grain size and processing variables.

The chemical composition of AlN (J-821) was determined using electron microprobe. The coating consisted of 52.1% Al (atomic%), 45.4% N, and 2.5% O indicating that the coating was rich in Al or contained an oxide phase. The elemental composition varied by no more than 2 % through the thickness of the coating.

Vertical Suspension Geometry. When the vertical suspension geometry was used (i.e., first seven experiments in Table 5-2), the AlN coating thickness was usually much higher at the bottom of the vertically suspended Al_2O_3 substrate than at the top. The thickness variation along the flow direction was not precisely measured, but was evident from SEM micrographs obtained from J-564 at various substrate positions as shown in Figure 5-37. It is noted that Figure 5-37 only shows the surface morphology. The thickness variation was measured using a micrometer. Also, a micrograph

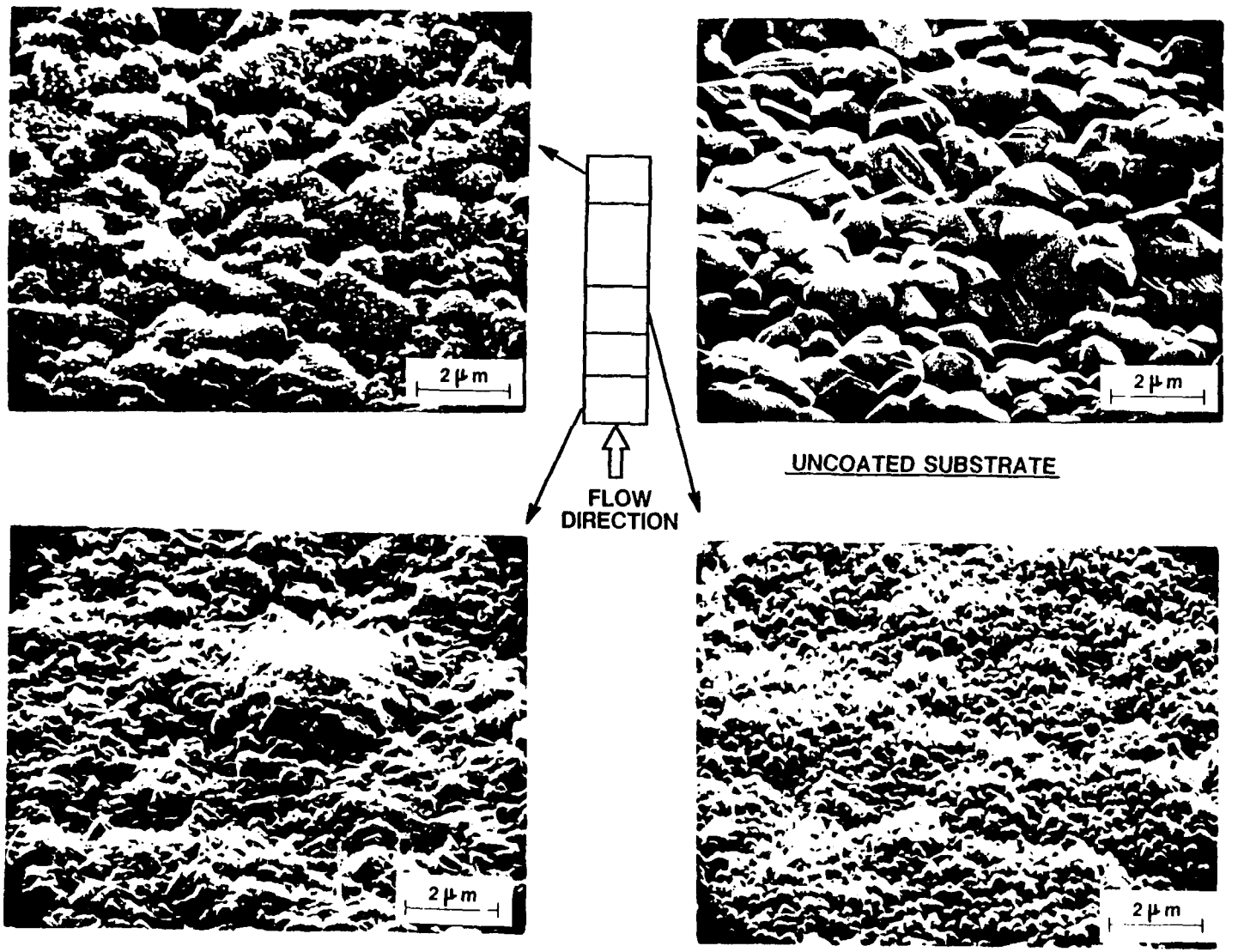

Figure 6-37. SEM micrographs of AlN (G-564) at various positions along flow direction.

of an uncoated Al_2O_3 substrate is included in Figure 5-37 for comparison.

The deposition rate decreased with increasing temperature from 700 to 1100°C (J-574, J-564, J-589) using the vertical suspension geometry. Figure 5-38 shows XRD spectra of AlN deposited at 700 and 900°C. No discernible AlN X-ray pattern was obtained for AlN deposited at 1100°C, as the amount of coating was insufficient. The slightly broadened AlN peaks at 700°C were assigned to randomly oriented polycrystalline AlN. The XRD interpretation was supported by the appearance of somewhat randomly oriented AlN whiskers in SEM micrographs as shown in Figure 5-39. An average grain size of about 120 Å was calculated based on the broadness of the (002) peak. At 900°C, the (002) peak dominated over the other major peaks indicating the presence of preferred orientation of the AlN grains.

Figure 5-40 shows a typical XPS spectrum obtained from the AlN coatings along with the corresponding surface elemental composition. The peak at 73.9 eV confirms the presence of the Al-N bonding. The small shoulder at 72.0 eV is a charging peak. Since the coating's top layers were not removed by sputtering, relatively large amounts of surface oxygen and carbon were detected.

The effect of the mixing length on the AlN deposition behavior was not studied. The AlN coatings obtained at 1200°C and 101 kPa (J-184, J-197, J-193) were suspected to be

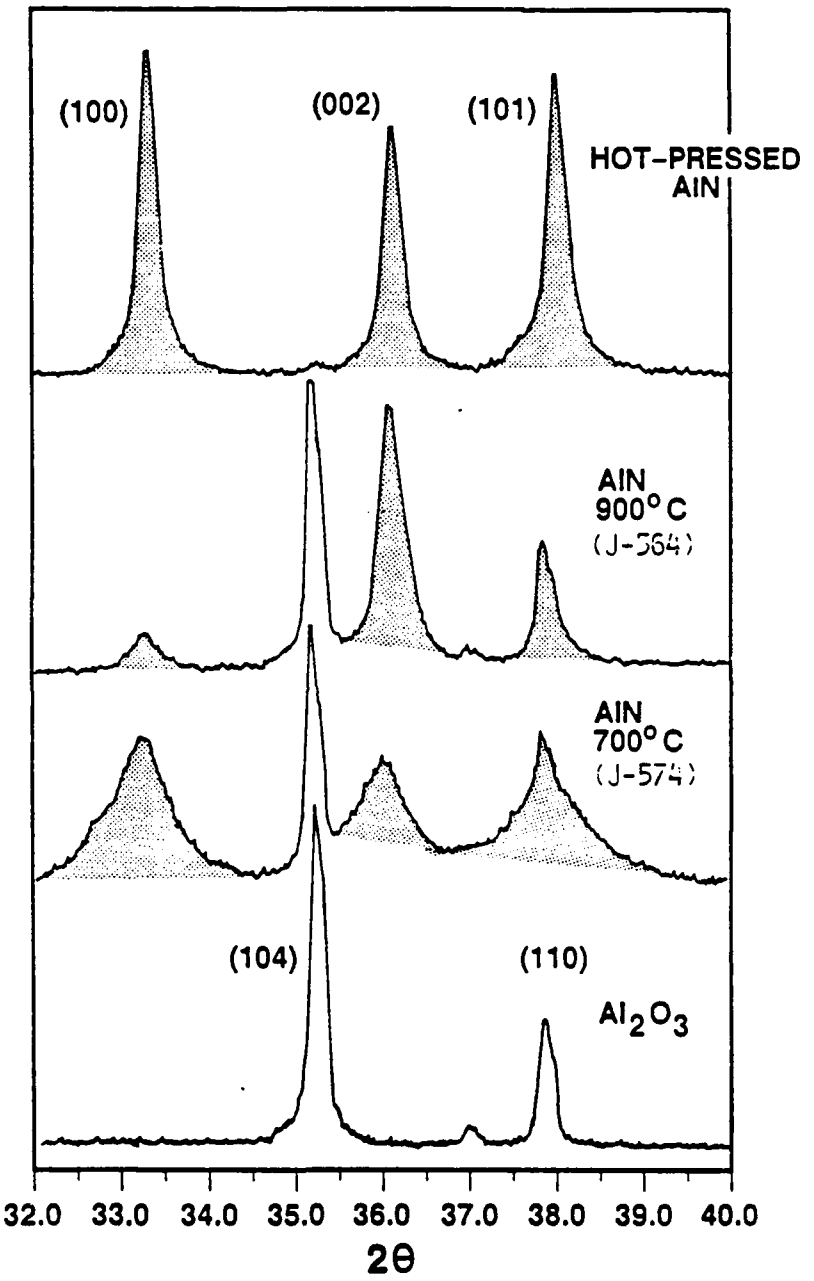

Figure 5-38. XRD patterns of AlN deposited at various temperatures using vertical suspension geometry.

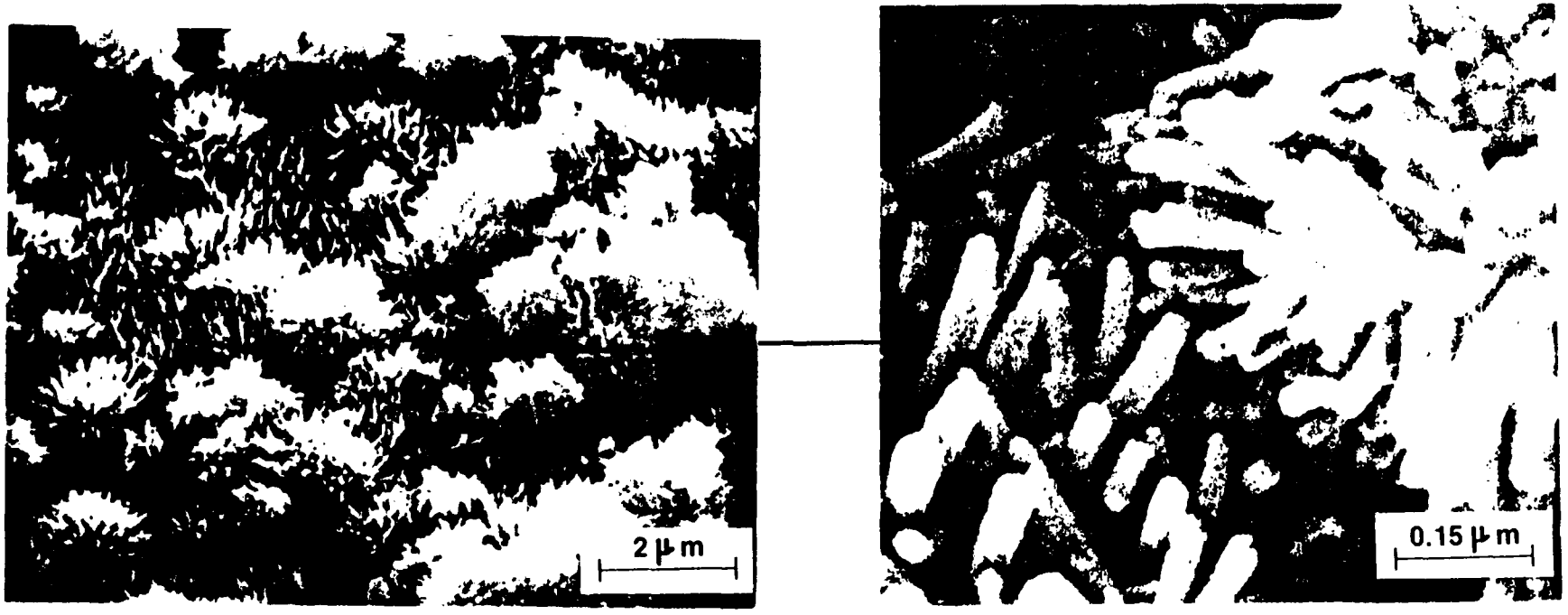

Figure 5-39. SEM micrographs of AlN whiskers deposited at 700°C (J-618).

ELEMENTAL COMPOSITION (atomic%)				
Al	N	O	C	Cl
29.4	15.5	21.7	32.2	1.5

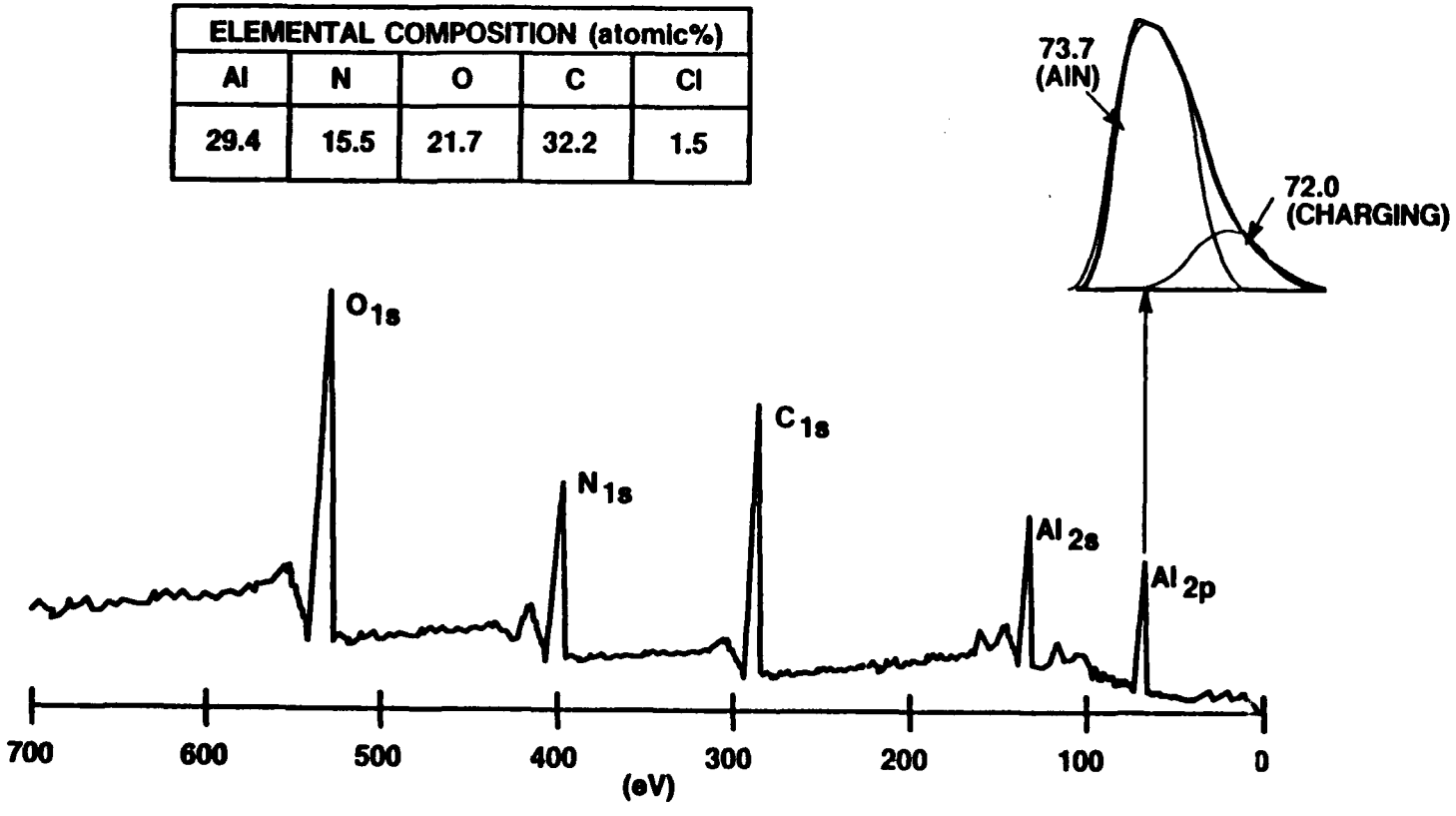

Figure 5-40. XPS spectrum of AlN.

nucleated from the gas phase as porous surfaces having small "snow-like" spherical particles were observed (See Figure 5-41). This behavior was also observed for the BN deposited at 101 kPa.

Kinetic Analysis and Interpretation

The AlN coatings obtained using the impinging jet geometry had uniform thickness inside the stagnation region. The average coating thickness, L, of each J-8xx coating was measured from the SEM micrographs shown in Figures 5-23 through 5-33. The measured thickness is listed in Table 5-2. From the coating thickness, the AlN deposition rate was determined using:

$$J_{AlN} = \frac{L\ \rho_{AlN}}{t\ M_{AlN}} \qquad (5\text{-}12)$$

where J_{AlN} is in moles/cm^2/sec, ρ_{AlN} is the density of AlN, t is the deposition time, and M_{AlN} is the molecular weight of AlN. The density of AlN was assumed to be 3.26 g/cm^3 which corresponds to the theoretical density of AlN. In the literature, Kelm [28] has been the only investigator who reported the density of AlN prepared by CVD. The AlN films deposited on silicon from $AlCl_3$*NH_3 had densities of about 3.15 to 3.2 g/cm^3. In the absence of reliable AlN density values, the theoretical density of AlN was assumed for our analysis.

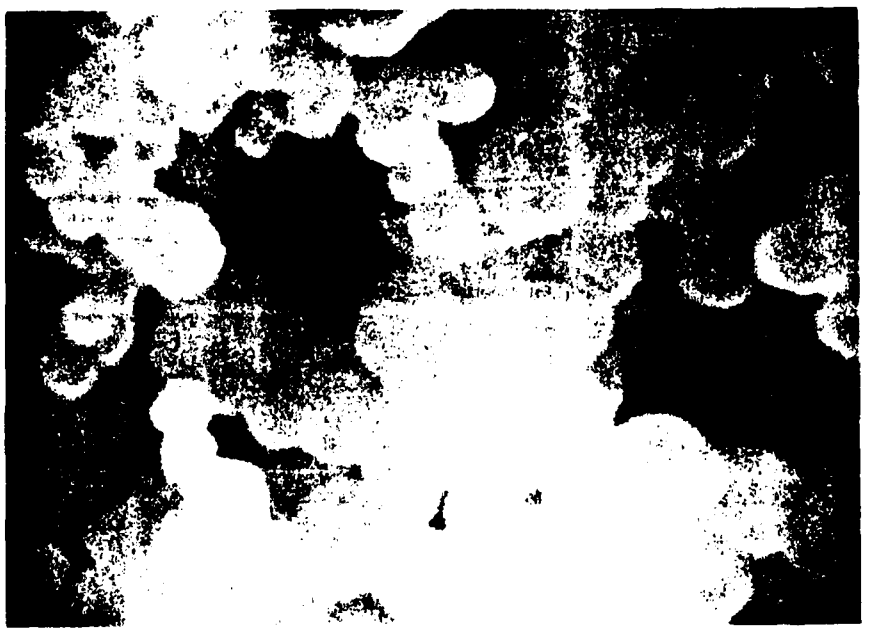

Figure 5-41. SEM micrograph of AlN showing homogenous nucleation (J-193); 2 cm = 1 μm.

As listed in Table 5-2, three types of experiments were performed in order to study the kinetics of the AlN-CVD system. First, the deposition temperature was increased from 700 to 1100°C using increments of 100°C (J-817, J-809, J-815, J-811, J-813). Second, inlet $AlCl_3$ partial pressure was varied from 0.1 to 0.3 torr at constant temperature and pressure by increasing the $AlCl_3$ flow rate while keeping the total flow rate constant at 2400 cm^3/min (J-807, J-806, J-815, J-821). Third, total pressure was varied from 30 to 150 torr at 900°C while the mole fraction of $AlCl_3$ in the reagent mixture was kept constant at 0.001 (J-801, J-815, J-819, J-820).

After performing these experiments, a surface kinetic rate equation(s) which would fit the deposition data was sought. However, the kinetics of the AlN-CVD process appeared to be fairly complex and could not easily be described by simple rate expressions. For example, the simple rate expression type of Eq. 5-2, which was sufficient in describing the BN-CVD process, was not adequate for the AlN-CVD process.

In order to understand the complexity of the AlN-CVD, several significant differences between the AlN-CVD and BN-CVD processes should be addressed. First, the Arrhenius relationship between the deposition rate and temperature observed for the BN-CVD was not apparent for the AlN-CVD in the same temperature region. Instead, the deposition rate of AlN decreased with increasing temperature from 900 to 1100°C

as shown in Figure 5-42. Second, when the pressure was increased from 40 to 150 torr, the AlN deposition rate decreased tremendously whereas the BN deposition rate increased almost linearly with pressure.

Instead of empirically fitting the deposition data, the data were first compared to "mass transfer-thermodynamic limits" (MT limits) in order to assess the role of thermodynamics in the AlN-CVD process. As discussed in Chapter IV, the MT limit is the maximum heterogeneous deposition rate obtainable in a CVD process as long as the extent of homogenous reactions and/or nucleation is not significant. As derived in Chapter IV, the MT limit $J_{AlN,mt}$ can be expressed as:

$$J_{AlN,mt} = \frac{D_{AlCl_3}}{\delta_{AlCl_3} RT} (P^{\circ}_{AlCl_3} - P^{eq}_{AlCl_3}) \qquad (5\text{-}13)$$

where $P^{\circ}_{AlCl_3}$ is the inlet $AlCl_3$ partial pressure and $P^{eq}_{AlCl_3}$ is the equilibrium partial pressure of $AlCl_3$ at the deposition surface. The magnitude of $J_{AlN,mt}$ can be calculated using the computer codes CVDWYL and SOLGASMIX. The computation procedure was previously given in Chapter IV. In Figure 5-42, $J_{AlN,mt}$ was plotted versus temperature, and was compared with the actual deposition rate. Even though the actual deposition rate was not accurately matched with the MT limits, an order-of-magnitude type approximation was possible. Since the actual deposition rate and MT limits were of the same order

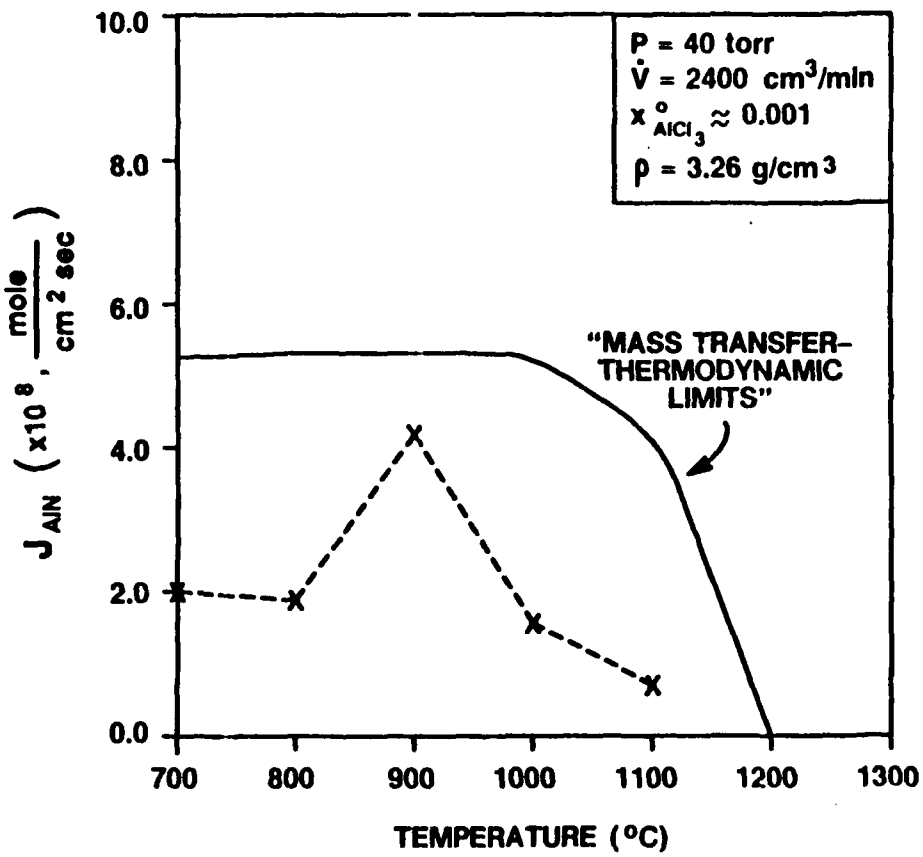

Figure 5-42. Deposition rate of AlN versus temperature and comparison to mass transfer-thermodynamic limits.

of magnitude, the kinetics of the AlN-CVD process seemed to be fairly fast, almost approaching the thermodynamic limits. More importantly, the unusual behavior of the AlN-CVD (i.e., decrease in the deposition rate with increasing temperature) was predicted by the MT limits. As shown in Figure 5-42, the MT limit started to decrease rapidly as the deposition temperature reached 1000°C, and no AlN deposition was predicted above 1200°C.

The decrease in the MT limit was caused by a decrease in the yield of AlN at equilibrium with increasing temperature. As shown in Figure 5-43, the AlN yield decreased from 83% at 700°C to 0% at 1200°C. The yield of AlN is defined here as the percentage of the $AlCl_3$ input converted to AlN at equilibrium as predicted by the SOLGASMIX calculations. The thermodynamic calculations showed that, above 1000°C, gas species like AlCl and $AlCl_2$ suddenly became much more stable in the gas phase compared to AlN, resulting in the rapid decrease in the AlN yield. Also, even the reagent specie $AlCl_3$ was found to be relatively stable up to 1000°C. Therefore, the complete conversion to AlN (100% yield) could not be thermodynamically achieved at any temperature. This should be compared to the BN-CVD system in which 100% conversion of BCl_3 to BN was predicted by SOLGASMIX at typical processing conditions.

Other investigators [32-36] also observed the decrease in the deposition rate of AlN with increasing temperature.

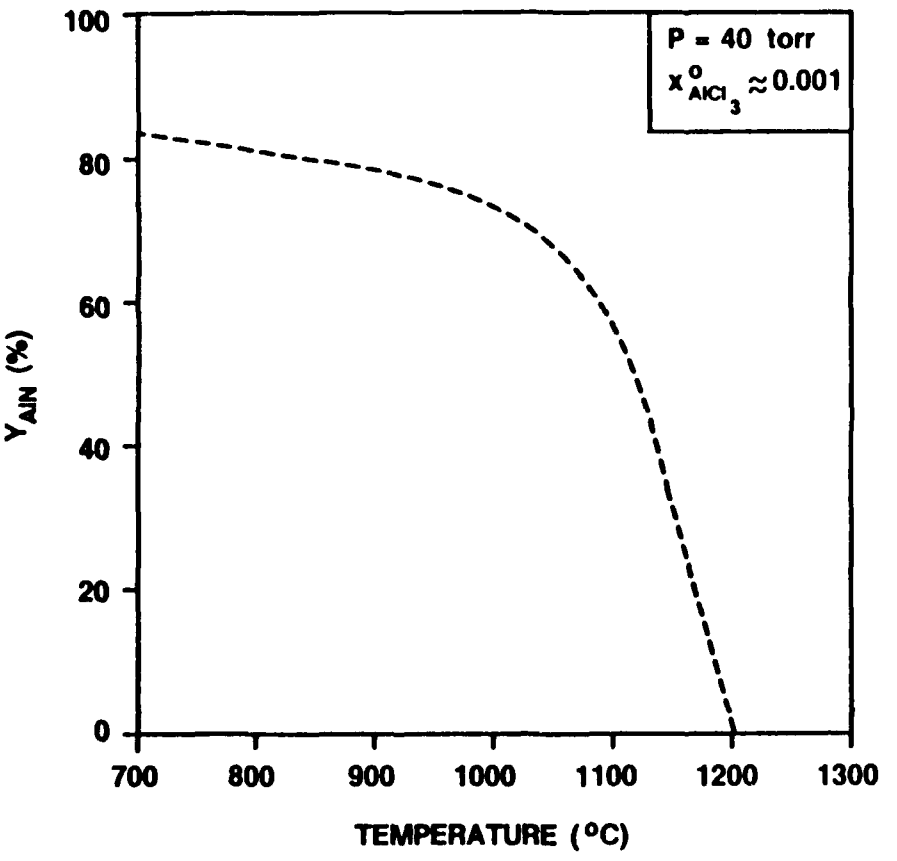

Figure 5-43. Thermodynamic yield of AlN versus temperature.

Pauleau et al. [33] cited that the reduction in the deposition rate was caused by an increase in the extent of homogenous nucleation with temperature. Also, as mentioned earlier, our XRD results indirectly indicated that homogenous nucleation might occur during the AlN deposition experiments performed at 1000 and 1100°C. Therefore, while homogenous nucleation could certainly be a possible reason for the decreased deposition rate, our thermodynamic analyses suggested that the thermodynamic yield of AlN was also another major contributor to the observed behavior.

The results from the second set of experiments were plotted and compared with the MT limits in Figure 5-44. The observed deposition rate remained relatively constant with increasing inlet $AlCl_3$ partial pressure although the rate was expected to increase from the MT limit calculations. Also, the actual deposition rate for an $AlCl_3$ partial pressure of about 0.02 torr was higher than the MT limit, which could not be possible if our assumptions were correct. However, the magnitude of the deviation was relatively small, and was within the expected uncertainties associated with the deposition data (e.g., density of AlN, absolute scale of SEM micrographs due to angle effects, etc.). Nevertheless, the actual deposition rate and the MT limits started to deviate significantly at higher $AlCl_3$ partial pressures.

Similar behavior was observed when total pressure was increased as shown in Figure 5-45. In the plot, the

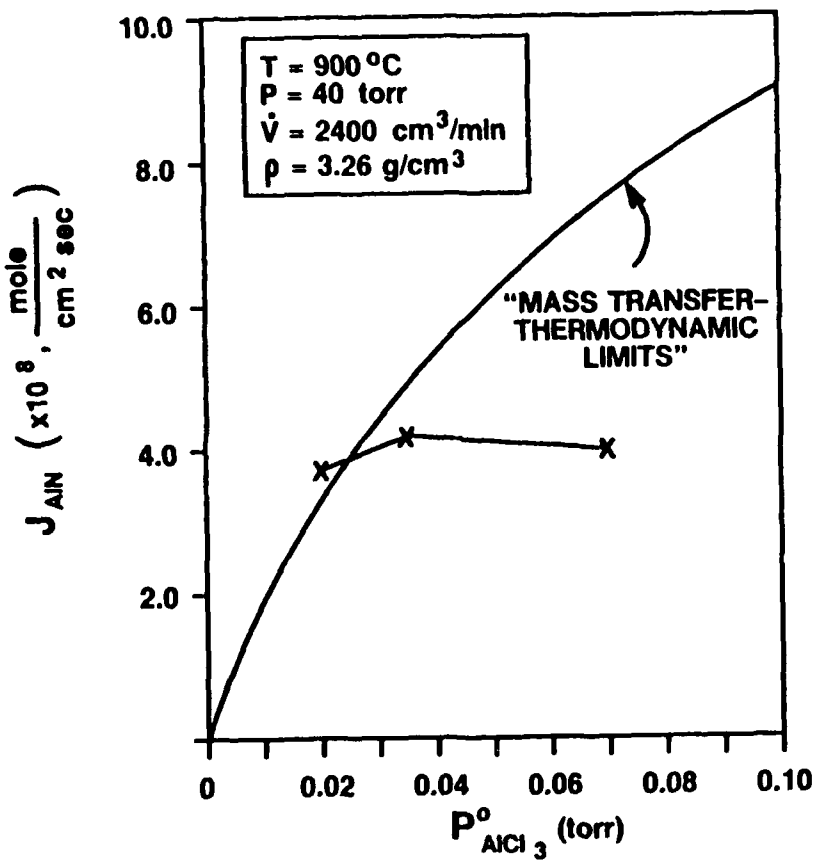

Figure 5-44. Deposition rate of AlN versus $AlCl_3$ partial pressure and comparison to mass transfer-thermodynamic limits.

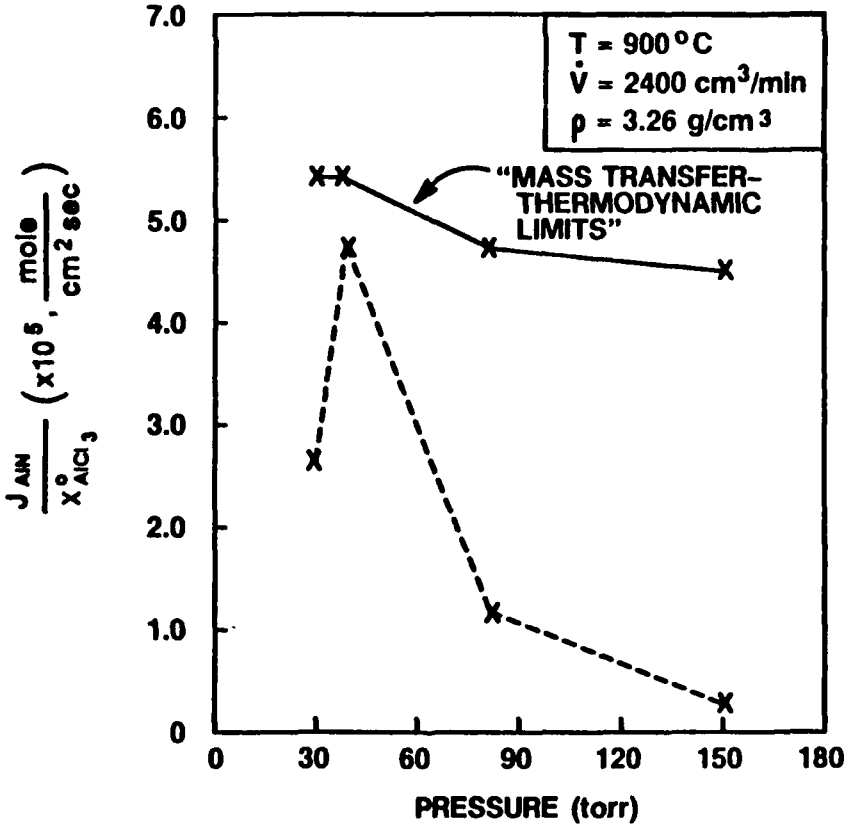

Figure 5-45. Normalized deposition rate of AlN versus pressure and comparison to mass transfer-thermodynamic limits.

deposition rate was normalized for various $x^{\circ}_{AlCl_3}$ values used for these experiments. The flow rate of $AlCl_3$ could not be kept constant since the accurate control over the vaporization of $AlCl_3$ became difficult as the $AlCl_3$ vaporizer's pressure increased with increasing furnace pressure. The actual deposition rate decreased tremendously with increasing pressure. However, the thermodynamic calculations predicted that the AlN yield at equilibrium remained essentially constant with increasing pressure. It is noted that the absolute magnitude of $J_{AlN}/x^{\circ}_{AlCl_3}$ slightly decreased because higher $x^{\circ}_{AlCl_3}$ values were used as the furnace pressure was increased (see Table 5-2).

Therefore, the last two data sets (Figures 5-44 and 5-45) suggested that the actual deposition rate deviated more significantly from the MT limits at high $AlCl_3$ concentrations (by increasing either the mole fraction of $AlCl_3$ or total pressure). Initially, homogeneous nucleation was suspected as a possible source for the deviation. However, the XRD studies already indicated that the AlN coatings obtained at the high $AlCl_3$ concentrations became more crystalline and preferentially oriented (see Figures 5-35 and 5-36) although the coating thickness became smaller. If the extent of homogeneous nucleation became more significant with increasing $AlCl_3$ concentration, the coatings' crystalline structure should become more isotropic and/or amorphous. Therefore, the possibility of homogenous nucleation was discarded.

While the decrease in the AlN deposition rate with increasing $AlCl_3$ concentration could not be explained by either thermodynamics or homogenous nucleation, the last two data sets could be empirically fitted using the following kinetic rate expression:

$$J_{AlN} = \frac{k_{AlN} P^{s}_{AlCl_3}}{(1 + K_{AlN} P^{s}_{AlCl_3})^2} \qquad (5\text{-}14)$$

where k_{AlN} is a rate constant and K_{AlN} is the equilibrium adsorption constant of $AlCl_3$. Eq. 5-14 can be rewritten in the form of y = mx + b:

$$\left(\frac{P^{s}_{AlCl_3}}{J_{AlN}}\right)^{1/2} = \frac{K_{AlN}}{k_{AlN}^{1/2}} (P^{s}_{AlCl_3}) + \frac{1}{k_{AlN}^{1/2}} \qquad (5\text{-}15)$$

Since the net mass transfer rate of $AlCl_3$ should be the same as the consumption rate of $AlCl_3$ (or production rate of AlN) at the deposition surface, $P^{s}_{AlCl_3}$ can simply be determined using the following mass transfer equation:

$$J_{AlN} = \frac{D_{AlCl_3}}{\delta_{AlCl_3} RT} (P^{o}_{AlCl_3} - P^{s}_{AlCl_3}) \qquad (5\text{-}16)$$

As shown in Figure 5-46, the linear relationship between $(P^{s}_{AlCl_3}/J_{AlN})^{1/2}$ and $P^{s}_{AlCl_3}$ indicated that Eq. 5-14 might represent the kinetics of the AlN-CVD process for high $AlCl_3$ concentrations.

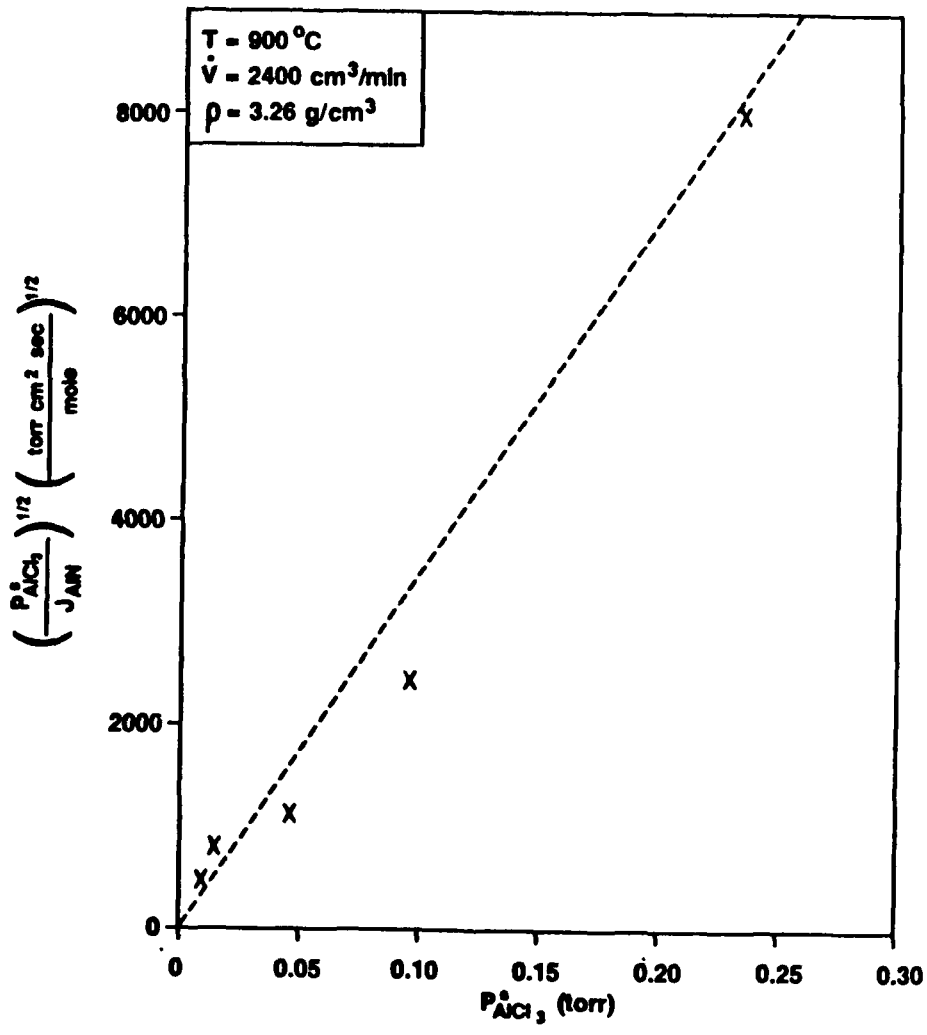

Figure 5-46. $(P^{s}_{AlCl3}/J_{AlN})^{\frac{1}{2}}$ versus P^{s}_{AlCl3}.

The intercept $1/k_{AlN}^{1/2}$ of the straight line was very close to zero so the magnitude of $k_{AlN}^{1/2}$ was expected to be very high. Also, the magnitude of the slope $K_{AlN}/k_{AlN}^{1/2}$ was high. Therefore, Eq. 5-14 can be approximated as:

$$J_{AlN} \approx \frac{k_{AlN}}{K_{AlN}^{2}\ P^{s}_{AlCl_3}} \qquad (5\text{-}17)$$

It is obvious from Eq. 5-17 that the deposition rate would decrease with increasing pressure or partial pressure of $AlCl_3$.

A possible surface kinetic mechanism which would be represented by Eq. 5-14 can be postulated. If the rate limiting step is a surface reaction between adsorbed $AlCl_3$ and a vacant surface site, the deposition rate can be expressed as [99]:

$$J_{AlN} = k_{AlN}\ \theta_{AlCl_3}\ \theta_v \qquad (5\text{-}18)$$

Using the Langmuir equation, Eq. 5-18 can be written as:

$$J_{AlN} = \frac{k_{AlN} P^{s}_{AlCl_3}}{(1 + \Sigma\ K_i P^{s}_{i})^{2}} \qquad (5\text{-}19)$$

Also, if gas species other than $AlCl_3$ are weakly adsorbed on the surface, Eq. 5-19 essentially reduces to Eq. 5-14.

It should be cautioned that the above derived kinetic mechanism portrayed a highly idealized situation with the limited kinetic data. Nevertheless, at high $AlCl_3$

concentrations, the AlN-CVD process could be described by the relatively simple surface reaction mechanism involving $AlCl_3$ adsorbed on the deposition surface. On the other hand, at low $AlCl_3$ concentrations or temperatures above 1000°C, the AlN-CVD process could be approximated by calculating the mass transfer-thermodynamic limits. Therefore, by utilizing the two models (i.e., mass transfer-thermodynamic limits and adsorption mechanism of $AlCl_3$), the deposition behavior of the AlN-CVD system can be predicted over a fairly wide range of processing conditions.

BN+AlN-CVD

This section starts with an overview of our experimental approaches which were used to solve some of difficulties encountered in studying the BN+AlN-CVD system. The overview summarizes several different types of codeposition experiments performed during the present investigation. In the next section, microstructure and morphology of the BN+AlN composite coatings will be discussed. The relationship between the coatings' microstructure and processing parameters will be analyzed and compared with those observed for the BN-CVD and AlN-CVD processes. Finally, the deposition data will be compared with predictions from the SOLGASMIX calculations in order to test the predictive capability of the thermodynamic calculations as well as to address their limitations.

Overview

More than 120 codeposition experiments were attempted in the present investigation. During the early stages of the investigation, the CVD furnace system was often clogged by either condensation of $AlCl_3$ and BCl_3 in the upstream or formation of NH_4Cl powder in the downstream. Due to the clogging problem, many deposition runs had to be aborted or their exact flow conditions could not be determined (accounting for about the one-fourth of the total experiments performed during this investigation). As discussed in Chapter III, the condensation of $AlCl_3$ and BCl_3 could be effectively minimized by heat tracing reagent lines and circulating hot oil through the injector. Also, the exhaust line and scrubber were frequently cleaned to remove the NH_4Cl powder build-up in the downstream. The powder build-up usually reduced the pumping efficiency resulting in an undesired pressure rise during low pressure CVD operations.

While the clogging problem was being dealt with, thirteen codeposition experiments were carried out using the vertical suspension geometry (Figure 3-7) over a wide range of processing conditions as tabulated in Table 5-3. Due to the condensation of $AlCl_3$ inside the injector, the stability and continuity of $AlCl_3$ flow into the furnace with respect to time could not be accurately assessed. The injector was weighed before and after the deposition runs to estimate the actual $AlCl_3$ flow rate into the furnace. Nevertheless, the coatings

Table 5-3. Experimental conditions for BN+AlN-CVD experiments performed using the vertical suspension geometry shown in Figure 3-7. Crystalline structure of BN+AlN coatings was determined by XRD.

Sample #	T (°C)	P (torr)	Flow Rates (cm³/min)					Run Time (min)	Mixing Length* (cm)	Crystallinity** (BN/AlN)
			BCl_3	$AlCl_3$	NH_3	H_2	Ar			
J-217	1200	760	25	6	100	-	3200	60	15	- /CAlN
J-221	1200	760	25	6	100	200	3200	60	15	- /CAlN
J-225	1200	760	14	6	212	250	3200	60	15	- /CAlN
J-594	700	150	10	8	50	-	1500	60	15	- / -
J-586	900	150	5	4	50	-	1500	120	15	- /CAlN
J-566	900	150	10	2	50	-	1500	60	15	- /PAlN
J-601	1100	150	10	6	50	-	1500	60	5	- /CAlN
J-621	900	150	10	7	50	-	1430	90	5	- /CAlN
J-645	900	150	30	6	50	100	1840	60	5	TBN/ -
J-655	900	150	10	10	50	100	1940	60	5	TBN/ -
J-627	1100	150	10	7	50	-	1430	60	5	- /CAlN
J-629	1100	150	10	8	50	100	1330	60	5	- /CAlN
J-651	1100	150	10	4	50	-	1940	60	5	TBN/ -

* Distance from the mixing position of $BCl_3/AlCl_3$ and NH_3 to the substrate.

** TBN = Turbostratic BN, PAlN = Polycrystalline AlN, CAlN = Anisotropic AlN.

were found to contain discrete BN and AlN phases. Furthermore, it was determined that the coatings' microstructure was strongly influenced by the processing variables.

However, in order to determine the intrinsic relationship between the microstructure and processing conditions, the vertical suspension geometry was found to be "unsuitable" for the following reasons. First, the flow pattern inside the furnace chamber sometimes deviated significantly from the expected fully developed and mixed flow due to channeling, improper mixing of reagents, etc., which were evidenced by some unexplainable observations such as non-uniform bands and sections of coatings on the same substrate. Second, the effects of mass transfer and reagent depletions along the flow direction on the coatings' composition and microstructure could not be readily resolved since the kinetics of the CVD process was not known. Therefore, a simpler geometry was preferred, and the impinging jet geometry shown in Figure 3-8 was chosen. The advantages of the geometry were previously described in Chapters II, III, and IV.

As summarized in Table 5-4, fifty-four codeposition experiments were performed using the impinging jet geometry shown in Figure 3-8. The composite coatings deposited from the first six experiments in Table 5-4 were extensively characterized by various techniques including XRD, SEM, electron microprobe, electron diffraction, TEM, ultra high

Table 5-4. Experimental conditions (or ranges) for BN+AlN-CVD experiments performed using the impinging jet geometry shown in Figure 3-8. Crystalline structure of BN+AlN coatings was determined by XRD.

Sample #	T (°C)	P (torr)	Flow Rates (cm³/min)					Run Time (min)	Mixing Hole Diameter (cm)	Crystallinity** (BN/AlN)
			BCl_3	$AlCl_3$	NH_3	H_2	Ar			
J-699	727	150	6	21	75	100	1900	60	NM*	- /PAlN
J-724	927	75	3	10	35	50	950	60	NM*	- /CAlN
J-729	927	75	3	6	40	50	950	60	2.54	- /CAlN
J-738	927	150	6	13	75	100	1900	60	2.54	- /CAlN
J-746	1127	150	10	5	50	-	1900	60	2.54	TBN/CAlN
J-747	1127	150	10	5	50	-	1900	60	2.54	TBN/CAlN
J-751 to J-769	800 to 1100	75 to 150	5 to 10	4.5 to 22.4	50	-	885 to 935	30	0.64	various combinations
(19 experiments)										
J-770 to J-798	900	15 to 150	6 to 10	1.7 to 10.6	50	-	935 to 2940	5 to 30	0.95 to 1.59	various combinations
(29 experiments)										
J-799	900	30	6	2.5	30	-	2361	20	1.59	TBN/CAlN

* NM = no mixing disc was used.

** TBN = Turbostratic BN, PAlN = Polycrystalline AlN, CAlN = Anisotropic AlN.

resolution TEM, etc. The coatings were usually thick and very adherent to the Al_2O_3 substrates. The characterization results will be discussed in detail in the next subsection. The coating characteristics (i.e., thickness, color, and composition) were not uniform in the radial direction inside of the stagnation region due to the improper mixing of reagent streams (described in Chapter III).

The next 19 experiments (J-751 through J-769) were performed using a mixing nozzle diameter of 0.64 cm (0.25 inches). This nozzle diameter was smaller than the outside diameter of the graphite extension tube (1.59 cm) so that the outer reagent stream containing NH_3 and Ar was forced to converge with the inner stream containing BCl_3, $AlCl_3$, and Ar. But, the reduction in the nozzle diameter had several, very severe undesirable effects. First, homogenous nucleation was more frequently observed in comparison to when the larger nozzle diameter (2.54 cm) was used. As an example, a micrograph of a typical coating obtained from these experiments (J-760) is shown in Figure 5-47. The spherical particles were less than 0.5 μm in size and were believed to be nucleated from the gas phase. Second, even when homogenous nucleation was not apparently visible, the surface coating morphology was very rough because the growth process was too rapid as shown in Figure 5-48. The coating deposited near the center position of the stagnation region was much rougher than that deposited outside of the stagnation region.

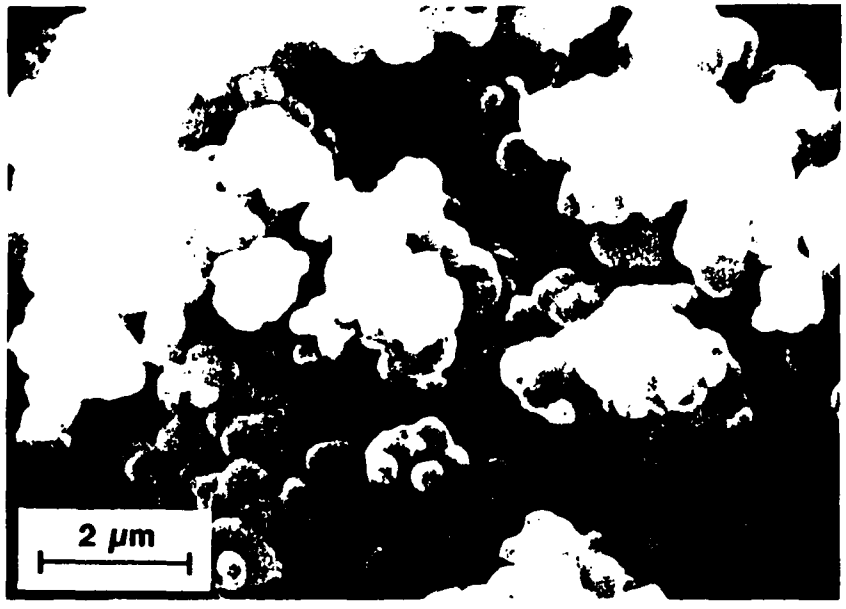

Figure 5-47. SEM micrograph of powdery BN+AlN coating (J-760).

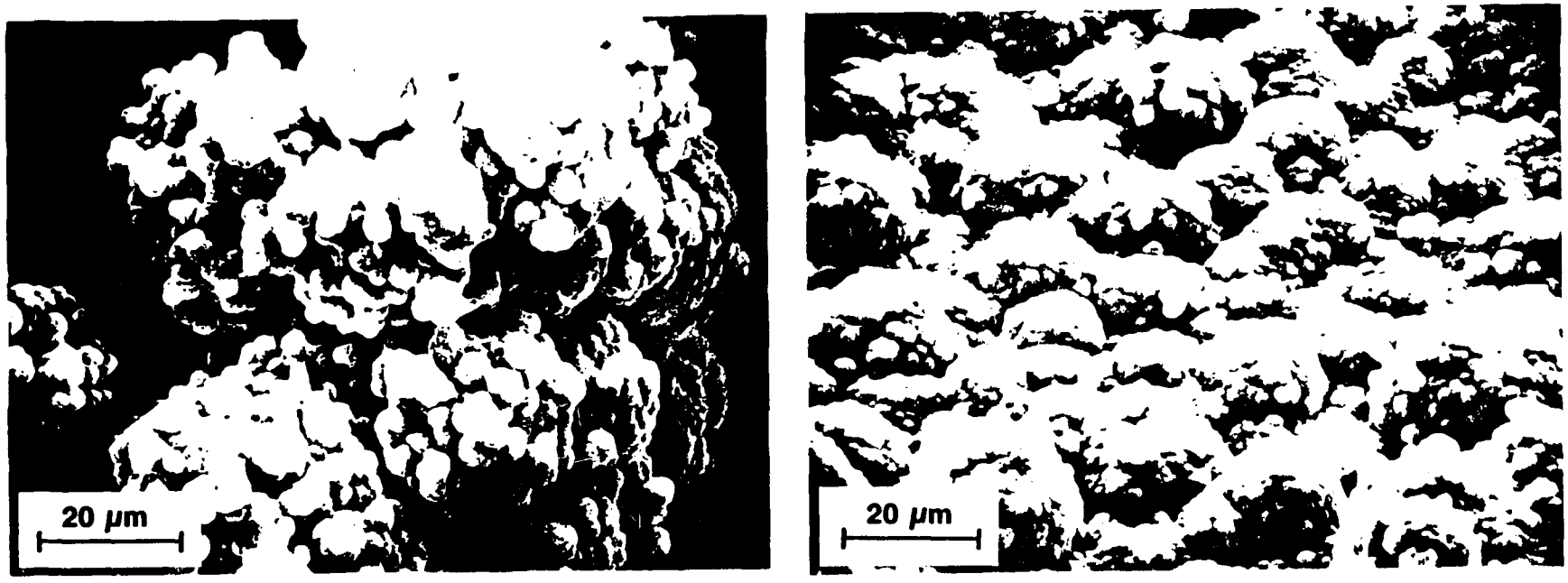

Figure 5-48. SEM micrographs of BN+AlN (J-769). The coating deposited near the center position of the stagnation region was much rougher (left) than that deposited outside of the stagnation region (right).

The next 29 experiments (J-770 through 798) were performed using nozzles with larger diameters; the diameters ranged from 0.95 to 1.59 cm. For these experiments, various combinations of the nozzle diameter, pressure (from 15 to 150 torr), and total flow rate (from 935 to 2940 cm^3/min) were used to control the extent of mixing between the inner and outer streams. The Peclet number (i.e., ratio of convective mass transfer rate versus diffusive mass transfer rate) could not be lowered enough to obtain a fully-mixed jet stream (described in Chapter III). As shown in Figure 5-49, ring patterns from J-773 were observed in the stagnation region indicating the reagents were not properly mixed along the radial direction. At an extreme case (J-771), no coating was deposited at the center region of the substrate. For J-771, a much higher gas flow rate through the inner path was used than through the outer path (2000 cm^3/min vs. 200 cm^3/min).

Finally, a smooth and radially-uniform coating (J-799) was deposited inside the stagnation region when the impinging jet geometry shown in Figure 3-9 was used. In this geometry, the inner stream was released from the side of the graphite extension tube. Details involving this arrangement are given in Chapter III. The fracture surface of the coating is shown in Figure 5-50. Using this geometry, twenty codeposition experiments (listed in Table 5-5) were performed to systematically observe and assess the effect of temperature, pressure, and $AlCl_3$ and BCl_3 concentrations on the codeposition

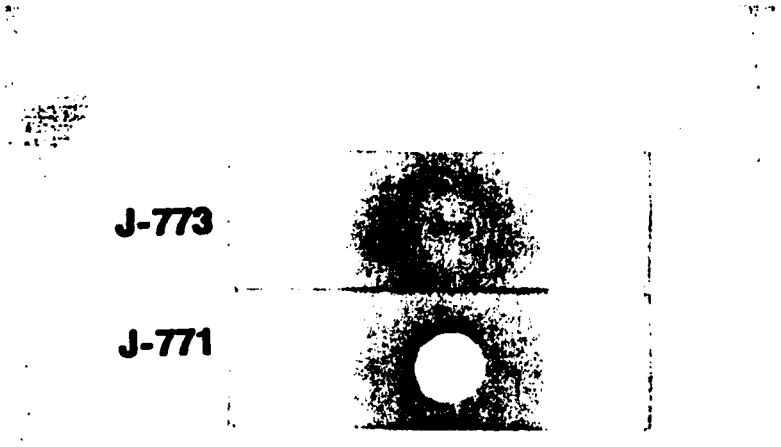

Figure 5-49. Non-uniform coatings deposited when reagents were not fully mixed.

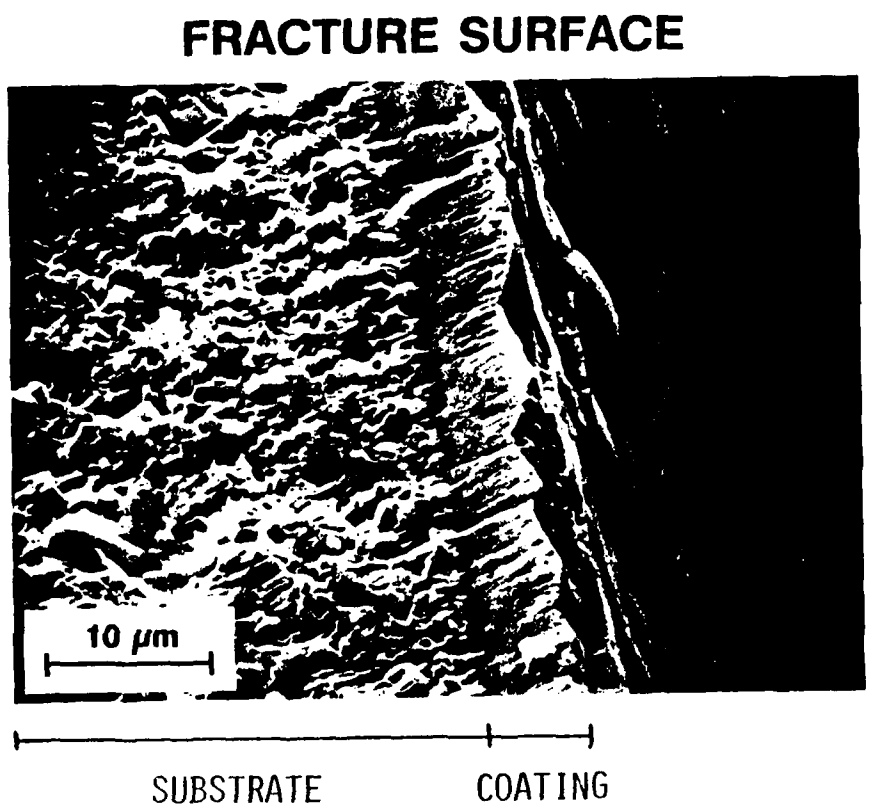

Figure 5-50. SEM micrograph of BN+AlN (J-799).

Table 5-5. Experimental conditions for BN+AlN-CVD experiments performed using the impinging jet geometry shown in Figure 3-9; hole diameter (d) = 1.59 cm and jet height (H) = 1.91 cm. All experiments were performed for 40 minutes. Crystalline structure of BN+AlN coatings was determined by XRD.

Sample #	T (°C)	P (torr)	Flow Rates (cm³/min)				Coating Thickness (μm)	Crystal-linity* (BN/AlN)
			BCl_3	$AlCl_3$	NH_3	Ar		
J-847	800	40	6	2.9	30	2361	40	TBN/CAlN(s)
J-850	800	80	6	2.9	30	2361	Cracked	TBN/CAlN(s)
J-853	800	150	6	2.5	30	2361	38	TBN/CAlN(s)
J-836	900	40	6	1.2	30	2363	30	TBN/ -
J-835	900	40	6	1.7	30	2362	40	TBN/ -
J-857	900	40	6	2.5	30	2361	40	- /CAlN(s)
J-862	900	40	6	3.8	30	2360	40	- /CAlN
J-858	900	40	6	4.2	30	2360	60	- /CAlN
J-859	900	40	3	3.8	30	2363	40	- /CAlN
J-861	900	40	12	4.2	30	2356	65	TBN/CAlN(s)
J-860	900	40	3	5.0	30	2362	40	- /CAlN
J-849	900	80	6	2.5	30	2361	50	TBN/CAlN
J-854	900	150	6	2.1	30	2362	44	- /CAlN
J-844	900	150	6	1.3	30	2363	13	TBN/ -
J-840	1000	40	6	2.1	30	2362	HN**	TBN/PAlN
J-851	1000	80	6	2.1	30	2362	40	- /CAlN(v)
J-855	1000	150	6	2.9	30	2361	27	- /CAlN(v)
J-846	1000	150	6	10.9	30	2360	20	- /CAlN(v)
J-841	1100	40	6	1.7	30	2362	HN**	TBN/PAlN
J-856	1100	150	6	2.5	30	2361	-	- /CAlN

* TBN = Turbostratic BN, PAlN = Polycrystalline AlN, CAlN = Anisotropic AlN; (s) small peaks and (v) highly (002) preferred orientation.

** HN = Homogeneous Nucleation.

process. The deposition and characterization results from these experiments will be the main focus for the remainder of this chapter.

Microstructure

Before discussing the effects of processing parameters on the BN+AlN-CVD process, it is first useful to recognize general microstructural features of the BN+AlN coatings. For this purpose, this section summarizes characterization results obtained from J-746 (Table 5-4); this coating was extensively characterized. Also, J-746 was selected because the sample portrayed many essential morphological features observed in other BN+AlN coatings. The coating (J-746) was found to contain distinctly different BN and AlN crystalline phases as identified by XRD. The XRD spectrum of the coated substrate is shown in Figure 5-51. The occurrence of broad (002) and (10x) BN peaks indicated that the BN phase was turbostratic. For AlN, the dominance of the (002) peak over (100) and (101) peaks and their sharpness suggested that the AlN phase was highly crystalline and preferentially oriented (i.e., anisotropic); c-axis perpendicular to the substrate. From the full-width at the half-maximum of the (002) BN peak, the average grain size of BN was estimated to be less than 20 Å. Also, the average grain size of AlN was approximated to be 120 Å from the broadness of the (002) AlN peak. SEM micrographs of the same coating are shown in Figure 5-52. It

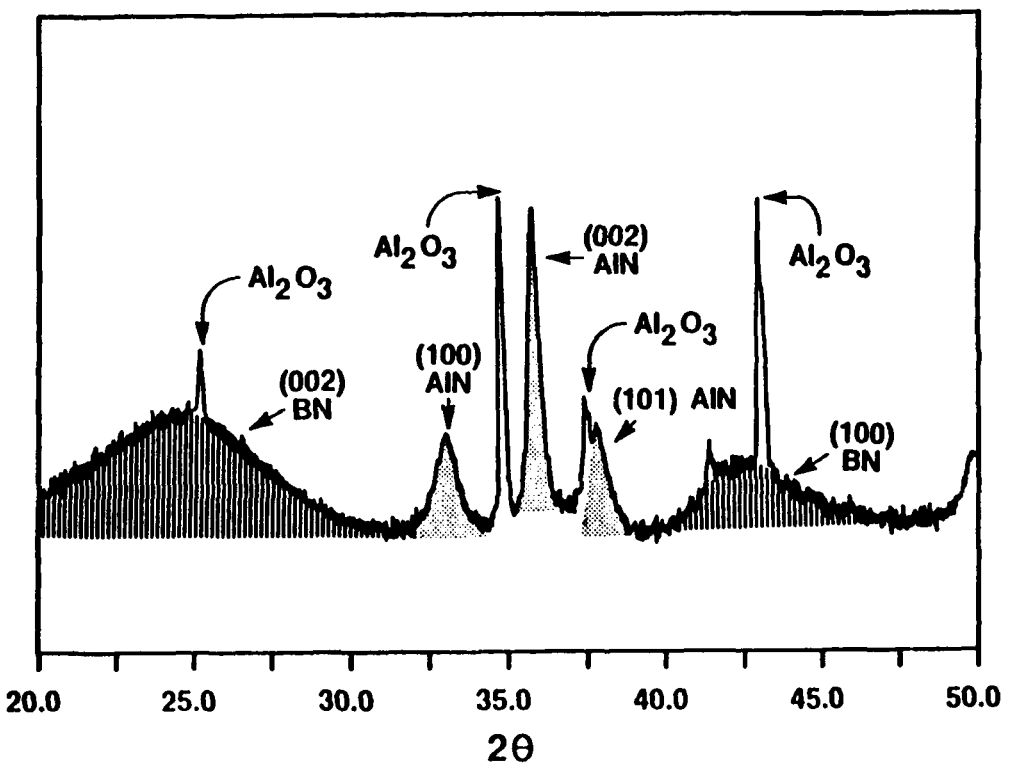

Figure 5-51. XRD pattern of BN+AlN (J-746) showing the presence of turbostratic BN and anisotropic AlN.

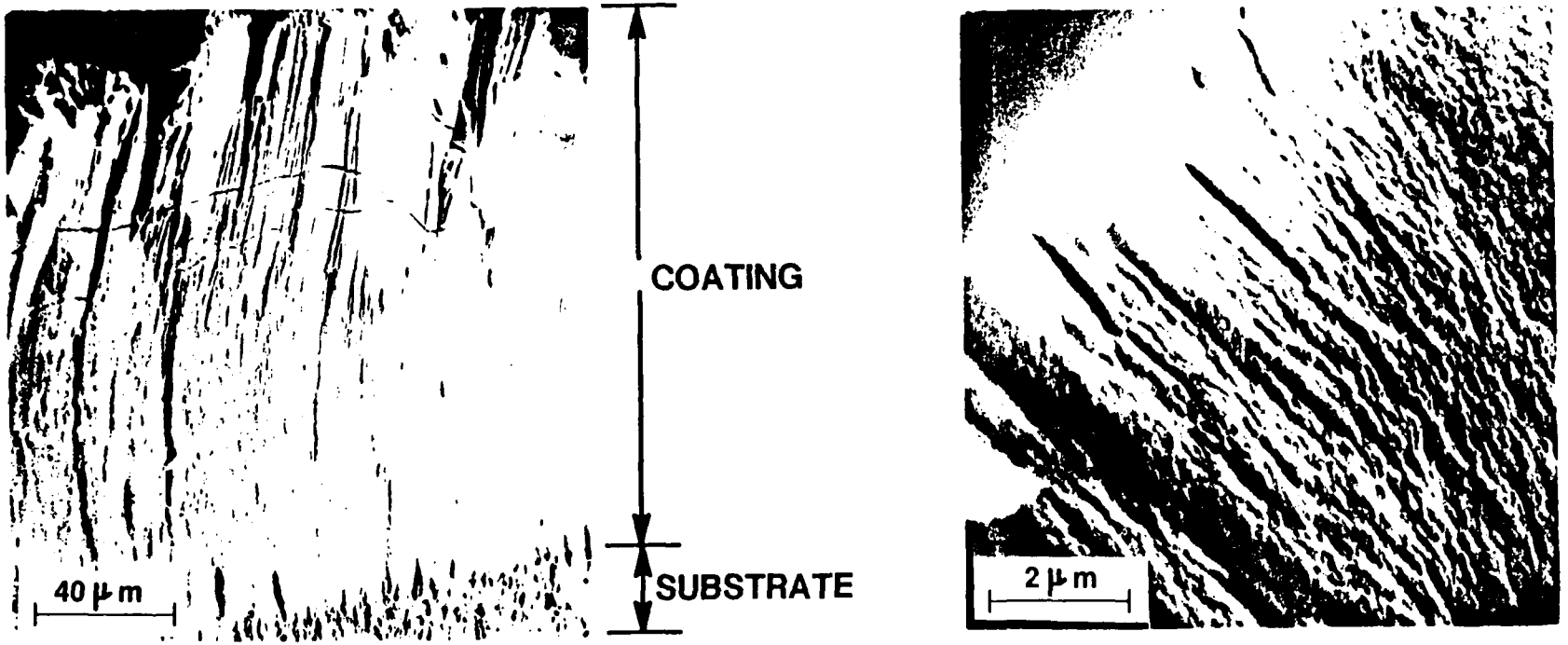

Figure 5-52. SEM micrographs of BN+AlN (J-746).

appeared from the micrographs that the coating grew in a columnar fashion.

A whisker morphology was observed from a TEM micrograph of the same sample as shown in Figure 5-53. The whiskers were identified to be AlN by electron diffraction whereas the lighter matrix phase was identified to be BN by electron diffraction. The electron diffraction patterns are also shown in Figure 5-53. The absence of any sharp spots in the electron diffraction pattern for BN confirmed that the BN phase was not highly crystalline as the XRD studies indicated (i.e., turbostratic). As shown in the TEM micrograph, the AlN whiskers were oriented perpendicular to the substrate surface. However, in some areas of the same coating, the preferred orientation of the AlN whiskers was not clearly observed (not shown in the micrograph) indicating the coating was not thoroughly uniform in its structure. Nevertheless, the appearance of the vertically oriented AlN whiskers in the TEM micrograph was in agreement with the strong (002) preferred orientation of AlN observed from the XRD pattern shown in Figure 5-51. This type of whisker microstructure was previously observed in the Si_3N_4+TiN-CVD system [100].

High resolution TEM was used to analyze the same coating. As shown in Figure 5-54, the turbostratic nature of the BN phase was indicated by "wavy" lines which represented the BN basal planes. This turbostratic microstructure was similar in appearance to that previously observed from turbostratic

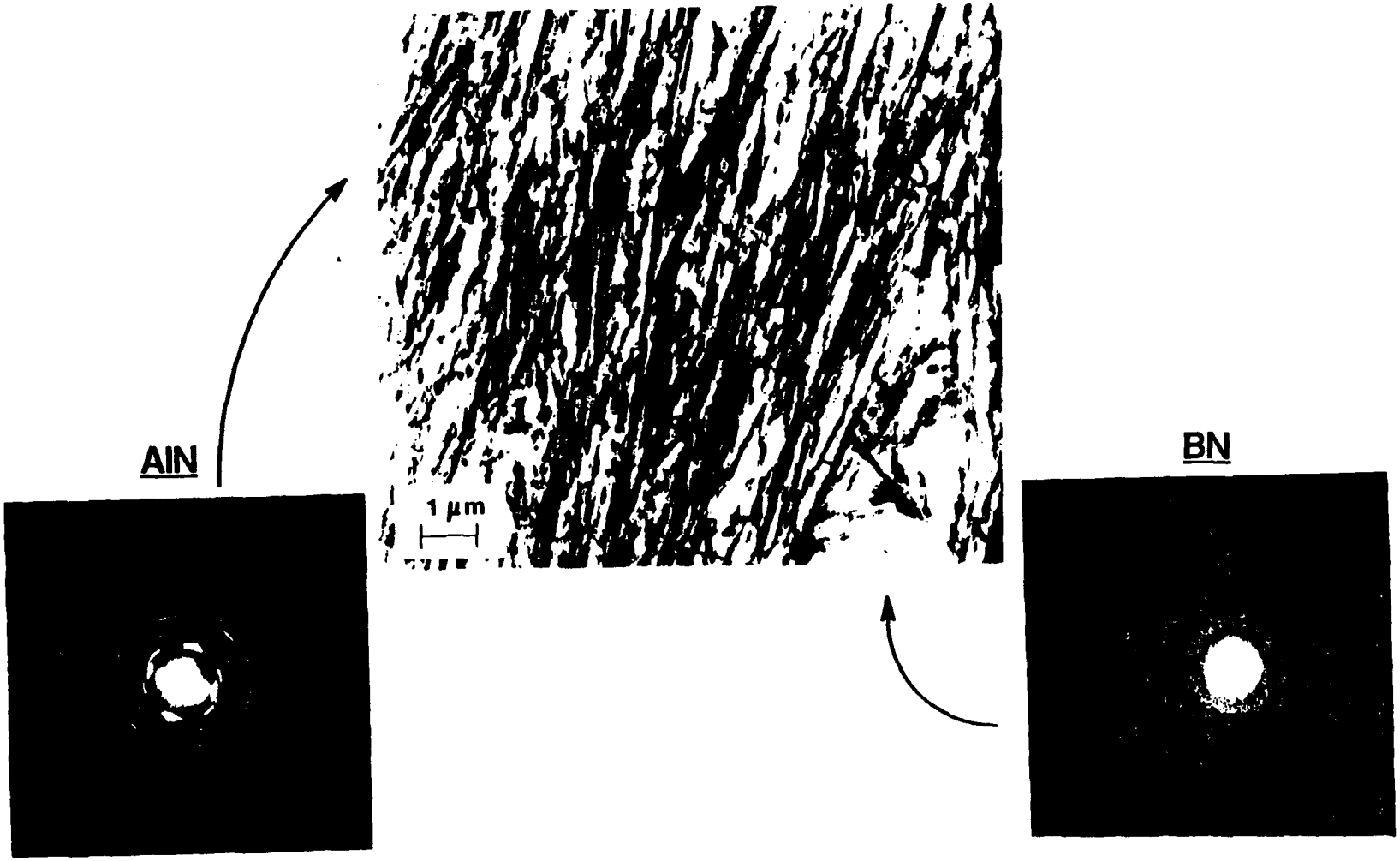

Figure 5-53. TEM micrograph of BN/AlN (J-746). Whiskers were identified as AlN and matrix phase (white background) was identified as BN by electron diffraction patterns.

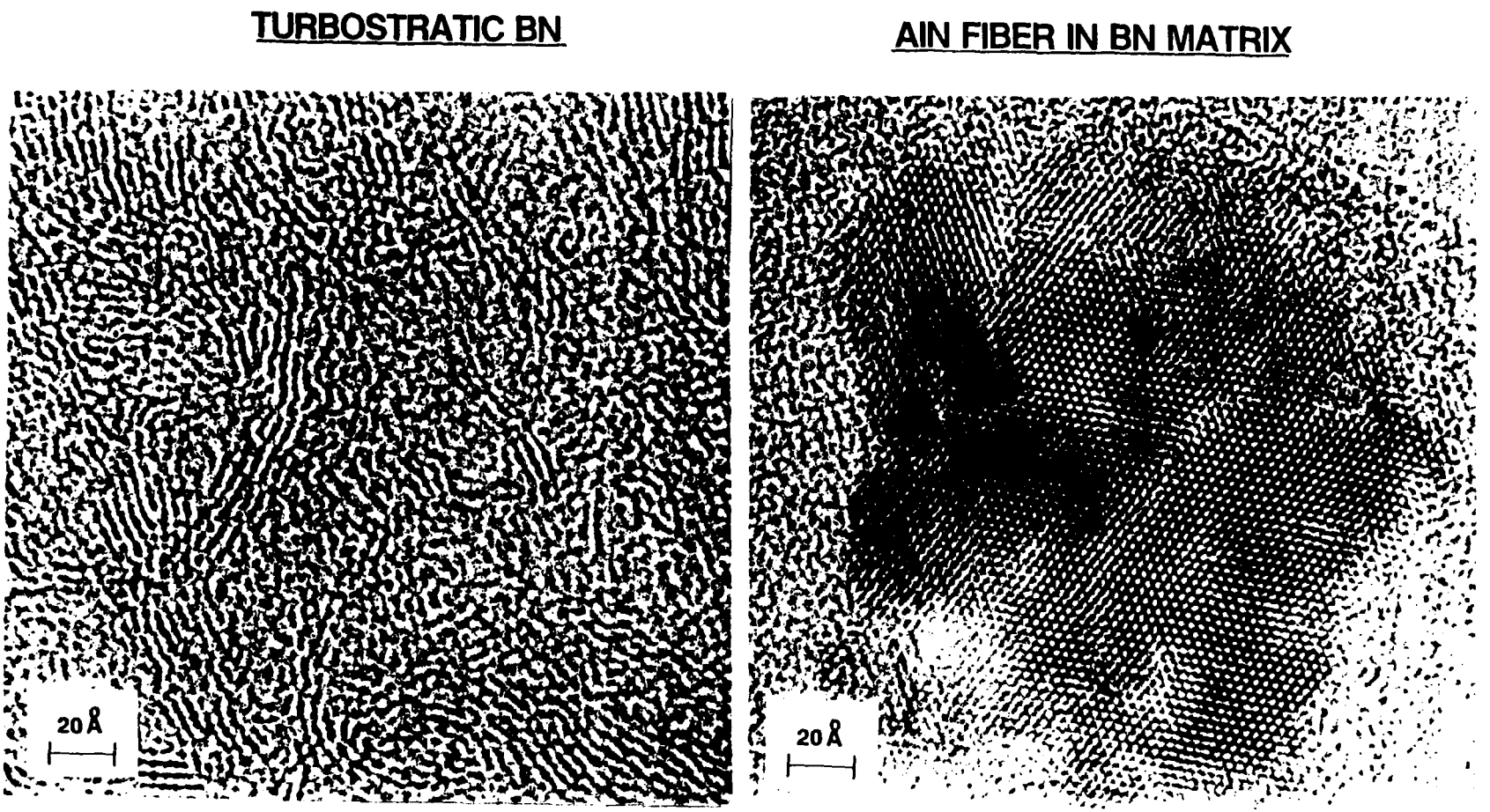

Figure 5-54. High resolution TEM micrographs of BN+AlN (J-746).

carbon [101]. A small number of the wavy lines was usually oriented together resulting in a somewhat crystalline (or layered) appearance. However, discontinuities were observed in the crystalline appearance after about 3 to 5 BN layers in average resulting in the formation of "microcrystal" or turbostratic BN grains consisting of only 3 to 5 BN layers. This short-range order corresponded to the definition of the turbostratic structure. This interpretation was supported by the fact that the average BN grain size of less than 20 Å was estimated from the XRD analysis. The random orientation of the turbostratic BN grains was evident from the micrograph suggesting that the BN phase was isotropic, as suspected from the appearance of the (10x) BN hump in the XRD pattern. From the micrograph, an average interlayer spacing of about 3.6 Å was measured. The theoretical interlayer spacing of BN is 3.33 Å. The increase in the interlayer spacing, which is a well-recognized behavior of turbostratic BN, probably caused (002) BN peak to be shifted about 2° (to a lower angle) compared to its theoretical position (see 5-51). Figure 5-54 also shows an AlN whisker imbedded in the BN matrix. The diameter of the whisker was about 200 Å, which favorably compared to the average diameter of 120 Å estimated from the broadness of the (002) AlN peak in Figure 5-51.

Based on all the characterization data, an idealized representation of J-746 was drawn in Figure 5-55. The diagram portrays a microstructure in which single crystal whiskers of

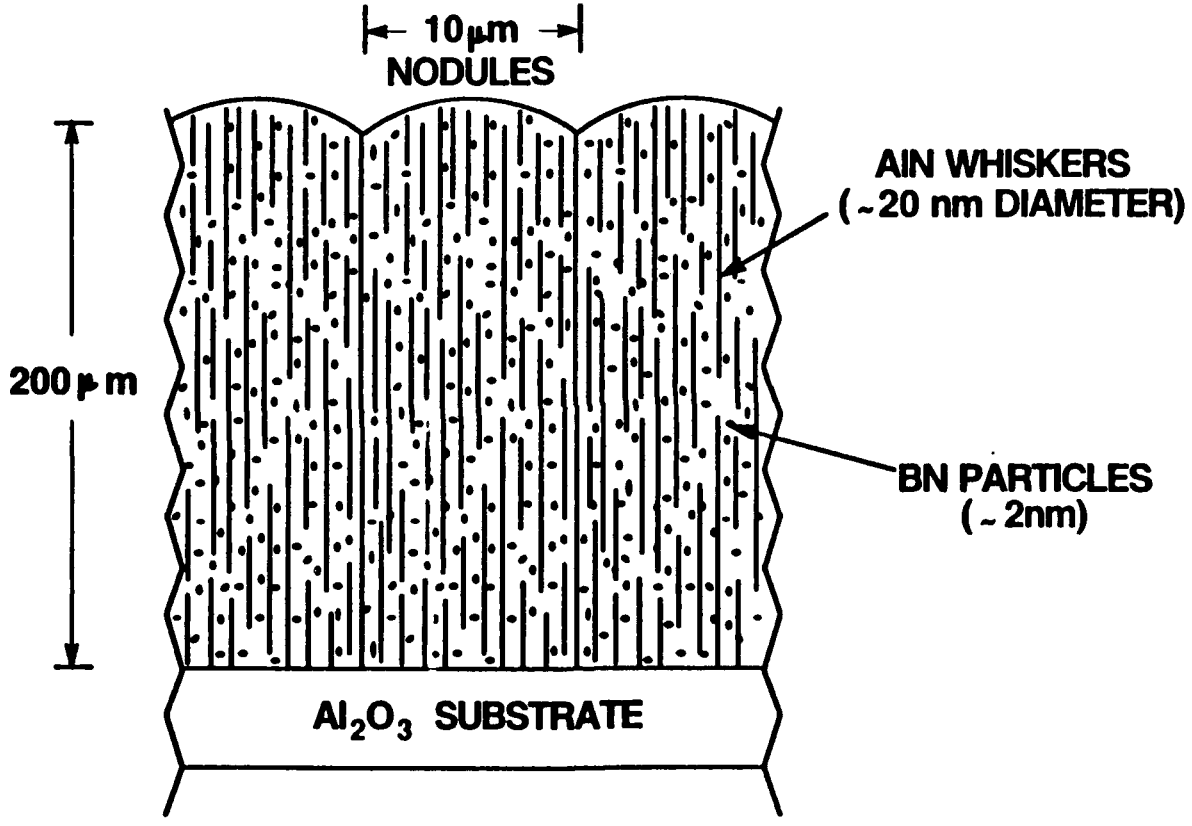

Figure 5-55. Ideal representation of BN+AlN (J-746).

AlN were imbedded in a matrix consisting of numerous turbostratic BN grains. Also, this particular coating showed high hardness in comparison to other materials such as hot pressed BN+AlN and hot pressed AlN as shown in Figure 5-56. In summary, some major microstructural features observed from the BN+AlN composite coating are noted as follows:

(1) BN and AlN were codeposited as distinctly different chemical and crystalline phases;

(2) BN was turbostratic and isotropic as determined by XRD, electron diffraction, and high resolution TEM;

(3) AlN was anisotropic and highly-crystalline as determined by XRD, electron diffraction, and high resolution TEM;

(4) BN grains were very small in size (about 20 Å) lacking long-range order;

(5) AlN grew as whiskers of about 100 to 200 Å diameter, which were preferentially oriented perpendicular to the substrate surface as determined by XRD, TEM, and high resolution TEM. In the XRD analysis, the preferred orientation could be identified by the dominance of the (002) AlN peak.

Effects of Processing Parameters on Microstructure

Pressure and Temperature. Deposition temperature and pressure were systematically varied as tabulated in Table 5-5. The mole fraction of BCl_3 used for the temperature and pressure variation experiments was always fixed at 0.0025 (i.e., 6 cm^3/min of BCl_3). The mole fraction of $AlCl_3$ was kept

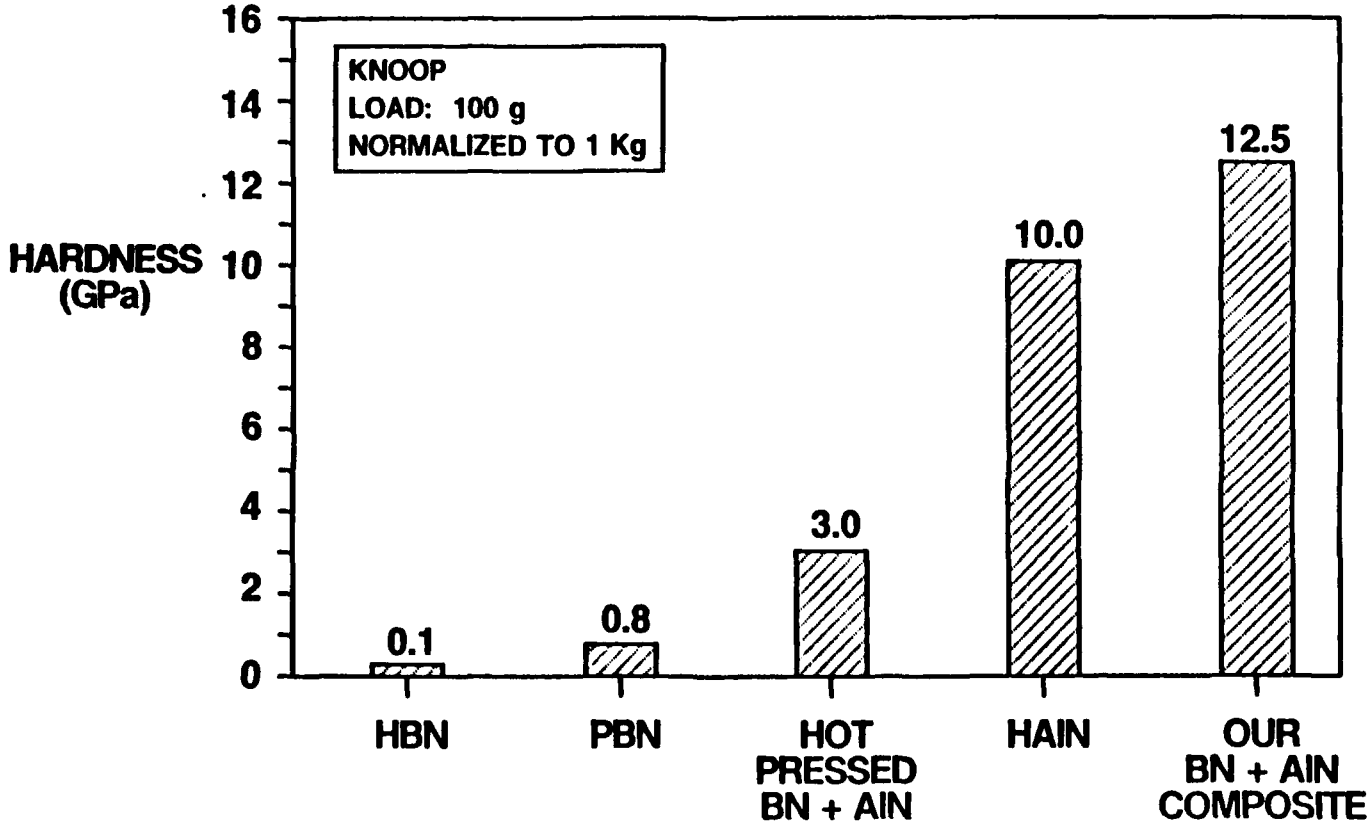

Figure 5-56. Hardness of BN+AlN (J-746) in comparison to other substrates; HBN = hot pressed BN from Union Carbide, PBN = pyrolytic BN from Union Carbide, HAlN = hot pressed AlN from Denka, hot pressed BN+AlN from Union Carbide (71%BN, 20%AlN, and 4%B_2O_3).

at a relatively constant level of 0.0009 to 0.0012 (i.e., 2.1 to 2.9 cm^3/min of $AlCl_3$).

Figure 5-57 shows XRD patterns of BN+AlN coatings deposited at 800°C using three different pressures; 40 torr (J-847), 80 torr (J-850), and 150 torr (J-853). The presence of both BN and AlN phases in the coatings were indicated by the appearance of (002) BN and (002) AlN peaks in the XRD patterns. But, the intensity of the peaks was weak suggesting that the coatings were not highly crystalline. For the BN phase, the area under the (002) peak increased by a small amount with increasing pressure from 40 to 150 torr. The intensity of the small (002) AlN peak remained relatively the same with the increase in pressure. Other major peaks of AlN such as (100) and (101) were not visible in these patterns. The absence of these AlN peaks indicated that some AlN grains were preferentially oriented. However, most of the AlN phase was expected to be amorphous since the (002) peak was very small.

The fracture surface and surface morphology of the same composite coatings are shown in Figures 5-58 (J-847), 5-59 (J-850), and 5-60 (J-853). The coating deposited at 80 torr (J-850) gradually cracked off from the Al_2O_3 substrate after removal from the CVD furnace. Thus, the coating was not visible from the fracture surface micrograph, but some coating debris was observed on the substrate surface (Figure 5-59). On the other hand, the composite coatings deposited at 40 and

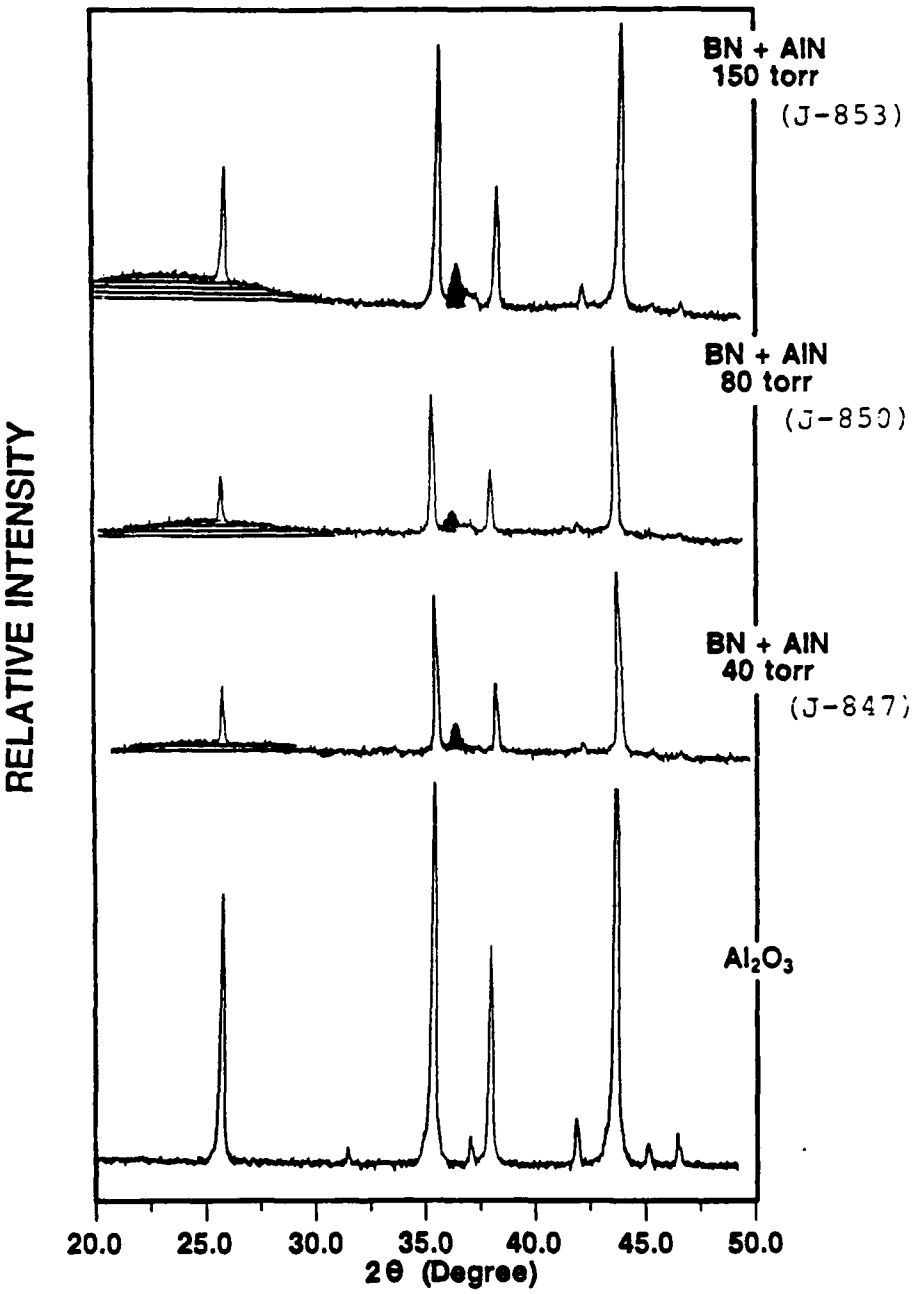

Figure 5-57. XRD patterns of BN+AlN deposited on Al_2O_3 at various pressures (temperature = 800°C, mole fraction of BCl_3 = 0.0025, and mole fraction of $AlCl_3$ ≈ 0.001).

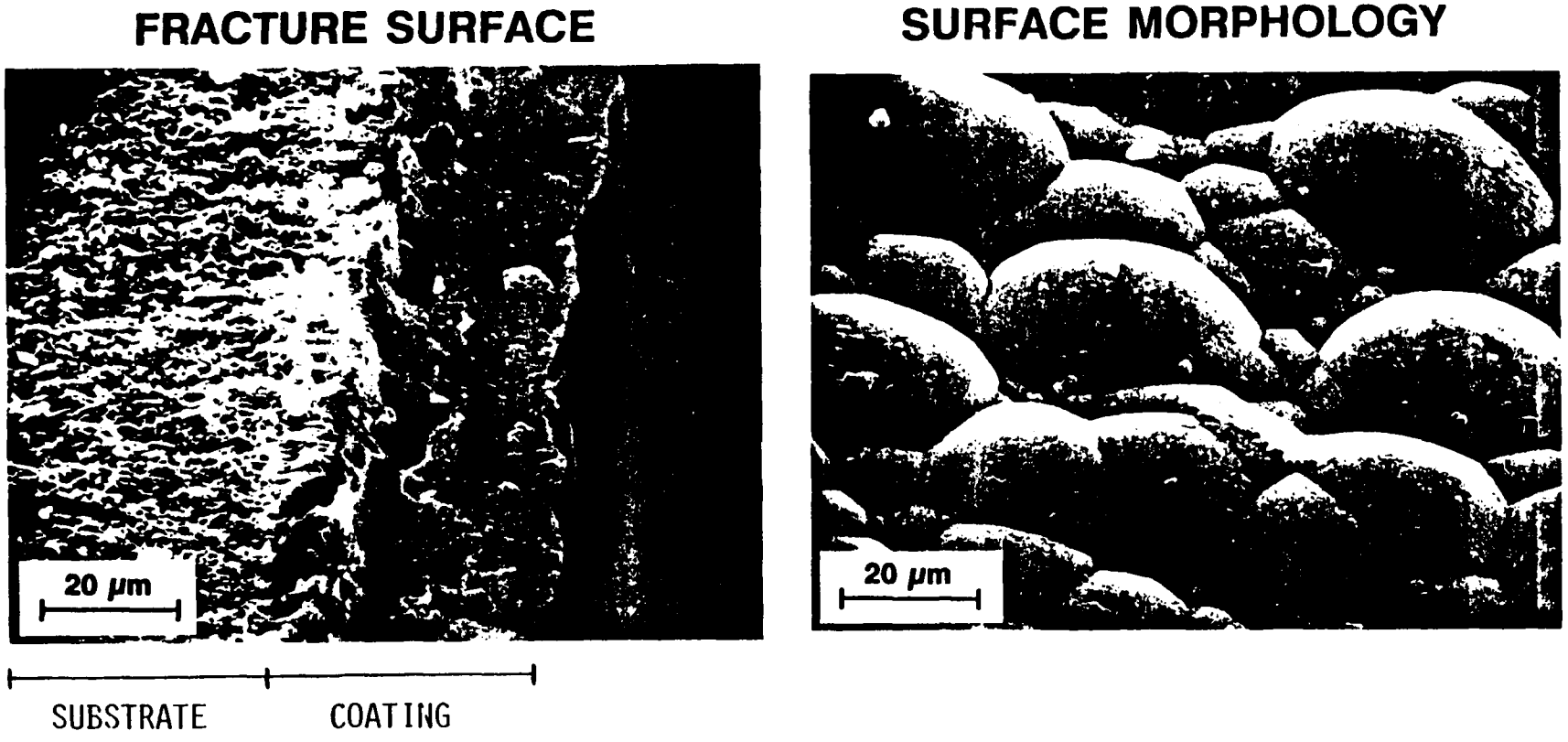

Figure 5-58. SEM micrographs of BN+AlN (J-847).

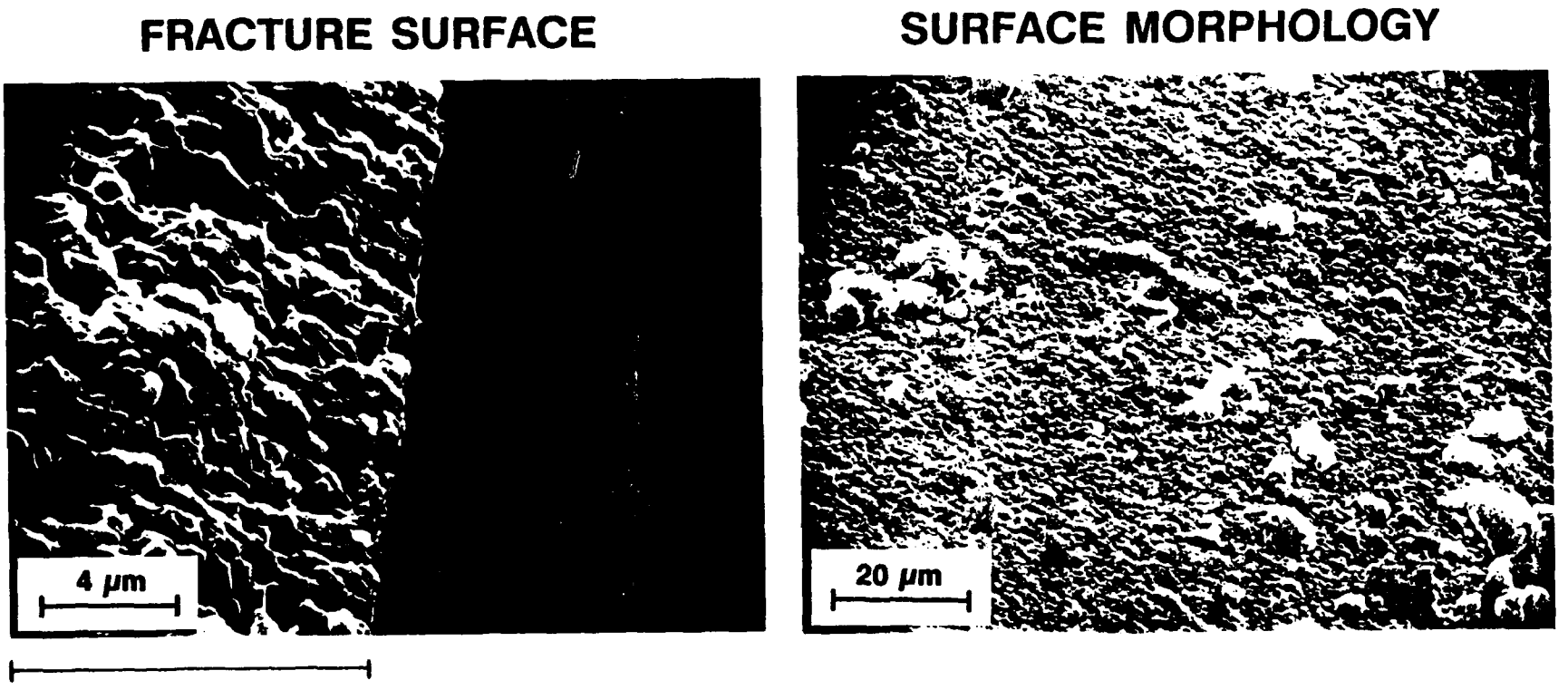

Figure 5-59. SEM micrographs of BN+AlN (J-850).

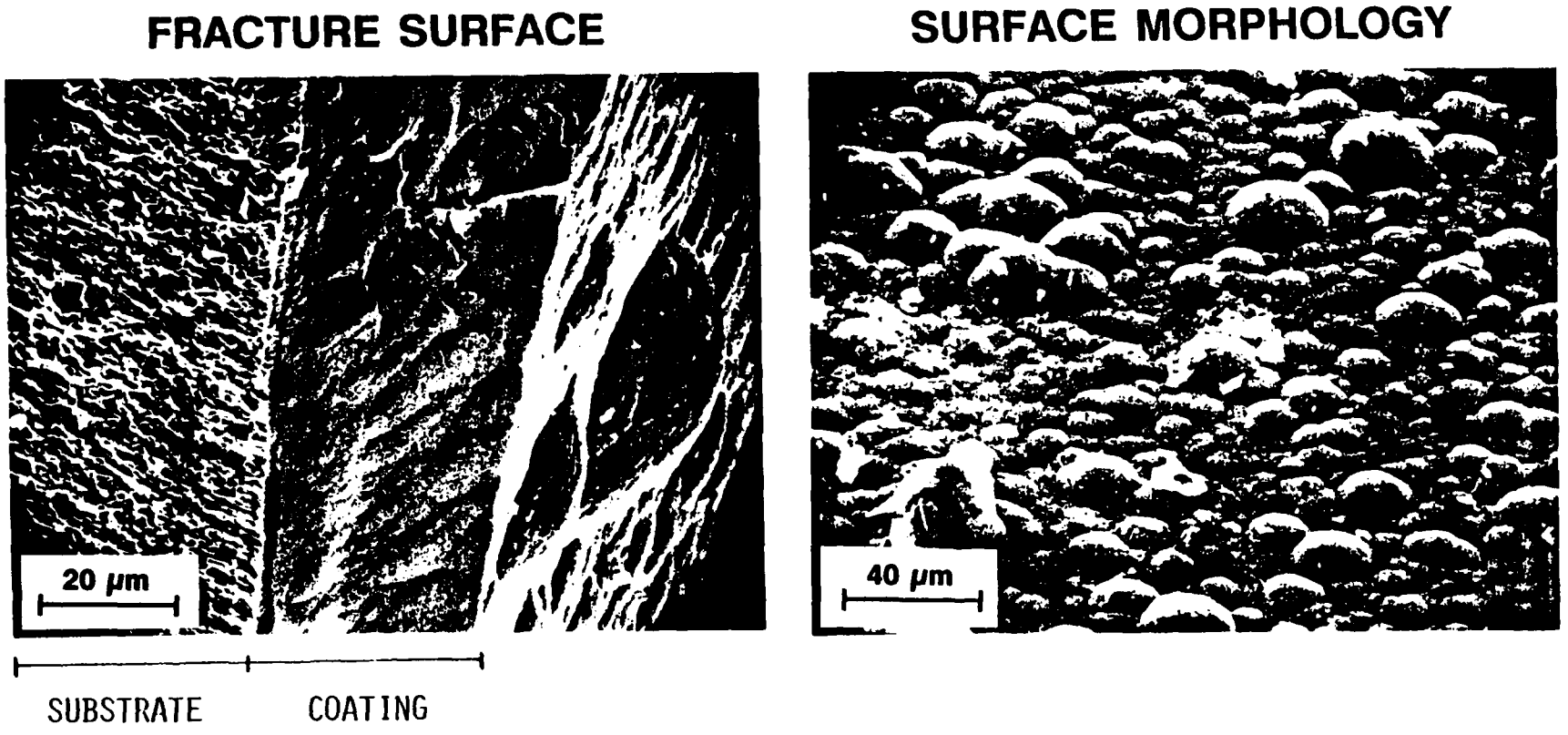

Figure 5-60. SEM micrographs of BN+AlN (J-853).

150 torr looked dense, were adherent to their substrates, and were not cracked. The coating thickness (or rate) of the two samples was almost the same (40 μm for J-847 versus 38 μm for J-853). As will be discussed in detail, deposition rates for the BN+AlN-CVD process was much higher than those for the BN-CVD or AlN-CVD process. The coatings were hard and translucent. Also, the nodules appearing on the surface of the coating were similar in shape and size (about 10 μm to 40 μm).

Therefore, it seemed that the XRD features and morphology of the coatings deposited at 800°C were not strongly influenced by the changes in pressure. However, at 900°C, the effect of pressure became more significant and interesting. As shown in Figure 5-61, the XRD peaks for AlN became much stronger in intensity on increasing the pressure from 40 to 150 torr. Also, the dominance of the (002) AlN peak over the other AlN peaks increased drastically with the increase in pressure indicating the AlN grains became more preferentially oriented. On the other hand, the weak XRD features attributable to the BN phase were difficult to differentiate from the patterns' base lines because of the rise in the base lines around 30° to 40°. Nevertheless, the absence of any drastic changes in the XRD features of BN suggested that the crystalline structure of BN was not strongly affected by pressure.

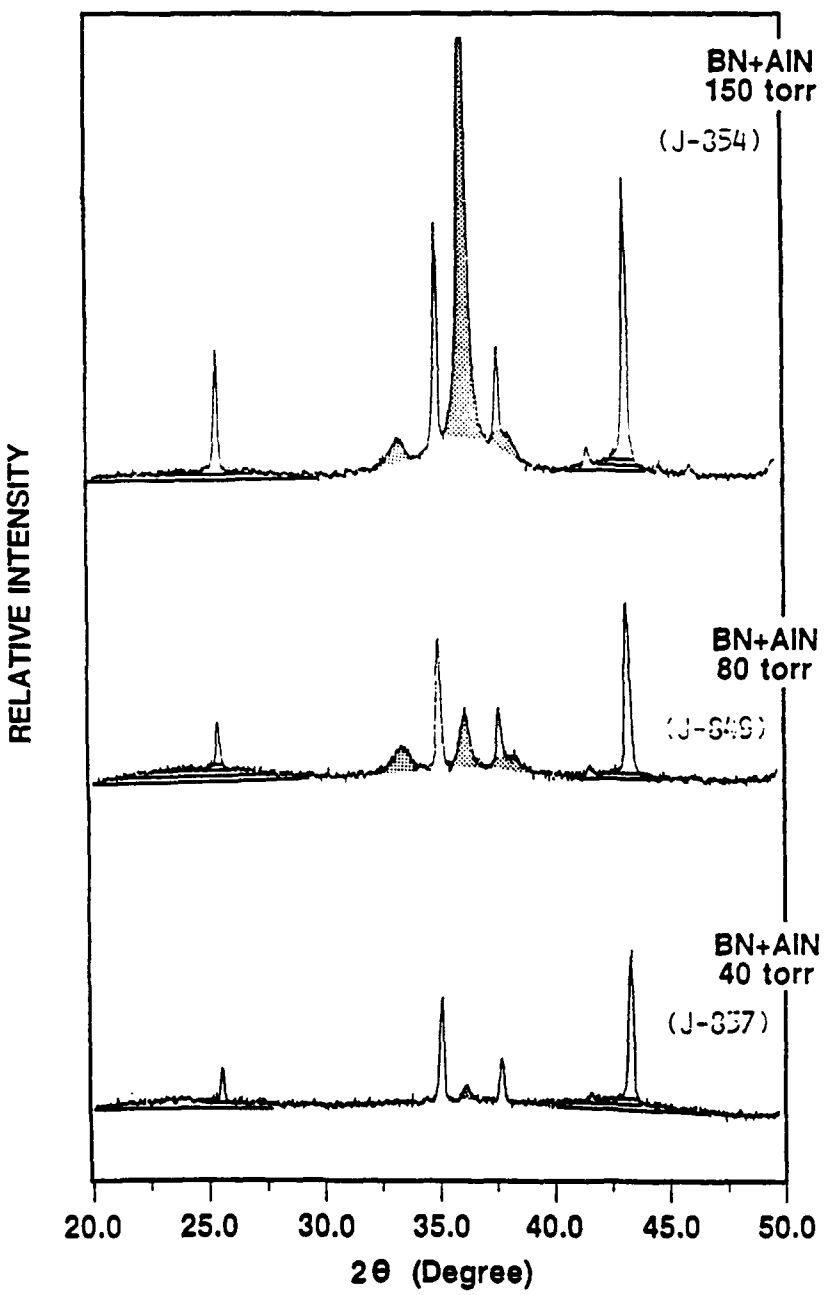

Figure 5-61. XRD patterns of BN+AlN deposited on Al_2O_3 at various pressures (temperature = 900°C, mole fraction of BCl_3 = 0.0025, and mole fraction of $AlCl_3$ ≈ 0.001).

At 40 torr and 900°C (J-857), growth features which looked like "cauliflower" were deposited as shown in Figure 5-62. The rough morphology was probably caused by too rapid growth. The coating was hard and translucent. In the previous section, the TEM studies demonstrated that the (002) preferred orientation of AlN was observed in the XRD pattern when AlN grew as whiskers in the BN matrix. This type of whisker morphology was also evident from the coatings deposited at 80 and 150 torr. At 80 torr (J-849), the coating appeared to grow in a columnar fashion as shown in Figure 5-63. This coating was hard and translucent. The whisker morphology became more apparent at 150 torr (J-854) as shown in Figure 5-64. The coating deposited at 150 torr was, however, soft and opaque-white. Also, the coating thickness decreased from about 50 to 13 μm with increasing pressure from 80 to 150 torr. The average diameter of the AlN whiskers was approximated to be 150 Å for J-849 (80 torr) and 200 Å for J-854 (150 torr) from the broadness of the (002) AlN peak.

As summarized in Table 5-6, some selected coatings were analyzed using electron microprobe to determine the elemental composition. It appeared that most of the composite coatings were deficient in nitrogen except for J-853. Although the stoichiometric amounts of B, Al, and N were not usually present in the coatings, the variation in the chemical composition with respect to the changes in the processing conditions could be clearly noticed. Also, the BN+AlN

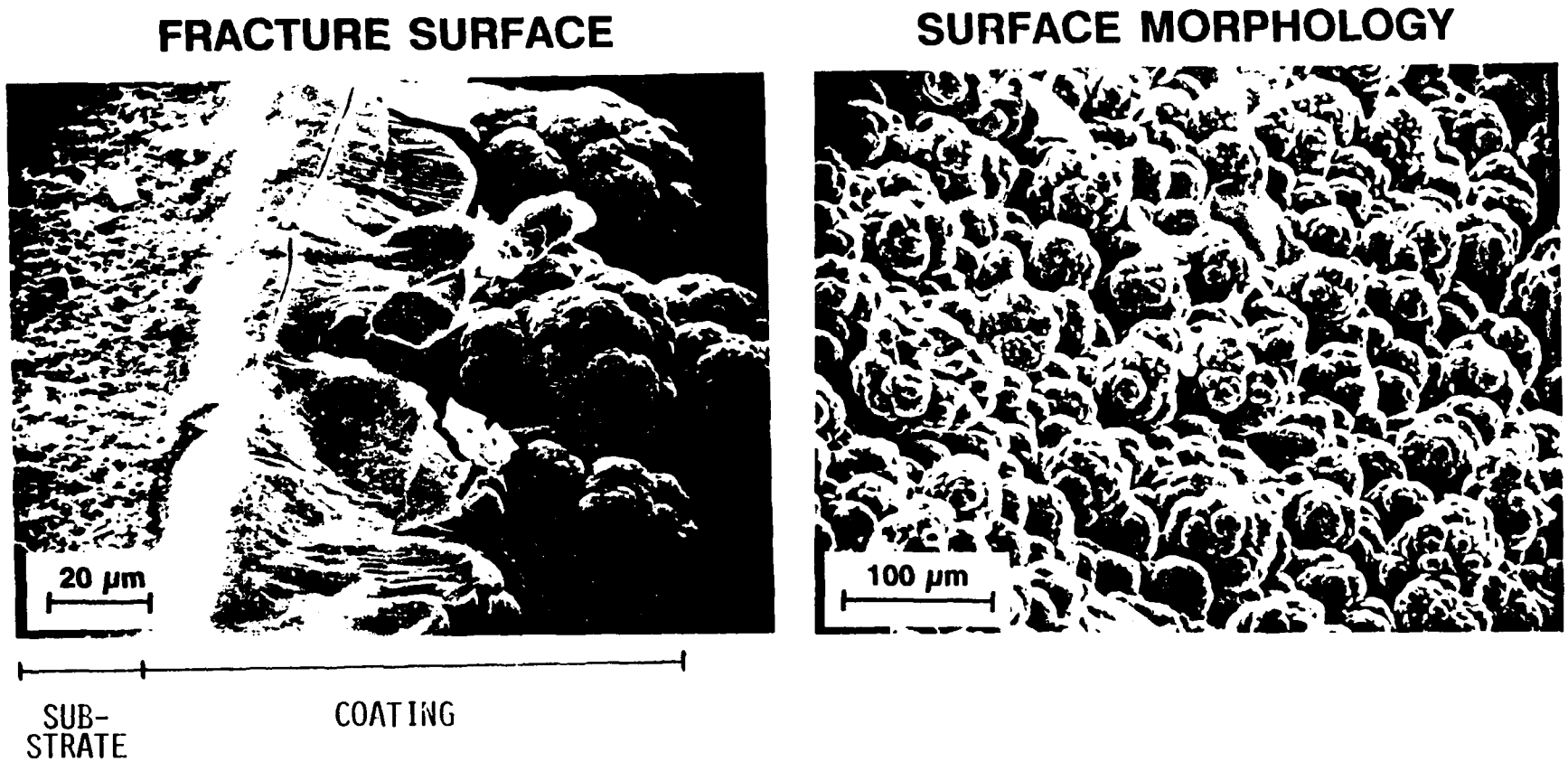

Figure 5-62. SEM micrographs of BN+AlN (J-857).

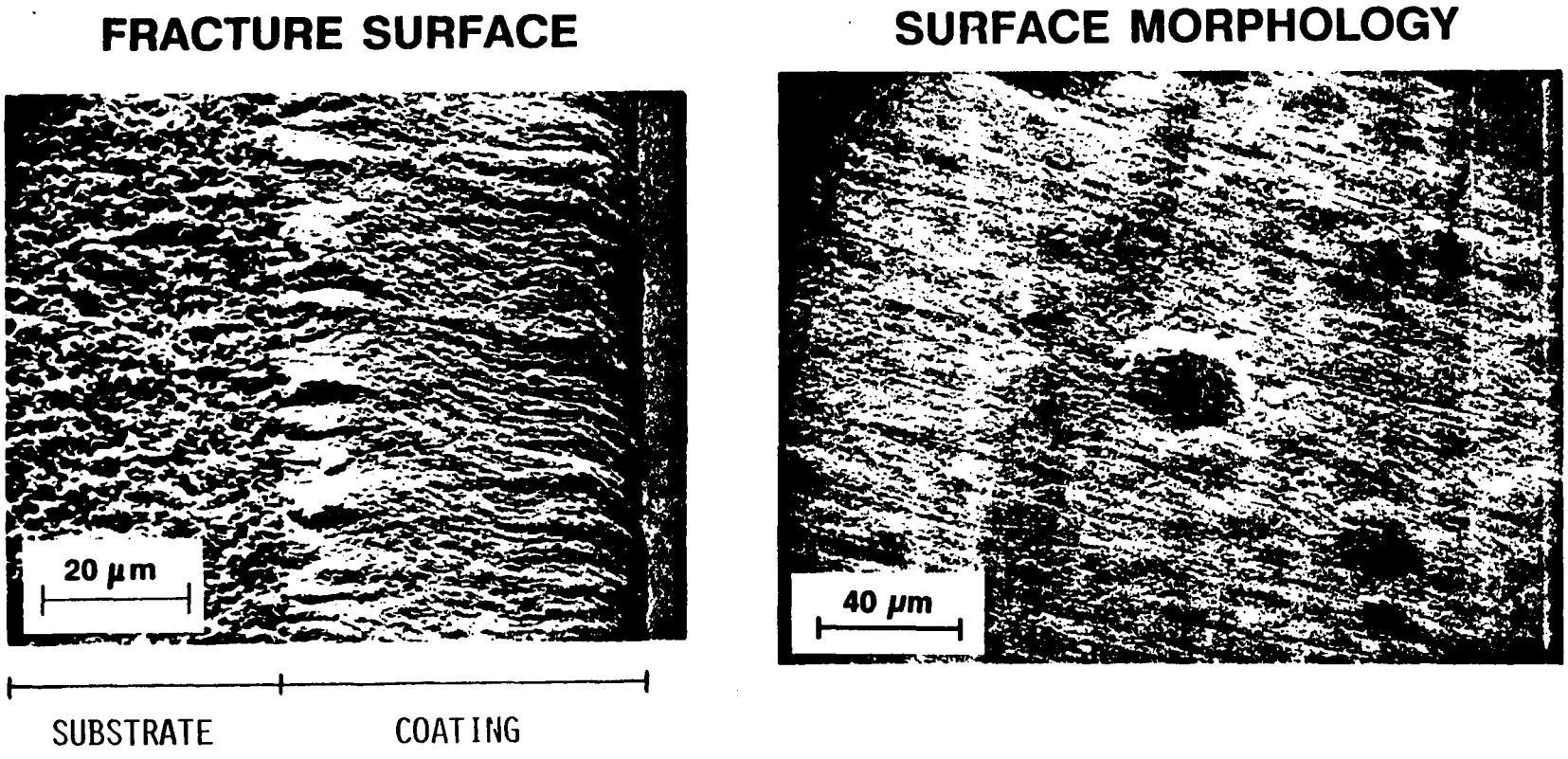

Figure 5-63. SEM micrographs of BN+AlN (J-849).

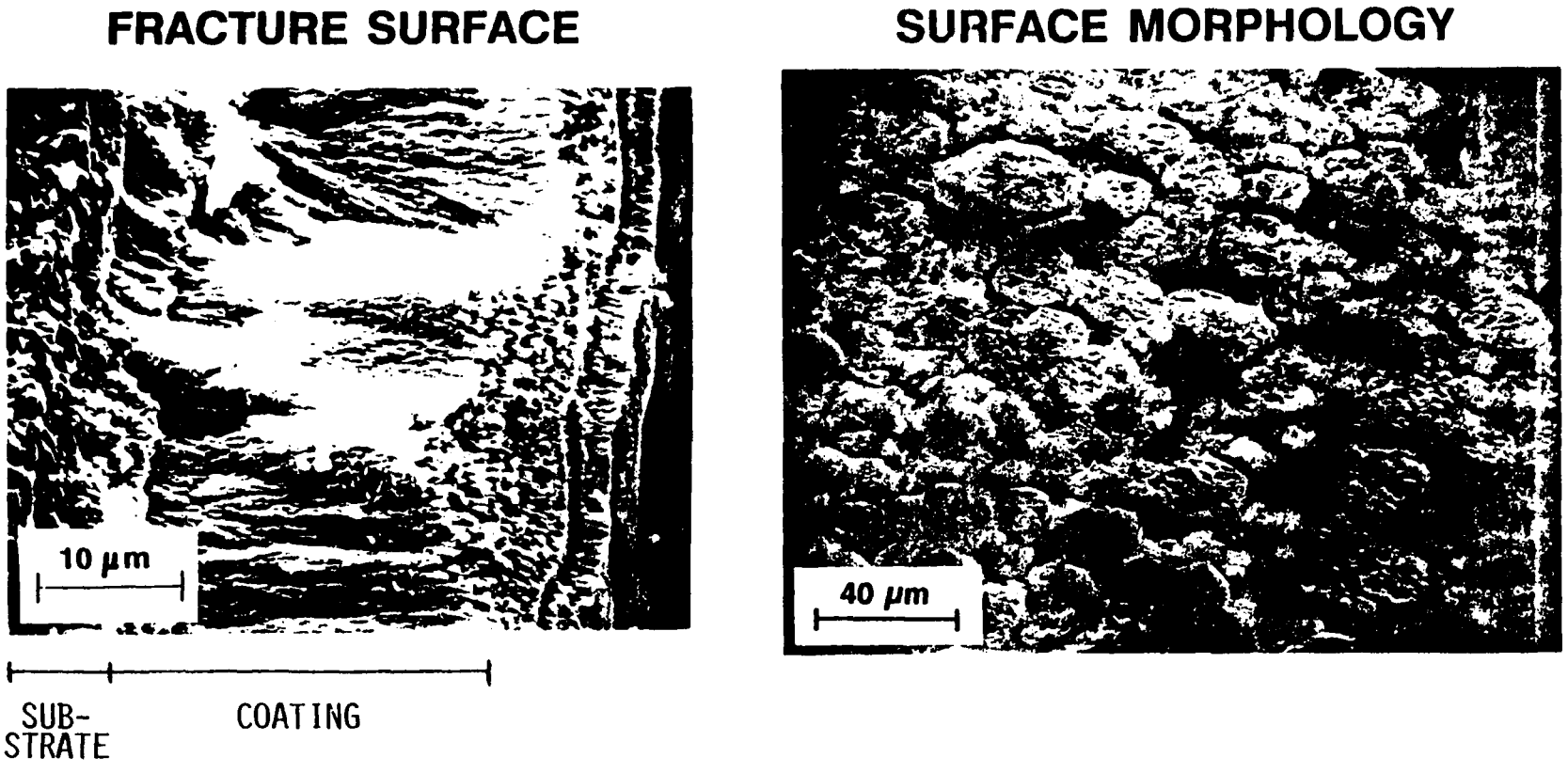

Figure 5-64. SEM micrographs of BN+AlN (J-854).

Table 5-6. Bulk chemical composition (atomic%) of BN+AlN coatings determined by electron microprobe and their hardness.

Sample	Al	B	N	O	Hardness (GPa)
J-857	14.0	41.6	43.5	0.8	7.5±3.0
J-854	12.5	43.1	42.2	2.2	1.1±0.3
J-853	24.2	26.7	48.1	1.0	6.8±1.0
J-855	9.5	50.2	39.7	0.6	1.8±1.0
J-859	31.5	27.4	40.6	0.5	15.5±4.0
J-861	6.9	51.0	41.7	0.4	-
J-836	24.4	35.8	39.1	0.7	-
J-858	61.9	18.7	19.2	0.2	15.5±3.0
J-816(BN)	-	53.1	45.9	1.0	-
J-821(AlN)	52.1	-	45.4	2.5	-

coatings contained a small amount of oxygen. In all the samples, the presence of oxygen was more evident near the interface with the Al_2O_3 substrate (by about a factor of two in comparison to the bulk average) indicating the possibility of oxygen diffusion from the oxide substrate into the coating during the CVD operations.

It was suspected that the growth of the AlN whiskers in the composites was caused by a reduction in the AlN deposition rate with increasing pressure. The electron microprobe results showed that the Al content in the composites actually decreased slightly from 14.0% (J-857) to 12.5% (J-854) with increasing pressure from 40 to 150 torr. This type of behavior was previously observed in the AlN-CVD system. With increasing pressure from 40 to 150 torr, the AlN deposition rate decreased rapidly resulting in more (002) preferred orientation of the AlN coating. Nevertheless, the BN+AlN coatings became apparently much softer with the growth of AlN whiskers. As shown in Table 5-6, hardness decreased from 7.5 for J-857 to 1.1 GPa for J-854.

Similar deposition behavior was observed at the deposition temperature of 1000°C. The whisker morphology was observed at 80 torr (J-851) and 150 torr (J-855). At these pressures, the (002) AlN peak was very intense and dominated the other major AlN peaks as shown in Figure 5-65. The Al content in J-855 was only 9.5% (Table 5-6) suggesting again the AlN whisker growth was triggered by the reduction in the

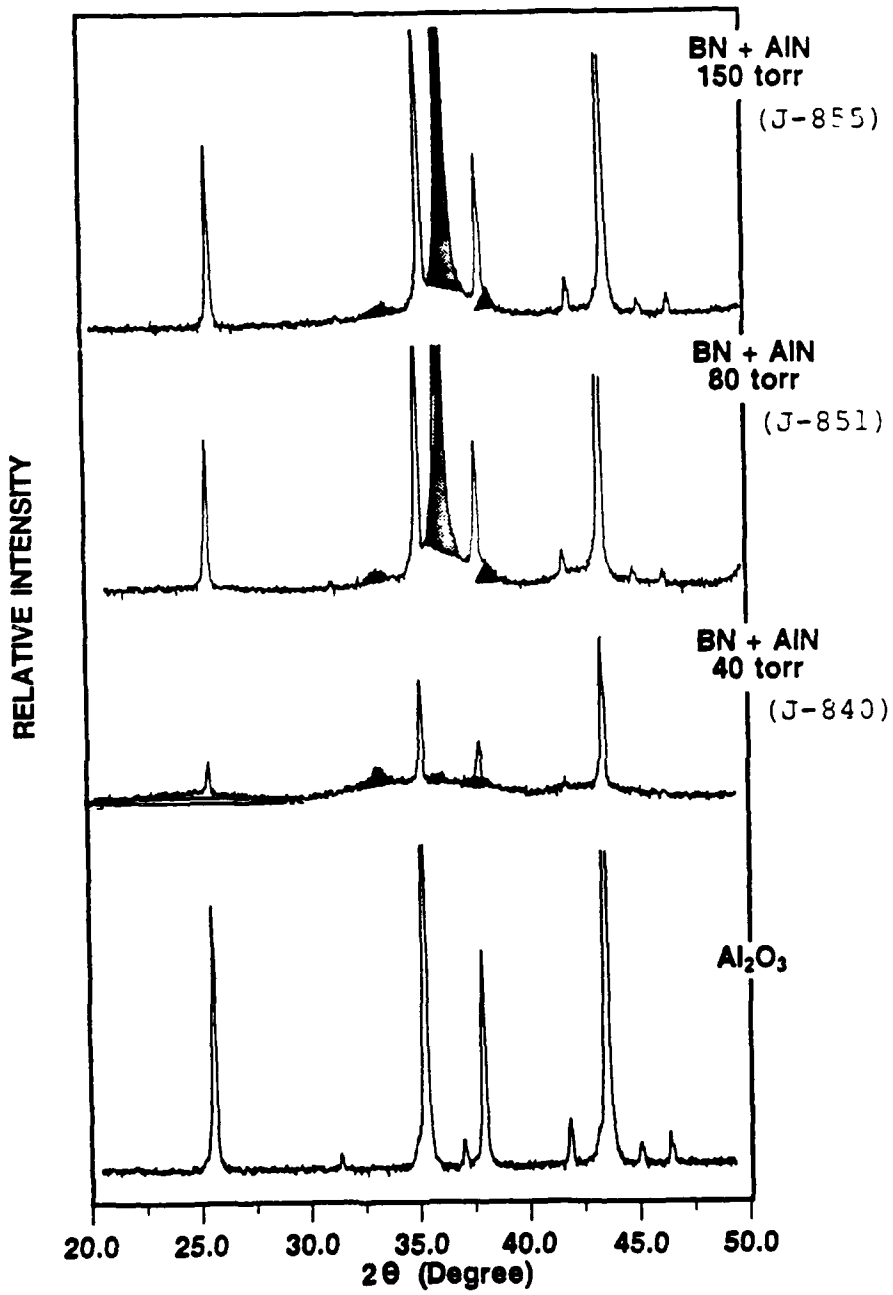

Figure 5-65. XRD patterns of BN+AlN deposited on Al_2O_3 at various pressures (temperature = 1000°C, mole fraction of BCl_3 = 0.0025, and mole fraction of $AlCl_3$ ≈ 0.001).

AlN deposition rate. The XRD features corresponding to BN were absent from these coatings although the coatings contained up to 50.2% B as determined by electron microprobe (J-855 in Table 5-6). SEM micrographs of the coatings deposited at 80 and 150 torr are shown in Figures 5-66 and 5-67, respectively. The coatings were uniform, but they were soft and white-opaque. The average diameter of the AlN whiskers was estimated to be about 300 Å from the broadness of the (002) AlN peak. At 40 torr and 1000°C (J-840), a coating having rough surface features was deposited as shown in Figure 5-68. This coating looked similar to J-857 (Figure 5-62) which was deposited at 40 torr and 900°C.

Figure 5-69 shows the XRD patterns of the coatings deposited at 40 torr in the temperature range of 800 to 1100°C. The XRD patterns from 800°C (J-847) and 900°C (J-857) looked almost identical. A small (002) AlN peak was observed in both patterns. However, at 1000°C (J-840), (100) and (101) XRD peaks for AlN started to appear in the XRD pattern. Also, the (100) was the most intense peak indicating that the AlN was probably isotropic. At 1100°C (J-841), the XRD features for AlN were similar to those observed at 1000°C. However, the presence of the (002) BN peak was more evident at 1100°C and the peak was shifted to the higher 2θ direction. The changes in the XRD patterns with the increase in temperature were similar to those previously observed from the BN-CVD and AlN-CVD systems. For AlN-CVD, homogenous

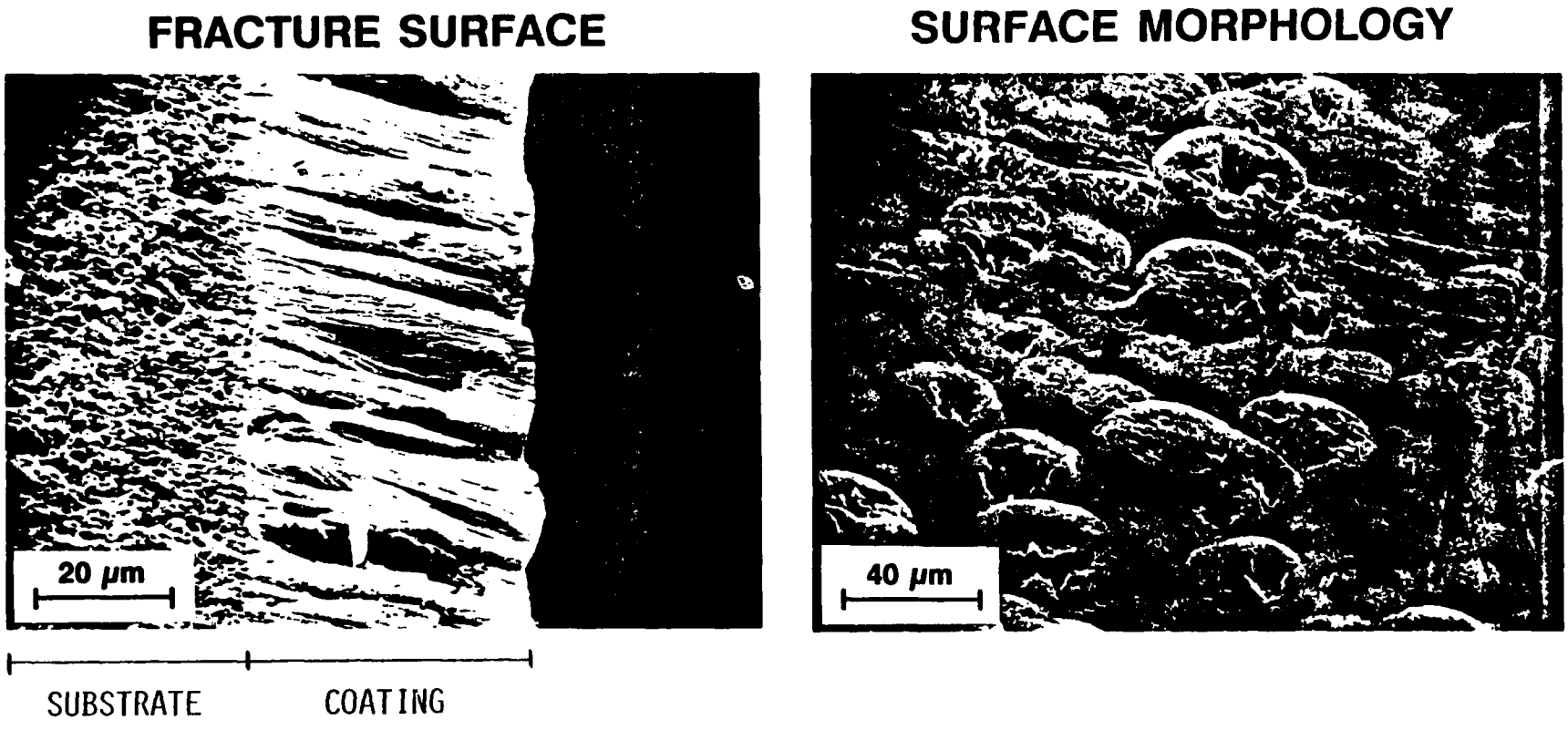

Figure 5-66. SEM micrographs of BN+AlN (J-851).

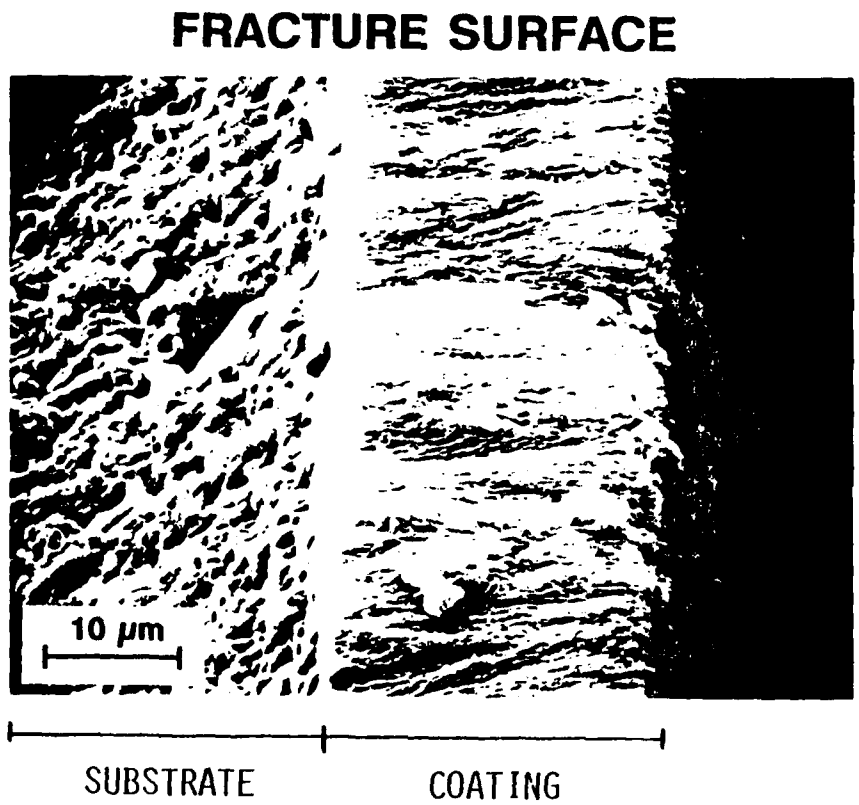

Figure 5-67. SEM micrograph of BN+AlN (J-855).

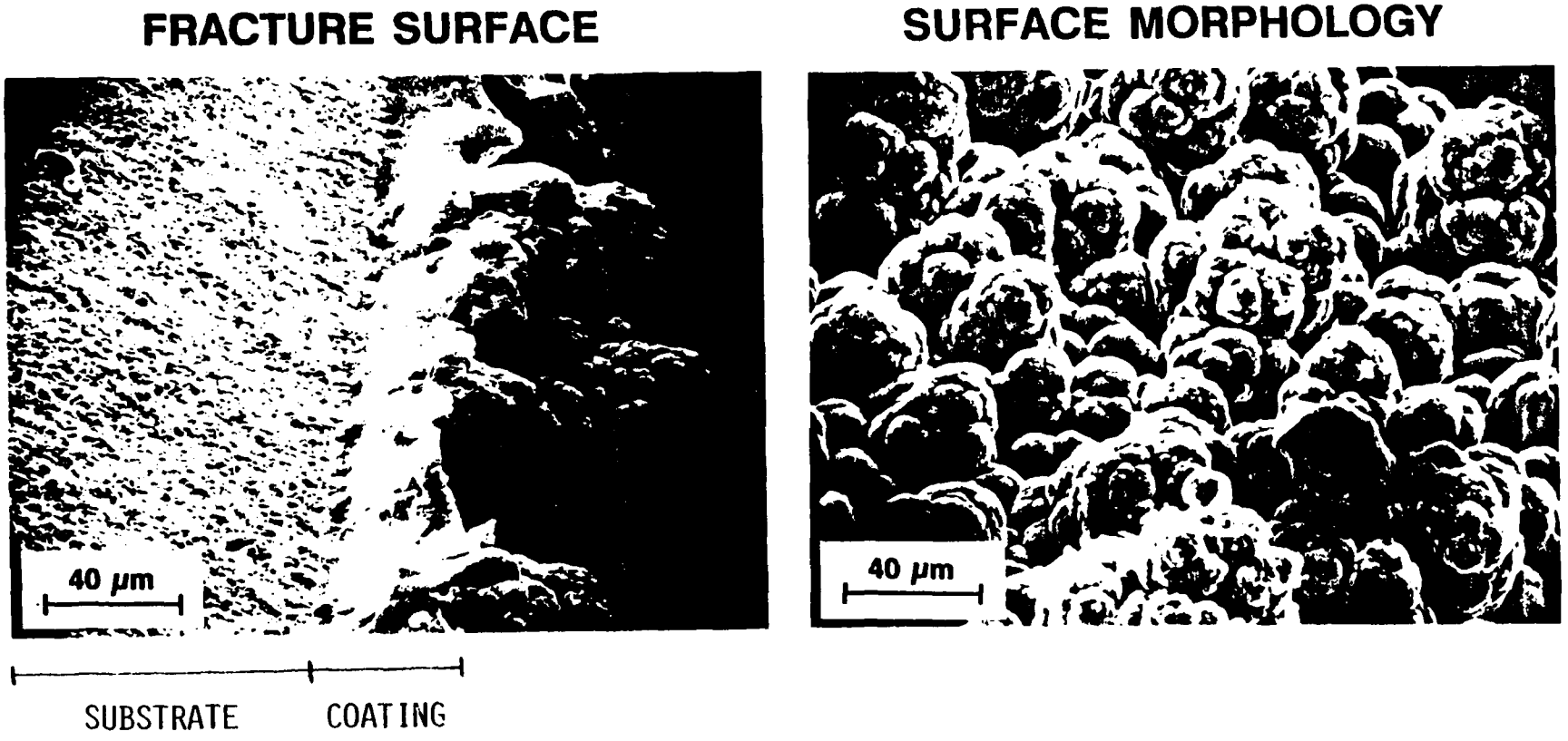

Figure 5-68. SEM micrographs of BN+AlN (J-840).

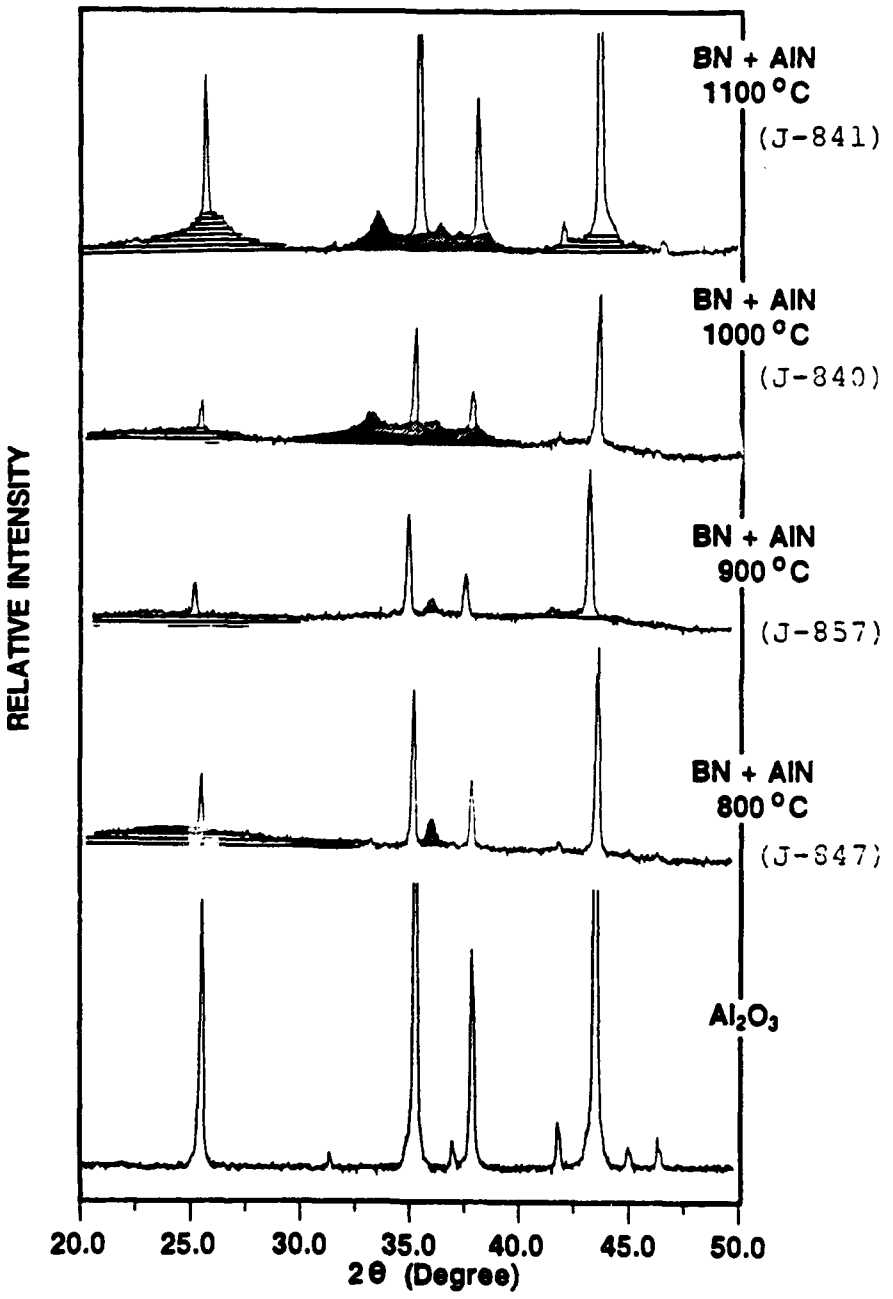

Figure 5-69. XRD patterns of BN+AlN deposited on Al_2O_3 at various temperatures (pressure = 40 torr, mole fraction of BCl_3 = 0.0025, and mole fraction of $AlCl_3$ ≈ 0.001).

nucleation of was suspected to start at about 1000°C. Furthermore, the XRD features of AlN obtained at 1000°C (see J-811 in Figure 5-35) were fairly close to those of the composite deposited at 1000°C (J-840). This suggested that homogenous nucleation of AlN also started to occur around 1000°C in the BN+AlN system. For BN-CVD, the occurrence of homogenous nucleation of BN at 1100°C was clearly indicated by SEM and XRD. The shape and position of the (002) XRD peak from BN deposited at 1100°C (see Figure 5-14) looked similar to those of J-841 shown in Figure 5-69. This also indicates that homogenous nucleation of BN probably occurred in the BN+AlN system at 1100°C. This interpretation was supported by the appearance of some spherical particles in the SEM micrographs of J-841 (deposited at 1100°C) as shown in Figure 5-70.

Furthermore, the extent of homogenous nucleation inside the CVD furnace could be speculated from indirect evidences. In our experimental arrangement, the reagent stream flows upward. Therefore, if the particles generated by homogenous nucleation became too heavy, they would fall down. The following equation can be used to calculate the critical size, d_p:

$$d_p = \frac{3\rho_g C_D V^2}{4\rho_p g} \qquad (5\text{-}20)$$

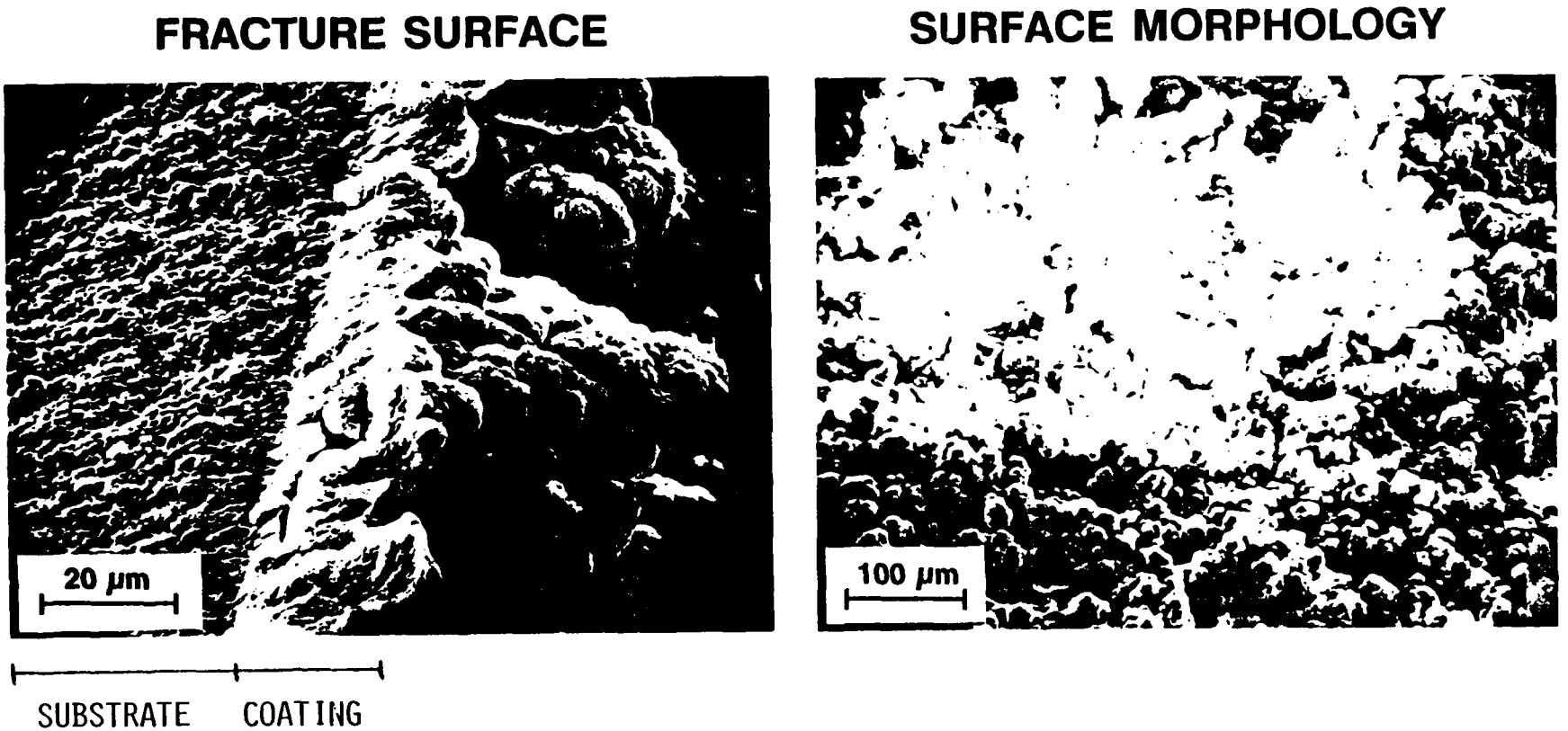

Figure 5-70. SEM micrographs of BN+AlN (J-841).

where ρ_g is the density of the gas mixture, C_D is the drag coefficient and is a function of the Reynolds number, v is the linear velocity of the gas stream, ρ_p the density of the particles formed in the gas phase, and g is the gravity constant. For typical processing conditions used in this study, the critical size for BN and AlN was calculated to be in the range of 0.1 to 0.3 μm. Larger particles would fall down onto the Al_2O_3 substrate which was placed perpendicular to the flow direction. Therefore, if homogenous nucleation was extensive enough to form particles larger than 0.1 to 0.3 μm in the gas phase, then the particles should be observed on the Al_2O_3 substrate. The particles formed in the gas phase were most likely to be spherical in shape (see Figures 5-18, 5-41, and 5-47). Such particles were not observed below 1000°C in our studies. Rather, highly crystalline whiskers were deposited on the top side of the Al_2O_3 substrate at 900°C as shown in Figure 5-71. The whiskers were identified to be AlN by XRD as shown in Figure 5-72. It is doubtful that these whiskers could be formed in the gas phase. Therefore, the whiskers likely grew via a heterogenous deposition process. Also, the absence of any spherical particles of 0.1 to 0.3 μm size at least excluded the possibility of extensive homogenous nucleation.

The effect of temperature on the microstructure of BN+AlN coatings deposited at 80 torr can clearly be seen from Figure

Figure 5-71. SEM micrograph of AlN whiskers deposited on the top side of the Al_2O_3 substrate (J-781).

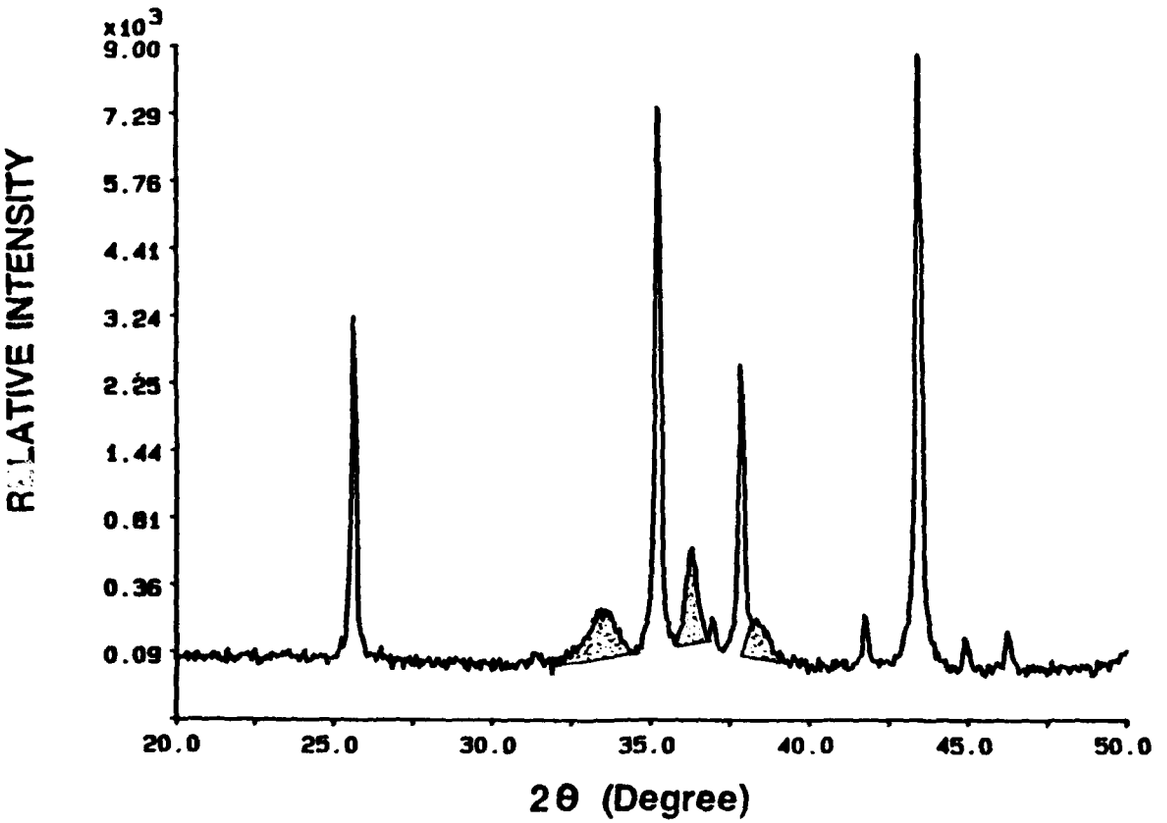

Figure 5-72. XRD pattern of BN+AlN (J-781).

5-73. The AlN phase became more crystalline and preferentially-oriented with increasing temperature from 800 to 1000°C. A similar trend was observed at 150 torr as shown in Figure 5-74. AlN became more crystalline and preferentially oriented with increasing temperature from 800 to 1000°C. However, the intensity of the AlN peaks decreased when temperature was further increased to 1100°C. Interestingly, the coating deposited at 1100°C was not visible under SEM (Figure 5-75) indicating the coating was very thin (e.g., less than 0.1 μm). The presence of turbostratic BN was apparent at 800°C, but was not noticeable at 900 and 1000°C.

At 150 torr, the increase in temperature from 800 to 1000°C resulted in a reduction of the Al content in the composites from 24.2% (J-853) to 9.5% (J-855) as determined by electron microprobe (see Table 5-6). Also, the coating became much softer with the decrease in the AlN content (or with the AlN whisker growth). These results agreed with our previous interpretation; the degree of whisker morphology (or (002) preferred orientation) increased with the decrease in AlN deposition rate. For the deposition experiments performed at 150 torr, homogenous nucleation of either BN or AlN was not evident from the SEM and XRD studies even at the deposition temperature of 1100°C. However, as discussed earlier, homogeneous nucleation of AlN started at 1000°C when the experiments were performed at 40 torr.

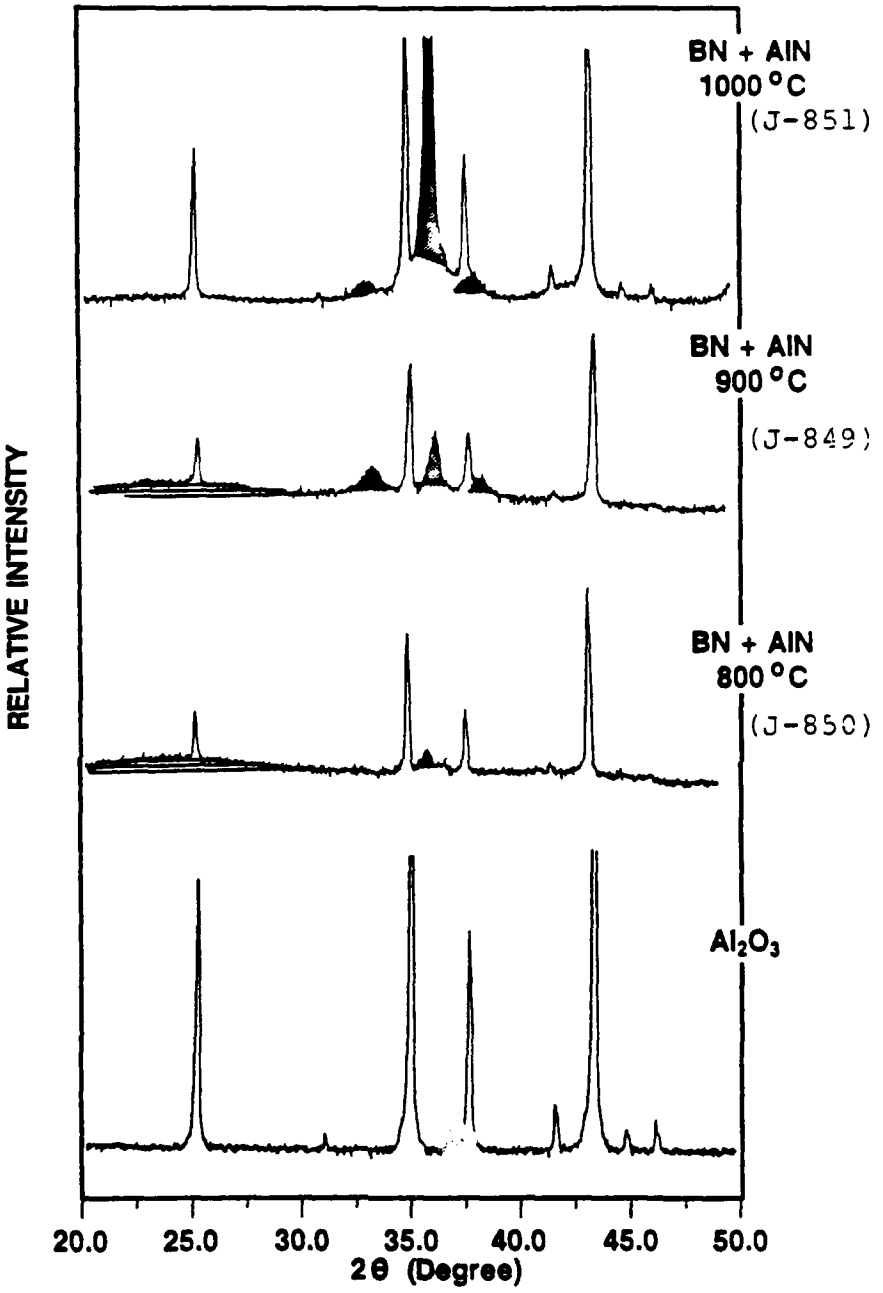

Figure 5-73. XRD patterns of BN+AlN deposited on Al_2O_3 at various temperatures (pressure = 80 torr, mole fraction of BCl_3 = 0.0025, and mole fraction of $AlCl_3$ ≈ 0.001).

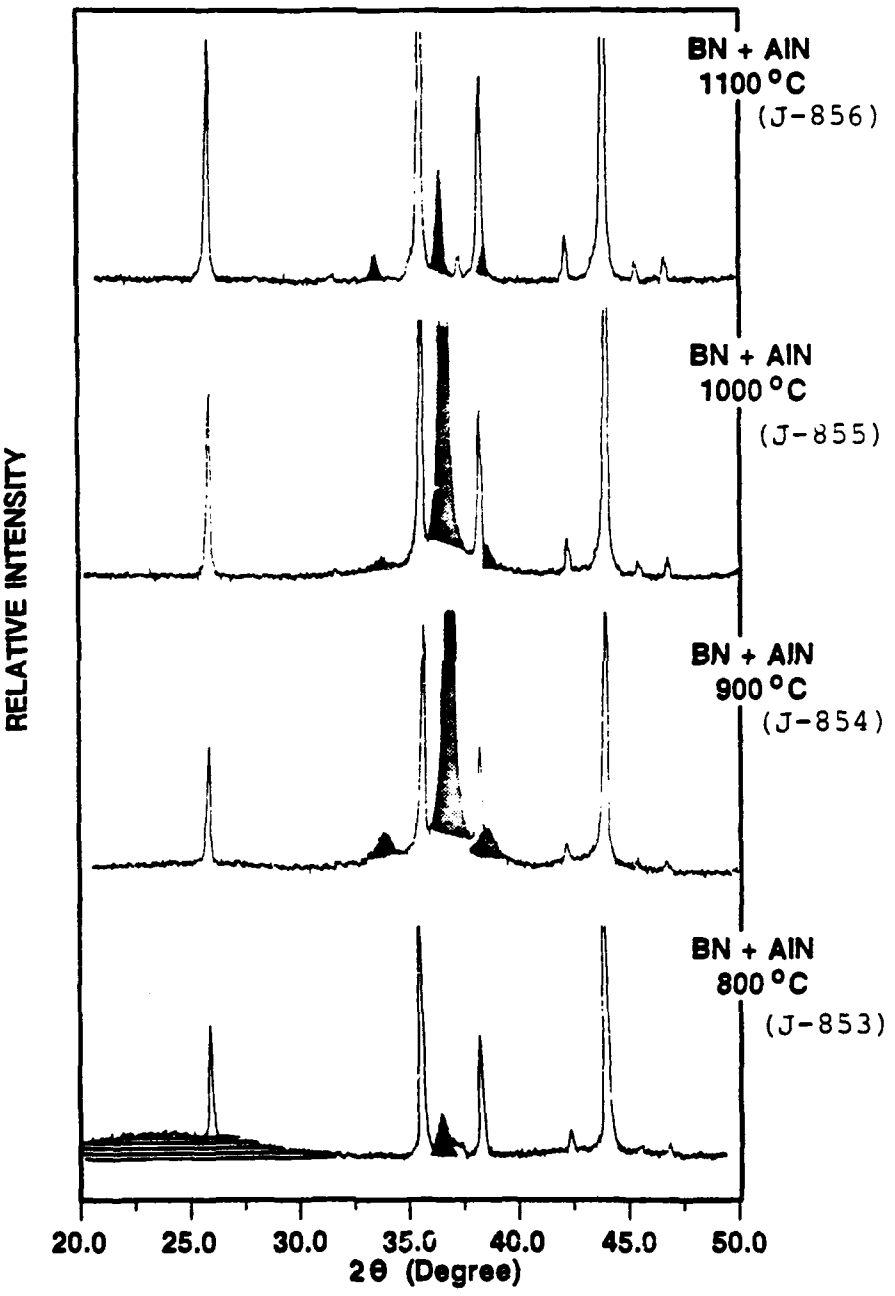

Figure 5-74. XRD patterns of BN+AlN deposited on Al_2O_3 at various temperatures (pressure = 150 torr, mole fraction of BCl_3 = 0.0025, and mole fraction of $AlCl_3$ ≈ 0.001).

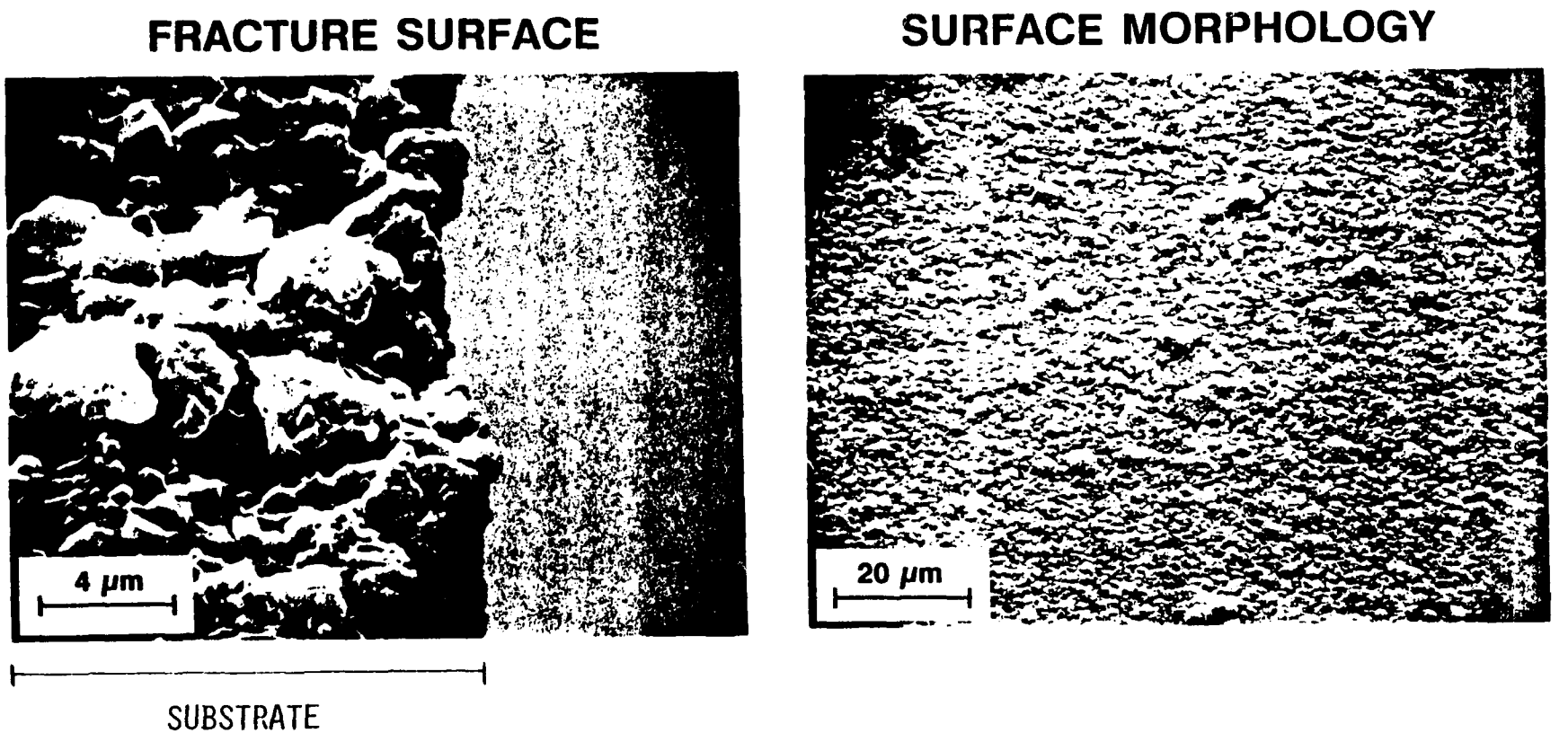

Figure 5-75. SEM micrographs of BN+AlN (J-856).

BCl_3 and $AlCl_3$ Concentrations. The effects of BCl_3 and $AlCl_3$ concentrations on the microstructure of BN+AlN coatings were as drastic as those of temperature and pressure. The changes in the XRD patterns with increasing $AlCl_3$ partial pressure can be seen in Figure 5-76. At a partial pressure of 0.02 torr, the AlN peaks were not visible, but the presence of BN was evident. As the partial pressure increased to 0.04 torr, the intensity of the BN phase decreased and a small (002) AlN peak appeared in the XRD pattern. With further increasing of the partial pressure to 0.065 torr, the AlN peaks became much more intense indicating that the AlN phase became more crystalline. Also, the (002) preferred orientation was noticed as the (002) peak was more intense than the other AlN peaks. But, it was difficult to tell the presence of the BN phase from the XRD pattern because of the rise in the baseline. Therefore, with the increase in the $AlCl_3$ partial pressure, the AlN phase became more crystalline whereas the BN phase became less-crystalline or remained at about the same crystalline level.

It appeared that the morphology of the coatings became increasingly rough with the increase in the $AlCl_3$ partial pressure. Figures 5-77 (J-836), 5-78 (J-835), 5-62 (J-857), and 5-79 (J-862) show the SEM micrographs of the composite coatings in the order of increasing $AlCl_3$ partial pressure. The Al content in the composites increased from 24.4% (J-836) to 61.9% (J-858) with the increase in the $AlCl_3$ partial

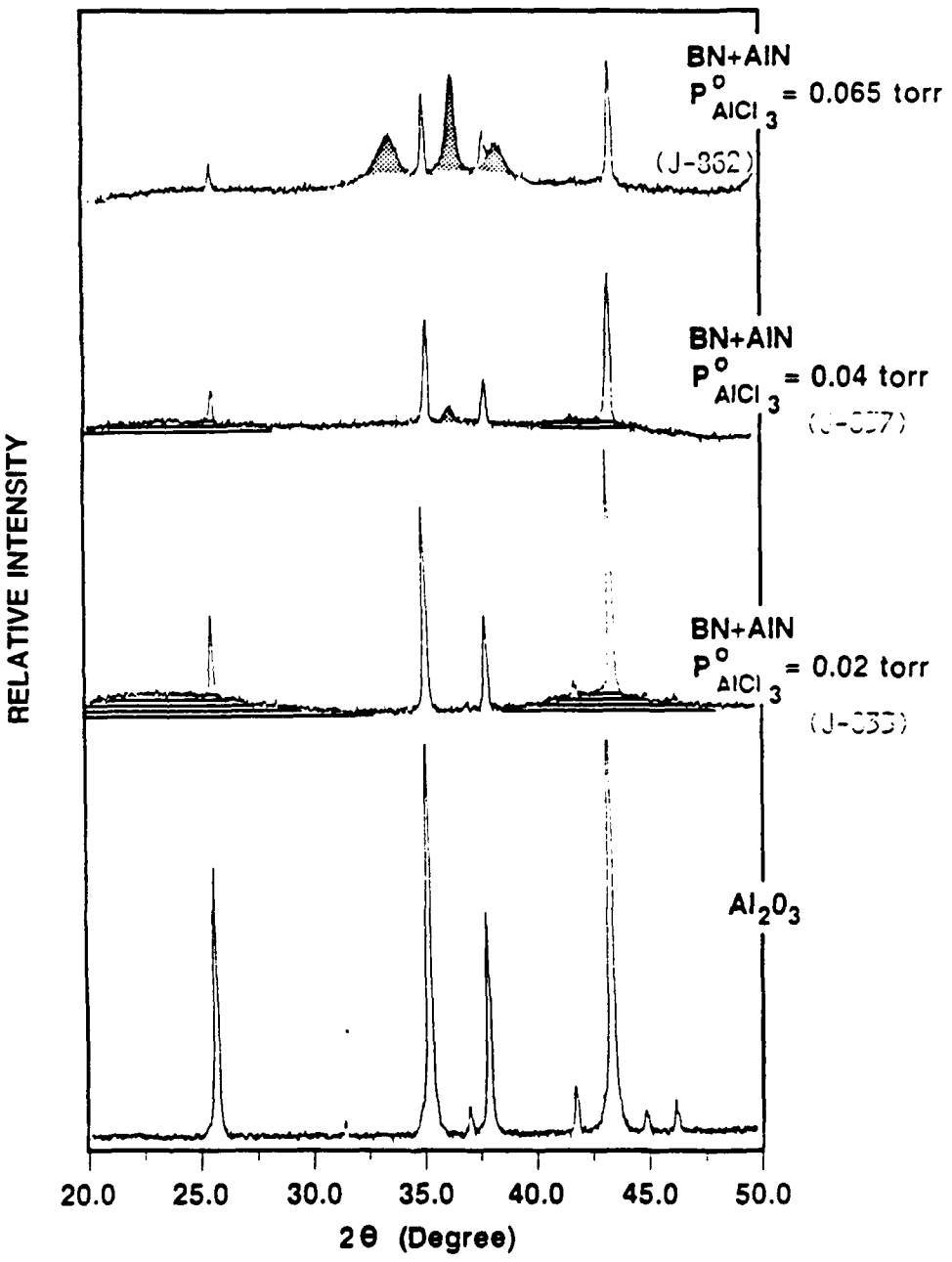

Figure 5-76. XRD patterns of BN+AlN deposited on Al_2O_3 at various $AlCl_3$ partial pressures (temperature = 900°C, pressure = 40 torr, and mole fraction of BCl_3 = 0.0025).

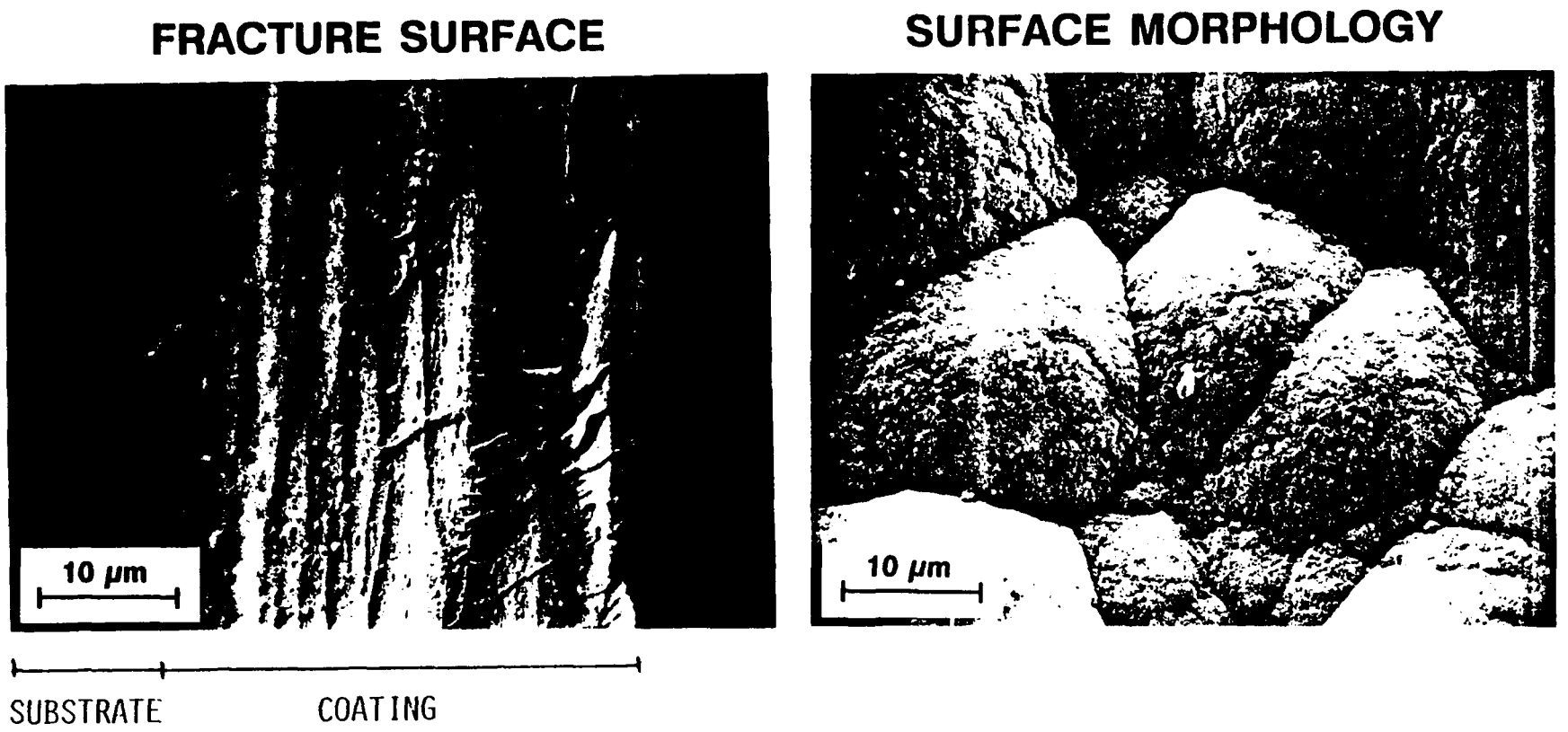

Figure 5-77. SEM micrographs of BN+AlN (J-836).

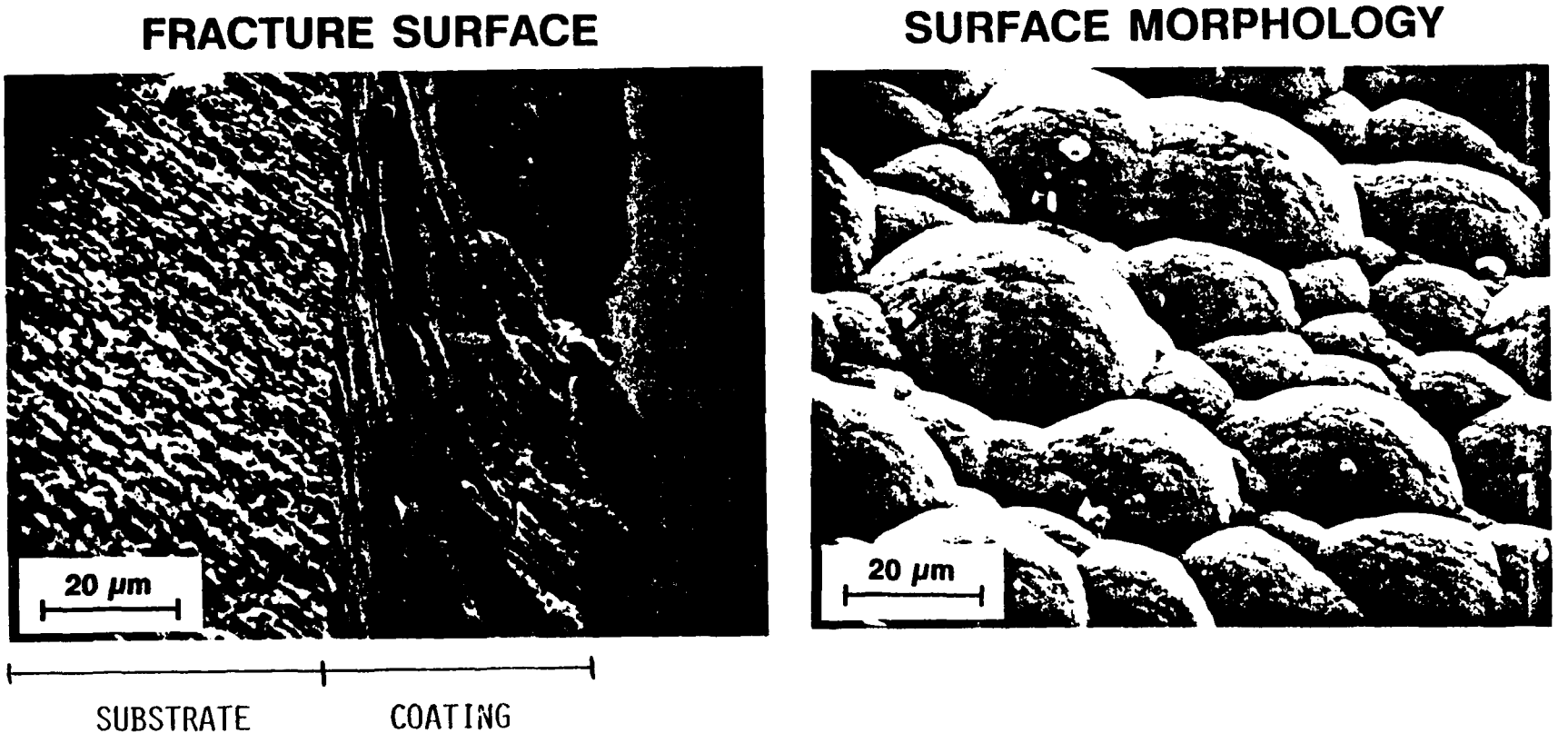

Figure 5-78. SEM micrographs of BN+AlN (J-835).

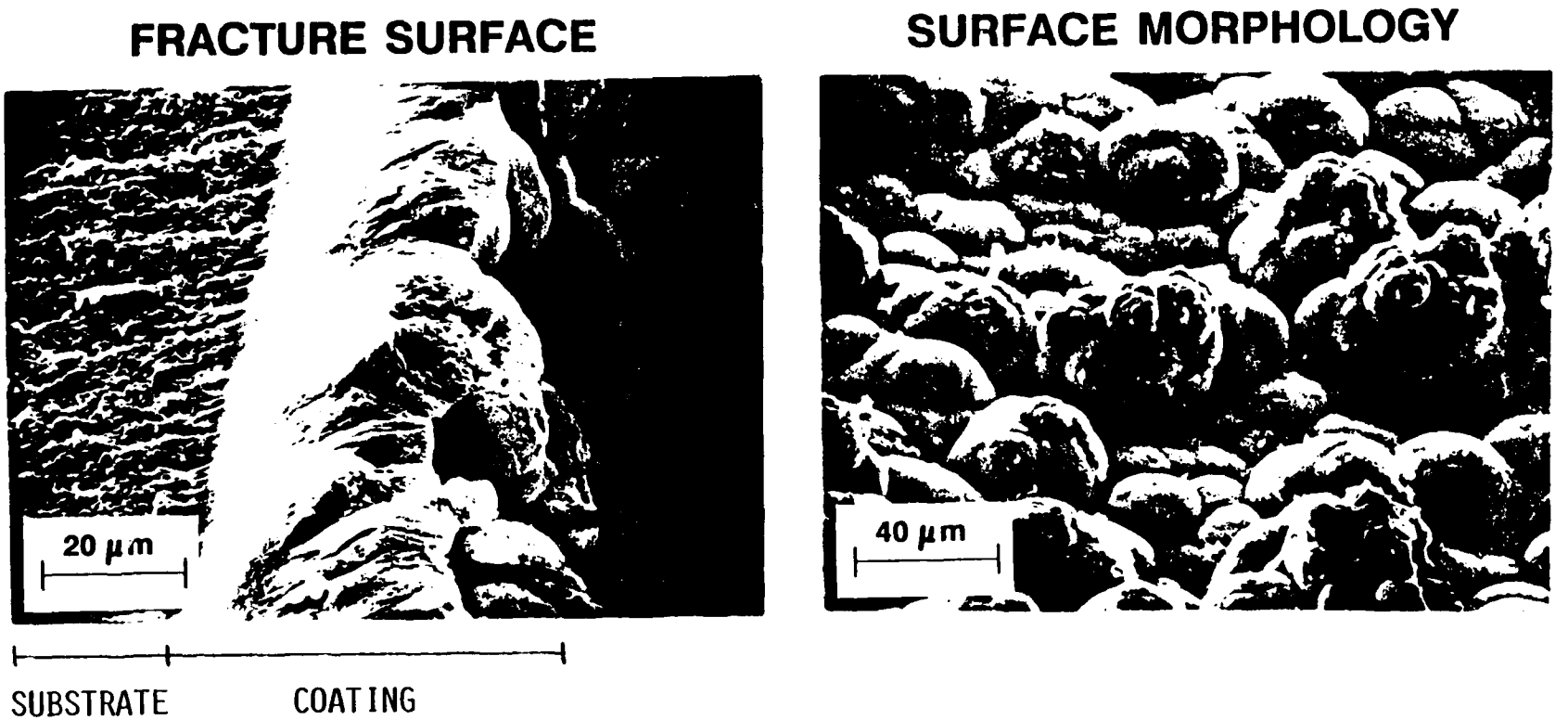

Figure 5-79. SEM micrographs of BN+AlN (J-862).

pressure. At the low concentrations (J-836 and J-835), the coatings had more uniform and smoother surfaces than those obtained at the high concentrations (J-857 and J-862).

With increasing BCl_3 partial pressure, a similar trend was observed. As shown in Figure 5-80, the intensity of the BN phase increased at the expense of the AlN phase on increasing the BCl_3 partial pressure from 0.1 to 0.2 torr. The B content in the composites also increased from 27.4% (J-859) to 51% (J-861) as shown in Table 5-6. The SEM micrographs are shown in Figures 5-81 (J-859), 5-82 (J-858), and 5-83 (J-861). It appeared from the micrographs that the coatings became somewhat more uniform and smoother on increasing the BCl_3 partial pressure (J-859).

The observations from the $AlCl_3$ and BCl_3 partial pressure variation experiments are summarized in Figure 5-84. The crystalline structure of the composite coatings determined by XRD were plotted as a function of the $AlCl_3$ and BCl_3 partial pressures. As shown in Figure 5-84, at the low BCl_3 and high $AlCl_3$ concentrations, the AlN phase was anisotropic whereas the BN phase appeared to be amorphous. Although the presence of the crystalline BN phase was not indicated by XRD, the electron microprobe analysis showed that BN was actually present in the composite coatings. For example, as shown in Table 5-6, J-859 contained up to 27.4% B confirming that the BN phase was amorphous. The opposite behavior was observed when high BCl_3 and low $AlCl_3$ concentrations were used. The

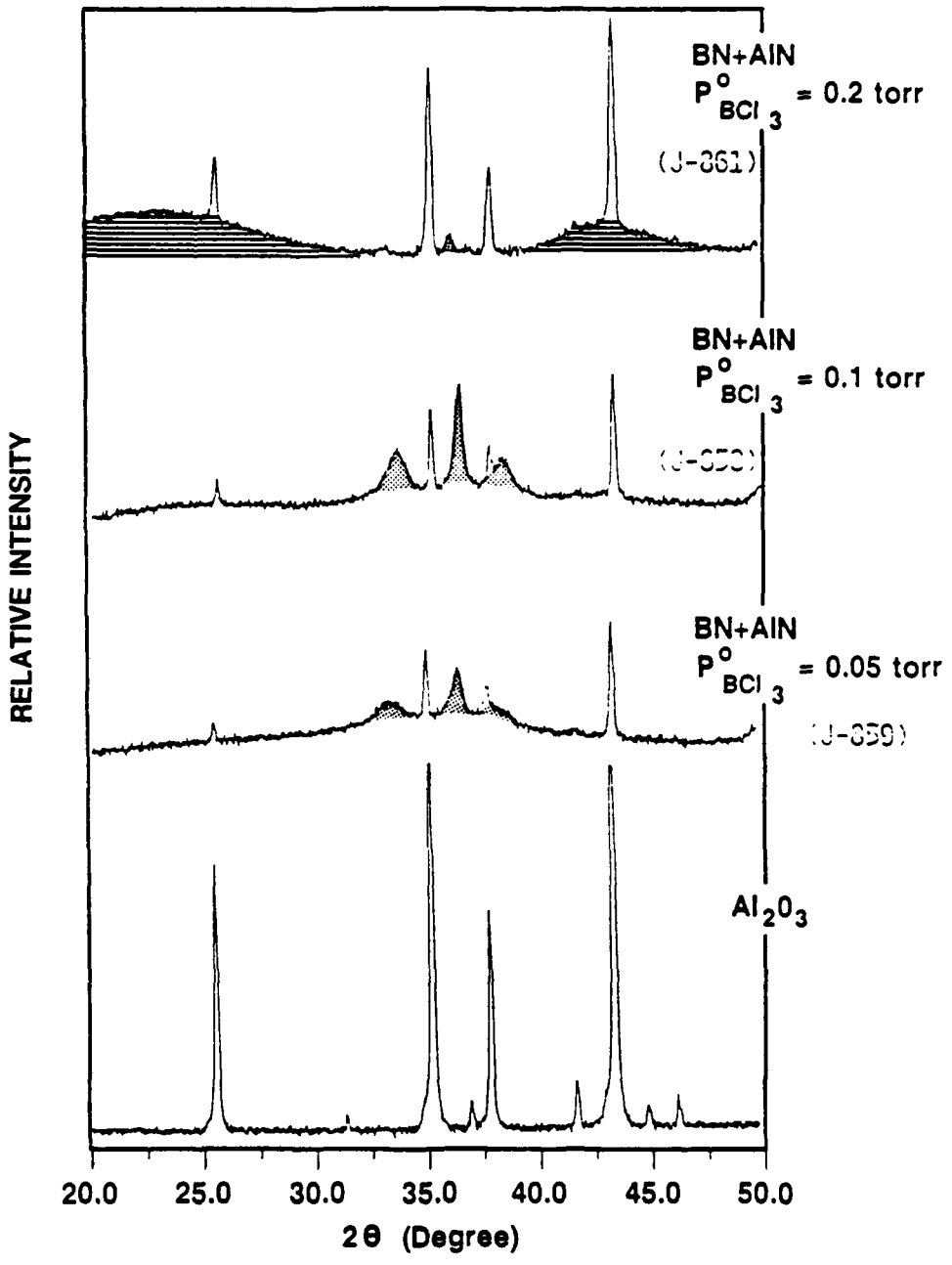

Figure 5-80. XRD patterns of BN+AlN deposited on Al_2O_3 at various BCl_3 partial pressures (temperature = 900°C, pressure = 40 torr, and mole fraction of $AlCl_3$ ≈ 0.001)

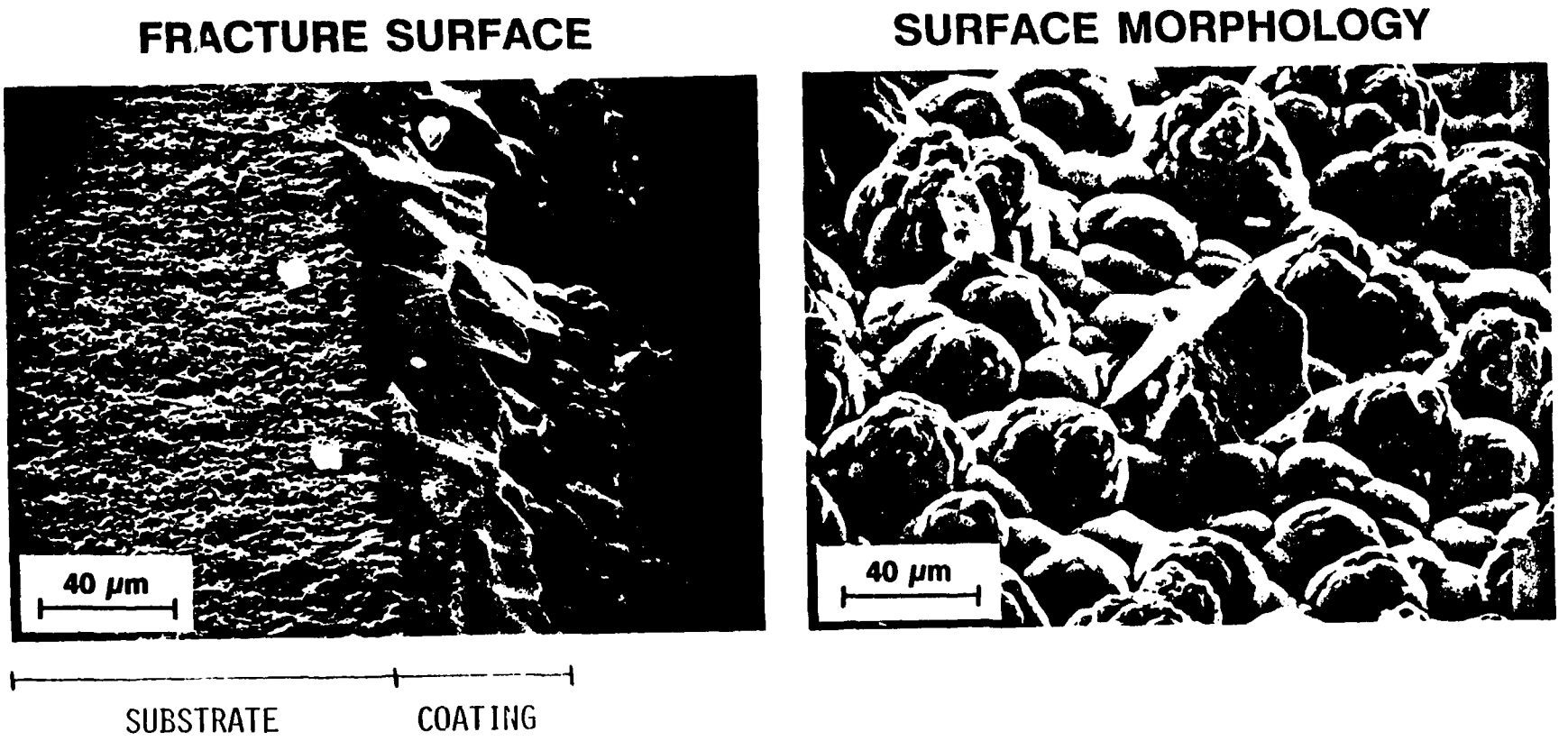

Figure 5-81. SEM micrographs of BN+AlN (J-859).

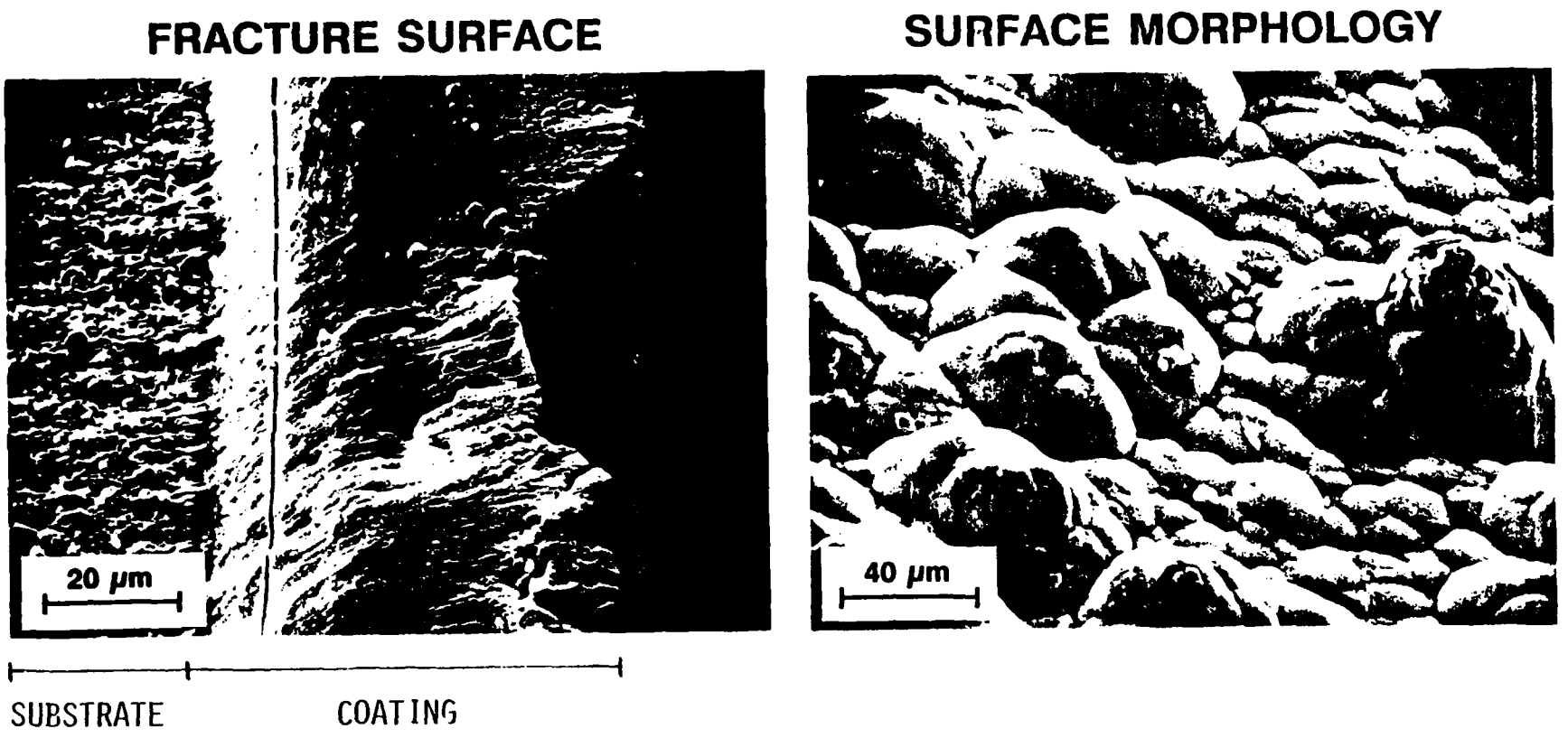

Figure 5-82. SEM micrographs of BN+AlN (J-858).

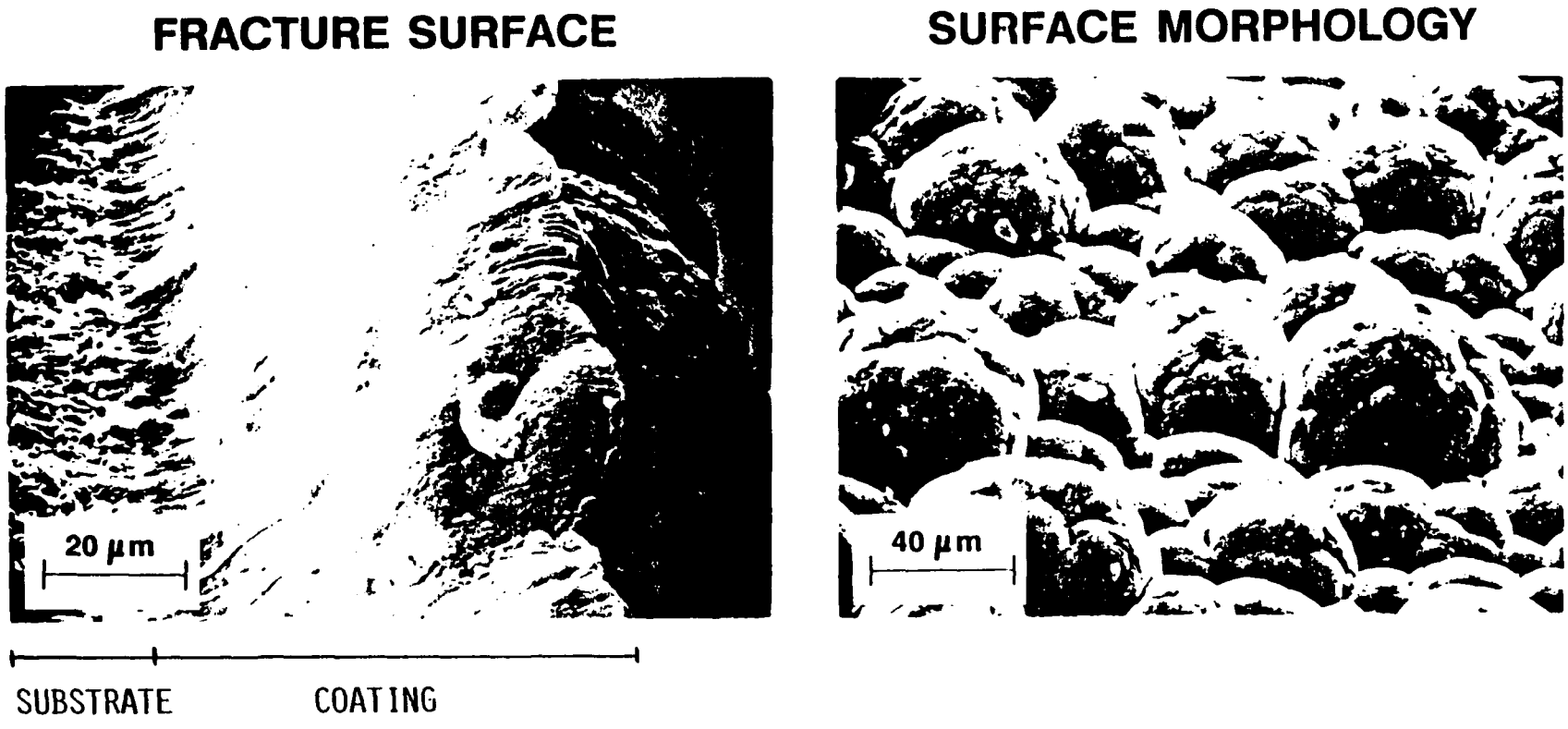

Figure 5-83. SEM micrographs of BN+AlN (J-861).

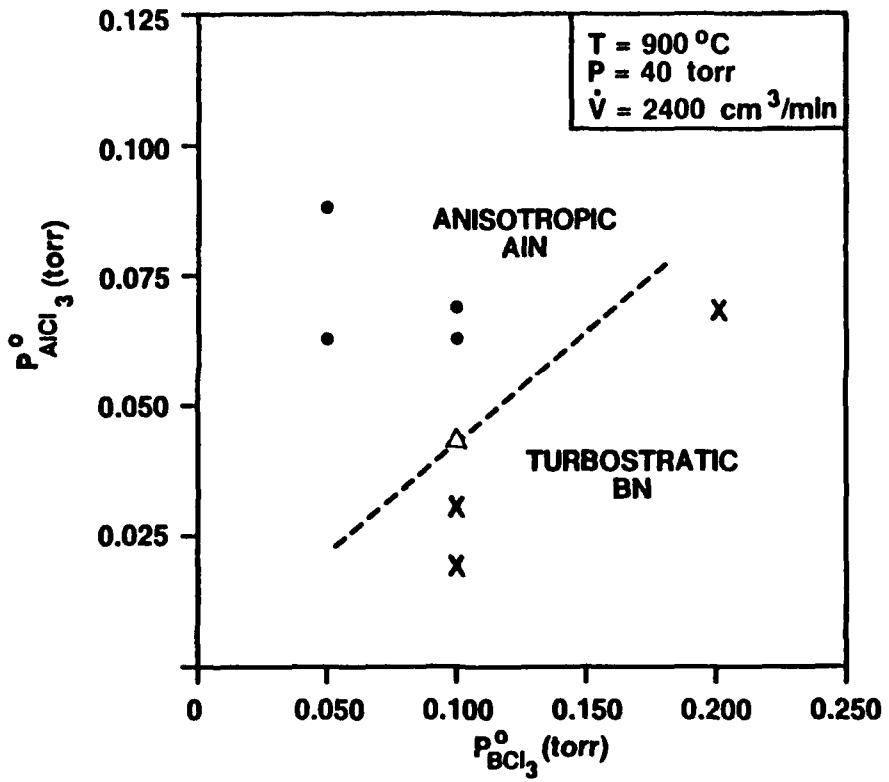

Figure 5-84. Crystalline structure of BN+AlN composites as a function of BCl_3 partial pressure and $AlCl_3$ partial pressure.

turbostratic BN phase was the dominating crystalline phase in the XRD patterns at these conditions. The electron microprobe results suggested that the AlN phase in these coatings was amorphous. For example, J-861 was found to contain about 6.9% Al suggesting that still a significant amount of the AlN phase was present in the composite.

Comparison with BN-CVD and AlN-CVD

The experimental results from the BN+AlN-CVD were compared to those from the BN-CVD and AlN-CVD in order to identify similarities and differences between the codeposition and the single phase processes. The following simplest portrayal of the BN+AlN-CVD process was used as the basis for the comparison studies:

$$\text{BN+AlN-CVD} = \text{BN-CVD} + \text{AlN-CVD} \qquad (5\text{-}21)$$

The expression represents codeposition as a CVD process in which both BN-CVD and AlN-CVD are independently progressing in the same space and time without any chemical and physical interactions. Obviously, the representation is a very ideal portrayal and therefore deviations are expected.

In order to show one of the major deviations observed in the present study, Eq. 5-21, can be rewritten in terms of deposition rate:

$$J_{BN+AlN} = J_{BN} + J_{AlN} \qquad (5\text{-}22)$$

Thus, the deposition rate from the BN+AlN-CVD is expected to

be the same as the simple sum of the individual rate from the BN-CVD and AlN-CVD processes. However, as shown in Figures 5-85 and 5-86, the actual deposition rate of the BN+AlN-CVD at various BCl_3 partial pressures and temperatures was usually much higher (by a factor of about 3) compared to that predicted by summing the BN and AlN deposition rates observed from the single phase processes at the same experimental conditions. Therefore, the BN+AlN process could not be described by the simple hypothesis behind Eq. 5-22.

Several possible reasons exist for the deviation. First, two types of deposition surfaces (i.e., BN and AlN) are present in the codeposition system at any given time. The surface chemistry of the codeposition process no longer resembles that of BN-CVD and AlN-CVD. Second, the thermodynamics of codeposition is different and can be furthermore complicated by kinetic factors, which is the subject of the next section. Because of the former reason, a detail kinetic analysis of the codeposition process (in a quantitative sense) becomes intractable in the absence of necessary surface chemistry data, and obtaining this type of data is beyond the scope of the present study. Nevertheless, our comparison studies provide enough clues for qualitatively understanding the physicochemical nature of the BN+AlN-CVD process.

One of the most intriguing observations made from the present study was that the changes occurring in the

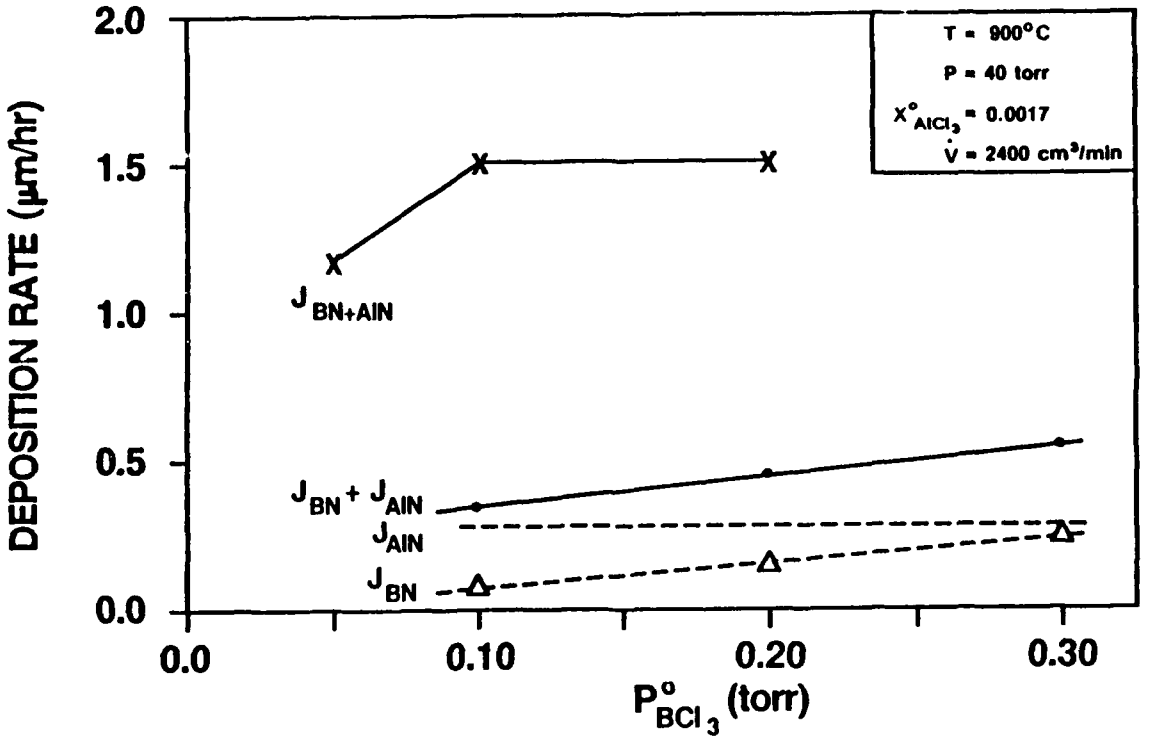

Figure 5-85. Comparison between J_{BN+AlN} and $J_{BN}+J_{AlN}$ as a function of BCl_3 partial pressure.

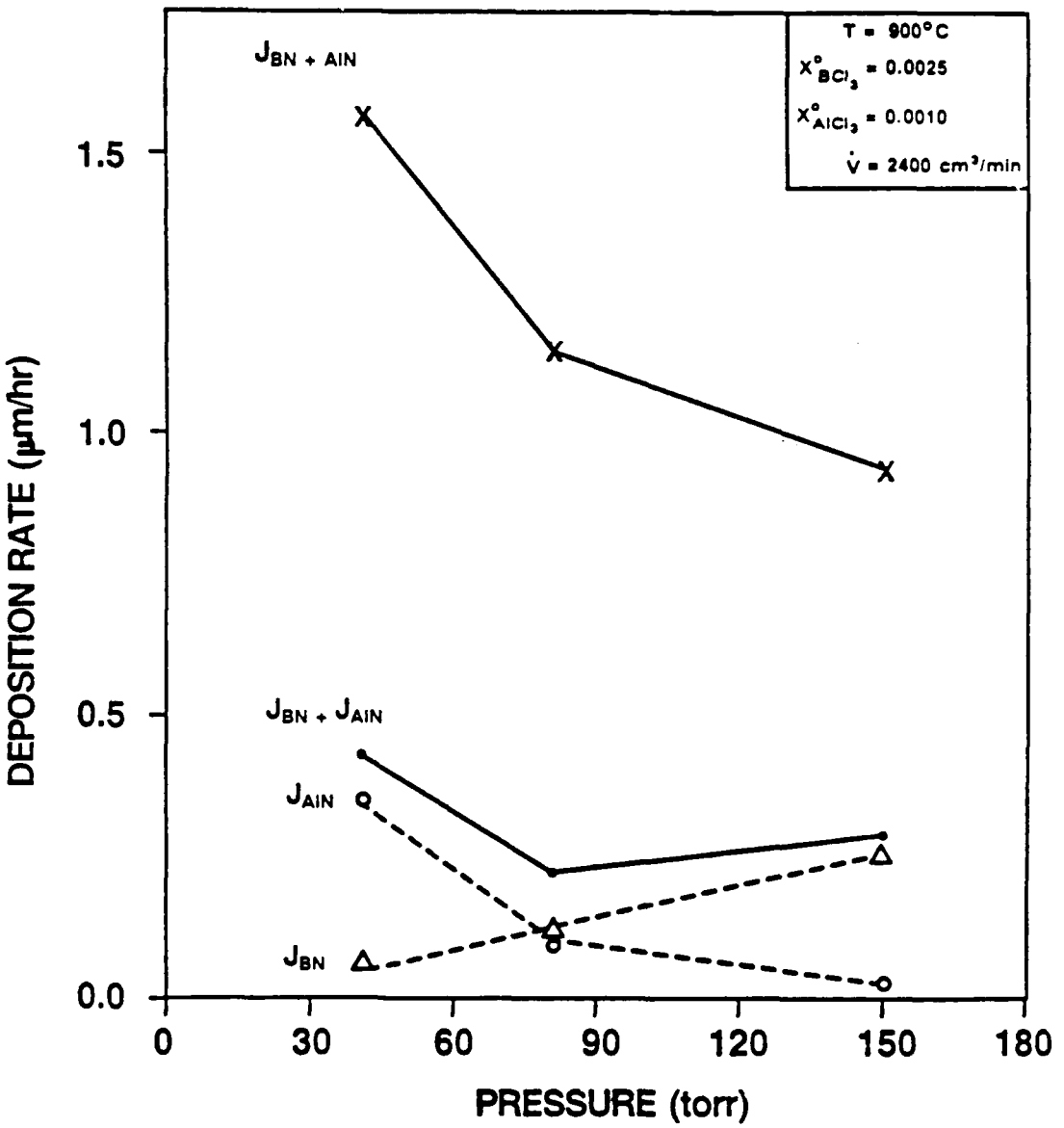

Figure 5-86. Comparison between J_{BN+AlN} and $J_{BN}+J_{AlN}$ as a function of temperature.

crystalline structure of the BN+AlN coatings with deposition temperature or pressure were fairly similar to those observed from the BN-CVD and AlN-CVD. In the previous section, it was learned that the AlN phase in the composite coatings became more crystalline and anisotropic on increasing the pressure from 40 to 150 torr at 900°C (see Figure 5-61). A similar trend was also observed for the AlN-CVD as was shown in Figure 5-34. The only difference between the two CVD systems was that the (002) AlN peak from the BN+AlN-CVD was much more intense than that from the AlN-CVD. This indicated that the degree of the (002) preferred orientation was much higher in the BN+AlN-CVD. On the other hand, the XRD features of BN were not strongly affected by pressure in either the BN+AlN-CVD or BN-CVD systems.

Furthermore, with increasing temperature, the XRD patterns obtained from the BN+AlN-CVD and AlN-CVD were also affected in a somewhat similar manner. As shown in Figures 5-69 and 5-35, the (100) AlN peak became more intense than the other AlN peaks at or above 1000°C for both CVD processes. Also, the shift of the (002) BN peak to higher 2θ direction, which was believed to be caused by homogenous nucleation, was observed to occur at 1100°C for both BN+AlN-CVD and BN-CVD processes (see Figures 5-69 and 5-9).

Based on the above observations, it seemed that the BN+AlN-CVD followed the essential features of the BN-CVD and AlN-CVD processes. For example, the increased crystallinity

of AlN in both BN+AlN-CVD and AlN-CVD with increasing pressure was due to a decrease in the AlN deposition rate. Also, the deposition rate of BN in both BN+AlN-CVD and BN-CVD increased with increasing pressure and temperature. Although the qualitative features of the BN+AlN-CVD were favorably compared to the BN-CVD and AlN-CVD, several differences were noticed as will be described in the following paragraphs.

In Figure 5-87, the XRD, SEM, and XPS results were combined to schematically illustrate the BN+AlN-CVD process in comparison to the BN-CVD and AlN-CVD processes. Based on results obtained from the BN-CVD section, the single phase BN coating is depicted as having a uniform and smooth morphology and consisting of numerous randomly-oriented turbostratic BN particles 20 Å in size. The single phase AlN coating from the AlN-CVD was found to have a rough morphology, and the (002) preferred orientation was usually observed as a result of the growth of AlN whiskers. The average diameter of the AlN whiskers was estimated to be several hundred angstroms. For the BN+AlN-CVD, two extreme cases were portrayed. The first case was when $J_{BN} > J_{AlN}$, corresponding to samples such as J-855. In this case, BN probably covered most of the deposition surface at any given time resulting in a reduction of the density of the AlN stable nuclei and, thus, in the number of AlN whiskers. This interpretation was supported by the XRD studies which indicated that the average diameter of the AlN whiskers increased from about 150 Å for the AlN-CVD to about

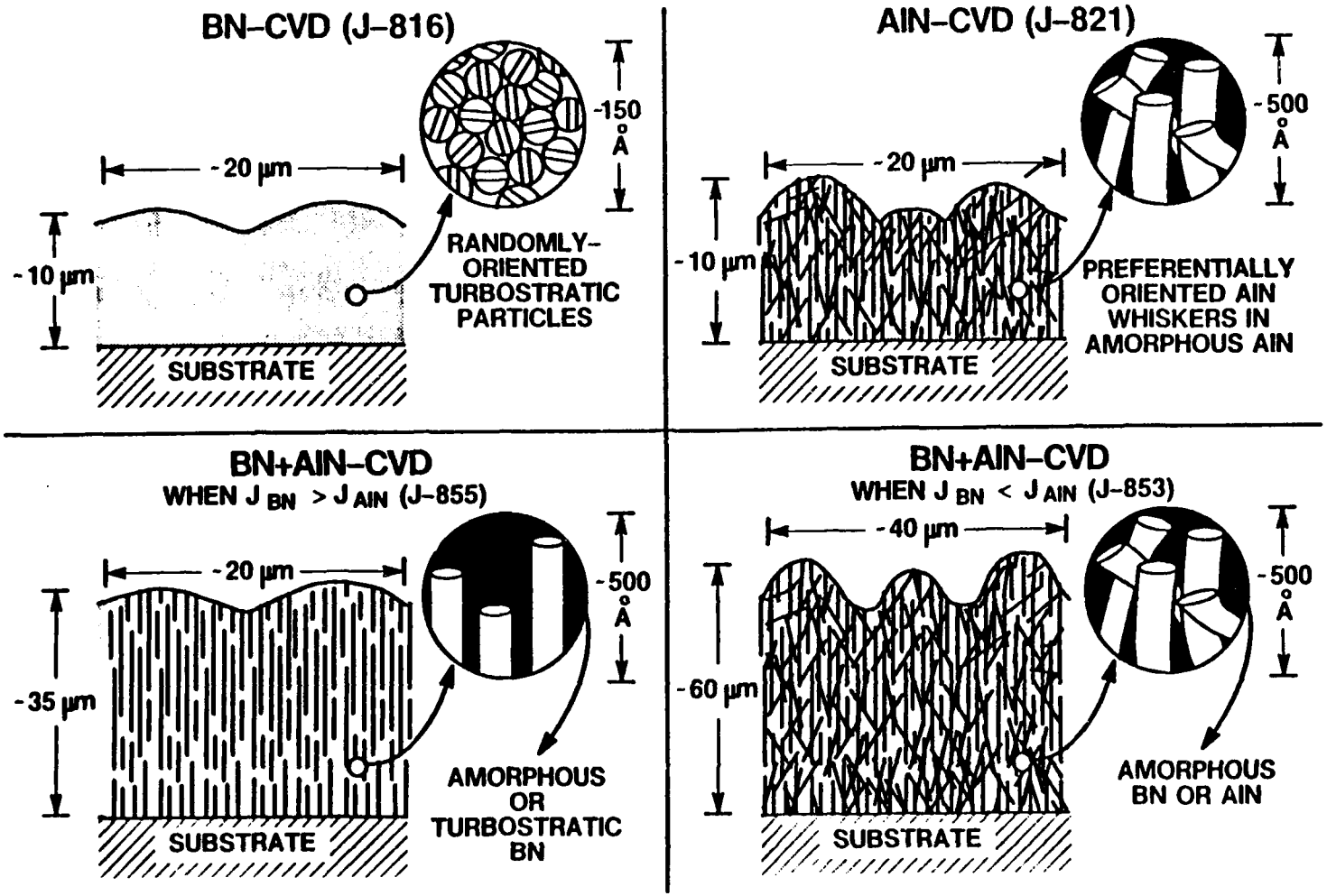

Figure 5-87. Ideal illustration of BN, AlN, and BN+AlN coatings.

300 Å for the BN+AlN-CVD. Also, the AlN deposition rate was low causing the growth of crystalline and preferentially oriented AlN whiskers. The AlN whiskers were more preferentially oriented as the AlN deposition rate decreased. The AlN whisker morphology was more evident in the BN+AlN-CVD than in the AlN-CVD. For the other extreme case when $J_{BN} < J_{AlN}$ (e.g., J-853), the coating morphology was essentially that observed from the AlN-CVD except for the additional amorphous BN phase incorporated within the coating structure.

There was another major deviation observed for the BN+AlN-CVD process in comparison to the BN-CVD and AlN-CVD processes. In the single phase deposition processes, turbostratic BN was always deposited at 900°C (see Figures 5-10 and 5-11) whereas either anisotropic or somewhat amorphous AlN was usually deposited at 900°C depending on the $AlCl_3$ partial pressure (see Figures 5-34 and 5-36). However, for the BN+AlN composites prepared at 900°C, the presence of turbostratic BN was not observed in the XRD patterns with increasing the $AlCl_3$ partial pressure or decreasing the BCl_3 partial pressure as shown in Figure 5-84.

The crystal growth behavior observed from the XRD studies can be qualitatively explained. The important basis of the hypothesized explanation is that the codeposition of two chemically different phases (i.e., BN+AlN) is a competitive process in which the growth of one phase interferes with and/or limits the growth of the other. For example, it is

recalled from the BN-CVD studies that the average crystallite size of BN obtained at 900°C is less than 20 Å. If the growth of AlN is favored over that of BN, BN grains will be out-grown by AlN grains and the BN grains will become even smaller in the codeposited material than in the single phase coating. Such small BN particles are probably not large enough to be classified as turbostratic (i.e., the structure could be said to be amorphous) and thus are not detected by XRD. This type of behavior was previously observed by Hirai et al. [4,5] for the Si_3N_4+BN-CVD system. They reported that turbostratic BN was detected only when the B content of the composites was greater than 33% by weight. The Si_3N_4 phase in the composite structure was amorphous.

As a summary, the major observations from the comparison studies are noted as follows:

(1) The BN+AlN-CVD system could not be described in a quantitative manner by superimposing the individual BN-CVD and AlN-CVD processes (i.e., $J_{BN+AlN} \neq J_{BN} + J_{AlN}$).

(2) Qualitatively, the BN+AlN-CVD followed the essential deposition characteristics observed for the BN-CVD and AlN-CVD such that: (a) growth of AlN whiskers became more apparent with increasing pressure or temperature, (b) AlN deposition rate decreased with increasing pressure, and (c) BN deposition rate increased with increasing pressure and temperature.

(3) The growth of AlN whiskers was accentuated in the BN+AlN-CVD compared to the AlN-CVD.

(4) A physical competition between BN and AlN grains was suspected to cause the reduction in the ultimate grain size of BN and AlN in the BN+AlN-CVD composites.

(5) The BN+AlN coatings became harder with an increase in the Al content.

Comparison with Thermodynamic Predictions

Figure 5-88 shows a deposition diagram obtained from the previous thermodynamic studies on the BN+AlN composite system [61,68]. The diagram shows solid phases which would be stable (i.e., deposited) at equilibrium as a function of reagent concentrations (i.e., $AlCl_3$, BCl_3, and NH_3) at 927°C and a pressure of 150 torr (20.2 kPa). The region of importance in the diagram is the two phase region identified as BN+AlN, located near the right side of the composition triangle. Codeposition of BN and AlN is predicted within this region. Details about the deposition diagram as well as the thermodynamic calculations are discussed in Chapter II. Additional diagrams were constructed in order to evaluate the influence of temperature, pressure, and hydrogen concentrations on the codeposition process. In summary it was found that: (1) increasing temperature from 923 to 1423°C significantly reduced the BN+AlN phase region, (2) the addition of H_2 slightly increased the area of the BN+AlN region and caused the disappearance of the AlB_{12} phase, and (3)

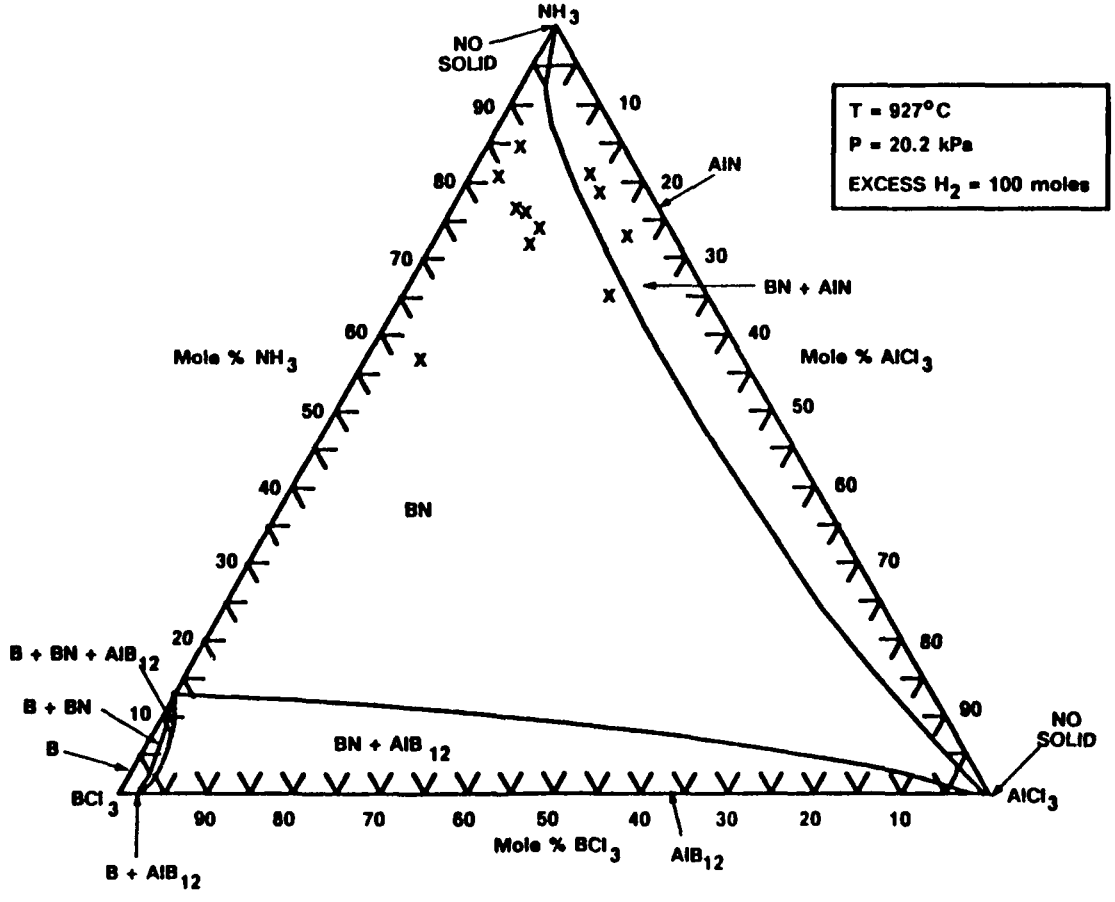

Figure 5-88. Deposition diagram obtained from thermodynamic calculations. Experimental results obtained at 900 to 927°C and 150 torr are plotted as X marks.

altering pressure did not have much effect on the deposition behavior at lower temperatures. Nevertheless, the studies showed that the BN+AlN composite may be prepared over a fairly wide range of temperatures and reagent concentrations resulting in a BN content ranging from 0 to 100%.

Experimental results from the BN+AlN-CVD experiments performed at 900 to 927°C and 150 torr are also plotted on the same deposition diagram shown in Figure 5-88 in order to compare the thermodynamic predictions with the observed deposition behavior. It is noted that the conditions used for the thermodynamic calculations and CVD experiments are quite similar except that a rather large amount of Ar was used in the experiments. However, the addition of Ar in the thermodynamic calculations is equivalent to lowering total system pressure, which is found to have negligible influence on the deposition behavior at this temperature. Therefore, the comparison attempted in Figure 5-88 is valid. As can be seen in Figure 5-88, BN+AlN composites were successfully deposited for reagent compositions occurring both inside and outside the predicted two phase region.

Several possible reasons exist which explain why BN and AlN can be deposited for conditions located outside of the predicted BN+AlN region. First, the question of achieving a thermodynamic equilibrium state in the open-flow CVD process is uncertain. For the BCl_3-$AlCl_3$-NH_3 system, the kinetic contributions to the observed deposition behavior have not

been quantitatively identified to assess the importance of kinetic effects. However, in order to show how kinetics can override the thermodynamic predictions, the following example can be considered. The major reaction paths for the BN+AlN-CVD are assumed as follows:

$$\begin{array}{lll} BCl_3 & \xrightarrow{1} & BN + 3HCl \\ + \ 2NH_3 & & \\ AlCl_3 & \xrightleftharpoons{2} & AlN + 3HCl \end{array} \qquad (5\text{-}23)$$

Furthermore, path 1 is assumed to be kinetically-controlled and path 2 is assumed to be fast enough to reach an equilibrium state. From the BN-CVD studies, the BN-CVD was found to be kinetically-controlled at 900°C. Also, the AlN-CVD at 900°C could be approximated by the mass transfer-thermodynamic limits. Therefore, the above assumptions are reasonable. The thermodynamic calculations show that BCl_3 is always completely converted to BN whereas the formation of AlN from $AlCl_3$ and NH_3 is thermodymically less-favorable than the BN deposition. Figure 5-88 shows that BN+AlN can only be deposited when the BCl_3 concentration is low. Since reaction path 2 is fast, a local equilibrium state for the deposition of AlN with respect to the BCl_3 conversion (or how fast the BN deposition is taking place) can be established at the deposition surface. For example, Figure 5-89 shows the changes in the thermodynamic yield of AlN as a function of the

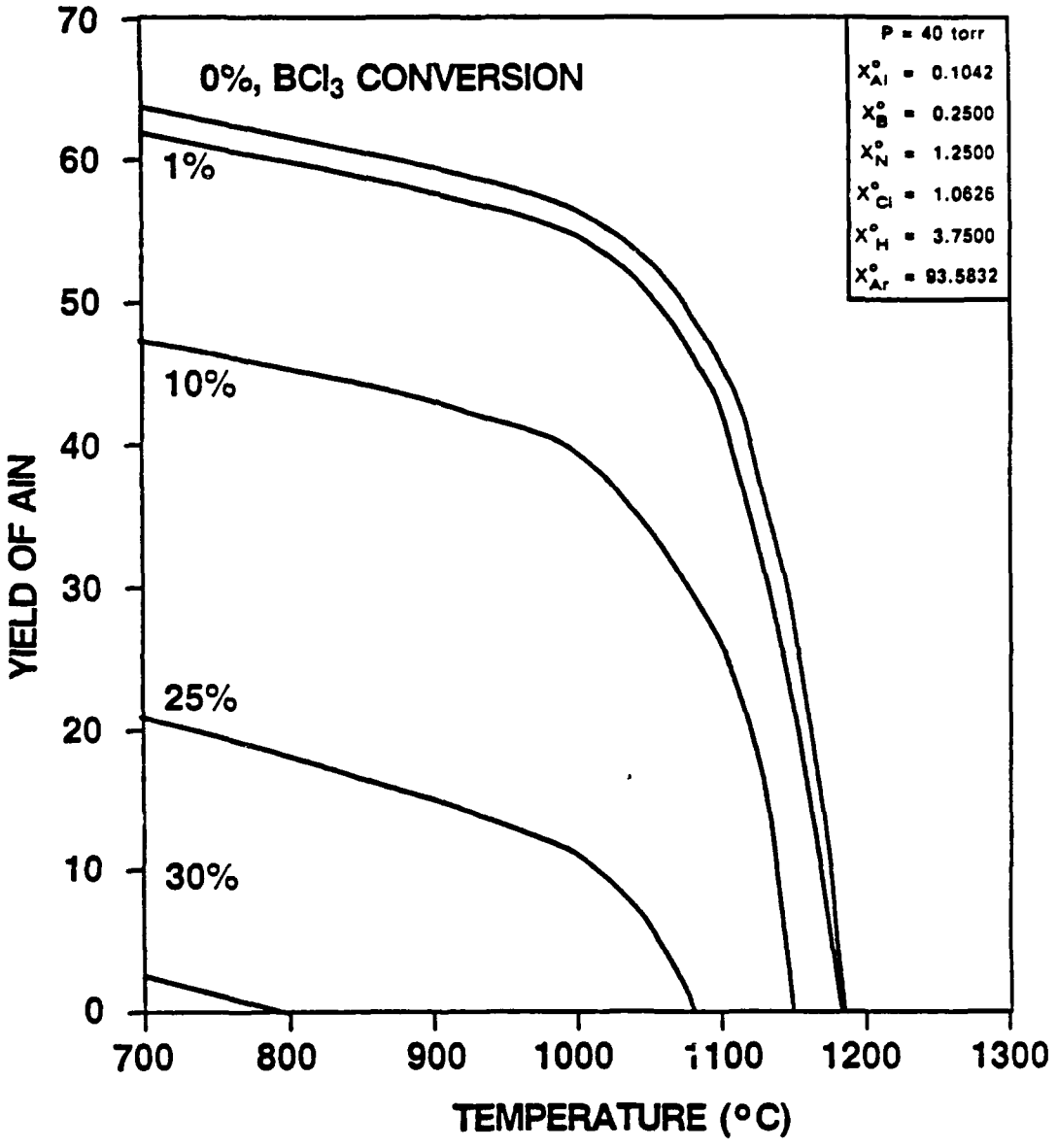

Figure 5-89. Thermodynamic yield of AlN as a function of %BCl, conversion to BN at various temperatures.

"actual" BCl_3 conversion in the BN+AlN system. The actual conversion is determined by kinetics whereas the thermodynamic conversion of BCl_3 to BN is always predicted to be 100%. When the BCl_3 conversion is 0% (i.e, AlN-CVD), the yield of AlN is predicted to be about 59% at 900°C. The BCl_3 conversion predicted by the thermodynamic calculations is 100% for both BN+AlN-CVD and BN-CVD. For the 100% BCl_3 conversion, the deposition of AlN is not predicted. However, the BN deposition is slow so that the actual BCl_3 conversion is expected to be much lower than the 100% predicted by thermodynamics. When the actual BCl_3 conversion is lower than 30%, the deposition of AlN is predicted.

Therefore, the "local equilibrium" analysis suggested the possibility of codepositing BN and AlN at input conditions located outside of the BN+AlN region shown in Figure 5-88. Other possible reasons for disagreement between the experimental results and the thermodynamic predictions are: (1) the presence of homogeneous nucleation which will deplete reagents and (2) uncertainty in thermodynamic data reported in the JANAF Tables [102,103].

CHAPTER VI

CONCLUSIONS AND RECOMMENDATIONS

Dispersed phase composite coatings containing BN and AlN were deposited by CVD (BN+AlN-CVD) over a wide range of processing conditions. Also, single phase BN and AlN coatings were prepared (BN-CVD and AlN-CVD). The BN-CVD process was determined to be kinetically-controlled for temperatures in the range 800 to 1000°C. A simple rate expression which had a first-order dependency on the BCl_3 concentration and an activation energy of 39.4 Kcal/mole was adequate to describe the deposition process. The deposition rate of BN varied from 1 to 15 μm/hr depending on the processing conditions. The deposition rate increased with pressure, temperature, and BCl_3 concentration. The BN coatings were usually turbostratic and isotropic. The average grain size of the BN coatings was less than 20 Å. The surface of the BN coatings usually looked uniform and consisted of nodules 1 to 4 μm in diameter.

The AlN-CVD process could be approximated by calculating mass transfer-thermodynamic limits at low temperatures and $AlCl_3$ concentrations. Above 1000°C, the deposition rate of AlN decreased tremendously due to an increase in the thermodynamic stability of gas species such as $AlCl_2$ and AlCl. At high $AlCl_3$ concentrations, the process appeared to be

limited by a surface reaction involving $AlCl_3$ adsorbed on the deposition surface. The AlN coatings became highly crystalline and preferentially oriented with an increase in pressure. The AlN deposition rate was in the range of 1 to 20 μm/hr depending on processing conditions. The surface morphology of the AlN coatings was generally rough and much less-uniform in comparison to that observed from the BN-CVD.

Codeposition of BN and AlN as two distinctly different chemical and crystalline phases was successful as determined by various characterization techniques such as XRD, SEM, XPS, TEM, and high resolution TEM. Furthermore, the morphology and crystalline structure of the BN+AlN composite coatings were strongly influenced by temperature, pressure, $AlCl_3$ concentration, and BCl_3 concentration. In general, the deposition characteristics observed for the codeposition were similar to those expected from the single phase deposition processes. However, several interesting differences were observed. For example, the growth of AlN whiskers was accentuated in the BN+AlN-CVD in comparison to that in the AlN-CVD.

Hardness of the BN+AlN coatings increased with increasing AlN content. The relative amounts of BN and AlN in the composites could be predicted and controlled by understanding the kinetics and thermodynamics of the BN-CVD and AlN-CVD process. Also, the present research has provided a fundamental basis for improving the understanding of the

physicochemical nature of codeposition processes. The following recommendations are made for any future research activities or interests in the preparation of dispersed phase ceramic composites by CVD:

(1) The BN-, AlN-, and BN+AlN-CVD processes can be scaled-up to accommodate more complex geometries by using intrinsic deposition mechanisms identified in the present investigation and also utilizing a two-dimensional model. It will be a real challenge to fabricate composite coatings which will have uniform composition and microstructure over the entire area of the substrate(s). The use of rotating substrates or multi-nozzles for the introduction of reagents into the CVD chamber may be a solution to the above problem.

(2) The role of initial substrate surface (i.e., BN, AlN, graphite, etc.) on the deposition kinetics and coating microstructure needs to be studied in more detail.

(3) Differences and similarities between codeposition and alternate-deposition (i.e., layered composite structure) can be explored. This type of investigation will be valuable in understanding the role of surface chemistry in these complex CVD processes.

(4) Other codeposition systems such as HfB_2+HfC, HfB_2+SiC, TiB_2+TiC, ZrB_2+ZrC, etc. can be studied and compared to assess any similarities or trends among the codeposition processes.

APPENDIX

COMPUTER PROGRAM; CVDWYL

```
C   THIS PROGRAM (CVDWYL) CALCULATES:
C
C       (1) VISCOSITY OF BCL3(1)-ALCL3(2)-NH3(3)-AR(4)
C           -H2(5) GAS MIXTURE;
C
C       (2) DIFFUSION COEFFICIENT OF EACH GAS SPECIE;
C
C       (3) THICKNESS OF CONCENTRATION BOUNDARY LAYER OF EACH
C           GAS SPECIE IN IMPINGING JET GEOMETRY;
C
C       (4) DIFFUSIONAL FLUX OF BCL3 AND ALCL3 THROUGH
C           THEIR CONCENTRATION BOUNDARY LAYERS (I.E., UPPER
C           LIMITS FOR BN & ALN DEPOSITION RATES);
C
C       (5) APPARENT & INTRINSIC KINETIC RATE CONSTANTS OF BN
C           & ALN BY INDENTIFYING MASS TRANSFER CONTRIBUTIONS
C           TO DEPOSITION RATES OBSERVED EXPERIMENTALLY.
C
C   THIS PROGRAM USES CGS UNITS UNLESS INDICATED OTHERWISE.
C
C
C
C                              BY
C
C                          WOO Y. LEE
C                         GEORGIA TECH
C                            1989
C
C
C
      DIMENSION FLOWRT(5),X(5),EK(5),VISCO(5),DIFFUC(5)
     1,DELTAC(5)
      REAL JALN,JBN,KINVIS,MDIA(5),MW(5)
C
C UNIVERSAL GAS CONSTANT
C
      R=82.05
C
C PROCESSING PARAMETERS IN CGS UNITS
C (CENTIMETER,GRAM,SEC,ATM,KELVIN)
C
      WRITE(*,*) 'TEMPERATURE (K) ==> '
      READ(*,*) TEMP
      WRITE(*,*) 'TOTAL PRESSURE (TORR) ==> '
      READ(*,*) PREST
      WRITE(*,*) 'BCL3 FLOW RATE (SCCM) ==> '
      READ(*,*) FLOWRT(1)
      WRITE(*,*) 'ALCL3 FLOW RATE (SCCM) ==> '
      READ(*,*) FLOWRT(2)
      WRITE(*,*) 'NH3 FLOW RATE (SCCM) ==> '
      READ(*,*) FLOWRT(3)
      WRITE(*,*) 'AR FLOW RATE (SCCM) ==> '
```

```
      READ(*,*) FLOWRT(4)
      WRITE(*,*) 'H2 FLOW RATE (SCCM) ==> '
      READ(*,*) FLOWRT(5)
      WRITE(*,*) 'JET DIAMETER (INCHES) ==> '
      READ(*,*) DIAI
      WRITE(*,*) 'JET HEIGHT (INCHES) ==> '
      READ(*,*) HEII
      WRITE(*,*) 'DEPOSITION TIME (S) ==> '
      READ(*,*) TIME
      WRITE(*,*) 'EXPERIMENTAL BN DEP THICKNESS (CM) ==> '
      READ(*,*) ETBN
      WRITE(*,*) 'EXPERIMENTAL ALN DEP THICKNESS (CM) ==> '
      READ(*,*) ETALN
C
C CONVERSION TO CGS UNITS
C
      PRES=PREST/760.0
      HEI=HEII*2.54
      DIA=DIAI*2.54
      TOFLOW=FLOWRT(1)+FLOWRT(2)+FLOWRT(3)+FLOWRT(4)+FLOWRT(5)
      DO 103 L=1,5
      X(L)=FLOWRT(L)/TOFLOW
  103 CONTINUE
C
C PHYSICAL/THERMODYNAMIC PROPERTIES OF X(I)
C
C   EK=CHARACTERISTIC ENERGY/BOLTZMANS CONSTANT
C
      EK(1)=337.7
      EK(2)=524
      EK(3)=558.3
      EK(4)=93.3
      EK(5)=59.7
C
C   MOLECULAR DIAMETER
C
      MDIA(1)=5.127
      MDIA(2)=5.5
      MDIA(3)=2.900
      MDIA(4)=3.542
      MDIA(5)=2.827
C
C   MOLECULAR WEIGHT
C
      MW(1)=117.17
      MW(2)=133.34
      MW(3)=17.0
      MW(4)=39.95
      MW(5)=2.0
C
C SUBROUTINE CALVIS TO CALCULATE VISMIX & KINVIS
C
```

```
      CALL CALVIS(TEMP,PRES,R,X,EK,MDIA,MW,VISCO,
     1     VISMIX,DENAVG,KINVIS)
C
C WRITING PROCESSING PARAMETERS
C
      WRITE(*,1) TEMP,PRES,TOFLOW,DIA,HEI,TIME
    1 FORMAT(///5X,'TEMP=',F6.1,5X,'PRES=',F6.5,5X,
     1'FLOWRT=',F6.1,5X,/,1X,'DIA=',F6.3,5X,'HEI=',F6.3,5X,
     2'TIME=',F6.1)
      WRITE(*,2)  X(1),X(2),X(3),X(4),X(5)
    2 FORMAT(1X,'X(I)',6X,E10.5,5X,E10.5,5X,
     1E10.5,5X,E10.5,5X,E10.5)
C
C WRITING RESULTS FROM CALVIS
C
      WRITE(*,3)VISCO(1),VISCO(2),VISCO(3),VISCO(4),VISCO(5)
    3 FORMAT(1X,'VISCO(I)',2X,E10.5,5X,E10.5,5X,E10.5,5X,
     #      E10.5,5X,E10.5)
      WRITE(*,4) VISMIX,DENAVG,KINVIS
    4 FORMAT(1X,'VISMIX=',E10.5,5X,'DENAVG=',E10.5,5X,
     #      'KINVIS=',E10.5)
C
C SUBROUTINE CALDIF TO CALCULATE: RE, DELTAC, DIFFUC, JBN,
C                                 JALN
C
      CALL CALDIF(TEMP,PRES,R,X,EK,MDIA,MW,DIA,HEI,TIME,
     1TOFLOW,KINVIS,RE,DELTAC,DIFFUC,JBN,TBN,JALN,TALN,
     2OEBCL,COEALC,BNDEN,ALNDEN,BNMW,ALNMW)
C
C CONVERSION OF EXPERIMENTAL DATA
C    ETBN, ETALN
C    TO EJBN, EJALN
C    APPARENT KINETIC RATE CONSTANTS, AKBN, AKALN
C    INTRINSIC KINETIC RATE CONSTANTS, EKBN, EKALN
C
      EJBN=(ETBN/TIME)*(BNDEN/BNMW)
      EJALN=(ETALN/TIME)*(ALNDEN/ALNMW)
      IF(X(1).LE.0.0) GOTO 80
      AKBN=EJBN*R*TEMP/(X(1)*PRES)
   80 IF(X(2).LE.0.0) GOTO 81
      AKALN=EJALN*R*TEMP/(X(2)*PRES)
   81 IF(EJBN.LE.0.0) GOTO 82
      EKBN=COEBCL/(JBN/EJBN-1.0)
   82 IF(EJALN.LE.0.0) GOTO 83
      EKALN=COEALC/(JALN/EJALN-1.0)
C
C WRITING EXPERIMENTAL RESULTS
C
   83 WRITE(*,71)BNDEN, ALNDEN
   71 FORMAT(//1X,'BNDEN=',F6.3,5X,'ALNDEN=',F6.3)
      WRITE(*,72) ETBN,ETALN
   72 FORMAT(1X,'ETBN=',F7.5,5X,'ETALN=',F7.5)
```

```
      WRITE(*,73) EJBN,EJALN
   73 FORMAT(1X,'EJBN=',E10.5,5X,'EJALN=',E10.5)
      WRITE(*,74)AKBN,AKALN
   74 FORMAT(1X,'AKBN=',E10.5,5X,'AKALN=',E10.5)
      WRITE(*,75)EKBN,EKALN
   75 FORMAT(1X,'EKBN=',E10.5,5X,'EKALN=',E10.5)
C
C
C WRITING RESULTS FROM CALDIF
C
      WRITE(*,5) RE
    5 FORMAT(1X,'RE=',7X,E10.5)
      WRITE(*,6) DELTAC(1),DELTAC(2),DELTAC(3),DELTAC(4),
     1DELTAC(5)
    6 FORMAT(1X,'DELTAC(I)',1X,E10.5,5X,E10.5,5X,E10.5,5X,
     #     E10.5,5X,E10.5)
      WRITE(*,7) DIFFUC(1),DIFFUC(2),DIFFUC(3),DIFFUC(4),
     1DIFFUC(5)
    7 FORMAT(1X,'DIFFUC(I)',1X,E10.5,5X,E10.5,5X,E10.5,5X,
     #      E10.5,5X,E10.5)
      WRITE(*,9) COEBCL,COEALC
    9 FORMAT(1X,'MASS TRAN COEF. BCL3=',F7.3,5X,'MASS TRAN
     #COEF. ALCL3=',F7.3)
      WRITE(*,8) JBN,JALN,TBN,TALN
    8 FORMAT(1X,'JBN=',E10.5,5X,'JALN=',E10.5,5X,'TBN=',E10.5,
     #      5X,'TALN=',E10.5)
      STOP
      END
C
C
C
      SUBROUTINE CALVIS(TEMP,PRES,R,X,EK,MDIA,MW,VISCO,
     1VISMIX,DENAVG,KINVIS)
      DIMENSION X(5),EK(5),VISCO(5),THETA(5,5)
      REAL MW(5),MDIA(5),KINVIS,OMEGA
C
C  VISCOSITY  CALCULATIONS  USING  CHAPMAN-ENSKOG  RELATIONSHIP
C           FROM REID, PRAUSNITZ, SHERWOOD
C
      A=1.16145
      B=0.14874
      C=0.52487
      D=0.77320
      E=2.16178
      F=2.43787
      DO 11 I=1,5
      TSTAR=TEMP/EK(I)
      OMEGA=A/(TSTAR**B)+C/EXP(D*TSTAR)+E/EXP(F*TSTAR)
      VISCO(I)=26.69E-6*(MW(I)*TEMP)**0.5/(MDIA(I)**2.0*OMEGA)
   11 CONTINUE
C
C VISCOSITY OF GAS MIXTURES USING WILKE'S APPROXIMATION
```

```
C
      DO 12 I=1,5
      DO 13 J=1,5
      THETA(I,J)=(1.0+(VISCO(I)/VISCO(J))**0.5*
     1(MW(J)/MW(I))**0.25)**2.0/(8.0*(1.0+MW(I)/MW(J)))**0.5
   13 CONTINUE
   12 CONTINUE
      VISMIX=0.0
      DO 14 M=1,5
      SUMN=0.0
      DO 15 N=1,5
      SUMN=SUMN+X(N)*THETA(M,N)
   15 CONTINUE
      VISMIX=(X(M)*VISCO(M))/SUMN+VISMIX
   14 CONTINUE
C
C DENSITY OF GAS MIXTURE USING IDEAL GAS LAW
C
      AVGMW=0.0
      DO 16 I=1,5
      AVGMW=X(I)*MW(I)+AVGMW
   16 CONTINUE
      DENAVG=(PRES*AVGMW)/(R*TEMP)
C
C KINEMATIC VISCOSITY, KINVIS
C
      KINVIS=VISMIX/DENAVG
      RETURN
      END
C
C
C
      SUBROUTINE CALDIF(TEMP,PRES,R,X,EK,MDIA,MW,DIA,HEI,
     1TIME,TOFLOW,KINVIS,RE,DELTAC,DIFFUC,JBN,TBN,
     2JALN,TALN,COEBCL,COEALC,BNDEN,ALNDEN,BNMW,ALNMW)
      DIMENSION X(5),EK(5),DIFFUC(5),DELTAC(5)
      REAL MDIA(5),MW(5),MDIAAV,JALN,JBN,KINVIS,OMEGAD
C
C DIFFUSION COEFICIENT CALCULATIONS USING CHAPMAN-ENSKOG
C THEORY
C ALSO, PSEUDO BINARY MIXURE OF X(I) AND X(4) IS ASSUMED
C(EXCESS AR).
C
      AD=1.06036
      BD=0.15610
      CD=0.19300
      DD=0.47635
      ED=1.03587
      FD=1.52996
      GD=1.76474
      HD=3.89411
      DO 21 I=1,5
```

```
      EKAVG=(EK(I)*EK(4))**0.5
      MDIAAV=(MDIA(I)+MDIA(4))/2.0
      TDSTAR=TEMP/EKAVG
      OMEGAD=AD/TDSTAR**BD+CD/EXP(DD*TDSTAR)+
     1ED/EXP(FD*TDSTAR)+GD/EXP(HD*TDSTAR)
      DIFFUC(I)=1.858E-3*(TEMP**1.5)*((MW(I)+MW(4))/
     1(MW(I)*MW(4)))**0.5/(PRES*OMEGAD*(MDIAAV**2.0))
   21 CONTINUE
C
C BOUNDARY LAYER THICKNESS CALCULATIONS
C
      PI=3.14
      AREA=(PI/4.0)*DIA**2.0
      VEL=((TOFLOW/60.0)*(TEMP/273)*(1.0/PRES))/AREA
C
C   REYNOLDS NUMBER
C
      RE=VEL*DIA/KINVIS
C
C   CORRELATIONS GIVEN BY CHIN & TSANG FOR CONCENTRATION
C   BOUNDARY LAYER THICKNESS
C
      HBAR=HEI/DIA
      ASTAR=1.5129*(HBAR**(-0.204))
      AAA=ASTAR*VEL/DIA
      DELTAM=2.76*(KINVIS/(2.0*AAA))**0.5
C
C
      DO 31 I=1,5
      SC=KINVIS/DIFFUC(I)
      GSC=1-0.084593/(SC**(1/3))-0.016368/
     1(SC**(2/3))-0.0057398/SC+0.0014288/(SC**(4/3))
      DELTAC(I)=DELTAM/(GSC*SC**(1.0/3.0))
   31 CONTINUE
      COEBCL=DIFFUC(1)/DELTAC(1)
      COEALC=DIFFUC(2)/DELTAC(2)
C
C DENSITY & MW OF BN AND ALN
C
C  BNDEN BASED ON MOORE'S DATA
C
      BNDEN=1.60
      BNMW=24.81
      ALNDEN=3.26
      ALNMW=40.98
C
C DEPOSITION RATE, J, AND THICKNESS, T, OF BN AND ALN
C
      JBN=DIFFUC(1)*X(1)*PRES/(R*TEMP*DELTAC(2))
      TBN=JBN*TIME*BNMW/BNDEN
      JALN=DIFFUC(2)*X(2)*PRES/(R*TEMP*DELTAC(2))
      TALN=JALN*TIME*ALNMW/ALNDEN
```

```
      RETURN
      END
```

BIBLIOGRAPHY

1. D.P. Stinton, T.M. Besmann, and R.A. Lowden, "Advanced Ceramics by Chemical Vapor Deposition Techniques," Ceramic Bulletin, 67, 350 (1988).

2. W.J. Lackey, A.W. Smith, D.M. Dillard, and D.J. Twait, "Codeposition of Dispersed Phase Ceramic Composites," pp. 1008-1027 in Proceedings of the 10th International Conference on Chemical Vapor Deposition, ed. G.W. Cullen, The Electrochemical Society, Inc., Pennington, NJ, 1987.

3. T. Hirai and T. Goto, "CVD Fabrication of In-Situ Composites of Non-Oxide Ceramics," pp. 165-177 in Materials Science Research Vol. 20, ed. R.E. Tressler et al., Plenum Press, New York, 1986.

4. T. Hirai, T. Goto, and T. Sakai, "Preparation of Si_3N_4-BN Composites by Chemical Vapor Deposition," pp. 347-358 in Materials Science Research Vol. 17, ed. R.F. Davis et al., Plenum Press, New York, 1984.

5. T. Hirai, "CVD of Si_3N_4 and Its Composites," pp. 329-345 in Materials Science Research Vol. 17, ed. R.F. Davis et al., Plenum Press, New York, 1984.

6. N.J. Archer, "The Preparation and Properties of Pyrolytic Boron Nitride," pp. 167-180 in High Temperature Chemistry of Inorganic and Ceramic Materials, ed. F.P. Glassen and P.E. Potter, The Chemical Society, Burlington House, London, 1976.

7. Private Communication with A.W. Moore, who has studied BN for more than twenty years and is currently with the Specialty Products Group of the Union Carbide Corporation, Cleveland, Ohio, June 1989.

8. "Boroalloy; Pyrolytic Boron Nitride", Product Specification from the Union Carbide Corporation, Cleveland, Ohio.

9. E.L. Muetterties, "The Chemistry of Boron and Its Compounds," John Wiley & Sons, New York, 1967.

10. G. Clerc and P. Gerlach, "Pyrolytic Boron Nitride," pp. 777-785 in Proceedings of the 5th International Conference on Chemical Vapor Deposition, ed. J.M. Blocher et al., The Electrochemical Society, Princeton, NJ, 1975.

11. C.E. Frahme, "The Chemical Vapor Deposition of Pyrolytic Boron Nitride", Ph.D. Dissertation, Rutgers University, 1966.

12. H. Tanji, K. Monden, and M. Ide, "CVD Mechanism of Pyrolytic Boron Nitride," pp. 562-569 in Proceedings of the 10th International Conference on Chemical Vapor Deposition," ed. G.W. Cullen, The Electrochemical Society, Pennington, NJ, 1987.

13. G. Malé and D. Salanoubat, "Preparation of Pyrolytic Boron Nitride (PBN) by CVD at Reduced Pressure," pp. 391-397 in Proceedings of the 7th International Conference on Chemical Vapor Deposition, ed. T.O. Sedgwick and H. Lydtin, The Electrochemical Society, Princeton, NJ, 1979.

14. T. Matsuda, N. Uno, H. Nakae, and T. Hirai, "Synthesis and Structure of Chemically Vapour-Deposited Boron Nitride," J. Mater. Sci., 21, 649 (1986).

15. T. Takahashi, H. Itoh, and A. Takeuchi, "Chemical Vapor Deposition of Hexagonal Boron Nitride Thick Films on Iron," J. Crystal Growth, 47, 245 (1979).

16. T. Takahashi, H. Itoh, and M. Kuroda, "Structure and Properties of CVD-BN Thick Film Prepared on Carbon Steel Substrate," J. Crystal Growth, 53, 418 (1981).

17. S. Motojima, Y. Tamura, and K. Sugiyama, "Low Temperature Deposition of Hexagonal BN Films by Chemical Vapor Deposition," Thin Solid Films, 88, 269 (1982).

18. J. Thomas, N.E. Weston, and T.E. O'Conner, "Turbostratic Boron Nitride, Thermal Transformation to Ordered-Layer-Lattice Boron Nitride," J. Am. Chem. Soc., 84, 4619 (1963).

19. A.W. Moore, "Compression Annealing of Pyrolytic Boron Nitride," Nature, 221, 1133 (1969).

20. T. Matsuda, H. Nakae, and T. Hirai, "Density and Deposition Rate of Chemical-Vapour-Deposited Boron Nitride," J. Mater. Sci., 23, 509 (1988).

21. M. Sano and M. Aoki, "Chemical Vapor Deposition of Thin Films of BN onto Fused Silica and Sapphire," Thin Solid Films, 83, 247 (1981).

22. H. Hannache, R. Naslain, and C. Bernard, "Boron Nitride Chemical Vapour Infiltration of Fibrous Materials From BCl_3-NH_3-H_2 or BF_3-NH_3 Mixtures: A Thermodynamic and Experimental Approach," J. Less-Common Metals, 95, 221 (1983).

23. Y. Kurokawa, K. Utsumi, and H. Takamizawa, "Development and Microstructural Characterization of High-Thermal-Conductivity Aluminum Nitride Ceramics," J. Am. Ceram. Soc., 71, 588 (1988).

24. T. Yogi, K. Shinozaki, N. Ishizawa, N. Mizutani, M. Kato, and A. Tsuge, "Effect of Silicon Dioxide on the Thermal Diffusivity of Aluminum Nitride Ceramics," J. Am. Ceram. Soc., 71, C-334 (1988).

25. N. Iwase, K. Anzai, and K. Shinozaki, "Aluminum Nitride Substrates Having High Thermal Conductivity," Solid State Technology, 135, (October 1986).

26. M. Morita, N. Uesugi, S. Isogai, K. Tsubouchi, and N. Mikoshiba, "Epitaxial Growth of Aluminum Nitride on Sapphire Using Metalorganic Chemical Vapor Deposition," Japanese J. Appl. Phys., 20, 17 (1981).

27. W.M. Yim, E.J. Stofko, P.J. Zanzucchi, J.I. Pankove, M. Ettenberg, and S.L. Gilbert, "Epitaxially Grown AlN and Its Optical Band Gap,", J. Appl. Phys., 44, 292 (1973).

28. R.M. Kelm, "Aluminum Nitride as a Dielectric for Silicon Devices," Ph.D. Dissertation, Southern Methodist University, 1973.

29. J. Bauer, L. Biste, and D. Bolze, "Optical Properties of Aluminum Nitride Prepared by Chemical and Plasmachemical Vapour Deposition," Phys. Stat. Sol., (a)39, 173 (1977).

30. L.V. Interrante, W. Lee, M. McConnell, N. Lewis, and E. Hall, "Preparation and Properties of Aluminum Nitride Films Using an Organometallic Precursor," J. Electrochem. Soc., 136, 472 (1989).

31. Y. Chubachi, K. Sato, and K. Kojima, "Reflection High Energy Electron Diffraction and X-ray Studies of AlN Films Grown on Si(111) and Si(001) by Organometallic Chemical Vapor Deposition," Thin Solid Films, 122, 259 (1984).

32. M. Suzuki and H. Tanji, "CVD of Polycrystalline Aluminum Nitride," pp. 1089-1097, in Proceedings of the 10th International Conference on Chemical Vapor Deposition, ed. G.W. Cullen, The Electrochemical Society, Inc., Pennington, NJ, 1987.

33. Y. Pauleau, A. Bouteville, J.J. Hantzepergue, J.C. Remy, and A. Cachard, "Thermodynamics and Kinetics of Chemical Vapor Deposition of Aluminum Nitride Films," J. Electrochem. Soc., 127, 1532 (1980).

34. Y. Pauleau, A. Bouteville, J.J. Hantzpergue, and J.C. Remy, "Kinetics of Deposition and Growth Mechanisms of Aluminum Nitride Films," pp. 104-115 in Proceedings of the 8th International Conference on Chemical Vapor Deposition, ed. J.M. Blocher et al., The Electrochemical Society, Inc., Pennington, NJ, 1981.

35. Y. Pauleau, A. Bouteville, J.J. Hantzepergue, J.C. Remy, and A. Cachard, "Chemical Vapor Deposition of Aluminum Nitride Films in the Aluminumbromide-Ammonia-Hydrogen System," Bull. Soc. Chim. France, I, 127 (1980).

36. H. Arnold, L. Biste, D. Bolze, G. Eichhorn, "Chemical and Plasmachemical Vapour Deposition of Aluminum Nitride Layers," Kristall and Technik, 11, 17 (1976).

37. S.H. Hyun and J.H. Kim, "Thermodynamic Equilibrium Compositions for a NH_3-$AlCl_3$-H_2 Vapor-Phase Reacting System and Synthesis of a High-Purity AlN," J. Korean Ceram. Soc., 23, 33, (1986).

38. V.K. Sarin, "Development of Adherent Ceramic Coatings to Reduce Contact Stress Damage of Ceramics," ORNL/TM-10705, Oak Ridge National Laboratory, Oak Ridge, TN, 1987.

39. I. Kimura, N. Hotta, H. Nukui, N. Saito, S. Yasukawa, "Synthesis of Fine AlN Powder by Vapour-Phase Reaction," J. Mater. Sci. Lett., 7, 66 (1988).

40. S.S. Kim and S.C. Lee, "Preparation of Fine Metal Nitride Powders (II) - Formation of Aluminum Powders by the Vapor Phase Reaction," J. Korean Institute of Metals, 23, 37 (1985).

41. H. Komiyama, T. Osawa, Y. Shimogaki, N. Wakita, M. Minamiyama, and T. Ueoka, "Particle Precipitation Aided Chemical Vapor Deposition for Rapid Growth of Ceramic Films - Preparation of 1mm-Thick AlN, TiO_2, and ZrO_2 films," pp. 1119-1128, in Proceedings of the 10th International Conference on Chemical Vapor Deposition, ed. G.W. Cullen, The Electrochemical Society, Inc., Pennington, NJ, 1987.

42. T.M. Besmann, "Thermodynamic Analysis of the Chemical Vapor Deposition of Composite <Si_3N_4>-<BN> Coatings," J. Am. Ceram. Soc., **69**, 69 (1986).

43. S. Zirinsky and E.A. Irene, "Selective Studies of Chemical Vapor-Deposited Aluminum Nitride-Silicon Nitride Mixture Films," J. Electrochem. Soc., **125**, 305 (1978).

44. E.A. Irene, V.J. Silvestri, and G.R. Woolhouse, "Some Properties of Chemically Vapor Deposited Films of $Al_xO_yN_z$ on Silicon," J. Electron. Mater., **4**, 409 (1975).

45. V.J. Silvestri, E.A. Irene, S. Zirinsky, and J.D. Kuptsis, "Chemical Vapor Deposition of $Al_xO_yN_z$ Films," J. Electron. Mater., **4**, 429 (1975).

46. C.A. Willkens, "Chemical Vapor Deposition of Materials in the Silica-Aluminum-Carbon-Nitrogen System," M.S. Thesis, University of Illinois at Urbana-Champaign, 1981.

47. T. Hirai and S. Hayashi, "Preparation and Some Properties of Chemically Vapour-Deposited Si_3N_4-TiN Composite," J. Am. Ceram. Soc., **17**, 1320 (1982).

48. J.M. Blocher, Jr., "Nuclear Fuel Particles Coated with Mixture of Pyrolytic Carbon and Silicon Carbide," U.S. Patent No. 3,249,509, May 3, 1966.

49. J.L. Kaae and T.D. Gulden, "Structure and Mechanical Properties of Codeposited Pyrolytic C-SiC Alloys," J. Am. Ceram. Soc., **54**, 605 (1971).

50. R.J. Akins and J.C. Bokros, "The Deposition of Pure and Alloyed Isotropic Carbons in Steady-State Fluidized Beds," Carbon, **12**, 439 (1974).

51. D.P. Stinton and W.J. Lackey, "Simultaneous Chemical Vapor Deposition of SiC-Dispersed Phase Composites," Ceramic Eng. Sci. Proc., **6**, 707 (1985).

52. D.P. Stinton, W.J. Lackey, R.J. Lauf, and T.M. Besmann, "Fabrication of Ceramic-Ceramic Composites by Chemical Vapor Deposition," Ceramic Eng. Sci. Proc., 5, 668 (1984).

53. J.J. Nickl, K.K. Schweitzer, P. Luxenberg, and A. Weiss, "Chemical Vapor Deposition of the Systems Ti-Si-C and Ti-Ge-C," pp. 4-23 in Proceedings of the 3rd International Conference on Chemical Vapor Deposition, ed. F.A. Glaski, The American Nuclear Society, Hinsdale, IL, 1972.

54. J.J. Nickl and K.K. Schweitzer, "Preparation of Intermetallic Compounds by Chemical Vapor Deposition," pp. 297-327 in Proceedings of the 2nd International Conference on Chemical Vapor Deposition, eds. J.M. Blocher, Jr. and J.C. Withers, The Electrochemical Society, NY, 1970.

55. K.S. Mazdiyasni, R. Ruh, and E.E. Hermes, "Phase Characterization and Properties of AlN+BN Composites," Am. Ceram. Soc. Bull., 64, 1149 (1985).

56. W.B. White, W.M. Johnson, and G.B. Dantzig, "Chemical Equilibrium in Complex Mixtures," J. Chem. Phys., 28, 751 (1958).

57. G. Eriksson, "Thermodynamic Studies of High Temperature Equilibria, III. Solgas, a Computer Program for Calculating the Composition and Heat Condition of an Equilibrium Mixture," Acta. Chem. Scand., 25, 2651 (1971).

58. G. Eriksson, "Thermodynamic Studies of High Temperature Equilibria, XII. Solgasmix, a Computer Program for Calculation of Equilibrium Compositions in Multiphase Systems," Chem. Sci., 8, 100 (1975).

59. T.M. Besmann, "SOLGASMIX-PV, a Computer Program to Calculate Equilibrium Relationships in Complex Chemical Systems," ORNL/TM-5775, Oak Ridge National Laboratory, Oak Ridge, TN, April 1977.

60. H. Rebenne and R. Pollard, "Theoretical Analysis of Chemical Vapor Deposition of Ceramics in an Impinging Reactor," J. Am. Ceram. Soc., 70, 907 (1987).

61. D.J. Twait, "Codeposition of Boron Nitride Plus Aluminum Nitride Composites by Chemical Vapor Deposition," M.S. Thesis, Georgia Institute of Technology, June 1989.

62. M.S. Wang and K.E. Spear, "Experimental and Thermodynamic Investigations of the V-Si-H-Cl System," pp. 98-111 in Proceedings of the 9th International Conference on Chemical Vapor Deposition, ed. McD. Robinson et al., The Electrochemical Society, Pennington, NJ, 1984.

63. A.I. Kingon, L.J. Lutz, P. Liaw, and R.F. Davis, "Thermodynamic Calculations for the Chemical Vapor Deposition of Silicon Carbide," J. Am. Ceram. Soc., 66, 558 (1983).

64. A.I. Kingon, L.J. Lutz, and R.F. Davis, "Thermodynamic Calculations for the Chemical Vapor Deposition of Silicon Nitride," J. Am. Ceram. Soc., 66, 551 (1983).

65. L. Singheiser, G. Wahl, and F. Hegewaldt, "Deposition of Boron from $BCl_3/H_2/N_2$ Gas Mixtures on Steels with Low Alloy Content," pp. 625-638 in Proceedings of the 9th International Conference on Chemical Vapor Deposition, ed. McD. Ronbinson et al., The Electrochemical Society, Pennington, NJ, 1984.

66. G.S. Fischman and W.T. Petuskey, "Thermodynamic Analysis and Kinetic Implications of Chemical Vapor Deposition of SiC from Si-C-Cl-H Gas Systems," J. Am. Ceram. Soc., 68, 185, (1985).

67. R.G. Behrens, L.R. Newkirk, and T.C. Wallace, "Thermodynamics of the Tantalum-Carbon-Chlorine-Hydrogen System Applied to the CVD of Carbide/Carbon Materials," Report presented at the 82nd Annual Meeting of the American Ceramic Society, LA-UR-80-1252, U.S.D.O.E., Los Alamos Scientific Laboratory, Los Alamos, NM, 1980.

68. D.J. Twait, W.J. Lackey, A.W. Smith, W.Y. Lee, and J.A. Hanigofsky, "Thermodynamic Analysis of the Chemical Vapor Deposition of BN+AlN Composite Coatings," Submitted to J. Am. Ceram. Soc. (1989).

69. D.W. Hess, K.F. Jensen, and T.J. Anderson, "Chemical Vapor Deposition: a Chemical Engineering Perspective," Rev. Chem. Eng., 3, 97 (1985).

70. K.F. Jensen, "Modeling of Chemical Vapor Deposition Reactors", pp. 3-20 in Proceedings of the 9th International Conference on Chemical Vapor Deposition, ed. McD Robinson et al., The Electrochemical Society, Pennington, NJ, 1984.

71. L. Vandenbulcke, "Mass Transfer, Equilibrium, and Kinetics in the CVD of a Polycomponent System: Application to Boron-Carbon," pp. 315-331 in Proceedings of the 7th International Conference on Chemical Vapor Deposition, ed., T.O. Sedwick and H. Lydtin, The Electrochemical Society, Princeton, NJ, 1979.

72. L. Vandenbulcke and G. Vuillard, "Kinetics in Chemical Vapor Deposition of Boron Carbide," pp. 95-103 in Proceedings of the 8th International Conference on Chemical Vapor Deposition, ed. J.M. Blocher et al., The Electrochemical Society, Pennington, NJ, 1981.

73. K.F. Roenigk and K.F. Jensen, "Analysis of Multicomponent LPCVD Processes: Deposition of Pure and In-Situ Doped Poly-Si," J. Electrochem. soc., 132, 448 (1985).

74. K.F. Roenigk and K.F. Jensen, "Low Pressure CVD of Silicon Nitride," J. Electrochem. Soc., 125, 1461 (1987).

75. G.F. Froment, "Model Discrimination and Parameter Estimation in Heterogeneous Catalysis", AIChE J., 21, 1041 (1975).

76. D-T. Chin and C-H. Tsang, "Mass Transfer to an Impinging Jet Electrode", J. Electrochem. Soc., 125, 1461 (1978).

77. H. Schlichting, "Boundary Layer Theory," pp. 70-73, McGraw-Hill Book Co., New York, 1955.

78. J.W. Daily and D.R.F. Harleman, "Fluid Dynamics," Addison-Wesley Co., Massachusetts, 1966.

79. C. Houtman, D.B. Graves, and K.F. Jensen, "CVD in Stagnation Point Flow", J. Electrochem. Soc., 133, 961 (1986).

80. L. Vandenbulcke and G. Vuillard, "Chemical Vapor Deposition of Boron on Massive Substrates," J. Electrochem. Soc., 123, 278 (1976).

81. M. Michaelidis and R. Pollard, "Analysis of Chemical Vapor Deposition of Boron," J. Electrochem. Soc., 131, 860 (1984).

82. G. Wahl, "Hydrodynamic Description of CVD Processes," Thin Solid Films, 40, 13 (1977).

83. W.A.P. Claassen, J. Bloem, W.G.J.N. Valkenburg, and C.H.F. Van den Brekel, "The Deposition of Silicon from Silane and Low-Pressure Hot-Wall Systems," J. Crystal Growth, 57, 259 (1982).

84. M.E. Coltrin, R.J. Kee, and J.A. Miller, "Mathematical Model of the Coupled Fluid Dynamics and Chemical Kinetics in a Chemical Vapor Deposition Reactor," J. Electrochem. Soc., 131, 425 (1984).

85. J.P. Hirth and G.M. Pound, "Condensation and Evaporation-Nucleation and Growth Processes," Pergamon Press, NY, 1966.

86. W.D. Kingery, H.K. Bowen, and D.R. Uhlman, "Introduction to Ceramics," 2nd ed., John Wiley & Sons, New York, 1976.

87. G.A. Somorjai, "Principles of Surface Chemistry," pp. 101-105, Prentice-Hall, Englewood Cliffs, NJ, 1972.

88. J.J. Wu and R.C. Flagan, "Onset of Runaway Nucleation in Aerosol Reactors," J. Appl. Phys., 61, 1365 (1987).

89. M.K. Alam and R.C. Flagan, "Controlled Nucleation Aerosol Reactors: Production of Bulk Silicon," Aero. Sci. and Tech., 5, 237 (1986).

90. J.J. Wu, D.W. Cooper, and R.J. Miller, "Formation of Submicron Particles from Chemical Vapor Deposition," Presented at the Symposium on Particulate Contamination Control in Microelectronics, the American Association for Aerosol Research, Chapel Hill, NC, October 10-14, 1988.

91. D. Walton, "Nucleation of Vapor Deposits", J. Chem. Phys., 37, 2182 (1962).

92. B. Lewis and D.S. Campbell, "Nucleation and Initial Growth Behavior of Thin-Film Deposits," J. Vac. Sci. Tech., 4, 209 (1967).

93. J. Bloem, "Nucleation of Silicon on Amorphous and Crystalline Substrates," pp. 41-58 in Proceedings of the 7th International Conference on Chemical Vapor Deposition, ed. T.O. Sedgwick and H. Lydtin, The Electrochemical Society, Princeton, NJ, 1979.

94. J. Bloem, "Nucleation and Growth of Silicon by CVD," J. Crystal Growth, 50, 581 (1980).

95. R.F. Davis, "Interfacial Phenomena during Chemical Vapor Deposition," pp. 379-390 in Materials Science Research Vol. 14, ed. J. Pask and A. Evans, Plenum Press, NY, 1981.

96. C.W. Thomas, "Anhydrous Aluminum Chloride in Organic Chemistry," American Chemical Society-Monograph Series, Reinhold Publishing Corp., NY.

97. A.H. Shapiro, "Turbulent Transfer Processes in Parallel Jets," pp. 141-143 in Symposium on Hydrodynamics in Modern Technology, M.I.T., Hydrodynamics Laboratory, 1951.

98. R.C. Reid, J.H. Prausnitz, and T.K. Sherwood, "The Properties of Gases and Liquids," 3rd ed., McGraw-Hill Book Co., NY, 1977.

99. C.G. Hill, "An Introduction to Chemical Engineering Kinetics & Reactor Design," John Wiley & Sons, NY, 1977.

100. K. Hiraga, M. Hirabayashi, S. Hayashi, and T. Hirai, "High Resolution Electron Microscopy of Chemically Vapor-Deposited β-Si_3N_4-TiN Composites," J. Am. Ceram. Soc., 66, 539 (1983).

101. J.L. Kaae, "The Mechanism of the Deposition of Pyrolytic Carbons," Carbon, 23, 665 (1985).

102. JANAF Thermochemical Tables, 2nd ed., Nat. Stand. Ref. Data Ser., Nat. Bur. Stand. (U.S.), 37, 1141 pages (1971).

102. JANAF Thermochemical Tables, 3rd ed., Vols. I and II, ed. David R. Lide, Jr., American Chemical Society and American Institute of Physics for Nat. Bur. Stand. (U.S.), 14, 1856 pages (1985)

ACKNOWLEDGMENTS

This report is largely based on the Ph.D. dissertation of Woo Y. Lee of the School of Chemical Engineering. His excellent contribution to this project is gratefully acknowledged. The financial support of Dr. Donald E. Polk of the Office of Naval Research made this work possible. On several occasions his efficient management contributed to the success of this project. The capable assistance of Ruth Thompson in preparing this report is appreciated.